SPIN QUBITS IN SILICON FIN FIELD-EFFECT TRANSISTORS

Inauguraldissertation
zur
Erlangung der Würde eines Doktors der Philosophie
vorgelegt der
Philosophisch-Naturwissenschaftlichen Fakultät
der Universität Basel
von

Simon Geyer

2023

Genehmigt von der Philosophisch-Naturwissenschaftlichen Fakultät
auf Antrag von

Erstbetreuer: Prof. Dr. Richard J. Warburton

Zweitbetreuer: Prof. Dr. Dominik M. Zumbühl

Externer Experte: Prof. Dr. Arne Laucht

Basel, den 20. Juni 2023

Prof. Dr. Marcel Mayor
Dekan

ABSTRACT

Quantum computing holds the promise of solving certain tasks faster than any classical computer. The fundamental building block of a quantum computer is the qubit, which can be realised in various different systems including trapped ions, superconducting circuits or semiconductor quantum dots. The latter platform is used to host spin qubits, where the spin state of a single electron or hole is used to encode quantum information. Spin qubits in silicon offer distinct advantages over other materials in terms of scalability by leveraging well-established complementary-metal-oxide-semiconductor technology from the classical computer industry.

While spin qubits typically operate at milikelvin temperatures, classical control electronics are maintained at room temperature, leading to a wiring bottleneck and challenges in cooling, which hinder scalability. Silicon, in this regard, presents a solution: by elevating the spin qubit operation temperature above 1 Kelvin, where cooling power is dramatically increased, it becomes feasible to integrate classical control electronics and quantum hardware in the same package, paving the way for a truly scalable unit cell. Recent advancements have demonstrated the operation of electron spin qubits in silicon at elevated temperatures. Hole spins, an alternative to electron spins, possess unique advantages such as fast, all-electric spin control via a strong intrinsic spin-orbit interaction, absence of valleys and sweet spots for charge and nuclear spin noise. However, despite their potential, hole spin qubits in silicon still lag behind their electron counterparts in crucial aspects, including operation at elevated temperatures and the demonstration of entangling two-qubit gates, which are essential for universal quantum computing.

This thesis explores the potential of hole spin qubits hosted in silicon fin field-effect transistors, one of the industry's standard transistors. The device design is optimised for quantum applications through the introduction of a self-aligned gate layer and its ability to host quantum dots is demonstrated. The devices are used to define hole spin qubits, which are driven all-electrically via electric-dipole spin resonance, and their spin state is read out using Pauli spin blockade. A driving speed exceeding 100 MHz and a qubit coherence time T_2^* greater than 400 ns is observed and a single-qubit gate fidelity of $\sim 99\%$ is reported at 1.5 K. The robustness of these hole spin qubits against further increase of temperature is demonstrated by operating the qubit even above 4 K, albeit with a reduction of coherence and a whitening of the noise spectrum. Furthermore, the anisotropy of hole spins in silicon is investigated by measuring and modelling the magnetic field orientation-dependence of the effective g-factor and the qubit driving speed and coherence, showcasing sweet spots in the qubit quality factor. Disentangling the influence of two driving mechanisms enables control over the type of driving by applying the microwave driving tone to different gate electrodes. Additionally, a formalism is developed to model the anisotropic nature of the exchange interaction between two neighbouring qubits, enabling the extraction of the full exchange matrix. The model for anisotropic exchange allows sweet spots for fast, high-fidelity two-qubit gates to be predicted and in a close-to-optimal configuration a CROT operation is demonstrated in just 24 ns. Furthermore, a conceptually different drive to the standard Rabi drive, the phase drive, is explored. By incorporating a second far-detuned driving tone, resonant Rabi oscillations can be suppressed and reappear at tunable sidebands, offering opportunities for global driving schemes and noise mitigation. In summary, the interesting physics of hole spins in silicon is investigated, and key technological milestones for hole spin qubits in silicon fin field-effect transistors are demonstrated throughout this work.

CONTENTS

1

INTRODUCTION

This chapter provides an introduction to the topics of quantum computing, spin qubits and quantum dots. Furthermore, silicon fin field-effect transistors are introduced and their potential as a host for spin qubits is discussed.

A quantum computer exploits quantum mechanical phenomena to exponentially speed up certain computations, making it potentially more powerful than any classical computer. However, the quantum computer's greatest challenge is scaling up. Several decades ago, classical computers faced the same problem and a single solution emerged: very-large-scale integration (VLSI) using silicon. Today's silicon chips consist of tens of billions densely integrated metal-oxide-semiconductor field-effect transistors (MOSFETs) and provide enormous computational power. VLSI is achieved using high-yield complementary-metal-oxide-semiconductor (CMOS) processes, in which football-field sized cleanroom facilities are used to pattern silicon wafers of up to 450 mm diameter with transistors of a few 10s of nm [HL21]. One of the latest transistor designs is the fin field-effect transistor (FinFET) [Aut12; Aut17], where the current flow along the fin-shaped channel is controlled by wrap-around gates. In the quest of scaling up the transistor density, transistors are continuously miniaturised down to the point where quantum effects start to dominate over their classical behaviour. While this is problematic for classical computers, it provides an attractive opportunity for quantum applications: at low temperature, a single charge can be trapped under the gate and serve as a spin quantum bit (qubit) [LD98], the quantum equivalent of a classical bit.

While a classical bit can take either the value of 0 (off) or 1 (on), a qubit can occupy the states $|0\rangle$, $|1\rangle$ or a superposition of the two states. Unlike classical bits, multiple qubits can be entangled, such that their properties can no longer be described independently. The quantum phenomena of superposition and entanglement allow a quantum computer to encode exponentially more states than a classical computer and promise an exponential speed-up for certain algorithms [NC10]. Well-known examples for such quantum algorithms promise high impact on real-life applications, such as prime factorisation to decipher encrypted messages [Sho94] or molecule simulations to increase efficiency in production of e.g. fertiliser [Rei17].

Quantum states are very sensitive to small fluctuations in the environment, which can lead to information loss. In recent years, qubits have been optimised, achieving error rates below 1% in a wide range of systems [Hon20; Rol19; Bal16; Chr20; Shi22; Bra19; Mad22]. These slightly noisy qubits are now available in numbers of up to hundreds, allowing quantum algorithms for the first time to have an advantage over their classical counterparts [Aru19; Wu21]. This regime of quantum computing is called noisy intermediate-scale quantum computing (NISQ) [Pre18], because it still relies on qubits that are intrinsically prone to errors. To overcome this issue and achieve universal quantum computing, researchers have proposed quantum error correction algorithms [Sho95; Kit03; Cai21]. These algorithms use many physical qubits with sufficiently low error rates to create a single logical qubit that is immune to errors. The redundancy of physical qubits enables the detection and elimination of errors, allowing for fault-tolerant quantum computing. However, a significant number of physical qubits is needed to form a single logical qubit, typically ranging from 1,000 to 1,000,000 [Fow12]. Hence, performing a useful quantum algorithm without errors can easily require millions of physical qubits.

In principle any quantum mechanical two-level system can encode a qubit. Currently, there are several advanced and commercially available qubit platforms; prime examples are superconducting qubits by IBM [IBMa], Google [Aru19] and Rigetti [Rig] and trapped ion qubits by IonQ [Ion] and Honeywell [Pin21]. Theses systems feature tens to hundreds of high-quality qubits. However, scaling up these platforms to millions of qubits remains an open challenge. Here, quantum dot spin qubits [LD98; Bur21] promise an advantage over other technologies, even though the currently most advanced spin qubit processor contains only six qubits [Phi22]. These qubits can be hosted in structures similar to classical transistors, potentially allowing for dense integration on semiconductor chips by leveraging decades of experience of the semiconductor industry [Gon21].

In a spin qubit, information is encoded onto the spin state of an electron or hole confined to a quantum dot (QD), a potential well in a semiconductor. Initial research on spin qubits focused on the III-V material gallium arsenide [Elz04; Pet05; Col13; Now07], where most isotopes have a non-zero nuclear spin. The nuclear spin ensemble forms a noisy magnetic environment that couples to the spin qubit, reducing coherence [Pet05; KNV08]. More recently, silicon (Si) and germanium (Ge) emerged as the materials of choice [Sca20; Gon21], with a small natural abundance of non-zero nuclear spin isotopes and the option for isotopic purification. Silicon's compatibility with commercial CMOS processes presents the prospect of high-yield and large-scale fabrication. Additionally, Si-based classical control electronics can be integrated on-chip with dense arrays of interconnected spin qubits [Van17; Vel17; Bot22], promising to overcome the challenge in wiring up large numbers of qubit devices [Fra19]. Integrating classical electronics [Xue21] requires qubit operation at elevated temperatures [Pet20a; Pet20b; Yan20; Cam22] to overcome heat dissipation, since the available cooling power scales with temperature. Furthermore, Si spin qubits offer outstanding properties such as long coherence times [Vel14], fast manipulation [Mau16; Cam22; Fro21b] and high quality factors [Tak16; Yon17; Yan19].

Spin qubits come in two distinct flavours: electron [Vel14; Kaw14; Tak16; Yon17; Pet20a; Yan20; Zaj18; Wat18a] and hole [BL05; Mau16; Voi15; Wat18b; Hen20b; Hen20a; Hen21; Fro21b]. Hole spins can be manipulated all-electrically via electric-dipole spin resonance (EDSR) [GBL06; Now07; BL07; Nad10a; Kat03; Are13; Voi15; Cri18]. The strong intrinsic spin-orbit interaction (SOI) [Win03] in holes couples an oscillating electric field to the spin degree of freedom. In contrast, electron spins are typically manipulated using magnetic fields or artificial spin-orbit interaction, which requires additional components such as microwave transmission lines [Vel14; Pet20a] or micromagnets [Kaw14; Tak16; Yon17]. These extra components increase device complexity and hinder scalability. Recently, ways to engineer a strong SOI for all-electric spin manipulation were also explored for electrons [Gil23]. Both electric and magnetic spin drives enable single-qubit operations with high fidelity above 99.9% [Yon17; Phi22; Yan19; Law21; Hen21]. Hole spins in a strong one-dimensional confinement potential are subject to an exceptionally strong and fully tunable SOI, enabling a switchable coupling strength and a way to mitigate the effects of charge noise [KTL11; KL13; KRL18; BHL21; Fro21b; Mic23; Pio22]. Moreover, hole spins are better protected against nuclear spin noise than their electron counterparts due to their weak hyperfine interaction [KLG02; Pre16; BL21] and do not posses a valley degree of freedom [Zwa13]. In conclusion, hole spins offer advantages in terms of fast, all-electric manipulation, sweet spots for low noise and lower device complexity.

Universal quantum computation requires both single-qubit control and two-qubit interactions. Native two-qubit gates for spins such as the $\sqrt{\text{SWAP}}$ [LD98; Pet05], the controlled phase (CPHASE) [Vel15; Wat18a; Mil22; Xue22] or the controlled rotation (CROT) [Zaj18; Wat18a; Hua19; Pet20a; Noi22; Phi22; Hen20a; Hen21] rely on the exchange interaction, which arises from the wave function overlap between two adjacent QDs. For electrons in Si, two-qubit gate fidelities have recently surpassed the minimum threshold [Fow12] for fault-tolerance of 99% [Noi22; Xue22; Mil22]. However, the challenges in obtaining a controllable exchange interaction [Fan23] prevented the demonstration of two-qubit logic for holes in Si or in FinFETs until the demonstration in this work.

This thesis investigates the potential of spin qubits based on Si FinFETs [Mau16; Pio22; Kuh18; Zwe22]. Chapter 1 provides a brief introduction to the relevant theoretical concepts. In chapter 2, we present a fabrication process for Si FinFETs, which are adapted for qubit integration by introduction of a self-aligned second gate layer. The multi-electrode layout enables control of the potential along the fin, and ambipolar contacts permit both electron and hole currents.

In chapter 3, we employ these devices to form hole double QDs (DQDs) and measure key properties in electric transport measurements. We observe Pauli spin blockade (PSB) [Ono02; Joh05; Li15], where the spin state of a hole or electron blocks the electric transport through a DQD, which can be used for spin readout. The dependence of PSB on electric and magnetic fields is explored.

In chapter 4, we demonstrate the FinFET's ability to host two hole-spin qubits by performing qubit initialisation, manipulation and readout. We use all-electric EDSR spin driving for fast spin manipulation with a speed exceeding 100 MHz and determine a spin coherence T_2^* above 400ns. Using a temperature-robust readout scheme relying on PSB, we are able to operate the qubit at elevated temperatures. We determine a single-qubit gate fidelity of $\sim 99\%$ at 1.5 K. When further increasing the temperature to above 4 K, the qubit coherence is reduced, gate fidelity decreases to $\sim 98\%$ and a whitening of the noise colour is observed.

Chapter 5 investigates the properties of FinFET qubits as a function of magnetic field orientation. We find a highly anisotropic effective g-factor, which is fitted by a phenomenological 3x3 g-tensor and a microscopic model. We find that a rotated confinement potential or strain could be the cause for the misalignment between g-tensor and device axes. Qubit driving is investigated for its magnetic field dependence, allowing us to separate EDSR driving into two mechanisms, motional EDSR [GBL06] and g-tensor modulation [Cri18]. We find that driving a qubit with different gates allows us to choose the driving mechanism. Finally, we investigate the qubit coherence and find sweet spots in the magnetic field orientation with low noise and high coherence [Pio22].

In chapter 6, we turn on the exchange interaction between two neighbouring qubits in a FinFET using electric fields. We find a strong anisotropy and develop a theoretical model based on SOI to extract the full exchange matrix. The model allows us to predict magnetic field configurations for fast and high-fidelity two-qubit gates. We demonstrate the first two-qubit gate for holes in Si by performing a CROT in just $\sim 24\,\mathrm{ns}$, comparing favourable to other CROT implementations [Noi22; Hen20a; Hen21].

In chapter 7, we investigate a hole spin qubit phase drive, which is fundamentally different from the spin-flip Rabi drive. In this method, a far-detuned oscillating field couples to the qubit phase, resulting in highly non-trivial spin dynamics when combined with a conventional Rabi drive. We demonstrate a controllable suppression of resonant Rabi oscillations, and their revivals at tunable sidebands. Phase-driving further has the potential to decouple a spin qubit from noise by exploiting a gapped Floquet spectrum, which also opens up the possibility to investigate and engineer Floquet states [BDP15; RL20].

Finally, in chapter 8 we summarise the current state of the project and provide an outlook. Firstly, we discuss possible improvements to the FinFET devices and their layout. Secondly, limitations in the measurement techniques are identified and possible ways to overcome these restrictions are presented. Thirdly, different paths to improve the qubit properties are discussed. Lastly, we discuss at the FinFET hole spin qubit platform's potential to scale up the number of qubits and their compatibility with concepts for large-scale integration.

1.1. QUANTUM DOTS

The spin qubits investigated in this thesis are hosted by hole spins confined to semiconductor QDs [LD98]. A QD is a potential well which confines charges in three dimensions resulting in discrete energy levels. The spacing of these energy levels is given by the charging energy $E_\mathrm{C} = e^2/2C_\mathrm{QD}$, a result of the quantisation of charge, and the confinement energy (on average $E_\mathrm{dot} = \hbar^2/m^*r^2$), resulting from the small spacial confinement. Here, e is the electron charge, C_QD is the total capacitance of the dot, $\hbar$ is the reduced Planck's constant,

m^* is the effective mass and r is the length of the QD confinement. The confinement is usually achieved by a mix of band structure engineering and design of the electric fields. For our purposes, gate-defined QDs are the most relevant type of QDs, where metallic gate electrodes are used to carefully shape the electrostatic environment in a semiconductor to trap charges. The QD can reside in a sandwich of semiconductor materials (e.g. a 2D hetero-structure or a 1D nanowire), or, alternatively, can be trapped at the interface of a semiconductor and an insulating layer. The latter mechanism is key for metal-oxide-semiconductor (MOS) devices such as FinFETs. More information on Si QD devices of various structures can be found in Refs. [Zwa13; Gon21].

Once a QD is formed, tunnel-coupled source and drain reservoirs are used to probe its spectrum. At low temperature $T \ll E_\mathrm{C}/k_\mathrm{B}$ and small bias voltage $V_\mathrm{bias} < E_\mathrm{C}/e$, where k_B is the Boltzmann constant, charges can be transported through the QD only sequentially. For certain energy configurations of the QD, transport is completely blocked by Coulomb blockade [Han07] if there are no QD energy levels available in the bias window. By shifting the potential of the QD using a plunger gate, the Coulomb blockade can be lifted and current flows. How effective a gate G can manipulate the QD's potential is reflected in the lever arm $\alpha = C_\mathrm{G}/C_\mathrm{QD}$, where C_G is the capacitance between gate G and the QD. Adding a second QD in series (see Fig. 1.1 a), which is tunnel-coupled to the first QD, makes charge transport dependent also on the alignment of the energy levels of the two QDs. At finite bias voltage triangular regions of conductance form in the plunger gate space (see Fig. 1.1 c). These signature features of DQD, known as bias triangles, contain characteristic information such as charging and orbital energies and gate lever arms. The charge state of a DQD is denoted as (n_1, n_2), where n_1/n_2 is the number of charges in the respective QD. We recommend the extensive reviews of transport signatures of QDs provided by Refs. [Wie02; Zwa13] for further information.

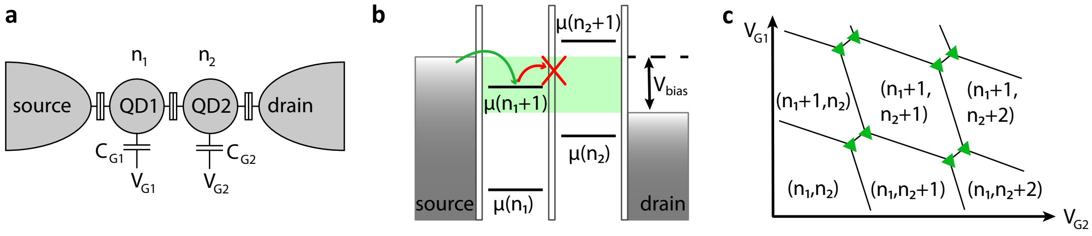

Fig. 1.1.: **DQD charge states.** **a**, Schematic of a tunnel-coupled DQD showcasing source and drain reservoirs and capacitively plunger gates G1 and G2 **b**, Energy level diagram of a DQD in Coulomb blockade. The transport of an electron or hole through the DQD is blocked since there is no charge state of the second QD available in the transport window (green), defined by the bias voltage V_bias. **c**, Schematic of a DQD charge stability diagram indicating bias triangles (green) where charge transport is observed. (n_1, n_2) indicated the charge configuration of the DQD in the respective cell.

The charge carriers confined to QDs can be electrons or holes. This is mostly dependent on the type of device, band structure alignment in the valence and conduction band

and the types of charge carriers available in the contacts. Some devices can host both electron and hole QDs using ambipolar contacts and electrically reversible confinement potentials [Kuh18; Dua21; Mue15]. Since electrons and holes have opposite charge and different effective masses, switching between the two forms of charge carriers results in the formation of quantum dots and tunnel barriers with distinct properties.

1.2. HOLE SPINS

Electrons and holes do not only differ by their charge, but also by their spin properties: whereas electrons have spin quantum number $s = 1/2$ resulting in z-projections with $m_s = \pm 1/2$, holes are more complex. Due to the p-type Bloch wave function in the valence band of Si and Ge [Pre16], holes come with an additional orbital angular momentum given by the quantum number $l = 1$, such that the eigenstates of the total angular momentum operator $J = L + S$ have to be considered. Here, L is the orbital momentum operator and S the spin operator. In total six states can be found: four states with quantum number $j = 3/2$ and z-projections $m_j = \pm 1/2, \pm 3/2$ and two states with $j = 1/2$ and $m_j = \pm 1/2$. In Si, the finite intrinsic spin-orbit interaction energetically splits off the $j = 1/2$ states by the spin orbit splitting $\Delta_{\mathrm{so}} = 44\,\mathrm{meV}$ [Zwa13], which is called the spin-orbit split-off band. The four $j = 3/2$ states are degenerate at zero momentum in bulk Si and are separated into light holes (LH) with $m_j = \pm 1/2$ and heavy holes (HH) with $m_j = \pm 3/2$. This system is typically described by a 6x6 Luttinger-Kohn Hamiltonian [Win03].

When taking into account strain and confinement, the degeneracy of HH and LH is lifted. Well-known examples are the two-dimensional quantum wells in Ge, which can either have HH-like [Sca20] or LH-like [Ass22] ground states. In a strong confinement such as a QD or a nanowire, HH and LH start to mix, such that the eigenstates are not of pure HH or LH character. However, a pseudospin $f = 1/2$ can be assigned to the two lowest states in energy independent of their mixture of HH and LH [KTL11], such that we can describe hole QDs in many cases using the same formalism as for electrons [Sca20]. For example when applying an external magnetic field B, the Zeeman splitting for electrons or holes in QDs is given by $E_{\mathrm{Z}} = g^* \mu_{\mathrm{B}} B$, where g^* is the effective g-factor of the electron or hole and μ_{B} is the Bohr magneton. Further information on hole spin states in Si and Ge is provided in Refs. [Sca20; CP66; Fan23].

1.3. PAULI SPIN BLOCKADE

Returning to single-charge transport through a DQD, we note that spin states can also influence the charge transport. A prime example is Pauli spin blockade (PSB) [Ono02; Joh05], where the current through an electron or hole DQD is blocked by the spin states of single particles. PSB occurs if the DQD is in the $(1,1)$ charge state and charge transport has to go via the $(0, 2)$ state, where only a spin singlet state $|(0, 2)\mathrm{S}\rangle$ is energetically allowed (see Fig. 1.2 a). This tunnelling process is forbidden by spin conservation if the two spins in the $(1, 1)$ state occupy a triplet state $|(1, 1)\mathrm{T}_+\rangle$, $|(1, 1)\mathrm{T}_0\rangle$ or $|(1, 1)\mathrm{T}_-\rangle$. A difference in g^*-factor or a gradient magnetic field can mix the unpolarised triplet $|(1, 1)\mathrm{T}_0\rangle$ with the singlet $|(1, 1)\mathrm{S}\rangle$, which lifts the blockade for these states [See21]. Other mechanisms can also mix the polarised triplet states with the singlet state, which completely lifts PSB. The most prominent ones are SOI, hyperfine interaction and spin-flip co-tunnelling [DN09; Nad10b]. PSB is often used as spin-to-charge conversion mechanism in qubit readout schemes [Fog18; Zha19; Wes19; See21], due to its protection against elevated temperatures [Pet20a; Pet20b; Yan20], compatibility with small magnetic fields and high speed [Wes19; Nur22; Hut19; See21].

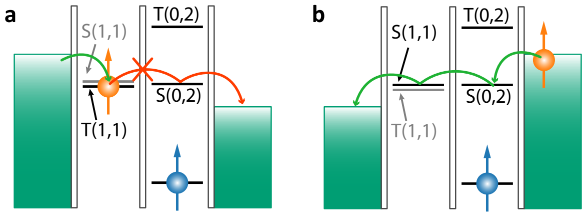

Fig. 1.2.: **Schematic of PSB. a**, Pauli spin blockade blocks the transport through a DQD in a specific charge configuration as described in the main text. **b**, Same charge configuration but under reverse bias, where transport is not blocked.

1.4. SPIN-ORBIT INTERACTION

A particle's spin, which is a magnetic angular momentum, usually couples only to magnetic fields. However, special relativity tells us that a particle moving through an electric field will experience an apparent magnetic field. This effect is captured by the SOI, which couples the particle's spin to electric fields. In a semiconductor, the electric potential of the nuclei gives rise to an intrinsic spin-orbit interaction, which as a rule of thumb scales with the charge of the nuclei, i.e. is stronger for heavier elements. SOI leads to the renormalisation of electron or hole g-factors in a semiconductor and spin splitting of electronic bands at zero magnetic field [Win03].

Spatial inversion asymmetry gives rise to additional SOI terms such as the linear-in-momentum Dresselhaus or Rashba SOI. Dresselhaus SOI arises either from a microscopic inversion asymmetry of the crystal structure (bulk inversion asymmetry) or from an anisotropy of the chemical bonds at material interfaces [Joc18; Win03]. For holes in Si and Ge, which both have a inversion-symmetric diamond crystal lattice, this contribution is usually small.

Rashba SOI, in contrast, originates from the macroscopic structure inversion asymmetry of the system, which comes from e.g. layers of different materials, an inversion asymmetric cross-section of a nanowire or applied electric fields. The effect can be described in terms of an effective electric field $\mathbf{E}$, which gives rise to the Rashba SOI Hamiltonian [Win03]

$$H_{\mathrm{so,R}} = \alpha \boldsymbol{\sigma} \cdot (\mathbf{k} \times \mathbf{E}), \tag{1.1}$$

where $\mathbf{k}$ is the momentum operator, $\boldsymbol{\sigma}$ is the spin operator and α is the Rashba spin-orbit coefficient. The Hamiltonian is sometimes rewritten using an effective magnetic field $\mathbf{B}_{\mathrm{so}} \propto \mathbf{k} \times \mathbf{E}$, which allows us to think about the effect of SOI in terms of an additional magnetic field.

For holes in Si or Ge, a strong confinement to one dimension in combination with a perpendicular electric field gives rise to an additional significant linear-in-momentum term, the so-called direct-Rashba SOI (DRSOI) [KTL11; KRL18]. DRSOI is formally identical to standard SOI, but is predicted to be much stronger and to exhibit a non-monotonic electric tunability. The different electric tunability enables turning on and off SOI for certain device geometries at finite electric fields [KRL18; BHL21]. For a SOI-driven qubit this lets us turn on respectively off the coupling between the qubit and the environment for fast driving and low noise, respectively [Fro21b].

2

FABRICATION

Parts of this chapter have been published in:

Self-aligned gates for scalable silicon quantum computing
Applied Physics Letters **118**, 104004 (2021), doi:10.1063/5.0036520
Simon Geyer, Leon C. Camenzind, Lukas Czornomaz, Veeresh Deshpande,
Andreas Fuhrer, Richard J. Warburton, Dominik M. Zumbühl
and Andreas V. Kuhlmann

This chapter reports on the fabrication of silicon FinFET devices with a self-aligned gate layer. First, the device layout is presented, followed by a detailed description of the individual steps of the process flow for the silicon fin, the metallic gates and the ohmic contacts. Finally, post-fabrication device screening is discussed.

Classical computers are made of Si integrated circuits that consist of billions of fully operational MOSFETs. Their quantum analogue is represented by Si-MOS QD devices [Ang07; Lim09], which, in their role as hosts for coherent and high-fidelity spin qubits [LD98; KL13; Vel14; Pet20a; Yan20; Zaj18; Wat18a; Yon17; Mau16], are among the prime candidates for implementing large-scale quantum processors [Vel17; Van17; VE19]. While MOSFETs work with three terminals (source, drain, and gate), a multilayer gate stack is often required for quantum dot devices [Ang07; Lim09; Vel14; Pet20a; Yan20; Zaj18; Wat18a; Een19; Law20]. Consequently, tight requirements on feature size and layer-to-layer alignment make quantum dot device fabrication highly demanding. Furthermore, the high gate count leads to challenges in wiring up of large-scale qubit systems because of low-temperature operation [Fra19; Vel17; Van17; Bot22]. It is, therefore, too simplistic to assume that Si spin qubits based on industrial manufacturing processes are a priori scalable. Yet, the current quantum dot device fabrication standards need to be adapted for scalable integration. In order to limit device complexity, all-electrical spin control schemes [Mau16; Wat18b; Hen20b; Hen21; Voi15; Now07; GBL06; Gil23] should be preferred over spin manipulation relying on additional components such as transmission lines [Vel14; Pet20a] or micromagnets [Yan20; Pio08].

In the Si industry, self-alignment techniques are used to reduce feature sizes and to overcome alignment limitations. Here, the key idea is to make use of an existing patterned structure on a device to define the pattern of a subsequent process, resulting in an intrinsically perfect layer-to-layer alignment. A prime example from the electronics industry is to employ the gate of a MOSFET as a mask for the definition of source and drain regions by means of ion implantation [Vad69; Bow68].

In this chapter, we present a process flow to fabricate Si FinFET devices with two layers of gates that can host multiple quantum dots for qubit applications. The second gate layer is realised using a self-alignment technique, where the first gate layer acts as a mask for the subsequent one. With this approach, multi-gate stack integration is facilitated, and ultra-small gate lengths $\simeq 15\,\mathrm{nm}$ as well as perfect layer-to-layer alignment can be achieved. While this chapter will explain the main steps of the fabrication, details such as process parameters are provided in Ref. [Gey19a]. Finally, device screening methods are discussed.

2.1. PROCESS FLOW

Fig. 2.1 shows the device layout. The Si mesa (red) is narrowed down in the centre of the device to form the Si fin. Source (S) and drain (D) ohmic contacts (green) are connected to the fin via lead gates L1 and L2 (yellow), which accumulate charge reservoirs in the Si to either side of the fin. The nano-scale gates (G1-3) can be used to control the current flow through the fin. At cryogenic temperatures, these gates accumulate

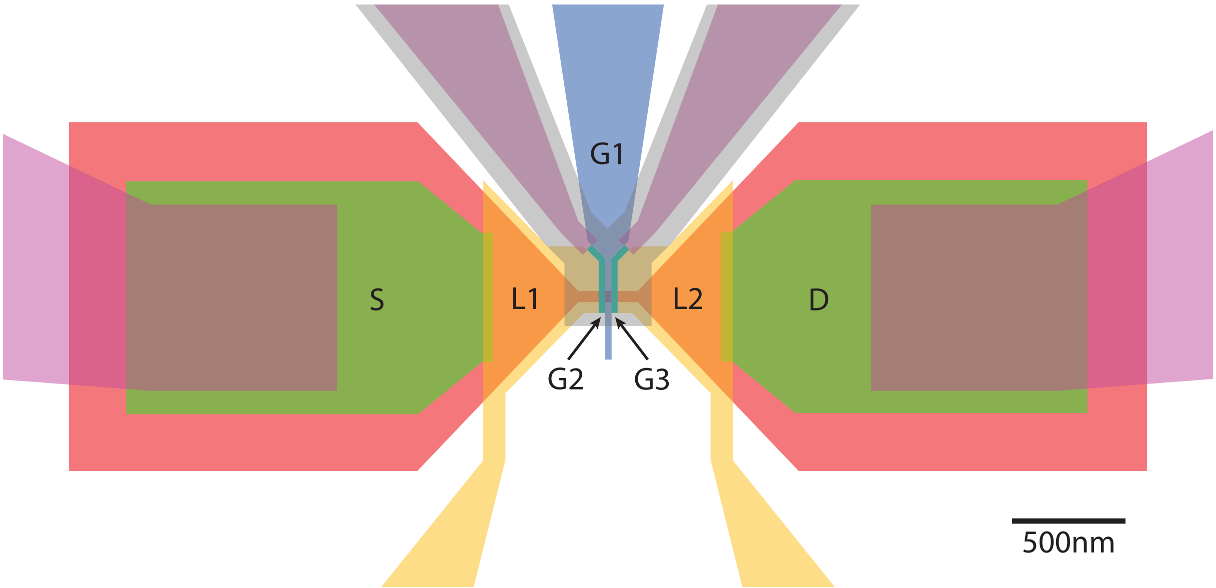

Fig. 2.1.: **Device layout** showing the main lithography masks for the fin, gates and contacts as well as the self-aligned gates G2 & G3. A close-up of the nano gates G1-3 is provided in Fig. 2.2.

quantum dots and form barriers. The fabrication process flow for these devices starts with a natural, near-intrinsic Si substrate ($\rho > 10\,\mathrm{k\Omega cm}$, (100) surface). We define the Si fin along the [110] crystal direction by electron-beam lithography (EBL) with negative hydrogen silsesquioxane (HSQ) resist and a dry-etch in an inductively-coupled plasma (ICP) etcher using hydrogen bromide (HBr). Subsequently, the fin is narrowed down to the desired width of $w = 10 - 25\,\mathrm{nm}$ by an oxidation-etch cycle. It consists of an isotropic dry thermal oxidation of the top few nm of Si and a wet etch using buffered hydrogen fluoride, which dissolves only the oxidised Si. When the fin is narrowed to its final width, a last thermal oxidation step is used to grow a thin silicon dioxide (SiO_2) layer, typically 6-8 nm, which serves as a gate oxide for the first gate layer.

The fist gate layer is defined by EBL and dry etching, which allows for more uniform gate fabrication and smaller dimensions as compared to the typically used lift-off processes [Zwe21]. First, the SiO_2 is covered with 20 nm of the metal titanium nitride (TiN) in a uniform atomic-layer deposition (ALD). EBL using HSQ is used to define the layout of the first gate layer, consisting of lead gates L1 and L2 and the central gate G1 (yellow and blue in Fig. 2.1). A subsequent ICP dry etch using HBr, which is highly selective towards TiN in comparison to SiO_2, removes the metal outside of the desired area. The HSQ on top of the gates remains and forms a low-quality Si oxide. The topography of this gate layer is crucial for the upcoming step.

Next, the self-aligned gates are fabricated. In Fig. 2.2 (a) a scanning electron microscope (SEM) image of a device at this stage is shown. The gaps separating the gates of the previous gate layer create channels (turquoise highlights in Fig. 2.2 (a)) that will serve as a template for the second gate layer. By means of ALD the gate stack, consisting of

$\simeq 4.5\,\mathrm{nm}$ silicon oxide (SiO_x) and $\simeq 20\,\mathrm{nm}$ metallic TiN, is deposited with highly uniform surface coverage (see Fig. 2.2 (b)). Provided the width of the gaps separating G1 from L1/L2 is less than twice the thickness of the deposited material, the channels are almost evenly filled with metal. The thin SiO_x layer ensures electrical isolation of the two gate layers (breakdown voltage $\gtrsim 6\,\mathrm{V}$, see appendix A.1.1).

Subsequently, an anisotropic ICP dry etch using HBr is applied for a duration that corresponds to the deposited TiN thickness of $\simeq 20\,\mathrm{nm}$ (see Fig. 2.2 (c)). While the gate metal is removed during etching from the flat surfaces of the device, leftovers are found at the topography steps. The TiN residues inside the predefined channels naturally form gates G2 and G3 of the second gate layer. The fan-out of the gates to micro-scale contact pads at larger distance from the fin is protected during etching by a resist mask (magenta highlights in Fig. 2.2 (c)), which is defined by means of EBL. The demands of this lithography step with regard to resolution and alignment accuracy are lowered by moving the channel endpoints further away from the centre of the fin.

At this stage, the gates of the second gate layer are still connected via the TiN that remains and is marked in red in Fig. 2.2 (c & d). This short circuit is eliminated by first protecting the gates with a resist mask, as shown in Fig. 2.2 (d), and then by selectively removing all the unintentional TiN residues by isotropic wet etching using RCA1 echant (see Fig. 2.2 (e)). The protective cover is defined by means of EBL.

After successful integration of the second gate layer, cross-sectional transmission electron microscope (TEM) images along and perpendicular to the fin direction are taken (see Fig. 2.2 (f)). These images confirm ultra-small gate lengths as well as perfect gate alignment. The high uniformity of our devices is typically only achieved in industrial clean room facilities [Zwe22].

To create contacts for the source and drain reservoirs accumulated below the lead gates, a metallic silicide contact is used.[1] A 200 nm thick bilayer resist mask consisting of methyl methacrylate and polymethyl methacrylate-methacrylic acid is defined by EBL. After surface cleaning through dry and wet etching, metal is deposited anisotropically using a sputter machine. A lift-off process and subsequent removal of the resist leaves behind a thin metallic layer only in the desired contact region (green area in Fig. 2.1). The metal is then annealed at a low temperature of 475°C for 10 min during which the metal diffuses into the Si, forming a metallic silicide next to and slightly below the lead gates, as shown in the cross-sectional TEM image in Fig. 2.3 (a). The naturally arising Schottky tunnelling-barriers between the metallic silicide and the semiconducting silicon are made more transparent by a strong electric field [Gey19a; Gey19b], originating from a large

---

[1] Alternatively, in-situ doped contacts have shown promising results in early tests, where the semiconducting contact region is heavily doped by thermal diffusion using deposited dopants. Using this method suppresses the formation of Schottky barriers at the contacts, resulting in more ohmic behaviour and lower contact resistance. Further investigation of this process is needed to determine its potential.

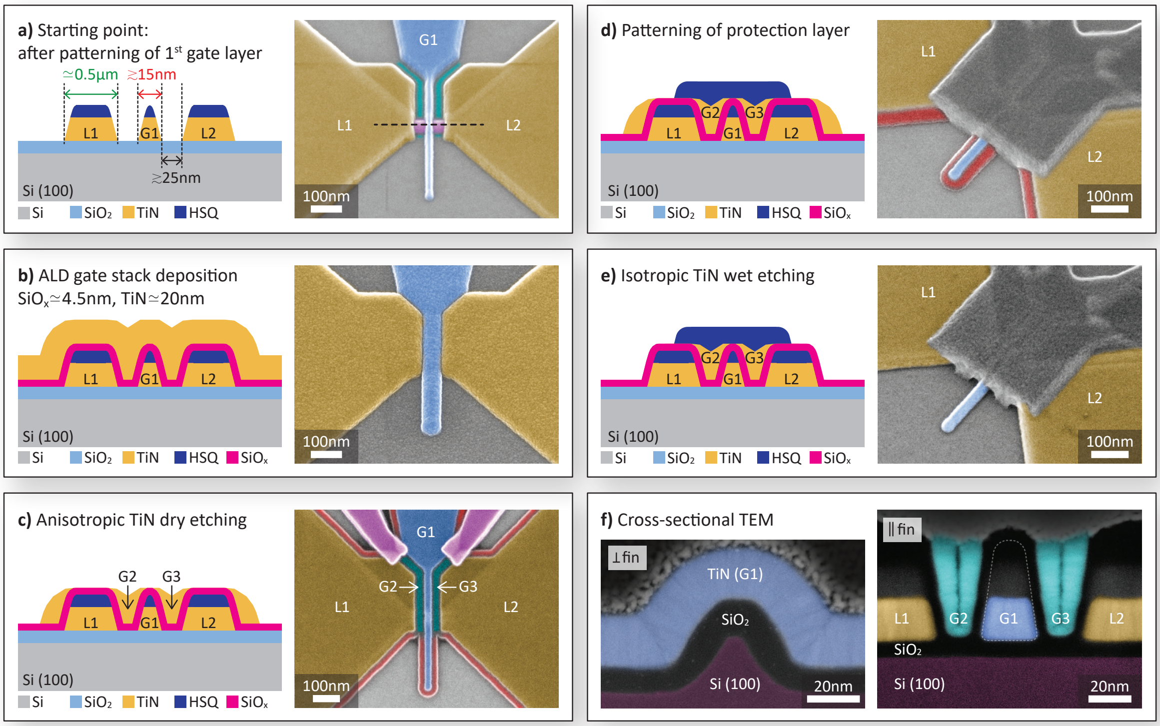

Fig. 2.2.: **Fabrication process flow**. (a-e, left panel) Schematic device cross-section along the black dashed line of the (a) false colour SEM image. The horizontal axes of the left and right panels are scaled differently. (a) Device with completed first gate layer, consisting of two lead gates L1 & L2 (yellow in SEM image) and a central finger gate G1 (blue) that is wrapped around the Si fin (magenta). EBL with HSQ resist is employed for gate definition. The gaps separating the gates (turquoise) act as a template for the second gate layer. (b) Deposition of the gate stack by means of ALD results in a uniform surface coverage, such that the gaps are almost evenly filled with material. (c) TiN is removed from the flat surfaces, which are not protected by resist (magenta), by timed dry etching. TiN residues (red) at topography steps still connect gates G2 & G3 of the second gate layer. (d, e) A protective resist mask is applied to remove all unintended TiN residues with an isotropic wet etch. (f) Cross-sectional TEM images perpendicular (left panel) and parallel (right panel) to the fin. Left: the quantum dot is induced at the apex of the roughly triangular-shaped Si fin (purple). Right: Gates G2 & G3 (turquoise) are perfectly aligned relative to the first gate layer. Good electrical isolation is ensured by a thin SiO$_x$ layer sandwiched between the two gate layers.

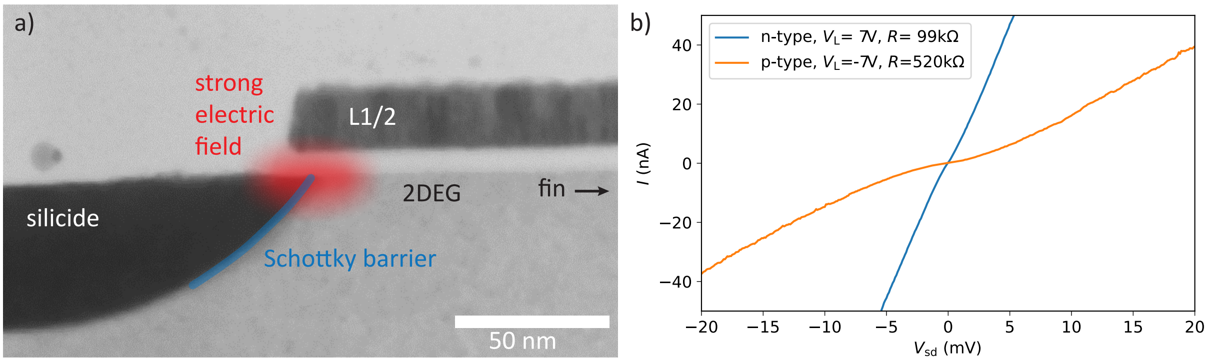

Fig. 2.3.: **Ohmic contacts**. (a) Cross-sectional TEM image showing the silicide-Si interface. The Schottky-barrier forming at this interface is influenced by the strong electric field applied via the overlapping lead gate. (b) IV characteristics of device N (see Tab. A.1) with nickel silicide contacts in ambipolar operation at $\sim 20\,\mathrm{mK}$. A small total resistance in the order of $\sim 100\,\mathrm{k\Omega}$ is reached by applying strong electric fields at the Schottky barrier interface. The deviation from ohmic behaviour at small bias is due to the rectifying behaviour of the Schottky barrier.

voltage applied to the lead gates.[2] Two different metals, platinum and nickel, were used in this process to form contacts. Platinum silicide has a Fermi energy that is close to the valence band of Si, making it suitable to inject holes into the Si channel. Nickel silicide, on the other hand, has an almost mid-band gap Fermi energy, leading to a larger Schottky barrier but enabling injection of both types of charge carriers into the channel.

Fig. 2.3 (b) shows the current-voltage (IV) characteristics for an ambipolar device with nickel silicide contacts. At low bias voltage, the curve flattens out, indicating a deviation from ohmic IV characteristics due to the rectifying nature of the Schottky contacts. This effect makes it difficult to define or measure the contact resistance and is pronounced when the channel resistance is low. Hence, we define the contact resistance R as the average resistance over the bias voltage $V_{\mathrm{sd}} = \pm 20\,\mathrm{mV}$. Despite this challenge, the quality of the contacts is sufficient to measure the changes in conductance of the device channel, which is the region of interest for our applications.

In the back end of line processing, a 100 nm thick protection layer of SiO_2 is deposited on the device by plasma-enhanced chemical vapour deposition. Vertical interconnects are opened up and filled with tungsten (W) to connect gates and the ohmic contacts to a metal fan-out ending in bonding pads.

After fabrication and visual inspection, a room-temperature probe station tests for channel turn-on and gate leakage. The device yield in this first stage varied significantly between different batches of fabrication, sometimes even for nominally identical parameters. The reason for this could be due to the fact that the process is not fully automated, leading to process variations due to naturally arising small differences in the manual steps.

---

[2] A more complex device design with separate gates to control the Schottky barrier transparency was also investigated, which turned out to reduce contact resistance and make quantum dot measurements easier. Therefore, this new method was adapted for device D (see Tab. A.1) and is included in future designs.

Alternatively, some process steps may depend on parameters outside of our control, such as the history of processes prior to our fabrication. After this initial screening, promising devices are wire-bonded and tested again at room temperature before being cooled down to cryogenic temperatures (4 K or mK) for the final test.

The low-temperature test procedure confirms the channel conductance and tests individual control from each gate. First, all gates are slowly ramped towards or slightly above their typical operation voltage until a small bias voltage results in a measurable source-drain current. Second, the voltage of each gate is individually ramped to zero and the pinch-off behaviour is recorded. A good device should have a high channel conductance and similar pinch-off voltages for each nano gate, indicating uniformity among the gates and hence a promising device for quantum dot experiments. Appendix A.1.2 provides an example of measurements for a well-performing device. This step could in principle already be performed in a cryogenic probe station setup [Kru23] before wire bonding. This would increase measurement speed and throughput as well as allowing better disentanglement of low-temperature failure modes originating from the fabrication process and from post-fabrication device handling and bonding.[3] At this stage of device screening, the most common failure mode was non-pinching gates. This might come from the small gate dimensions that push the boundaries of the EBL tool, which can lead to an interrupted connections to the gates. Our screening method allows us to sort out failing devices, but unfortunately, it cannot predict the device quality, especially the quantum dot properties. As a result, the yield for high-quality quantum dots capable of hosting qubits was lower than the bare device yield.

2.2. CONCLUSION & OUTLOOK

In conclusion, we have presented a novel fabrication flow for Si FinFET qubit devices with a small footprint. Our approach relies on a self-alignment technique for gate fabrication, which enables ultra-short gate lengths that are suitable for quantum applications. We have demonstrated quasi-ohmic behaviour of ambipolar Schottky contacts by tuning the Schottky-barrier transparency with electric fields.

The presented device can still be improved in various ways. The contact resistance and the contact's deviations from ohmic behaviour could be reduced by introducing doped contacts [Hut16; Ang07] to replace the rectifying Schottky contacts by a doped semiconductor-metal interface. Further device optimisations, improving various QD or qubit properties, are discussed in chapter 8. Furthermore, more complex devices will be required for future experiments beyond the scope of this thesis. We will discuss the

---

[3] We recommend the integration of such a cryogenic probe station into the screening procedure after struggles in separating the errors from electrostatic discharges during device handling and bonding and from fabrication errors.

necessary changes in device design, layout and dimensions in chapter 8.

3

QUANTUM DOT CHARACTERISATION

Parts of this chapter have been published in:

Self-aligned gates for scalable silicon quantum computing
Applied Physics Letters **118**, 104004 (2021), doi:10.1063/5.0036520
Simon Geyer, Leon C. Camenzind, Lukas Czornomaz, Veeresh Deshpande, Andreas Fuhrer, Richard J. Warburton, Dominik M. Zumbühl and Andreas V. Kuhlmann

This chapter presents the characterisation of a hole double quantum dot accumulated in a FinFET with two gate layers. Pauli spin blockade is observed and its dependence on electric field and magnetic field strength and orientation is investigated. Further, characteristic parameters of the system are extracted, indicating a promising platform for hole spin qubits.

QDs in Si-MOS structures offer a promising platform for hosting spin qubits [Vel17; Van17; Gon21] and have been studied extensively for both electrons [Ang07; Lim09; Vel14; Pet20a; Yan20] and holes [Mau16; Lil21; Li15]. Holes are particularly interesting because they offer a strong SOI which enables all-electric, fast qubit manipulation [GBL06; Mau16; Voi15]. When holes are strongly confined to a one-dimensional channel, as in nanowires or FinFETs, an especially strong and electrically controllable DRSOI is predicted [KRL18; BHL21].

QDs can be characterised through charge transport measurements that map out the QD's spectrum and charge state [Wie02]. In a DQD, specific configurations of electron or hole charge and spin states can exhibit PSB [Ono02], a blockade of charge transport by the spin state of the charge carrier. The PSB leakage current can be utilised to probe mechanisms that lift PSB such as SOI or hyperfine interaction [DN09; Li15; Zar17; QD22].

In this chapter, we examine the charge transport characteristics of a hole DQD hosted in a Si FinFET. We observe PSB and identify SOI as the dominant mechanism for spin blockade lifting. We analyse how the PSB leakage current changes with magnetic field orientation and attempt to explain the effect with a model based on SOI. Moreover, both the SOI coupling strength and the effective hole g-factor are obtained from an anticrossing between singlet and triplet spin states of the DQD measured in magneto-spectroscopy.

3.1. FinFET QUANTUM DOTS

We employ a FinFET device, that was fabricated according to the process flow presented in chapter 2, for QD characterisation experiments. The device layout with the three nano-scale gates B, P1 and P2 (in the previous chapter labelled as G1, G2 and G3) allows for both a single- and double-dot operation mode. In this chapter we focus on DQDs in p-type devices (see appendix A.2.1 for single-dot regime). Holes are accumulated in source (S) and drain (D) reservoirs through platinum silicide contacts by applying a strong, negative lead gate voltage ($V_{L1,L2} = -4.5\,V$). Gates P1 and P2 form dots 1 and 2 and control their occupancy (see inset of Fig. 3.1 (a) for a simplified equivalent circuit of the device). Gate B, which is located between P1 and P2, is used to control the inter-dot tunnel coupling (see appendix A.2.2). In this chapter we mainly investigate device A (see Tab. A.1) with gate lengths $l_B \simeq 25\,\mathrm{nm}$ for inter-dot barrier gate and $l_P \simeq 15\,\mathrm{nm}$ for the plunger gates.

The data presented here are obtained from direct current electrical transport measurements with the sample cooled to 0.55 K. In Fig. 3.1 (a), a double dot charge stability diagram [Wie02], showing the first observable pairs of bias triangles, is presented (see appendix A.2.3 for same measurement on a second device). The two triangles of each pair strongly overlap for a source-drain voltage of $V_{SD} = +10\,\mathrm{mV}$. While the lines of strong current flow parallel to the triangle base reveal elastic tunnelling between the ground

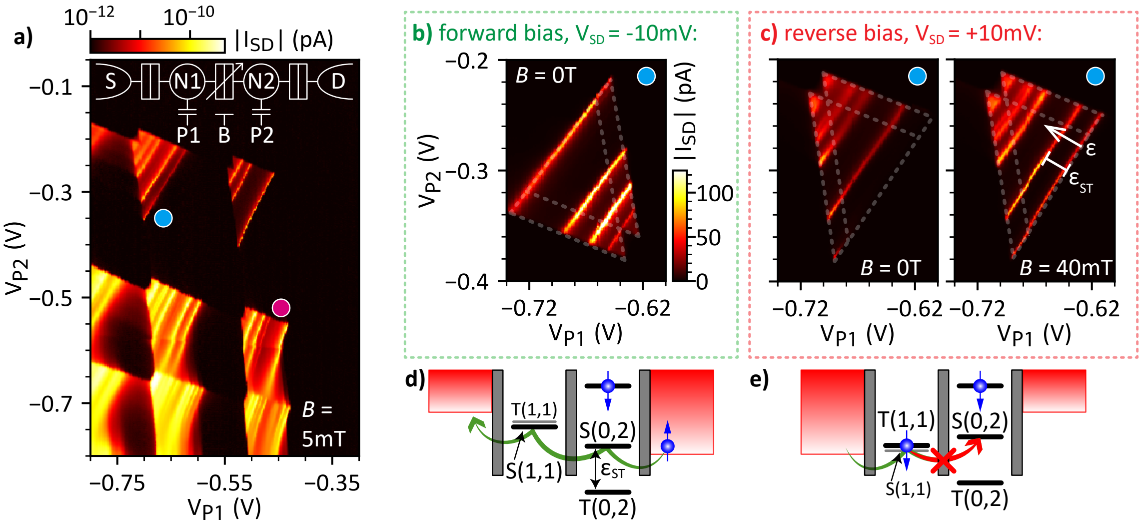

Fig. 3.1.: **Bias triangles and Pauli spin blockade for holes.** (a) Double dot charge stability diagram measured for $V_{SD} = +10\,\text{mV}$ and $V_B = -770\,\text{mV}$. The simplified equivalent circuit of the device is depicted in the inset. While the dot occupancies N1 and N2 are separately controlled by gates P1 and P2, the inter-dot tunnel barrier is tuned by B. The coloured circles mark the pairs of bias triangles for which signatures of PSB are observed. A close-up of the triangles indicated by the solid blue circle in (a) is presented for $V_B = -750\,\text{mV}$ in (b) for $V_{SD} = -10\,\text{mV}$ and (c) for $V_{SD} = +10\,\text{mV}$. While for negative V_{SD} current can freely flow through the base of the triangles, it is blocked for positive V_{SD} at zero magnetic field. PSB is lifted for a detuning $\varepsilon \geq \varepsilon_{ST}$ or by applying a small magnetic field, here $B = 40\,\text{mT}$. The detuning axis is defined as indicated by the white arrow. A charge transport cycle is depicted schematically in (d) for negative and (e) for positive V_{SD}.

or excited states of the double dot, the background current inside the triangles can be assigned to inelastic tunnelling [Wie02]. The triangles for more negative gate voltages are distorted by co-tunnelling processes because of the dots' increased tunnel coupling to the reservoirs [Fra01; Zum04].

3.2. PAULI SPIN BLOCKADE

In Figs. 3.1 (b), (c) a zoom-in on the pair of bias triangles, indicated by a solid blue circle in Fig. 3.1 (a), is presented for negative and positive V_{SD}. While current flow through the base of the triangles is observed for $V_{SD} = -10\,\text{mV}$, it is strongly suppressed for positive V_{SD} at zero magnetic field B. (For the bias triangles marked by a solid magenta circle in Fig. 3.1 (a) current suppression is observed for the opposite bias direction, see appendix A.2.4). This type of current rectification is a hallmark of PSB [Ono02; Joh05; Han07; Lai11; Li15] and is due to spin-conserved tunnelling, as schematically depicted in Figs. 3.1 (d), (e). If two hole spins reside on the same dot (here the right one), they must occupy a spin singlet state S(0, 2) as the triplet state T(0, 2) is shifted to higher energy by the single-dot singlet-triplet splitting ε_{ST} [Han07]. Here (m, n) denotes the effective hole occupancy of the left and right dot. While our data is consistent with observing the last hole, more sensitive charge detection methods are required to evaluate this [Fie93; Han07].

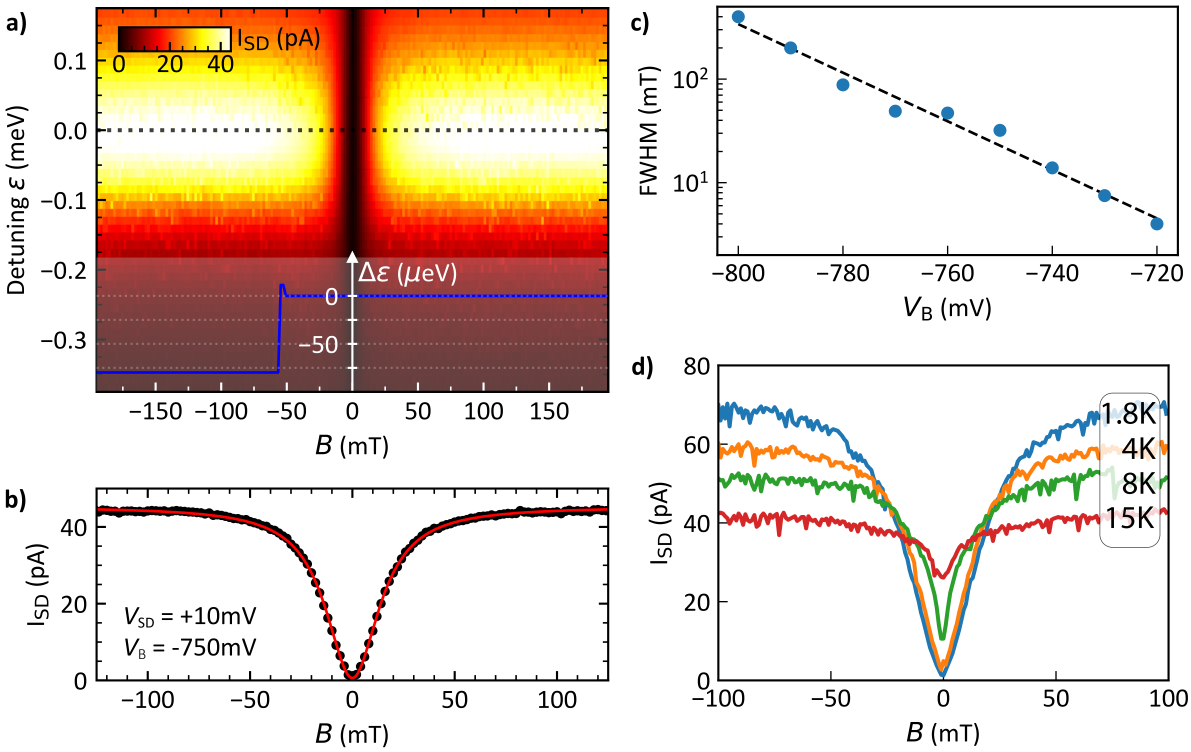

Fig. 3.2.: **Spin blockade leakage current**. (a) Source-drain current I_{SD} under reverse bias as a function of detuning ε and out-of-plane magnetic field B. Some of the vertical traces are shifted along the ε-axis to eliminate the random switching of a charge trap. The detuning correction $\Delta\varepsilon$ is plotted in the inset (blue). (b) Cut along B at $\varepsilon = 0$, as indicated by the black dashed line in (a). The data (black dots) are well fitted by a Lorentzian function (red curve) of FWHM = 32 mT. (c) FWHM of the Lorentzian dip in the leakage current (blue circles) as a function of barrier gate voltage V_B indicating an exponential dependence (black dashed fit). (d) Leakage current at $\varepsilon = 0$ as a function of B for temperatures from $T = 1.8\,\mathrm{K}$ to 15 K. PSB current suppression is partially lifted by elevated temperatures but measurable up to 15 K.

For a negative V_{SD} charge transport occurs from the $S(0,2)$ state to the $S(1,1)$ state, and a hole can escape the left dot to the reservoir. In contrast, for a positive V_{SD} current flow is blocked. If one hole spin resides on each dot, they can form either a $S(1,1)$ or $T(1,1)$ state, which are nearly degenerate in energy for weak inter-dot coupling. Once the $T(1,1)$ state is occupied by loading a hole from the reservoir to the left dot, transport is blocked by spin conservation during tunnelling.

PSB is lifted for an inter-dot energy level detuning ε exceeding ε_{ST}, since the $T(0,2)$ becomes accessible from the $T(1,1)$ state. Hence, the reappearance of current along the detuning axis determines $\varepsilon_{ST} \simeq 1.85\,\mathrm{meV}$. This allows us to give an upper-bound estimate of the effective dot size $\lambda_x \sim \hbar/\sqrt{m^* \varepsilon_{ST}} = 9.5\,\mathrm{nm}$ [Fas07], which is in good agreement with the device geometry. Here, we assume harmonic confinement and an effective hole mass $m^* = 0.45\,m_0$, where m_0 denotes the bare electron mass [KRL18].

For $\varepsilon < \varepsilon_{ST}$ spin relaxation leads to a leakage current through the spin blocked region of the bias triangles [Pfu07; Chu09; DN09; Nad10b]. For a small magnetic field of $B = 40\,\mathrm{mT}$ current leaks through the base of the triangles (see Fig. 3.1 (c)). For $B \neq 0$ the previously forbidden T(1, 1) → S(0, 2) transition becomes allowed since hole spins in Si experience a strong SOI [KRL18] that hybridises the T(1, 1) and S(0, 2) states [DN09; Nad10b].

The leakage current dependence on both B and ε for positive V_{SD} is shown in Fig. 3.2 (a). A dip in the leakage current, which is centred around zero magnetic field, is revealed by a line-cut along B at $\varepsilon = 0$ in Fig. 3.2 (b). This dip has a Lorentzian line shape with a full-width-at-half-maximum (FWHM) of 32 mT and a close-to-zero minimum value, signifying a very efficient blockade. The dip also confirms that lifting of PSB is dominated by SOI [DN09; Li15], since hyperfine interactions [Pfu07; Nad10b] or spin-flip co-tunnelling [QCW09; Lai11; Bie15] yield a zero-field peak. The magnetic field dependence of the observed current suppression can be tuned by the inter-dot tunnelling rate, as demonstrated in Fig. 3.2 (c). The interdot tunnelling rate is controlled by the barrier gate voltage V_{B}. We show exponential control over the FWHM of this dip in current over a wide range of $V_{\mathrm{B}} \sim 100$ mV. This is expected as typically $t \propto \exp(V_{\mathrm{B}})$ [Ans23] and FWHM $\propto t$ [DN09].

Interestingly, the PSB current suppression is robust against elevated temperatures, as shown by the measurements in Fig. 3.2 (d) performed in a variable temperature insert. We observe a close-to-full current suppression below 4 K and signatures of PSB up to 15 K. The saturation current at high magnetic fields decreases with increasing temperature T, which is expected as the $\varepsilon = 0$ transition smears out with T and its maximum conductance is $\propto 1/T$ [Bee91]. A detailed discussion of the relevant energy scales that protect PSB against temperature is provided in chapter 4 and in appendix A.3.8, where the effect was reproduced for device B.

Next, PSB is investigated for different magnetic field orientations using a vector magnet setup. Unlike the rest of this chapter, these data are measured on device D (see Tab. A.1) at a cryostat base temperature of ∼10 mK.[1] In Fig. 3.3 (a) we fix $\varepsilon = 0$ and map out the leakage current against magnetic field strength B and orientation (α, β) in three different planes (see schematic in Fig. 3.3 (c)). A striking modulation of the PSB leakage current by the magnetic field orientation is observed, which is expected for SOI-dominated systems [DN09]. The saturation current at $B = 50$ mT is shown in Fig. 3.3 (b) for each measurement. We fit a simple model (black curve), which only includes the SOI-induced PSB lifting mechanism, to the data. The model is described by [Zha21; DN09]

$$I_{\mathrm{SD}} = I_0 \frac{B^2}{B^2 + \left(\frac{B_0}{|\mathbf{b} \times \mathbf{n}_{\mathrm{so}}|}\right)^2} + I_{\mathrm{off}}, \tag{3.1}$$

where I_0, I_{off} and B_0 are fitting constants, $\mathbf{b}$ is a unit vector along the magnetic field orientation and $\mathbf{n}_{\mathrm{so}}$ is a unit vector along the effective spin-orbit field. This allows us to extract the effective SOI field orientation of $\alpha_{\mathrm{so}} = -17°, \beta_{\mathrm{so}} = 91°$, which is almost aligned

---

[1] Qualitatively similar effects have been observed on device C, but are not shown here.

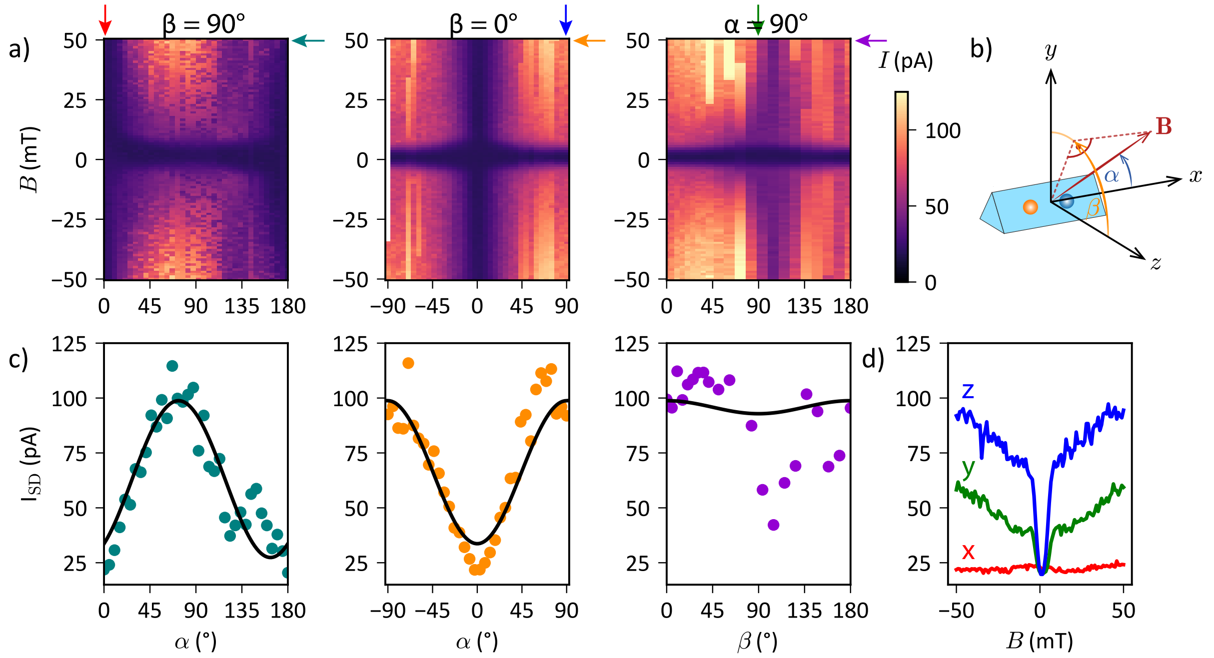

Fig. 3.3.: **Anisotropic PSB current suppression**. (a) Leakage current I_{SD} at $\varepsilon = 0$ as a function of magnetic field strength B and orientation (α, β) for three different planes. The data shows a strong anisotropy of PSB lifting. (b) Saturation current at $B = 50\,\mathrm{mT}$ for the different field orientations from (a). The directional dependence of the leakage current data (points) is fitted by eq. (3.1) based on SOI-effects (black curve). (c) The magnetic field orientation is parameterised by (α, β), where xz is the chip plane and the fin is oriented long x. (d) Leakage current along the main device axes x, y and z as function of B showing a different line shape as compared to Fig. 3.2.

with x, the orientation of the fin. In the case of dominating Rashba or direct-Rashba SOI, caused by structural inversion asymmetry of the device, we expect a spin-orbit field orientation along $\mathbf{k} \times \mathbf{E}$ [Win03]. Here, $\mathbf{k}$ is the momentum of the holes (along x) and $\mathbf{E}$ is the electric field (most likely along y due to the gate arrangement), such that Rashba SOI is oriented along z. In contrast, Dresselhaus SOI can be induced by the microscopic interface inversion asymmetry at the Si-SiO$_2$ boundary [Joc18]. For Dresselhaus SOI, the effective spin-orbit field can be aligned with the momentum vector $\mathbf{k}$ and hence the x-axis. In a system with a mixture of both Dresselhaus and Rashba SOI, the effective spin-orbit field can point along an arbitrary orientation, which is given by the ratio of strength of the two types of SOI [Zha21]. Hence, our extracted SOI field could be explained by large Dresselhaus SOI and small Rashba SOI, which would, however, contradict the theoretical prediction of strong Rashba SOI in our system [BHL21] and the experimental results presented in chapter 6. These experiments, which were performed on a similar device, were analysed using a different extraction method yielding a spin-orbit field that is mostly aligned with z, indicating dominating Rashba SOI. We therefore conclude that either device-to-device variability of SOI properties is huge, resulting in dominating Dresselhaus SOI in one device and dominating Rashba SOI in another device, or that the model used here to extract SOI does not suffice to capture the physics in our devices. The first explanation is unlikely since the device geometry, assuming that the QDs are located inside the fin, clearly favours DRSOI. The latter explanation is supported by the fact that some obvious features in the data are not captured by the model, which might originate from one of the neglected effects, such as anisotropic g-factors, a g-factor difference between the two dots, spin-flip co-tunnelling to the reservoirs and hyperfine interactions. A more elaborate model and analysis of the g-tensors (see chapter 5) could help to increase confidence in the results from this method. Ultimately, we conclude that the anisotropy of the PSB leakage current is more complex than assumed in our simple model, such that our analysis does not allow us to extract a reliable orientation of the spin-orbit field.

In Fig. 3.3 (d), we present cuts along the magnetic field axes x, y and z of the PSB leakage current. We find a similar leakage current suppression close to $B = 0$, but very different saturation currents. The line shape deviates heavily from the textbook-like Lorentzian current suppression that we observed in device A and is better fitted by a combination of two dips [QD22]. Furthermore, we present other measurements of PSB current suppression of device A in appendix A.2.5, which deviate from a Lorentzian current suppression. These features are not yet fully understood and call for further investigation.

3.3. QD SPECTRUM AT HIGH MAGNETIC FIELD

Next, we present an extension of the measurements in Fig. 3.2 (a) on device A to both larger magnetic fields and detunings in Fig. 3.4 (a), which reveals spin-orbit mediated singlet-triplet mixing. Resonant charge transport occurs for detunings, where $(1,1)$ and $(0,2)$ spin states are degenerate in energy and hybridised by a finite coupling (see Fig. 3.4 (d)). As seen in Fig. 3.4 (b), three current peaks are observed within the ε range of Fig. 3.4 (a), showing the B-dependence of the peak positions. For weak tunnel coupling and negative effective hole g-factor g^*, the bottom two curves in Fig. 3.4 (a) can be assigned to the $\mathrm{T}_-(1,1) \rightarrow \mathrm{S}(0,2)$ and $\mathrm{T}_-(1,1) \rightarrow \mathrm{T}_-(0,2)$ transitions [Li15]. Thus, the $\mathrm{T}_-(1,1)$ state can be used to probe the energy splitting of the $\mathrm{S}(0,2)$ and $\mathrm{T}_-(0,2)$ states (see Fig. 3.4 (c)).

While the central line remains at constant detuning for $B \lesssim 3\,\mathrm{T}$, signifying a spin-conserving transition, the bottom line shifts by the Zeeman energy $E_Z = g^*_{11}\mu_B B$, where g^*_{11} denotes the g^*-factor of the $(1,1)$ triplet states and μ_B the Bohr magneton. From the slope we can thus extract $|g^*_{11}| = 3.2 \pm 0.3$, corresponding to an effective hole g-factor of $|g^*| = 1.6 \pm 0.2$, a value similar to those reported before [Li15; Voi15]. When $g^*_{02}\mu_B B$ approaches $\varepsilon_{\mathrm{ST}}$, the $\mathrm{S}(0,2)$ and $\mathrm{T}_-(0,2)$ states first begin to align in energy but then anticross due to SOI (see Fig. 3.4 (c)) [Fas07]. This level repulsion causes the avoided crossing of the two bottom curves in Fig. 3.4 (a) at $B_c \simeq 10.9\,\mathrm{T}$. From the magnitude of the anticrossing we can extract the single-dot spin orbit gap $\Delta^{\mathrm{SD}}_{\mathrm{SO}} = 0.27 \pm 0.03\,\mathrm{meV}$. The spin-orbit length can be estimated to be $\lambda_{\mathrm{SO}} \sim g^*\mu_B B_c \lambda_x/(\sqrt{2}\Delta^{\mathrm{SD}}_{\mathrm{SO}}) = 48\,\mathrm{nm}$ [Fas07; Gao20], which is roughly half the value reported for holes in planar Si quantum dot

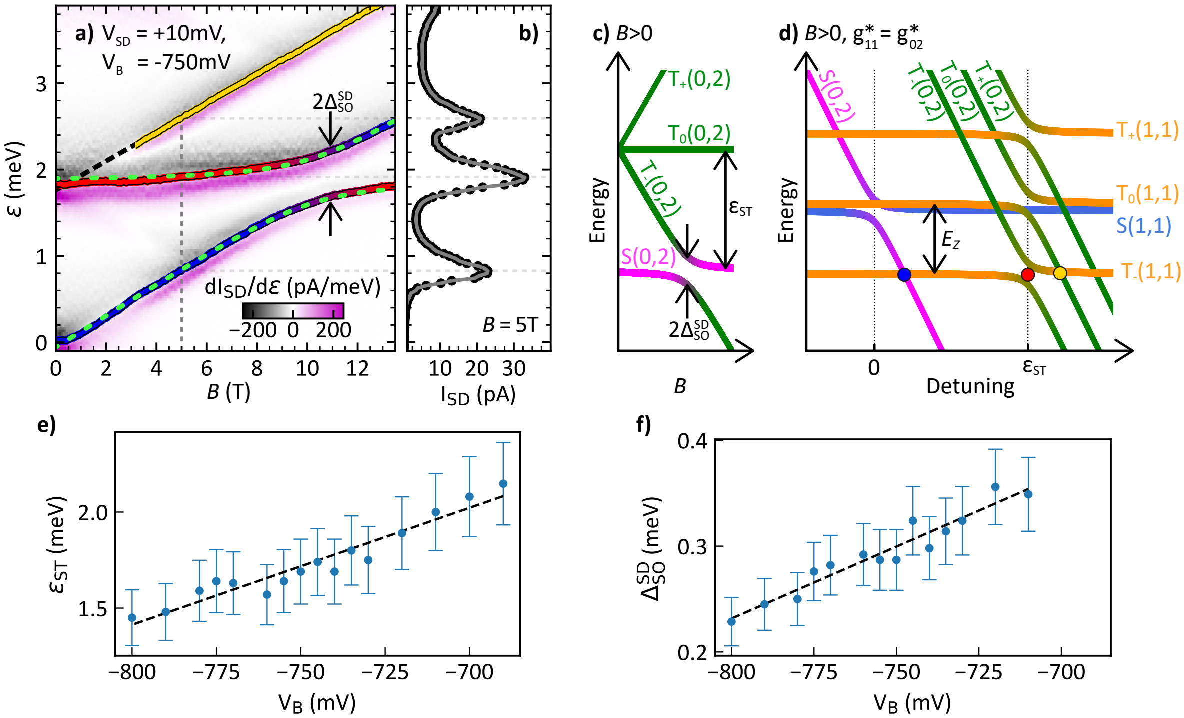

Fig. 3.4.: **Spin state mixing by SOI**. (a) Detuning energy of the three observed resonant current peaks as a function of magnetic field. The peak positions are extracted from current traces, such as the one presented in (b) for $B = 5\,\mathrm{T}$ (grey dashed line). The differentiated data $\mathrm{dI_{SD}}/\mathrm{d}\varepsilon$ is shown in the background. The anticrossing of the two bottom curves is fitted with the standard expression for two-level repulsion (green dashed curves). For $B \lesssim 3\,\mathrm{T}$ the energy splitting of the top and central peak cannot be resolved. (c) Magnetic field dependence of the double dot energy levels for $(0,2)$ charge configuration. The degeneracy of the triplet spin states T_+, T_0 and T_- is lifted by the Zeeman splitting E_Z. For $E_Z = \varepsilon_{\mathrm{ST}}$ the $\mathrm{S}(0,2)$ and $\mathrm{T}_-(0,2)$ states hybridise due to SOI and anticross. (d) Double dot energy diagram versus detuning at finite magnetic field. Spin-conserved tunnelling induces avoided crossings between states that share the same spin polarisation [Han07]. The blue, red and yellow dots mark the transitions denoted with the same colours in (a). (e),(f) Singlet-triplet splitting $\varepsilon_{\mathrm{ST}}$ respectively single-dot spin orbit gap $\Delta_{\mathrm{SO}}^{\mathrm{SD}}$ extracted for different barrier gate voltages V_{B} demonstrating electrical tunability following the linear fits (dashed lines).

structures [Li15]. Using $\varepsilon_{\mathrm{ST}} = 1.85\,\mathrm{meV}$ in addition to the parameters mentioned before we can overlay our data with the standard expression for two-level repulsion [Fas07] (green curves in Fig. 3.4 (a)) and find good agreement.

The barrier gate voltage V_{B} tunes $\varepsilon_{\mathrm{ST}}$ and $\Delta_{\mathrm{SO}}^{\mathrm{SD}}$ linearly, as indicated by the linear fits (dashed lines) in Figs. 3.4 (e), (f). This effect is observed over a range of $\sim 100\,\mathrm{mV}$, resulting in a change of almost 100%. Since $\lambda_x \sim \hbar/\sqrt{m^*\varepsilon_{\mathrm{ST}}}$ this tunability of $\varepsilon_{\mathrm{ST}}$ can be explained as a change of the confinement potential by V_{B}: increasing V_{B} decreases the confinement length along the fin, resulting in an increase of $\varepsilon_{\mathrm{ST}}$. The control over $\Delta_{\mathrm{SO}}^{\mathrm{SD}}$, on the other hand, is a result of the DRSOI, which is predicted to be strongly tunable by electric fields [KRL18; BHL21; Fro21b]. These results demonstrate excellent electrical control over the QDs and their properties.

3.4. CONCLUSION & OUTLOOK

In conclusion, we employed FinFET qubit devices for reproducible formation of low-disorder double quantum dots and study spin-dependent hole transport. We observe PSB current rectification and identify SOI as the dominant mechanism for PSB lifting. We observe an anisotropic PSB leakage current and try to model it to extract the SOI orientation. Magneto-spectroscopy experiments allowed us to extract a single-dot singlet-triplet splitting $\varepsilon_{\mathrm{ST}} \simeq 1.85\,\mathrm{meV}$, indicating high orbital energies due to ultra-small gate lengths. Further, an effective hole spin g-factor $|g^*| = 1.6$ and single-dot spin orbit gap $\Delta_{\mathrm{SO}}^{\mathrm{SD}} = 0.27\,\mathrm{meV}$ are derived by modelling a two-level anticrossing occurring at $B_c = 10.9\,\mathrm{T}$. We demonstrate electrical control over these QD parameters as well as the PSB leakage current. These results demonstrate that hole spins in Si FinFETs are a promising platform for hosting fast and electrically controllable qubits.

4

HOT HOLE SPIN QUBITS

Parts of this chapter have been published in:

A hole spin qubit in a fin field-effect transistor above 4 kelvin
Nature Electronics **5**, 178-183 (2022), doi:10.1038/s41928-022-00722-0
Leon C. Camenzind*, Simon Geyer*, Andreas Fuhrer, Richard J. Warburton, Dominik M. Zumbühl and Andreas V. Kuhlmann

This chapter introduces a cryogenic qubit measurement setup, in which for the first time hole spin qubits hosted in a bulk-Si FinFET were realised. Coherent operation at a temperature above 4 K is demonstrated, a necessary operation regime for large-scale integrated quantum processors. Fast electrical control of hole spins with driving frequencies up to 150 MHz and single-qubit gate fidelities at the fault-tolerance threshold, determined by randomised benchmarking, are achieved. The gate quality factor $\mathrm{Q} \gg 87$ *already matches or exceeds the reported values for other hole spin qubits at mK temperatures. The maximum coherence time of* 440 *ns is further increased by dynamical decoupling and the noise spectrum is investigated.*

QD spin qubits in Si [Zwa13; Gon21] have great potential for application in large-scale quantum computation [Fow12], owing to their long coherence times [Vel14] and high quality factors [Tak16; Yon17; Yan19]. Moreover, state-of-the-art CMOS manufacturing processes [Mau16; Kuh18; Gey21; Zwe22] can be employed to engineer a dense array of interconnected spin qubits [Van17; Vel17; Bot22]. Inspired by the great success of conventional integrated circuits, on-chip integration of the classical control electronics with the qubit array has been proposed to overcome the challenge in wiring up large numbers of multi-terminal QD devices [Fra19]. Since the electronics produce heat, the amount of control functionality that can be implemented strongly depends on the available cooling power. Therefore, it is highly beneficial to operate qubits at temperatures greater than 1 K, where cooling power is orders of magnitude higher than at mK temperatures [Pet20a; Pet20b; Yan20]. For instance, Intel's cryogenic control chip named Horse Ridge works at 3 K [Xue21].

Recently, electron spin qubits [Vel14; Kaw14; Tak16; Yon17] operating up to 1.5 K have been demonstrated [Pet20a; Pet20b; Yan20]. Hole spin qubits [BL05; Mau16; Wat18b; Hen20b; Hen20a; Hen21; Fro21b] present an intriguing alternative to electrons due to their strong SOI and weak hyperfine interaction, but have so far only been operated at mK temperature. Here, we show hole spin qubits working at 1.5 to 5 K, that is, in a temperature range where the thermal energy is much larger than the qubit level splitting and cryogenic control electronics can be operated [Xue21]. The spin qubits are hosted in CMOS-compatible FinFET devices that were fabricated in a flexible process with fast turn-around [Kuh18; Gey21]. The fin provides a one-dimensional confinement for the holes, enabling fast and electrically tunable effective spin-$\frac{1}{2}$ qubits [KRL18; BHL21; Fro21b]. We demonstrate EDSR-based spin control with Rabi frequencies up to 150 MHz and voltage-tunable qubit frequencies, a feature employed to implement z-rotations as fast as 45 MHz. Moreover, we show spin rotations around the x- and y-axis of the Bloch sphere with a single-qubit gate fidelity of 98.9 % at 1.5 K. A high robustness against temperature allows for qubit operation above the boiling point of liquid ^{4}He, albeit with a reduced dephasing time T_2^* compared to 1.5 K, which is consistent with an observed whitening of the spectral noise density on increasing temperature.

4.1. Measurement setup

This section introduces a cryogenic qubit measurement setup for direct current (d.c.) transport-based qubit readout. Over a time span of four years various small changes to improve the setup have been implemented, but its main features remained the same. We focus here on the final, improved setup shown in Fig. 4.1 a, detailed descriptions of intermediate configurations can be found in the appendix of each chapter. The silicon chiplets hosting 16 devices are attached to a printed circuit board (PCB) and wire bonded using aluminium wires. The PCB provides RC filtering with long time constants for 37 low-frequency lines and hosts three bias-tees which allow us to mix d.c. signals with the high-frequency pulses necessary for qubit control. Furthermore, the PCB can be equipped with a tank circuit for RF-based readout schemes [Vig23] as demonstrated in Ref. [Egg23], however, this feature is not used in this thesis.

The PCB is compatible with various different setups in our lab, ranging from room-temperature test setups for checking wire bonding to dilution refrigerator setups for detailed qubit analysis. In this chapter the measurements are performed using a variable-temperature insert (VTI) with a temperature range of $T \sim 1.4\,\mathrm{K}{-}50\,\mathrm{K}$. In chapters 5, 6 and 7 the PCB will be hosted by a Bluefors dilution refrigerator (XLD) which enables measurements at a cryostat base temperature of $T \sim 10\,\mathrm{mK}$. Besides the temperature, the main difference between the setups is the attenuation of the high-frequency lines, which is nominally 8 dB/25-30 dB for the VTI/XLD [Cam12; Cam19]. Moreover, the VTI provides a single-axis magnetic field up to 8 T, whereas the XLD hosts a 3-axis vector magnet with fields up to 1 T for arbitrary orientations.

The room-temperature component of the measurement setup consists of a standard transport measurement setup with additional high-frequency components. Constant voltage signals are provided by a low-noise voltage source (DAC) SP927 from BasPI and current is measured with a data acquisition card (DAQ) USB-6363 from National Instruments via a current-to-voltage amplifier (IV) at gain 10^9 (BasPI SP983c version LSK389A). For source-drain current measurements the signal is doubled by measuring the current at source and drain with two separate IVs and adding the signal using a BasPI SP944 before digitising, which, at the same time, rejects common mode noise.

The fast gate pulses are created with an arbitrary waveform generator (AWG) Tektronix AWG5208. Furthermore, the AWG provides the amplitude and quadrature (IQ) input signals for microwave (MW) pulse generation on a vector signal generator (VS) R&S SGS100A with or without sideband-modulation (SB). The fast gate pulses and the MW signal are combined using a diplexer WDKX11+10-DC-1000/1300-15000-60S3 from Wainwright, which allows signals of two different bands (here d.c.$-1\,\mathrm{GHz}$ and $1.3-15\,\mathrm{GHz}$) to be combined with minimal attenuation. Finally, the high-frequency coaxial lines are wound around a ferrite core to improve noise performance before the signal enters the cryostat. The resulting signal is shown in Fig. 4.1 c, which features a two-stage trapezoid pulse with amplitude A_P switching between the readout/initialisation stage and the manipulation stage. Since the bias-tee only couples the alternating current (a.c.) component of this signal and blocks out the d.c. component, we choose the waveform such that the time-average is zero, i.e. the pulse is symmetric around zero and the two stages are of equal length, to avoid charging up the bias-tee. Then, the d.c. offset is supplied by the DAC and added to the signal via the low-frequency input of the bias-tee, allowing the

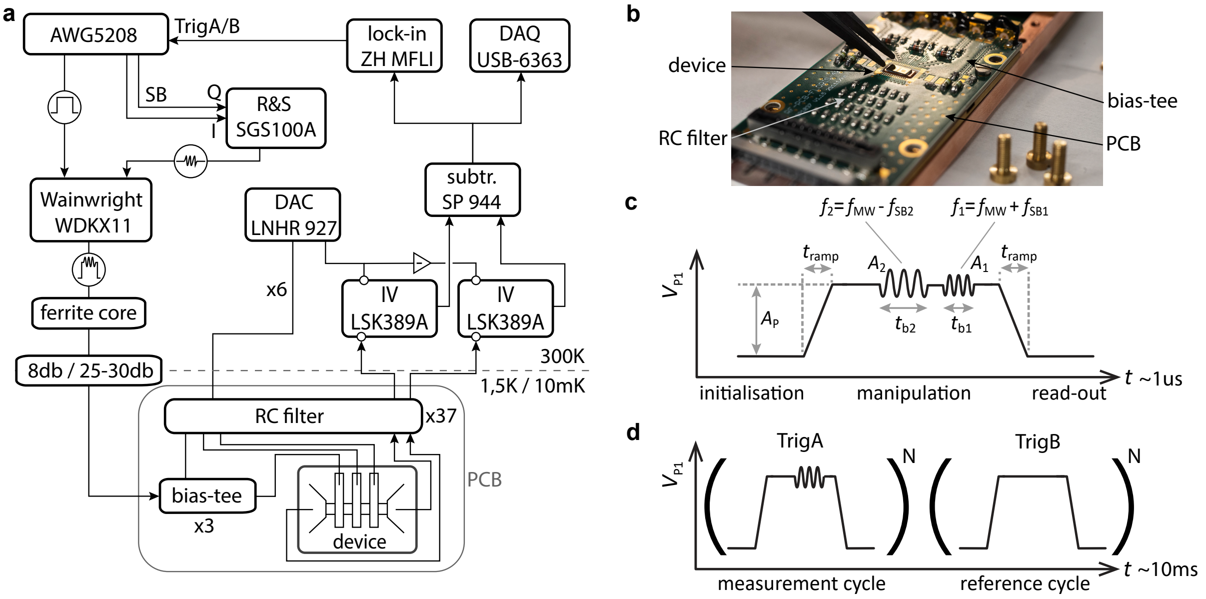

Fig. 4.1.: **Cryogenic qubit measurement setup.** **a**, Schematic of the VTI and XLD setup with room-temperature control electronics and PCB/device at cryogenic temperatures. **b** Image (adapted from Ref. [NCC]) of the PSB hosting the device under test. **c** Definition of the qubit control pulse parameters. **d** Low-frequency signal modulation using the lock-in amplifier for better noise rejection.

initialisation/readout stage voltage to be fixed and A_P to tune the manipulation stage voltage. A finite ramp time is introduced to avoid high-frequency components in the fast gate pulse, which cannot pass through the diplexer's low-frequency input.

In the manipulation stage MW bursts with amplitude A_n, length t_n, phase ϕ_n and frequency f_n are added to the trapezoid gate pulse. Different frequencies for the individual pulses can be achieved by means of SB modulation of a base tone f_{MW} of the VS with different control pulses from the AWG, which is useful to address multiple qubits. The typical length of the pulse cycle is of the order of $\sim 1\,\mu$s. To increase the signal-to-noise ratio we introduce a lock-in amplifier (Zurich Instruments MFLI) to modulate the MW signal at a frequency of 87.7 Hz for better noise rejection.[1] We sent a trigger signal from the lock-in amplifier to the AWG, which switches the output waveform between the measurement cycle and the reference cycle. Typically, a reference cycle without MW signals is chosen, but this scheme also allows for more complex reference cycles, e.g. with qubit projection onto opposite spin states [Hen20a].

The qubit control scheme used throughout this thesis works as follows: in the initialisation stage, the DQD is tuned close to the (1,1)-(0,2) charge transition, where PSB [Ono02; Joh05; Li15] occurs (see Fig. 4.2 d). In PSB hole tunnelling is forbidden by spin conservation if the two spins, one per QD, occupy a spin-polarised triplet state ($|(1,1)\mathrm{T}_+\rangle$ or $|(1,1)\mathrm{T}_-\rangle$) and are thus aligned parallel. The unpolarised triplet $|(1,1)\mathrm{T}_0\rangle$ is unblocked as a finite

---

[1] For a detailed description of the lock-in amplifier operation principle and its advantage for noise reduction we recommend to read chapter 6 of Ref. [ZhI].

difference in g^*-factor mixes it with the singlet $|(1,1)\mathrm{S}\rangle$, which itself is coupled to the singlet of the $|(0,2)\mathrm{S}\rangle$ such that hole transport occurs [See21]. After a possibly short time of hole transport, eventually a blocked state will be loaded onto the DQD, initialising the spin state of the two qubits. Next, qubit manipulation is performed deep in the (1,1) charge configuration in the Coulomb blockade regime, where the holes cannot escape despite applied MW pulses. The spin of each qubit can be flipped using EDSR [Now07; Nad10a; Mau16; Wat18b; Fro21b], which is performed by applying MW bursts to gate P1 (Fig. 4.2 b). EDSR takes place under the condition that the MW frequency f_{MW} equals the Larmor frequency $f_L = |g^*|\,\mu_B\,|B_{\mathrm{ext}}|/h$, where g^* denotes the effective hole g^*-factor along the magnetic field B_{ext} direction, μ_B Bohr's magneton and h Planck's constant. Finally, the DQD is tuned into PSB for qubit readout. Note that initialisation and readout are nominally identical. If the spin of either hole was successfully flipped during manipulation, one extra hole can tunnel during readout compared to a cycle without manipulation. By repeating this qubit control scheme at ~MHz frequency and using the above-mentioned lock-in amplifier we can integrate a current that is proportional to the spin-flip probability. The fast repetition, necessary to obtain a measurable current, limits the maximum time available for qubit initialisation, manipulation and readout to a few μs.

4.2. SPIN QUBIT OPERATION ABOVE 4 KELVIN

In this section, we show the first measurements of a hole spin qubit in a Si bulk FinFET qubit device, which was fabricated according to chapter 2. A SEM tilted side-view and a TEM cross-sectional view of a co-fabricated device are shown in Figs. 4.2 a, b. Since these FinFETs are fabricated using CMOS processes, they feature a highly uniform gate profile [Zwe22] and ultra-small gate lengths [Gey21] resulting in an estimated effective dot size of $\sim 7\,\mathrm{nm}$ (see appendix A.3.6). Here, we investigate device B whose dimensions are provided in Tab. A.1. By negatively biasing the gate electrodes, an accumulation-mode hole DQD, hosting two individual spin-$\frac{1}{2}$ qubits, is formed. Here, a pseudospin of $\pm\frac{1}{2}$ is assigned to the two lowest energy holes states, which for 1D-like holes systems can have large contributions of both heavy-hole and light-hole basis states [KRL18; BHL21]. We measure the direct current I_{DC} through the DQD, which is combined with PSB for spin-to-charge conversion to provides qubit readout functionality. For the device investigated, PSB is observed for the $(1,1) \rightarrow (0,2)/(2,0)$ charge state transitions and no additional transitions are observed when further depleting the QDs. Here (m, n) denotes the effective hole occupancy of the left/right QD, while the true hole occupancy is $(m + m_0, n + n_0)$ with possible additional holes m_0, n_0.

For high-temperature operation of spin qubits [Pet20a; Pet20b; Yan20], spin-to-charge conversion via PSB rather than energy-selective tunnelling [Elz04] is favourable, since the single-dot singlet-triplet splitting [Gey21] is typically much larger than the Zeeman energy.

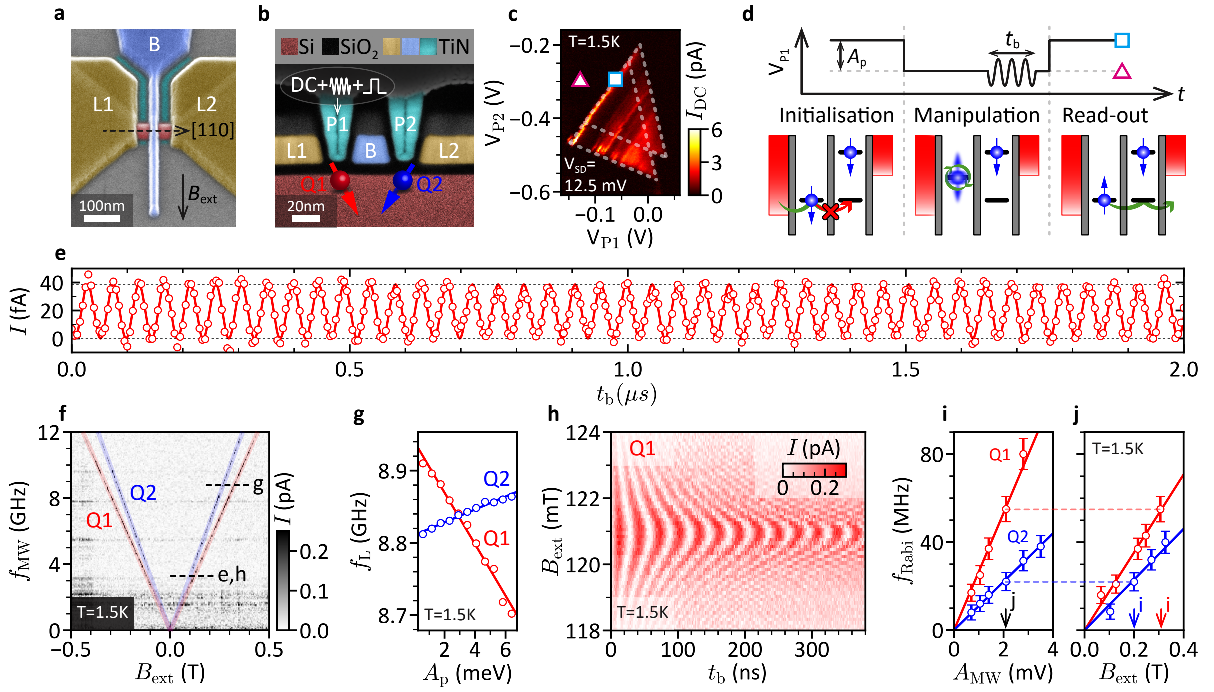

Fig. 4.2.: **Spin-orbit qubits in a FinFET.** **a**, False-colour SEM image of an unfinished device showing the two lead gates L1, L2 (yellow) as well as the inter-dot barrier gate B (blue, ∼35 nm). An in-plane external magnetic field B_{ext} is applied perpendicular to the fin (red). **b**, Cross-sectional TEM image along the black dashed line shown in **a** after integration of the QDs' plunger gates P1, P2 (turquoise, ∼15 nm). In addition to a DC voltage, fast pulses and microwaves can be applied to P1. Current flow is observed from source to drain via the fin-shaped channel. **c**, Measurement of a spin-blocked pair of bias triangles. The blue square and pink triangle mark the qubit initialisation/readout and manipulation point, respectively. **d**, Schematic illustration of the spin manipulation cycle with corresponding pulse scheme. **e**, Rabi oscillation with $f_{\text{Rabi}} = 22\,\text{MHz}$ measured on Q1 at $B_{\text{ext}} = 123\,\text{mT}$, $f_{\text{MW}} = 3.311\,\text{GHz}$, $A_{\text{MW}} = 1.1\,\text{mV}$ and $\text{T} = 1.5\,\text{K}$. The data has been corrected by removing a small constant offset, and is fitted (solid curve) to $I(t_{\text{b}}) = A\sin(2\pi f_{\text{Rabi}} t_{\text{b}} + \theta) + B$ with A, B, f_{Rabi} and θ as fit parameters. **f**, Measurement of the current as a function of f_{MW} and B_{ext}. Along the red (blue) line the spin resonance condition is met for Q1 (Q2). For each frequency the average current has been subtracted. **g**, Electrical tunability of the qubit frequency with the depth of the Coulomb pulse. Solid lines represent linear fits to the data. **h**, Detuned Rabi oscillations showing a typical chevron pattern, measured at $f_{\text{MW}} = 3.311\,\text{GHz}$ and $A_{\text{MW}} = 1.4\,\text{mV}$. Dependence of f_{Rabi} on A_{MW} **j** and B_{ext} **i**. Solid lines are linear fits to the data with zero offset.

Thus, the measurements can be performed at higher temperature and smaller external magnetic field, resulting in lower and technically less demanding qubit frequencies.

Using the qubit control scheme described in section 4.1, we map our the EDSR resonances in the f_{MW}-B_{ext} plane in Fig. 4.2 f, which appear as an increased current whenever $f_{\mathrm{MW}} = |g^*|\, \mu_B\, |B_{\mathrm{ext}}|/h$ is satisfied. The spin resonance conditions differ slightly for the two qubits (Q1, Q2), making them individually addressable. From the slope of the current lines, we extract absolute values for the g^*-factor of 1.94 ± 0.05 and 2.35 ± 0.05, respectively. These two different values indicate a sensitivity to the local electric fields, which also provides an additional control knob for the g^*-factor, and thus the qubit frequency [Vel14; Yon17; Cri18; Hen20b; Fro21b]. This is confirmed by Fig. 4.2 g, where the f_L-dependence on the square pulse amplitude A_{p} is shown.

When the MW drive is on resonance, the DQD current reveals Rabi oscillations as a function of the burst duration t_{b}. An example of a 22 MHz Rabi oscillation, whose decay time is too long to be observed within $87\,\pi$ rotations, corresponding to the longest applicable t_{b}, is given in Fig. 4.2 d. For a slightly detuned f_{MW} the qubit rotates around a tilted axis on the Bloch sphere, resulting in faster rotations of reduced contrast as demonstrated by the chevron pattern seen in Fig. 4.2 h. The Rabi frequency f_{Rabi} increases linearly not only with the MW amplitude A_{MW} (Fig. 4.2 i), but also B_{ext} (Fig. 4.2 j) as expected for SOI-mediated spin rotations [GBL06; Now07; Fro21b; Are13; Voi15; Cri18]. For these measurements, A_{MW} is calibrated using the photon-assisted-tunnelling response (see appendix A.3.3) [Now07]. The maximum f_{Rabi} observed is 147 MHz (see appendix A.3.5), which corresponds to a spin-flip time of just ~ 3.4 ns. Under the assumption that EDSR occurs due to a periodic displacement of the wave function as a whole, the g^*-factor is not modulated [Cri18] and f_{Rabi} depends on the spin-orbit length l_{SO} [Now07]. We can therefore state an estimate for l_{SO} in the range of 20 to 60 nm (see appendix A.3.7), that is, similar values to the one reported before [Gey21] and in very good agreement with theory predictions [KRL18].

A key parameter for the qubit controllability is the gate quality factor [SL22] defined as $\mathrm{Q} = 2 f_{\mathrm{Rabi}} T_2^{\mathrm{Rabi}}$, where T_2^{Rabi} is the decay time of the Rabi oscillations. For the data presented in Fig. 4.2 e no decay is observed within $\sim 2\,\mu$s, that is, $\mathrm{Q} \gg 87$. In terms of gate quality factors, our hole spin qubits therefore outperform their hot electron counterparts [Pet20a; Yan20].

Next, we evaluate the spin coherence by performing a Ramsey experiment. Here, two $\frac{\pi}{2}$-pulses separated by a delay time τ during which the qubit can freely evolve and dephase are applied. When f_{MW} is detuned from the qubit resonance, the current through the device shows coherent oscillations known as Ramsey fringes. The data of Fig. 4.3 a is measured at a temperature of $\mathrm{T} = 4.2$ K, which corresponds to the boiling point of liquid ^{4}He, and which can be achieved in a technically non-demanding way by immersing the sample in a

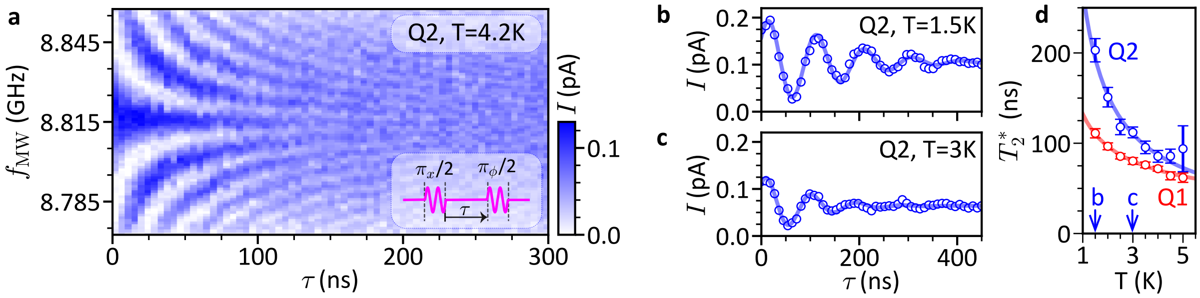

Fig. 4.3.: **Hot qubit coherence.** **a,** Ramsey-fringe experiment performed at 4.2 K. B_{ext} is fixed at 267 mT. The pulse sequence, which consists of two 15 ns-long $\frac{\pi}{2}$-bursts separated by the waiting time τ, is illustrated in the bottom right inset. ϕ denotes the phase of the second pulse with respect to the first one, here $\phi = 0$. Decay of Ramsey fringes at 1.5 K **b** and 3 K **c**. The data were taken on resonance with a τ-dependent phase $\phi(\tau)$, which adds an artificial oscillation [Wat18a]. Solid curves show fits to $A + B\sin(\omega\tau + \theta)\exp[-(\tau/T_2^*)^{\beta+1}]$ with temperature dependent β. **d,** Temperature dependence of the spin dephasing time revealing a power-law decay $T_2^* \propto \mathrm{T}^{-\eta}$, where $\eta = 0.46 \pm 0.02$ for Q1 and $\eta = 0.81 \pm 0.06$ for Q2, respectively.

liquid ^{4}He bath or at the second stage of a dry pulse-tube refrigerator. The dephasing time T_2^* is determined by fitting the envelope of the fringe decay to $\exp(-(\tau/T_2^*)^{\beta(\mathrm{T})+1})$, where β depends on temperature as discussed later. Despite the fact that our qubit readout is protected against temperature by the large orbital energies, which exceed the thermal energy available at 4.2 K by an order of magnitude, a degradation of the signal contrast on increasing temperature is observed (Fig. 4.3 b, c). The reasons for this are not yet fully understood, however we speculate that this is due to spin-flip co-tunnelling (see appendix A.3.8). The T-dependence of T_2^* in the range of 1.5 to 5 K is presented for both qubits in Fig. 4.3 d. While Q1 can be manipulated faster than Q2, it lags behind in coherence. The spin dephasing time drops with increasing temperature, described by a power-law decay $\propto \mathrm{T}^{-\eta}$ with $\eta = 0.5$ (0.8) for Q1 (Q2), a rather weak temperature dependence similar to previous reports [Yan20; Pet20a]. The obtained values for T_2^* are consistent with the EDSR spectral width (see appendix A.3.9), and a spin relaxation time $T_1 > 10\,\mu$s was found at 4.2 K (see appendix A.3.12). In the following the focus is on the more coherent Q2.

Spin rotations around at least two different axes are required to reach any point on the Bloch sphere. In Fig. 4.4 a we demonstrate two-axis qubit control at both 1.5 K and 4.2 K by employing a Hahn-type echo sequence. A modulation of the relative phase ϕ of the second $\frac{\pi}{2}$-pulse yields a set of Ramsey fringes that are phase-shifted by π for a π_x and π_y echo pulse, which is applied to extend the coherence. The performance of the hole spin rotations is characterised using randomised benchmarking [Kni08; Muh15] (see Fig. 4.4 b and appendix A.3.15). At 1.5 K, a single-qubit gate fidelity of $F_{\mathrm{s}} = 98.9 \pm 0.2\,\%$ is obtained, which is at the fault-tolerance level [Fow12; Vel14] and very similar to the values recently reported for hot electron spin qubits [Yan20; Pet20a]. We note that the fidelity is lower than expected from the gate quality factor [SL22], which might be due

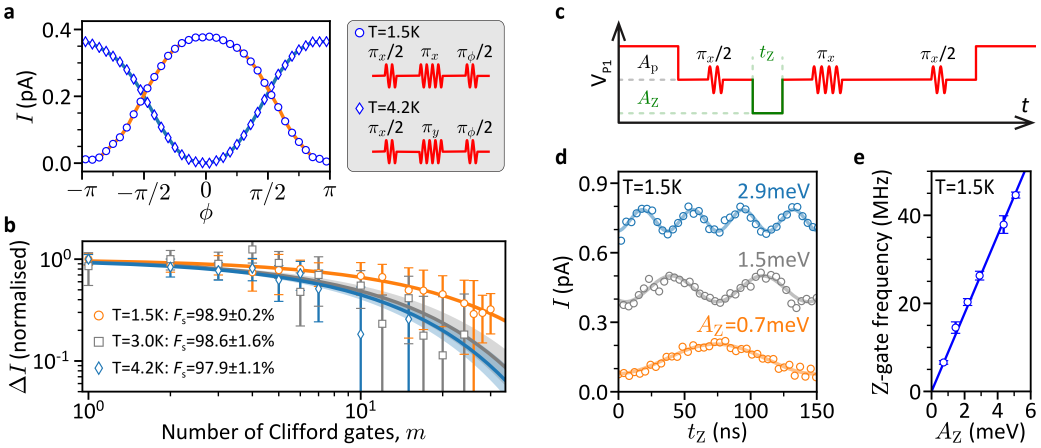

Fig. 4.4.: **X, Y and Z qubit gates. a**, Demonstration of two-axis qubit control by applying a Hahn-type echo sequence, where the relative phase ϕ of the second $\frac{\pi}{2}$-pulse is varied. The measurements at 1.5 K (circles) and 4.2 K (diamonds) are phase-shifted by π due to the two orthogonal echo pulses, as shown in the right panel. **b**, Standard randomised benchmarking at 1.5 K (circles), 3 K (squares) and 4.2 K (diamonds) is performed by applying a varying number of Clifford gates m and preparing either a $|\uparrow\rangle$ or $|\downarrow\rangle$ final state. The normalised difference of currents is fitted to a single exponential decay to extract the single-qubit gate fidelities F_s (see appendix A.3.15 for further details). The shaded regions show the one-sigma error range of the fit parameters. The maximum m decreases with increasing temperature due to a reduced readout contrast. **c**, Schematic representation of the pulse scheme used to demonstrate qubit rotations around the z-axis of the Bloch sphere. In a modified Hahn echo sequence a square pulse of amplitude A_Z and duration t_Z is applied to shift the qubit precession frequency (see Fig. 4.2 g). The resulting phase-shift-induced oscillations are shown in **d** for different A_Z. Solid curves represent fits to a sinusoidal function, where the oscillation frequency is given by the induced qubit frequency shift. Traces are offset by an increment of 0.3 for clarity. **e**, The speed of the z-rotations increases linearly with A_Z. The solid line represents a linear fit to the data, yielding a frequency-shift of 8.9 MHz/meV. The data presented in this figure was taken for Q2 at $f_\mathrm{MW} = 8.812$ GHz.

to T_2^* limiting the fidelity via our choice of implementation of the Clifford identity gate (see appendix A.3.15). The fidelity is reduced to $F_\mathrm{s} = 98.6 \pm 1.6\,\%$ ($97.9 \pm 1.1\,\%$) at 3 K (4.2 K), revealing a similar scaling with temperature as T_2^*. We thus expect to be able to enhance the gate fidelities further by improving the qubit coherence, and by optimisation of the gate pulses [Kel14].

Besides rotations around the x- and y-axis of the Bloch sphere, z-rotations can be realised by exploiting the electrical tunability of the qubit frequency (Fig. 4.2 g). For this purpose a square pulse of amplitude A_Z and duration t_Z is added to a Hahn echo sequence (Fig. 4.4 c) in order to rapidly detune the spin precession frequency, which leads to a phase pick up around the z-axis of the Bloch sphere [Yon17]. As a consequence, the DQD current oscillates as a function of t_Z (Fig. 4.4 d) at a frequency that increases linearly with A_Z up to ~ 45 MHz (Fig. 4.4 e).

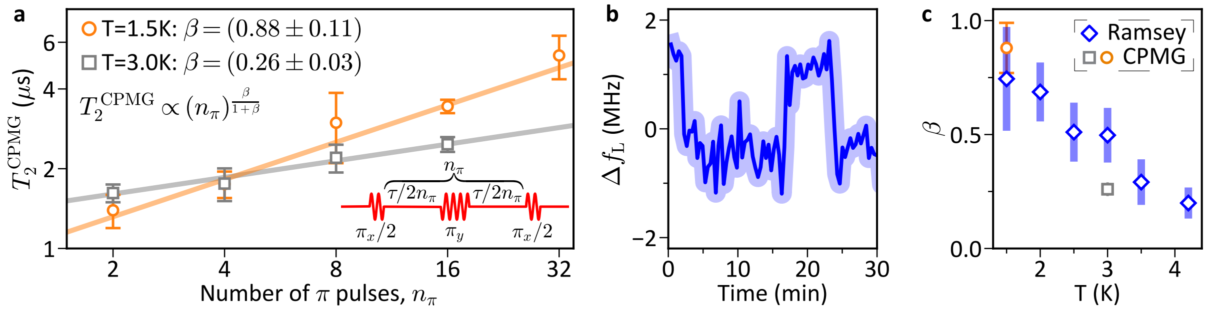

Fig. 4.5.: **Dynamical decoupling and noise spectroscopy.** **a**, The spin coherence time can be enhanced by decoupling the qubit from low-frequency noise using a CPMG pulse sequence (see bottom-right schematic). A power-law dependence of the coherence time on the number of refocusing pulses n_π is confirmed by fitting (solid lines) the data to $T_2^{\mathrm{CPMG}} = T_2^0 (n_\pi)^{\frac{\beta}{1+\beta}}$, where β represents the scaling exponent of a power-law noise spectrum, $S(f) \propto f^{-\beta}$. **b**, Time trace of the qubit frequency obtained from repeated Ramsey measurements. The shaded region indicates the frequency uncertainty due to readout noise. **c**, Temperature dependence of the noise exponent β extracted from either CPMG or Ramsey measurements. The data presented in this figure was taken for Q2 at $f_{\mathrm{MW}} = 8.812\,\mathrm{GHz}$.

4.3. NOISE SPECTRUM ANALYSIS

Finally, in order to gain insight into the sources of decoherence we perform noise spectroscopy by employing Carr-Purcell-Meiboom-Gill (CPMG) pulse sequences [MG58], where a series of n_π π_y-pulses is applied as a spectral filter for the environmental noise [Byl11; Med12; Mal16; Yon17]. For a power-law noise spectrum $S(f) \propto f^{-\beta}$, the CPMG coherence time T_2^{CPMG} is expected to scale as $T_2^{\mathrm{CPMG}} \propto (n_\pi)^{\frac{\beta}{1+\beta}}$ [Med12]. This dependency is confirmed by Fig. 4.5 a, and a β of 0.88 ± 0.11 (0.26 ± 0.03) is determined for 1.5 K (3 K), revealing a whitening of the noise on increasing the temperature and thus a reduced noise-decoupling efficiency. For $n_\pi = 32$, the maximum n_π achievable with our transport-based readout scheme, the hole spin coherence time is extended to 5.4 μs at 1.5 K, which corresponds to an increase by a factor of 27 compared to the unprotected qubit. While our CPMG measurements are sensitive to the noise at frequencies of $f \sim 10^5 - 10^7$ Hz, we independently probe $S(f)$ at $f \sim 10^{-3} - 10^{-1}$ Hz by tracking the Larmor frequency fluctuations through repeated Ramsey experiments [Yon17] (Fig. 4.5 b). The temperature dependence of β demonstrates a noise whitening in both frequency ranges, and the good agreement of the β-values for the two frequency windows suggests a similar coloured noise spectrum over a wide range of frequencies. In contrast, a recent study of electron spin qubits has found a temperature-independent β for low frequency noise, but confirms our trend of noise whitening for high frequencies [Pie23]. From the scaling of β with T we cannot uniquely identify the underlying noise sources, such as charge or nuclear spin fluctuations [Kuh13]. We note, however, that the longest T_2^* measured is $\sim$440 ns (see appendix A.3.10), which does not only exceed the dephasing times reported so far for hole spins in Si at mK temperatures [Hut18], but is also close to the estimated limit of $\sim$500 ns set by the hole spin hyperfine interaction (see appendix A.3.11). This sub-μs limit is a consequence of the hole spins interacting with a relatively small number of nuclear spins $N_s \sim 310$, which increases the Overhauser field fluctuations that scale with $1/\sqrt{N_s}$ [Ass11], and also represents a lower bound due the anisotropy of the hole hyperfine interaction [Pre16; BL21].

4.4. Conclusion & outlook

In conclusion, we have demonstrated hole spin qubits in Si FinFETs that operate above 4 K. On the one hand, the strong SOI allows for spin rotations as fast as 147 MHz, and on the other hand, the weak hyperfine coupling ensures T_2^* up to 440 ns. In addition to two-axis control, we implement fast z-rotations by employing the electrical tunability of the g^*-factor. At 1.5 K we achieve fault-tolerant single-qubit gate fidelities. These results have been accomplished using an industry-compatible FinFET device architecture, which is also well suited for implementing larger arrays of interacting qubits, for example a linear chain of exchange-coupled QD spins. Connectivity beyond nearest neighbours can be realised by coupling to a superconducting microwave resonator [Bor19] or coherent spin shuttling [Yon21].

In the quest for a higher qubit quality factor, hyperfine-induced dephasing can be prevented by engineering a nearly nuclear-spin-free environment [Vel14]. While a stronger SOI results in shorter gate times, it also increases the susceptibility to charge noise. For hole spins in Si FinFETs, however, an unusually strong and at the same time electrically tunable SOI, allowing for on demand switching between qubit idling and manipulation modes, has been predicted [KRL18; Fro21b; BHL21]. Furthermore, fast single-shot readout of hole spins is required for accurate qubit measurements. At few-kelvin temperatures this can be realised using a DQD charge sensor that exploits tunnelling between two quantised states [Hua21]. This technique is more resilient against temperature than a single sensor QD, and high-fidelity single-shot readout up to 8 K at a bandwidth greater than 100 kHz was demonstrated. In addition, a read time resolution $< 1\,\mu$s, i.e. fast compared to our hole spin lifetime, was demonstrated using radio frequency reflectometry of a Si DQD [Noi20]. These readout techniques can be combined with the advance reported here, a hole spin qubit in a FinFET at temperatures of 4 K and above.

5

Hole spin qubit anisotropy

This chapter reports on the anisotropy of various properties of hole spin qubits hosted in a Si FinFET. The qubit g^**-factor, its electric tunability, Rabi frequency and coherence time are mapped out against the magnetic field orientation and modelled. This enables the extraction of a g-tensor describing the anisotropic behaviour of* g^**, the separation of the Rabi drive into two driving mechanisms, the analysis of the noise environment of the qubits and the prediction of qubit quality factor sweet spots.*

(The development and fitting of the microscopic model for the g^*-factor anisotropy presented in this chapter was lead by Peter Stano.)

Holes in Si and Ge are an interesting and versatile platform for spin experiments. What they lack in complexity due to the absence of valleys, they make up for in terms of a p-type Bloch symmetry, yielding three distinct sub-bands (see section 1.2). These characteristics result into a strong intrinsic SOI and weak hyperfine interaction in the valence band. The interplay of SOI, confinement and strain lifts the degeneracy of the hole bands and leads to band mixing. Ground states of HH, LH or a mix of the two emerge depending on the details of confinement of the hole [Sca20; KRL18].

These hole states exhibit strongly anisotropic properties, which have been predicted and observed for different crystal orientations [BL21; BHL21; KRL18] or directions of magnetic field [BL21; BHL21; HKL20; KRL18; Pio22; Li15; Wat16; Wat18b; Lil21; Cri18; Mic23]. The most prominent effects are anisotropic mass, spin-orbit coupling, g^*-factors, their susceptibility to electric fields and hyperfine interaction. Recently, the observation of anisotropic exchange interaction [Gey22] has added yet another property to this list of anisotropies. The anisotropic behaviour of hole spins has sparked interest in sweet spots for qubit operation, which can be engineered to increase qubit speed [Bos21; Mic23; Ade22a; Are13; Cri18; KRL18; Fro21b] and gate fidelity [Gey22; Bos22] or suppress noise [Pio22; BHL21; BL21; Ade22a; Fro21b].

In this chapter, we investigate the anisotropy of two Si hole spin qubits in a FinFET device by applying an external magnetic field along different orientations. We observe a large g^*-factor anisotropy and discuss different models that reproduce the data, allowing us to extract the shape and orientation of the QDs. Furthermore, the anisotropy of Rabi frequency and g^*-factor susceptibility to electric fields are investigated and phenomenologically modelled. Using this data, we disentangle the influences of two different mechanisms for spin-orbit mediated qubit driving for the two qubits. We control the contribution of the two EDSR driving mechanisms by choosing different gate electrodes for the MW electric qubit drive. Finally, we map out the qubit coherence time T_2^* and use a model to extract charge noise and other noise contributions. The model allows us to predict magnetic field orientations with a high qubit quality factor, i.e., fast drive and long coherence.

5.1. g^*-FACTOR ANISOTROPY

Throughout this chapter we present experiments on two hole spin qubits hosted by a DQD in device C (see Tab. A.1). The measurements are conducted in the XLD setup at base temperature of $\sim 40\,\mathrm{mK}$ which is introduced in section 4.1. The same scheme for qubit initialisation, manipulation and readout as in chapter 4 is used. Also, qubit characteristics such as g^*-factor, Rabi frequency etc. are extracted in a similar way to the previous chapter and differences are described in appendix A.4.1, which also presents standard device and qubit metric measurements. The XLD setup features a vector magnet consisting of three superconducting magnets oriented along x, y and z-direction, which allow us to apply an external magnetic field in an arbitrary orientation.

In this section, we measure the EDSR resonance frequency of Q1 and Q2 for different magnetic field orientations. We extract the effective g-factor g^* via $f_L = g^* \mu_\mathrm{B} |\mathbf{B}|/h$ for each magnetic field orientation to investigate its anisotropy. The g^*-factors of both qubits are extracted at constant $|\vec{B}|$ while sweeping the magnetic field orientation in three different planes as indicated in Fig. 5.1 a and displayed as points in Fig. 5.1 b. We find for both qubits that g^* is strongly anisotropic and changes by a factor of two, which is typical for holes [Cri18; Lil21], but orders of magnitude more than observed for electrons in Si-MOS [Tan19]. Interestingly, the maximum g^* of the two qubits shows a shift of $\sim 45°$ in the xy-plane with respect to the experimental coordinate frame, but in opposite directions. The plane is spanned by the fin (x) and the direction perpendicular to the substrate (y). We observe a strong hysteresis of the magnetic field[1] which we estimate to induce errors of ±5° and ±10 mT on $\mathbf{B}$. This error is propagated when calculating g^* and shown as error bars in Fig. 5.1 b.

The data are well described by a phenomenological model consisting of a symmetric 3x3 tensor $\hat{\mathbf{g}}$, which is connected to the Larmor vector as follows:

$$\mathbf{f_L} = \frac{\mu_\mathbf{B}}{h} \hat{\mathbf{g}} \mathbf{B}. \tag{5.1}$$

Since we can experimentally measure only the Zeeman splitting $E_\mathrm{Z} = |\mathbf{f}_\mathrm{L}|/h$, not the Larmor vector, we introduce the symmetric Zeeman tensor $\hat{\mathbf{G}} = {}^t\hat{\mathbf{g}}\hat{\mathbf{g}}$ [Cri18]:

$$E_\mathrm{Z}^2 = \mu_\mathrm{B}^2 |\hat{\mathbf{g}}\mathbf{B}|^2 = \mu_\mathrm{B}^2\, {}^t\mathbf{B}\, {}^t\hat{\mathbf{g}}\, \hat{\mathbf{g}} \mathbf{B} = \mu_\mathrm{B}^2\, {}^t\mathbf{B} \hat{\mathbf{G}} \mathbf{B}. \tag{5.2}$$

where ${}^tA$ is the transpose of A. Since $\hat{\mathbf{G}}$ is symmetric, we can uniquely reconstruct it from measurements of E_Z for at least 6 different magnetic field orientations. Then, the 3x3 g-tensor $\hat{\mathbf{g}}$ can be determined up to a unitary transformation, which corresponds to a choice of Kramer's basis, leaving $E_\mathrm{Z} = \mu_\mathrm{B} |\hat{\mathbf{g}}\mathbf{B}|$ invariant. We use this formalism to fit the g-tensor of each qubit to our data with 6 independent fitting parameters, yielding

$$\hat{\mathbf{g}}^\mathrm{Q1} = \begin{pmatrix} 2.38 & 0.52 & -0.01 \\ 0.52 & 2.22 & 0.01 \\ -0.01 & 0.01 & 1.58 \end{pmatrix} \quad \text{and} \quad \hat{\mathbf{g}}^\mathrm{Q2} = \begin{pmatrix} 2.03 & -0.65 & 0.06 \\ -0.65 & 2.82 & -0.00 \\ 0.06 & -0.00 & 1.40 \end{pmatrix} \tag{5.3}$$

for Q1 and Q2 respectively. The three eigenvectors of $\hat{\mathbf{g}}$ are the principal magnetic axes, along which the minimum and maximum value of g^* can be observed.

We find a good agreement between $g^* = |\hat{\mathbf{g}}\mathbf{B}|/|\mathbf{B}|$ from the g-tensor model (dashed curves) and the measured data (points) in Fig. 5.1 b. A detailed description of the fitting procedure as well as the diagonalised matrices can be found in appendix A.4.2. While this

---

[1] We believe that a magnetic screw in the sample holder is responsible for a large part of this hysteresis.

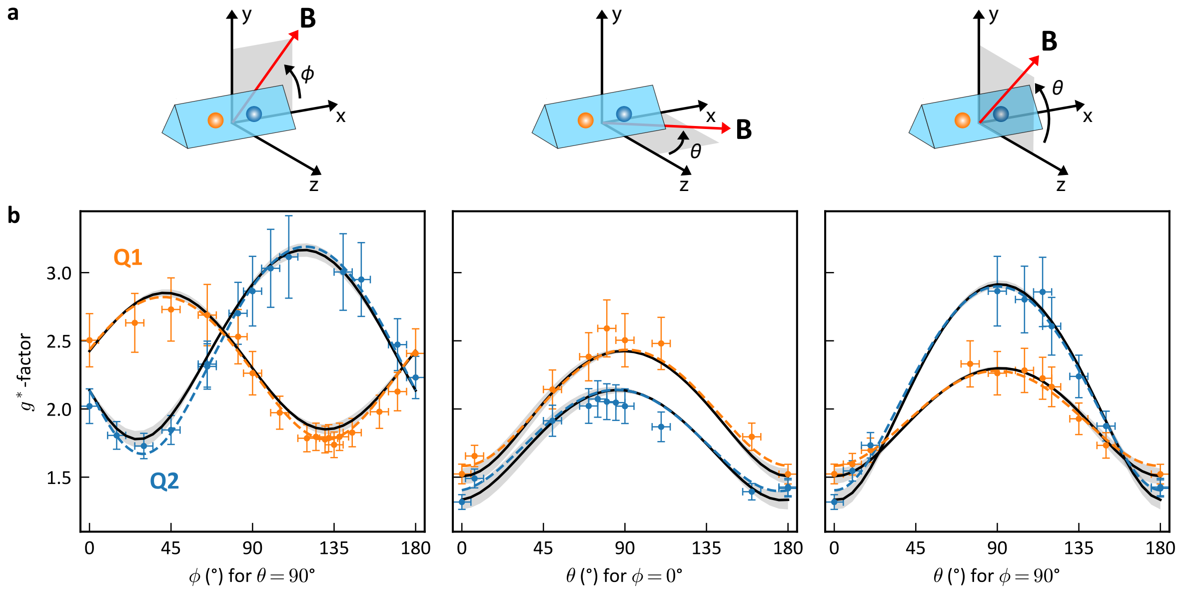

Fig. 5.1.: g^***-factors for different magnetic field orientations.** **a**, Schematic of the triangular fin (along x-axis) on top of the chip (xz plane) hosting two qubits. The magnetic field orientations during the three sweeps are indicated by red arrows. **b**, g^*-factor of Q1 (orange) and Q2 (blue) for different orientations of the magnetic field **B** measured at constant $f_\mathrm{L} = 4.5\,\mathrm{GHz}$. The gaps in the data are due to failing qubit readout for certain orientations. The g^*-factor is fitted by two different models: The dashed curves represent a phenomenological model using a 3x3 g-tensor. The solid black curves show the microscopic model including a rotated confinement described in the main text with the one-sigma confidence interval indicated in grey. The fitted parameters are given in Tab. 5.1.

model describes the data well, it does not explain the origin of the g-tensors.

Therefore, we use a microscopic model developed in Ref. [Sta21] to fit the data, where we assume a Luttinger-Kohn Hamiltonian $\mathcal{H}_\mathrm{LK} = T_\mathrm{LK} + V$ with harmonic confinement V. In this model, the kinetic energy is given by

$$\begin{aligned} T_\mathrm{LK} = &+\frac{\hbar^2}{2m_e}\gamma_1 \boldsymbol{k}^2 + 2\mu_B \kappa \boldsymbol{J}\cdot\boldsymbol{B} \\ &-\frac{\hbar^2}{m_e}\gamma_2[k_z^2(J_z^2 - \boldsymbol{J}^2/3) + \mathrm{c.p.}] \\ &-\frac{\hbar^2}{2m_e}\gamma_3[\{k_x, k_y\}\{J_x, J_y\} + \mathrm{c.p.}] \\ &+2\mu_B q[B_x J_x^3 + \mathrm{c.p.}] \end{aligned} \tag{5.4}$$

where m_e is the free-electron mass, $\boldsymbol{k}$ and $\boldsymbol{J}$ are the vectors of the hole momentum and spin operators, $\{A, B\} = AB + BA$ is the anti-commutator and c.p. stands for the cyclic permutation of the Cartesian indices, $x \to y \to z \to x$. The Si Luttinger parameters $\gamma_1 = 4.285$, $\gamma_2 = 0.339$ and $\gamma_3 = 1.446$ as well as the linear and cubic g-factor parameters $\kappa = -0.42$ and $q = 0.01$ from Ref. [Win03] are used. The harmonic confinement is taken along three spatial directions by

$$V = \frac{\hbar^2}{2m_e}\left(\frac{x^2}{l_x^4} + \frac{y^2}{l_y^4} + \frac{z^2}{l_z^4}\right), \tag{5.5}$$

and is parameterised by the confinement lengths l_x, l_y and l_z. Crucially, the confinement axes can be different from the device or crystallographic axes. We introduce three Euler angles φ, ϑ and ψ to describe the Euler rotation $\mathrm{E}_{\varphi,\vartheta,\psi}$ of the confinement axes with respect to the device axes. We find that the volume of the QDs $v = l_x l_y l_z$ has very little influence on the fitted g^*-factor[2] and the least-square method results in unrealistically small length scales. Hence, we find that fixing the QDs volume to e.g. $v = 20\,\mathrm{nm}^3$ and only fitting the ratios $r_{in} = l_z/\sqrt{l_x l_y}$ and $r_{xy} = l_x/l_y$ improves the reliability of the result.

The method of exact diagonalisation is used to find the eigenstates of this Hamiltonian and extract g^*. The model is fitted to the data using the least-square method with 5 fitting parameters (3 Euler angles and 2 ratios of confinement lengths) [Sta21]. We show the model as a solid curve in Fig. 5.1 b while the errors are indicated by the grey shaded area. The fitting parameters are presented in Tab. 5.1. The model predicts elongated dots, which are rotated away from the fin axis. This is in contrast to the more typically disc-like dots observed in planar structures, that are usually aligned with the device geometry.

The most interesting feature of the data is the misalignment of the maximum g^*, and hence the principal magnetic axes of the g-tensor, with the device geometry. Our model explains this tilted g-tensor with respect to the device geometry as a rotation of the dot confinement. It is unclear whether such a confinement shape is realistic within our device geometry. The model we use here is quite limited and does not include various other effects such as strain, strain gradients, interface roughness, interface disorder or crystal defects. Since these neglected factors could have a similar effect on the tilt angle of the g-tensor as the rotated confinement, we cannot rule out other explanations. In fact, a different model [Sta21] without a rotated confinement, but including a particular type of strain, fits the data also quite well (see appendix A.4.3). However, we find that various combinations of the seven fitting parameters for strain and confinement lead to similar predictions of g^*, indicating that only local minima are reached by fitting. We conclude that the model is too complex to fit our data. Hence, more detailed knowledge from simulations of the confinement shape [Din23] and strain environment in the FinFET devices are needed to narrow down the number and range of fitting parameters and to quantify the contribution

---

[2] The author of Ref. [Sta21] argues that, disregarding the Zeeman energy and the orbital effects of the magnetic field, the kinetic energy is quadratic in momentum and the confinement is quadratic in length. Hence, an overall-scaling of the confinement lengths can be "gauged away" by rescaling the length units accordingly and the g^*-factor does not depend on such a rescaling. When taking into account the orbital effects of the magnetic field, this invariance no longer holds, but it is still a good approximation for the ground state. However, the least-square method will try to find an optimum for this length scale, resulting in unrealistically small confinement lengths.

of the different mechanisms to the rotation of the g-tensors.

Other experiments have observed a similarly tilted g-tensor of a hole spin in a Si-MOS QD [Lil21]. Since this experiment is conducted in a planar MOS structure, the authors claim that a tilted confinement is unlikely. There, a model that includes a strain gradient also predicts a tilted g-tensor. The model consists of an elaborate numerical simulation of electrostatics, temperature-induced strain and quantum mechanical hole wave function (including a 6x6 Luttinger-Kohn-Hamiltonian and Bir-Pikus strain term). It qualitatively agrees with the experiment, but a quantitative disagreement might, again, point to the fact that some relevant effects are neglected. It says an open question if this model could also be applied to our experiments, since the 3D geometry of a FinFET device does not a priori exclude a rotation of the confinement.

We conclude that the rich physics of holes makes it difficult to explain the origin of the observed g^*-factors. We measure anisotropic and strongly tilted g-tensors which could be due to an elongated dot that is rotated with respect to the device geometry, but could also originate from strain or strain gradients. A more detailed analysis including numerical simulations of the device strain and confinement is needed for further conclusions.

Tab. 5.1.: The 5 fitted parameters as well as the derived relative confinement lengths for our microscopic g^*-factor model based on a rotated the confinement for Q1 and Q2.

parameter	qubit Q1	qubit Q2
φ	$-50° \pm 3°$	$26° \pm 3°$
ϑ	$-26° \pm 15°$	$-21° \pm 7°$
ψ	$-6° \pm 3°$	$171° \pm 2°$
r_{in}	$1.5 \pm 46\%$	$2.1 \pm 81\%$
r_{xy}	$1.14 \pm 13\%$	$1.3 \pm 10\%$
l_x	1.14	1.3
l_y	1	1
l_z	1.64	2.4

5.2. RABI DRIVE ANISOTROPY

Next we investigate the anisotropy of the Rabi frequency and how it relates to the Rabi driving mechanisms. First, we map out the Rabi frequency with a MW drive on gate P1 at constant $|\mathbf{f}_\mathrm{L}|$ in Fig. 5.2 a while sweeping $\mathbf{B}$ in the same three planes as defined in Fig. 5.1 a. We observe a strong modulation of the Rabi frequency by magnetic field orientation and find orientations for Q1 with close-to-zero Rabi drive. To understand the observed effect, we must take a closer look at two conceptually different mechanisms for EDSR qubit driving, the motional EDSR described by Refs. [GBL06; Now07] and the

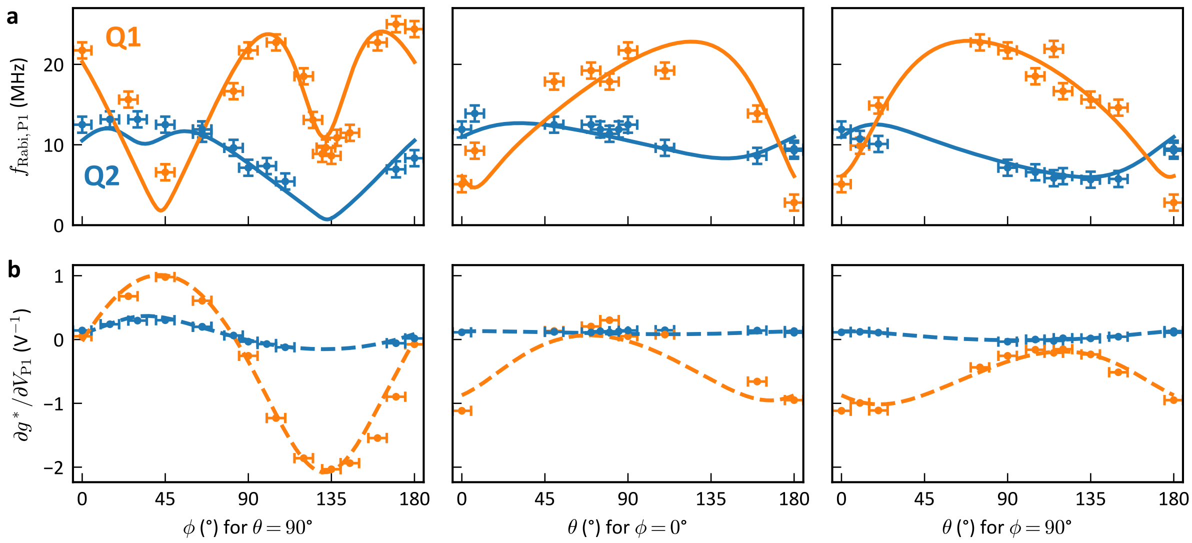

Fig. 5.2.: **Rabi frequency anisotropy with MW drive on plunger P1. a** We map out the Rabi frequency and **b** g^* derivative with respect to V_{P1} for the same magnetic field orientations as shown in Fig. 5.1 a. While the magnetic field is swept, the qubit Larmor frequency and the MW electric drive amplitude are kept constant at $f_{\mathrm{L}} = 4.5\,\mathrm{GHz}$ and $V_{\mathrm{MW,P1}} = 12\,\mathrm{mV}$, respectively. The models (curves) are fitted to the data (markers) as described in the main text individually for Q1/Q2 (orange/blue). The fits yield $\hat{\mathbf{g}}'$ as reported in appendix A.4.5 and $\beta_{\mathrm{P1}}^{\mathrm{Q1}} = 1.09$ / $\beta_{\mathrm{P1}}^{\mathrm{Q2}} = 2.50$ for Q1/Q2. The errors represent the uncertainty in magnetic field orientation **b** and 1 MHz as measurement uncertainty of f_{Rabi} and correspond to the 1σ interval.

g-tensor modulation EDSR described in Refs. [Kat03; Are13; Cri18].

Motional EDSR is a spin driving mechanism that originates from the periodic displacement of a spin by an alternating electric field $\mathbf{E}(t) = \mathbf{E}\sin(\omega t)$. It relies on Dresselhaus or Rashba SOI to couple the lateral motion to the spin degree of freedom. Assuming a harmonic confinement of the QD, a homogeneous electric field induces a displacement of the wave function without altering the confinement shape. Note that this implies that no change in the g^*-factor or Zeeman energy is expected. Originally this driving scheme was proposed for electrons (isotropic g^*) with a strong confinement in z, a harmonic confinement in x and y and linear-in-momentum SOI (see Ref. [GBL06]). For our 1D fin with strong confinement in z and y, we focus on the special case where the QD is only moved along a single axis ($\mathbf{E} = E_0\mathbf{e}_x$). In our case, where Rashba SOI dominates, the expression for the Rabi frequency can be written as [Fro21b]

$$f_{\mathrm{Rabi}} = \frac{g^*\mu_B B}{2h} 2E_0 \frac{em^* l^4}{\hbar^2 l_{so}} \, |\mathbf{b} \times \mathbf{n}_{so}|, \tag{5.6}$$

where e is the electron charge, m^* is the effective mass of the hole, l is the confinement length along the axis of motion, $E_0(t) = E_0\sin(\omega t)$ is the driving electric field along the axis of motion, l_{so} is the spin-orbit length, $\mathbf{b} = \mathbf{B}/|\mathbf{B}|$ is the magnetic field orientation and $\mathbf{n}_{so}$ is a unit vector along the direction of the effective spin-orbit field. This type of

Rabi drive is especially strong for a relaxed confinement along the direction of motion, as the Rabi frequency scales with l^4. Furthermore, it is linear in the electric driving field, the external magnetic field and the SOI strength. From Eq. (5.6) one can see that the Rabi frequency is anisotropic and vanishes for $\mathbf{B} \parallel \mathbf{n}_{so}$.

***g*-tensor modulation EDSR**, on the other hand, describes a Rabi driving mechanism that relies on the modulation of the **g**-matrix by the a.c. electric drive. The dependence of the g-tensor on electric fields originates ultimately from SOI. More specifically, many mechanisms can couple electric field and g-tensor, like e.g. squeezing of the confinement or locally varying properties such as strain when displacing the QD, which can change the mixture of HH and LH states and thus the properties of the system's ground states. The periodic modulation of the g-tensor $\hat{\mathbf{g}}' = \partial\hat{\mathbf{g}}/\partial V$ by a gate voltage can induce Rabi oscillations, if there is a component transverse to the Larmor vector $\mathbf{f}_\mathrm{L}$, i.e. $\hat{\mathbf{g}}'\mathbf{B} \times \mathbf{f}_\mathrm{L} \neq 0$. Early works only considered a modulation of the g^*-factors along the principal magnetic axes given by the device geometry [Kat03; Are13], but a more generalised formalism allowing for arbitrary g-tensor modulation is provided in Ref. [Cri18]:

$$\mathbf{f}_\mathrm{Rabi} = \frac{\mu_\mathrm{B} V_\mathrm{MW} B}{2hg^*} (\hat{\mathbf{g}}\mathbf{b}) \times (\hat{\mathbf{g}}'\mathbf{b}) = \frac{\mu_\mathrm{B} V_\mathrm{MW} B}{2h} \left(\frac{\mathbf{f}_\mathrm{L}}{|\mathbf{f}_\mathrm{L}|} \right) \times (\hat{\mathbf{g}}'\mathbf{b}) \,, \tag{5.7}$$

where $f_\mathrm{Rabi} = |\mathbf{f}_\mathrm{Rabi}|$ and V_MW is the microwave amplitude on the driving gate. This driving mechanism is also linear in the driving electric field $E_0 \propto V_\mathrm{MW}$ and the external magnetic field. Therefore, the observation of these linear dependencies does not allow any conclusion on the underlying driving mechanism (see appendix A.4.4 for exemplary measurement data). The dependence of the $\hat{\mathbf{g}}'$-driven Rabi frequency on magnetic field orientation is not straight-forwardly seen from the formula, as it strongly depends on the shape of $\hat{\mathbf{g}}'$. Notably, in the case considered by Refs. [Kat03; Are13], the Rabi frequency vanishes if $\mathbf{b}$ is aligned with the principal magnetic axes of the g-tensor.

Ref. [Cri18] shows that the previously discussed motional EDSR driving, although conceptually different from the g-tensor modulation EDSR driving, can be mapped onto the same formalism.[3] Hence, the g-tensor modulation EDSR formalism can be used to describe a mixture of both driving mechanisms, if $\hat{\mathbf{g}}'$ is chosen accordingly.

In principle, the g^*-factor derivative can be mapped out for all magnetic field orientations. One might think that this information should suffice to predict the Rabi frequency via Eq. (5.7). However, here we run into the problem that we cannot determine $\hat{\mathbf{g}}'$ in the same basis as $\hat{\mathbf{g}}$, due to the invariance of the measured g^*-factor under a unitary

---

[3] In their supplementary material the authors of Ref. [Cri18] present the necessary steps to map the formalism of motional EDSR onto the g-tensor EDSR formalism, but only for the exact case that was originally considered in Ref. [GBL06] where an isotropic g^*-factor was assumed. Further theoretical work is needed to show this for a more general case, e.g. for anisotropic $\hat{\mathbf{g}}$.

transformation of $\hat{\mathbf{g}}$.[4] This means that we cannot simply predict the Rabi frequency based on our measurements of g^* and $g^{*\prime}$, but need a more elaborate scheme to extract the relevant quantities. For this, we need to come back to the symmetric Zeeman tensor $\hat{\mathbf{G}} =^t \hat{\mathbf{g}}\hat{\mathbf{g}}$ introduced in chapter 5.1, which is independent of the choice of basis.

Following Ref. [Cri18], we classify the contributions to the Rabi drive into two categories: The first is contributions to the Rabi drive that come from a (measurable) change in $\hat{\mathbf{G}}$ which will be called g-TMR contributions; and the second category, that does not affect the Zeeman splitting for any magnetic field orientation, i.e. $\hat{\mathbf{G}}' = 0$, will be called iso-Zeeman ESDR (IZR). While the g-TMR contributions can be determined by extracting $\hat{\mathbf{G}}'$ from measurements of g^* and $g^{*\prime}$, it is impossible to measure the changes of the g-tensor that induce the IZR contributions by definition. Note that for IZR drive we have $\hat{\mathbf{G}}' = 0$, but $\hat{\mathbf{g}}' \neq 0$. This is e.g. the case if we map a pure motional EDSR drive onto this formalism. This comes from the fact that the lateral motion of the QD leaves the confinement shape and hence the g^*-factor and Zeeman vector invariant, i.e. $\hat{\mathbf{G}}' = 0$. However, the magnetic vector potential breaks translational symmetry such that $\hat{\mathbf{g}}' \neq 0$ [Cri18]. We can loosely associate IZR with a motional EDSR, i.e. a displacement of the wave function, and g-TMR with a change of g-tensors induced by deformations of the wave function.

Next, we want to find a decomposition $\hat{\mathbf{g}}' = \hat{\mathbf{g}}'_{\mathrm{TMR}} + \hat{\mathbf{g}}'_{\mathrm{IZR}}$ of the g-tensor derivative into contributions of our two categories of drive in the same basis as $\hat{\mathbf{g}}$. We note that

$$\hat{\mathbf{G}}' = ({}^t\hat{\mathbf{g}}\hat{\mathbf{g}})' = {}^t\hat{\mathbf{g}}\hat{\mathbf{g}}' + {}^t\hat{\mathbf{g}}'\hat{\mathbf{g}} \tag{5.8}$$

contains all the contributions to the g-TMR drive. Since $\hat{\mathbf{G}}$ is independent of the choice of basis, we can fully determine $\hat{\mathbf{G}}$ and $\hat{\mathbf{G}}'$ from measurements. We split ${}^t\hat{\mathbf{g}}\hat{\mathbf{g}}' = \hat{\mathbf{S}} + \hat{\mathbf{A}}$ into a symmetric $\hat{\mathbf{S}}$ and anti-symmetric $\hat{\mathbf{A}}$ matrix, such that $\hat{\mathbf{G}}' = 2\hat{\mathbf{S}}$. By choosing

$$\hat{\mathbf{g}}'_{\mathrm{TMR}} = {}^t\hat{\mathbf{g}}^{-1}\hat{\mathbf{S}} = {}^t\hat{\mathbf{g}}^{-1}\hat{\mathbf{G}}'/2 \tag{5.9}$$

and

$$\hat{\mathbf{g}}'_{\mathrm{IZR}} = {}^t\hat{\mathbf{g}}^{-1}\hat{\mathbf{A}} \tag{5.10}$$

we achieve that $\hat{\mathbf{g}}'_{\mathrm{TMR}}$ is fully determined by $\hat{\mathbf{G}}'$, and $\hat{\mathbf{g}}'_{\mathrm{IZR}}$ is completely independent of $\hat{\mathbf{G}}'$. Therefore, by mapping out $g^{*\prime}$ which uniquely determines $\hat{\mathbf{G}}'$, we can calculate $\hat{\mathbf{g}}'_{\mathrm{TMR}}$ but gain no information on $\hat{\mathbf{g}}'_{\mathrm{IZR}}$. The anti-symmetric matrix $\hat{\mathbf{A}}$ and hence $\hat{\mathbf{g}}'_{\mathrm{IZR}}$ capture pure rotations of the Kramer's basis. It can be parameterised by three independent variables,

---

[4] Alternatively, we can calculate $\hat{\mathbf{g}}'$ from two g-tensors measured at slightly different gate voltages. Again, we end up with the same problem: we cannot determine the two g-tensors in the same basis. The fact that we have a free choice of a Kramer's basis was not a problem in Eq. (5.1), since we were only interested in $|\mathbf{f}_{\mathrm{L}}|$, not its orientation. Now, however, when the orientation of $\mathbf{f}_{\mathrm{L}}$ matters and we need $\hat{\mathbf{g}}$ and $\hat{\mathbf{g}}'$ in the same basis, this is a big problem.

which can only be extracted by fitting this model to measurements of the Rabi frequency. The technical recipe for the procedure to obtain the full $\hat{\mathbf{g}}'$ in the same basis as $\hat{\mathbf{g}}$ is provided in appendix A.4.5.

Now we want to apply this method to our measurements of the Rabi frequency presented in Fig. 5.2 a. We start by determining $\hat{\mathbf{G}}'$ from the measured $g^{*\prime}$ (orange/blue points) for Q1/Q2 presented in Fig. 5.2 b. Then, using Eq. (5.9) one obtains $\hat{\mathbf{g}}'_{\mathrm{TMR}}$ and can plot the predictions from the model for $g^{*\prime} = (|(\hat{\mathbf{g}} + \hat{\mathbf{g}}'_{\mathrm{TMR}}\delta V)\mathbf{b}| - |\hat{\mathbf{g}}\mathbf{b}|)/\delta V$ for a small δV, since $\hat{\mathbf{g}}'_{\mathrm{IZR}}$ does not contribute to changes of g^* by definition. We show the model for $g^{*\prime} = \partial g^*/\partial V_{\mathrm{P1}}$ (dashed curves) in Fig. 5.2 b and find a good agreement with the data. Unsurprisingly, $\partial g^*/\partial V_{\mathrm{P1}}$ is generally larger for Q1 than for Q2 by almost an order of magnitude. This is due to the large difference in lever arms of driving gate P1 on Q1 and Q2, since Q1 is located right below P1 in contrast to Q2, which is located much further away (see appendix A.4.8). Next, we fit $\hat{\mathbf{g}}'_{\mathrm{IZR}}$ using four independent fitting parameters, where three parameters determine the anti-symmetric matrix $\hat{\mathbf{A}}$ and a correction factor β, which is multiplied to the calibrated MW amplitude V_{MW}, is fitted to correct for deviations in the calibration of V_{MW}, e.g. due to frequency dependence (see appendix A.4.5).

We show the model for $f_{\mathrm{Rabi}} = |\mathbf{f}_{\mathrm{Rabi}}|$ according to Eq. (5.7) (solid curves) in Fig. 5.2 a for both qubits and find that the model describes the data well. We observe a very different qualitative behaviour of f_{Rabi} for Q1 and Q2, which comes from a different composition of our two driving mechanisms as discussed later.

Then, the MW drive was applied to the central barrier gate B instead of the plunger gate P1. The same experiments and steps of analysis as presented above are repeated and displayed in Fig. 5.3. Again, we find a good agreement between experiment and model. With a more symmetrically located gate, the g^*-factor derivative $g^{*\prime} = \partial g^*/\partial V_{\mathrm{B}}$ is now of the same order of magnitude for both qubits, indicating a more symmetric driving configuration. Strikingly, the Rabi frequency for each qubit behaves qualitatively differently as a function of magnetic field orientation as compared to the previous configuration with plunger gate drive. We suspect that a change of the MW electric field orientation changed the contributions of g-TMR and IZR, inducing this qualitative change of $f_{\mathrm{Rabi}}(\mathbf{b})$. To analyse the influence of the two Rabi driving mechanisms on the Rabi frequency quantitatively, we will have a closer look at the two driving mechanisms individually.

g-TMR and IZR are characterised by their respective part of the decomposition of $\hat{\mathbf{g}}' = \hat{\mathbf{g}}'_{\mathrm{TMR}} + \hat{\mathbf{g}}'_{\mathrm{IZR}}$. First, analogously to Ref. [Cri18], we separate $\mathbf{f}_{\mathrm{Rabi}} = \mathbf{f}_{\mathrm{R,TMR}} + \mathbf{f}_{\mathrm{R,IZR}}$ into its contributions of g-TMR and IZR respectively. We model the Rabi frequency predicted for each qubit, each driving gate and each driving mechanism separately in appendix A.4.6. This allows us to easily see the difference in magnitude of the Rabi drive

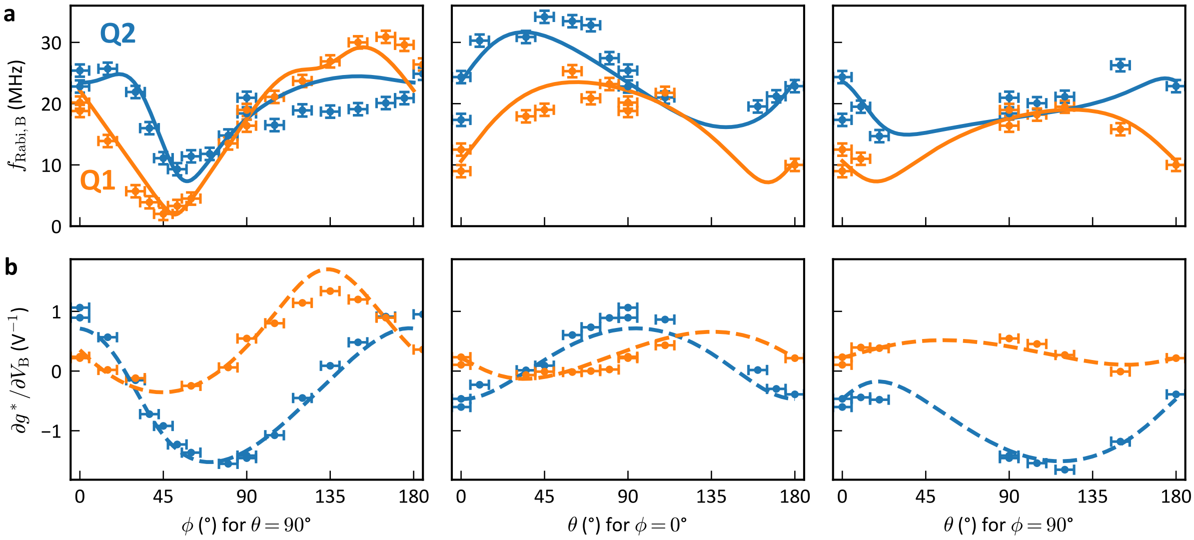

Fig. 5.3.: **Rabi frequency anisotropy with MW drive on barrier B.** The experiment is performed similar to Fig. 5.2 except microwaves are applied to the barrier gate, not the plunger gate, with amplitude $V_{\mathrm{MW,B}} = 13.5\,\mathrm{mV}$. We fit the data (points) with the model (solid curves) described in the main text. The fits yield $\hat{\mathbf{g}}'$ as reported in appendix A.4.5 and $\beta_{\mathrm{B}}^{\mathrm{Q1}} = 1.07$ / $\beta_{\mathrm{B}}^{\mathrm{Q2}} = 1.03$ for Q1/Q2. The errors are the same as in Fig. 5.2.

contributions, which add up to the total Rabi frequency as $|\mathbf{f}_{\mathrm{Rabi}}| \leq |\mathbf{f}_{\mathrm{R,TMR}}| + |\mathbf{f}_{\mathrm{R,IZR}}|$.[5] Qualitatively, we can see e.g. for Q1 and plunger gate drive that the influence of the g-TMR mechanisms is much greater than the IZR mechanism. To quantify this, we propose the following three metrics: First, we use a Frobenius matrix norm $||\cdot||$, allowing us to easily compare the size of the matrix elements of $\hat{\mathbf{g}}'_{\mathrm{TMR}}$ and $\hat{\mathbf{g}}'_{\mathrm{IZR}}$. We can define the dimensionless parameter $r \in [0,1]$ as the ratio of the matrix norms

$$r = \frac{||\hat{\mathbf{g}}'_{\mathrm{IZR}}||}{||\hat{\mathbf{g}}'_{\mathrm{IZR}}|| + ||\hat{\mathbf{g}}'_{\mathrm{TMR}}||} \tag{5.11}$$

where a pure g-TMR drive corresponds to $r = 0$ and only IZR drive corresponds to $r = 1$. We obtain $r_{\mathrm{P1}}^{\mathrm{Q1}} = 0.10$ for a plunger drive and Q1, confirming our previous observation of strong g-TMR contribution. In contrast $r_{\mathrm{P1}}^{\mathrm{Q2}} = 0.44$ indicates a much stronger IZR contribution for Q2. The simplicity of this approach comes with a caveat, namely that we do not compare the resulting EDSR driving, but only the magnitude of the matrix elements. In fact, only the matrix elements that result in a change perpendicular to the Larmor vector contribute to driving. Hence, we propose a second way to compare the two drive mechanisms: We numerically calculate the Rabi frequency average over the surface of the sphere $\overline{|\mathbf{f}_{\mathrm{R}}|}$ for IZR and g-TMR separately.[6] We define another dimensionless

---

[5] Here we can see that both drives can interfere constructively or destructively, since their Rabi frequencies are added as vectors.

[6] We sample $\mathbf{f}_{\mathrm{R,IZR}}$ and $\mathbf{f}_{\mathrm{R,gTMR}}$ separately for a roughly equidistant grid on the sphere generated by the Fibonacci sphere algorithm. We continuously increase the number of samples until $\overline{|\mathbf{f}_{\mathrm{R}}|}$ converges.

parameter $a \in [0,1]$ using the average Rabi frequency as

$$a = \frac{\overline{|\mathbf{f}_{\mathrm{R,IZR}}|}}{\overline{|\mathbf{f}_{\mathrm{R,IZR}}|} + \overline{|\mathbf{f}_{\mathrm{R,TMR}}|}}. \tag{5.12}$$

We obtain values that are very close to the values of r, namely $a_{\mathrm{P1}}^{\mathrm{Q1}} = 0.15$ and $a_{\mathrm{P1}}^{\mathrm{Q2}} = 0.57$ for Q1 and Q2 respectively.

A third way of comparing the driving strength is to focus on the optimal spot for fast manipulation, i.e. compare the maximum separate driving speeds. This allows us to define a third dimensionless parameter $m \in [0,1]$

$$m = \frac{\max(|\mathbf{f}_{\mathrm{R,IZR}}|)}{\max(|\mathbf{f}_{\mathrm{R,IZR}}|) + \max(|\mathbf{f}_{\mathrm{R,TMR}}|)} \tag{5.13}$$

analogously to r and a. Note that these maximum speeds might not be reached in the experiment as the Rabi frequencies are added as vectors. An overview over all values for r, a and m is provided in Tab. 5.2, where we can see that the different methods all lead so similar results.

Tab. 5.2.: Extracted values of r, a and m.

	plunger P1 drive			barrier B drive		
	r_{P1}	a_{P1}	m_{P1}	r_{B}	a_{B}	m_{B}
Q1	0.10	0.15	0.12	0.44	0.55	0.52
Q2	0.44	0.57	0.53	0.48	0.72	0.56

In general we identify two cases: mostly g-TMR and a strong mixing of both driving mechanisms. When driving Q1 with plunger P1 small ratios are obtained, indicating mostly g-TMR. This is expected, since the mostly vertical a.c. electric field[7] below P1, where Q1 is located, is expected to only change the confinement shape. We expect negligible motion of the QD wave function in vertical direction due to the strong vertical confinement at the MOS interface and only a small lateral motion due to the small residual lateral component of the a.c. field. These are perfect conditions for the g-TMR drive to thrive.

In all other cases we find both driving contributions IZR and g-TMR to have a considerable influence. Here, all ratios are spread around 0.5.[8] For the barrier drive mode we find very similar ratios when comparing Q1 and Q2, reflecting the symmetry of this

---

[7] In Ref. [Din23] the authors simulate the electric field orientation in a device similar to the device used in this thesis and find a strong dependence of the orientation on the number of holes in each dot. For an increasing number of holes the electric field becomes closer aligned with the vertical axis. Assuming that we operate the device with more than 5 holes (which might very well be the case), the electric field is predicted to be $\leq 6°$ from the vertical axis at the location of Q1.

[8] Except for the value of $a_{\mathrm{B}}^{\mathrm{Q2}}$ which tells a different story. Here not an equal mixture of driving contributions, but a strong IZR driving mechanisms is indicated. At the moment it is not fully

drive configuration. Furthermore, we expect the horizontal component of the electric field at the position of the qubits to be stronger in this case as compared to before, since the driving gate is not vertically aligned with the qubit. For Q2 and a plunger drive configuration we also find a mix of driving mechanisms. The electric field at the position of Q2 is expected to have both vertical and horizontal contributions,[9] which enables a mixture of both driving mechanisms. Interestingly, both driving mechanism lead to similar Rabi frequencies for Q1. However, since $f_{\mathrm{Rabi}} \propto l^4$ for IZR, we expect IZR to be generally stronger for more elongated QDs, which could be beneficial for faster qubit manipulation.

Notably, in the configuration of plunger driving Q2 a correction factor $\beta_{\mathrm{P1}}^{\mathrm{Q2}} = 2.50$ has been obtained from the fit (see appendix A.4.5). The correction factor should be close to 1 assuming only small frequency-dependence in the MW signal transmission through the device. Here, however, we find a much larger β, calling for further investigations. Therefore, an alternative analysis is presented in appendix A.4.7 where $\beta = 1$ is fixed, which explains the data with dominating IZR drive. Comparing this fit to the data, we note that, even though it generally fits worse than the fit in the main text, e.g. at $\phi \sim 45°$ the trend of the data is captured better in this model which requires less fitting parameters. The fit with fixed $\beta = 1$ would indicate that also the regime of predominant IZR drive can be realised in the FinFET devices. We note that measuring f_{Rabi} over the full surface of the sphere and not restricting ourselves to three planes might be helpful to determine which model fits better, as our current approach might leave the orientations with large differences between the two models unmeasured. Without microscopic simulations of the driving electric fields in the device it is not possible to discard $\beta_{\mathrm{P1}}^{\mathrm{Q2}} = 2.50$ as unrealistic, such that we have to consider both explanations.

In conclusion, we modelled the Rabi drive anisotropy using a phenomenological approach, which described the data well. Furthermore, the model is used to separate driving into IZR and g-TMR, which correspond roughly to displacement respectively deformation of the wave function. We use different locations of the driving gate to select a composition of these driving mechanisms. IZR is favoured when driving with a more lateral electric field, while g-TMR prevails when driving perpendicular to the chip plane. Hence, we have demonstrated control over the type of ESDR mechanism.

---

understood why a disagrees with r and m in this situation and further investigation of the meaning of these ratios is required.

[9] In Ref. [Din23] the electric field at the presumed location of Q2 is analysed in the case of P1 drive. The authors find the reverse trend as in the previous comment, namely that the electric field becomes more horizontal for an increasing number of holes. Specifically, for more than 5 holes in each dot the angle of the electric field towards the vertical axis is $\geq 15°$, indicating a considerable horizontal component.

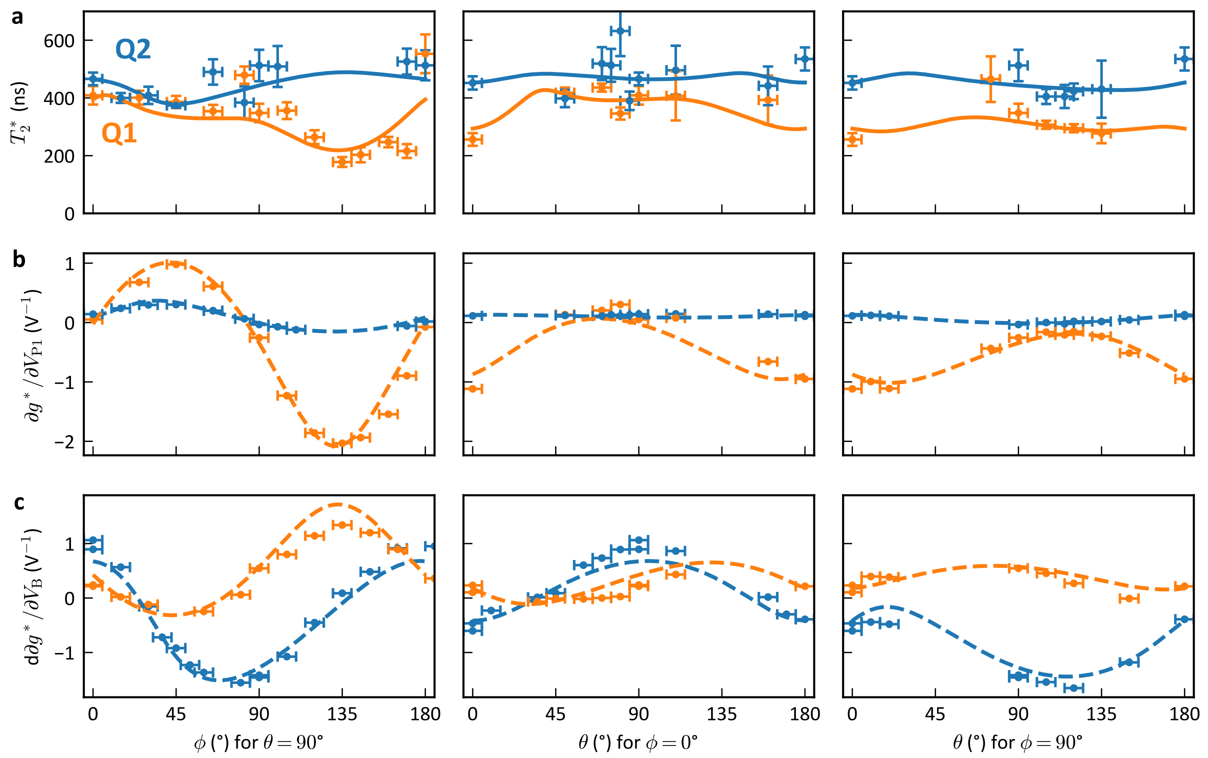

Fig. 5.4.: **Coherence anisotropy.** **a** T_2^* measured for Q1 and Q2 (points) for the same magnetic field orientations as defined in Fig. 5.1 a and for $f_\mathrm{L} = 4.5\,\mathrm{GHz}$ using a plunger gate drive. The solid curves are a fit of the model in Eq. (5.14) with fitting parameters given in Tab. 5.3. **b,c** Measured (points) and fitted (dashed curves) derivatives of the g^*-factor which are used in the model in **a**.

5.3. COHERENCE ANISOTROPY

In this section we investigate the anisotropy of qubit coherence. We present the dephasing time T_2^* for both qubits in Fig. 5.4 a for the three planes of magnetic field orientations defined in Fig. 5.1 a, using a constant f_L and driving gate P1. We observe a strong anisotropy with changes larger than a factor of 2, but the data has to be taken with a grain of salt as not all measurements have been performed using the same integration time.[10] Furthermore, the large error bars originate from the fact that only a fraction of the decay was observed and fitted, introducing a large uncertainty to the decay constant. By eye we see a correlation between a long coherence and small values of $|\partial g^*/\partial V_i|$ which are presented for gates P1 and B in Figs. 5.4 b, c.

We develop a model to fit the magnetic field dependence of T_2^*. First, the sources of noise are separated into charge noise $T^*_{2,\mathrm{charge}}$ and other contributions $T^*_{2,\mathrm{other}}$ following Ref. [Tan19] and assuming Lorentzian noise, where the other contributions could e.g. originate from the hyperfine interaction with nuclear spins. We assume that the coupling

---

[10] To extract T_2^* from the measurements according to appendix A.4.1 a sizeable fraction of the decay should be measured. Hence, for longer T_2^* sometimes the length of the manipulation stage had to be increased, which lead to a smaller signal. To balance the signal-to-noise ratio it was necessary to integrate longer in these cases, which lowers the extracted T_2^* as demonstrated in Ref. [Pio22].

to charge noise is dependent on the magnetic field orientation, but the other noise sources are independent of magnetic field orientation.[11] The charge noise is described by a model developed in Ref. [Pio22], which connects the angular dependence of the measured $g^{*\prime}$ with decoherence. Notably, for the decoherence only the change of the g^*-factor along the Larmor frequency vector is important, while for the previously discussed EDSR driving only the perpendicular components are of interest [Mic23]. The full model is described by

$$\frac{1}{T_2^*} = \frac{1}{T_{2,\text{charge}}^*} + \frac{1}{T_{2,\text{other}}^*} = 2\pi\sqrt{\ln\left(\frac{f_h}{f_l}\right) f_0 \sum_i \left(D_{\text{G}i} S_{\text{G}i}\right)^2} + \frac{1}{T_{2,\text{other}}^*}, \tag{5.14}$$

where

$$D_{\text{G}i} = \frac{\partial f_\text{L}}{\partial V_{\text{G}i}} = \frac{\partial g^*}{\partial V_{\text{G}i}} \frac{f_\text{L}}{g^*} \tag{5.15}$$

are the angular dependent changes of the qubit splitting by gates Gi, f_h and f_l are frequency cut-offs as defined in Ref. [Pio22] and $S_{\text{G}i}$ are the noise amplitude spectral density. Further, $S_{\text{G}i} = \sqrt{S_{\text{G}i}^P}$ with noise power spectral density $S_{\text{G}i}^P = S_{\text{G}i}^P (f_0/f)^\alpha$, where α defines the noise colour and $f_0 = 1\,\text{Hz}$. Here, we assume $\alpha = 1$ for pink noise, a commonly observed noise spectrum for semiconductors [Pal14], which is also consistent with previous reports on a different FinFET device [Gey22].

We fit the model to our data using three independent fitting parameters, which are given in Tab. 5.3, and find good agreement. Interestingly, the fitted isotropic coherence limit of both qubits is close to the predicted hyperfine coherence limit in this type of device [Cam22]. For the noise amplitude in terms of an equivalent gate voltage we observe an anti-correlation with the lever arms (see Tab. A.7) of the respective gate and qubit. Here, we have to be careful with the interpretation of this model: even though we multiply the noise power on a gate by its coupling to the qubit splitting, the physical origin of the charge noise is not voltage noise on the gates, as this noise is typically orders of magnitude smaller than our fitted values. The model allows us to separate the noise in the vicinity of the qubits, most likely in the oxide layer of the device, into contributions that look like they originate from the gates under investigation. In our case, we use the two neighbouring gates P1 and B, which create a different mixture of horizontal and vertical electric fields at the two qubit positions, to separate the local noise environment. For these two gates we already have mapped out $g^{*\prime}$ in the previous section, allowing us to calculate D_{P1} and D_B. When assuming a roughly equal distribution of noise sources around the qubits, we indeed expect larger equivalent voltage fluctuations on the gates located further away with a smaller lever arm, which is consistent with the fitted noise amplitude.

The coherence model allows us to separate the influence of charge noise from other noise, indicating that we might operate the qubits close to the hyperfine limit. The model

---

[11] Note that this might not be the case for noise from hyperfine interaction, as this interaction is also predicted to be anisotropic in our system [BL21; Pio22].

describes the data reasonably well, but there is some room for improvements. First, we believe that T_2^* should be measured again with a constant integration time, such that always the same frequency range of the noise spectrum is probed. Second, including a larger number of gates in the vicinity of the qubits could improve the model. This might be especially helpful to better capture the anisotropy of Q2, as the closest gate P2 was not considered in this analysis. However, this requires further measurements, since $\partial g^*/\partial V_{\mathrm{P2}}$ was not recorded.

Tab. 5.3.: Fitting parameters of the model for qubit decoherence presented in the main text.

	charge noise		other
	$S_{\mathrm{P1}}(\mu\mathrm{V}/\sqrt{\mathrm{Hz}})$	$S_{\mathrm{B}}(\mu\mathrm{V}/\sqrt{\mathrm{Hz}})$	$T^*_{2,\mathrm{other}}$ (ns)
Q1	79.3 ± 7.4	48.2 ± 5.8	493 ± 21
Q2	81.8 ± 20.8	28.2 ± 7.6	521 ± 24

5.4. QUBIT QUALITY FACTOR ANISOTROPY

An important metric to compare qubits is their quality factor [SL22], which compares the speed of operations to the qubit coherence. The gate quality factor Q, given by the ratio of Rabi frequency and decay of the Rabi oscillation, was found to be too large to be observed in our system with limited readout capabilities (see chapter 4). In this section we want to focus on the qubit quality factor Q^* (see appendix A.3.13), which we define as

$$Q^* = T_2^* \cdot 2f_{\mathrm{Rabi}} = T_2^*/t_\pi \tag{5.16}$$

where t_π is the spin-flip time. Q^* can be interpreted as the number of spin-flip operations that can be executed while another idling qubit stays coherent and is an important metric when e.g. operating multiple qubits sequentially. As expected, the anisotropy of f_{Rabi} and T_2^* observed in the previous two sections results in a highly anisotropic Q^*. We use the previously discussed models to predict Q^* for arbitrary orientation in Fig. 5.5. We find that Q1 and Q2 exhibit a very different behaviour and the sweet spots for ideal operation, i.e. where Q^* is maximum, do not perfectly align. However, the Q^* sweet spot for Q1 and Q2 and barrier drive appear for very similar magnetic field orientations, such that a close-to-optimum operation for both qubits is possible. When scaling to larger numbers of qubits, relying on a lucky alignment of sweet spots is not a viable option. Instead, individual electric control of the sweet spot orientation could be used to align the sweet spots of multiple qubits, such that they can simultaneously be operated in their optimal configuration in a global external magnetic field. We can already observe in Fig. 5.5 that the sweet spot orientations can be manipulated using different driving gates, i.e. by choosing a different orientation of the a.c. electric field, indicating that there is some degree

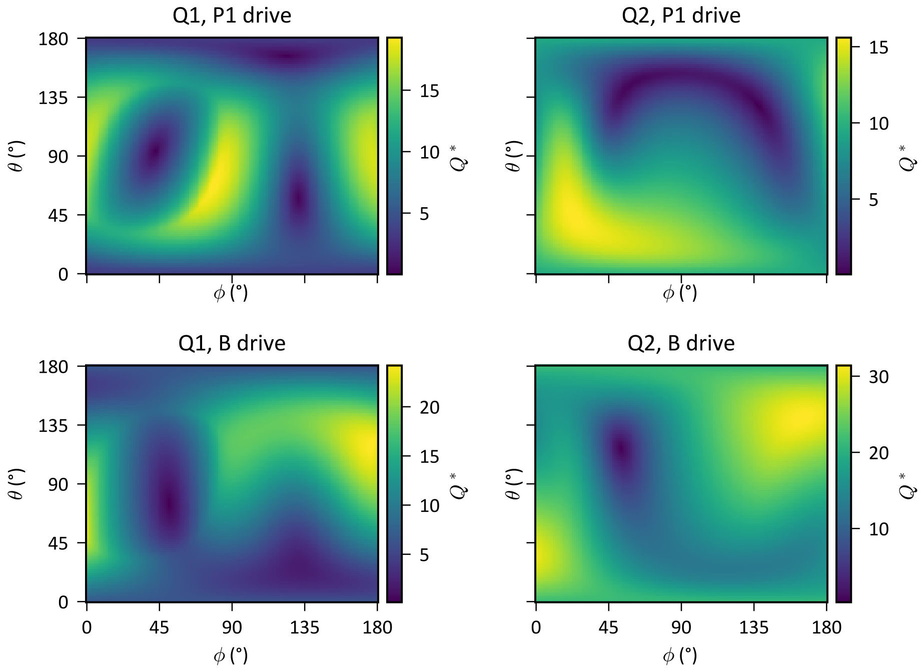

Fig. 5.5.: **Prediction of Q^* factor** using the previously discussed models for T_2^* and f_{Rabi} showcasing sweet spots for Q1/Q2 and driving gates P1/B.

of electrical control of the sweet spots present in this device. Here we only demonstrate control of the Q^* sweet spot by the a.c. electric field, but future experiments should also investigate and could benefit from electrostatic tuning of the sweet spot orientation.

We note that the maximum $Q^* \sim 30$ presented here is rather small (even smaller than the maximum Q^* presented in appendix A.3.13 at 1.5 K), which comes from the fact that this measurement series was performed at relatively low MW amplitude $V_{\mathrm{MW}} \sim 12 - 13.5\,\mathrm{mV}$. Since in theory T_2^* is independent of the MW power during the Ramsey $\pi/2$ pulses, a larger V_{MW} (up to 45 mV possible, see appendix A.4.4) and thus a faster spin-flip could result in $Q^* \sim 100$. We also note that Q^* is independent of f_{L}, since $f_{\mathrm{Rabi}} \propto B$ and $T_2^* \propto 1/B$ as demonstrated in appendix A.4.4.

The prediction of optimal qubit operation points is only possible by combining the models for qubit driving and qubit coherence. To improve the reliability of these predictions we suggest to investigate the models discussed in the previous two sections in more detail and implement the already mentioned improvements.

5.5. Conclusion & outlook

In conclusion, hole spin qubits are highly anisotropic objects. We have observed and modelled the anisotropy of g^*-factors, g^*-factor derivatives, Rabi frequency and coherence time of two hole spin qubits by probing magnetic field orientations within three distinct planes. We have used this information to make predictions of the QD confinement, disentangled the influence of g-TMR and IZR drive and analysed contributions of charge noise and other noise sources. Further, we predict sweet spots in the qubit quality factor for fast qubit driving and long coherence.

This study is based on a large data set collected over the course of months. However, some improvements in the measurements could increase confidence in the analysis. First, we only measured the qubits in three magnetic field planes, but more evenly distributed grid of measurements of the full surface of the sphere is believed to strengthen the analysis [Cri18]. Second, the vanishing PSB qubit readout for some orientations kept us from measuring the qubits at some points of interest, where e.g. our model predicts f_{Rabi} to approach zero. To improve qubit readout we recommend to further investigate the magnetic field dependence of the PSB readout, which was already started in chapter 3 but requires better modelling for a greater understanding of the underlying effects. Furthermore, we also note that the various models used throughout this chapter show some weaknesses. First, the microscopic model for the g-tensor requires more information than just the measurements of g^*-factors for confident predictions of microscopic properties, as the number of fitting parameters is too large. The analysis would greatly benefit from detailed simulations of the electrostatic and strain environments in the device. Second, the interpretation of the phenomenological model for the Rabi driving, which relies on the formalism of Ref. [Cri18], could be improved by investigating the connection between motional EDSR and IZR in the presence of an anisotropic g^*-factor. This would allow us to fully separate the driving mechanisms into a squeezing and a displacement of the wave function. Third, the different metrics to compare the strength of the driving mechanisms should be evaluated in more general situations to gain a better understanding of their meaning. Finally, the model for qubit coherence could be improved by including additional gates, allowing to better separate charge noise and other noise contributions. With these improvements the confidence of predictions of Q^* sweet spots could be improved, which could be useful for quantum applications.

6

Two-qubit gates with anisotropic exchange

Parts of this chapter have been published in:

Two-qubit logic with anisotropic exchange in a fin field-effect transistor
arXiv (2022), doi:10.48550/arXiv.2212.02308
Simon Geyer, Bence Hetényi, Stefano Bosco, Leon C. Camenzind, Rafael S. Eggli, Andreas Fuhrer, Daniel Loss, Richard J. Warburton, Dominik M. Zumbühl and Andreas V. Kuhlmann

This chapter explores the FinFET qubits' potential for short-range two-qubit gates. Firstly, a highly tunable exchange interaction between two neighbouring qubits is measured that can be tuned from above 500 MHz to close-to-off. Next, the full exchange matrix is mapped out allowing us to predict magnetic field orientations for high-fidelity two-qubit gates. Finally, we demonstrate the first two-qubit gate for holes in silicon in the form of a CROT, where a conditional spin-flip is achieved in just 24 ns.

(Bence Hetényi, Stefano Bosco and Daniel Loss lead the development of the theoretical models presented in this chapter.)

Universal quantum computation requires both single-qubit control and two-qubit interactions. Native two-qubit gates for spins such as the $\sqrt{\text{SWAP}}$ [LD98; Pet05], the CPHASE [Vel15; Wat18a; Mil22; Xue22] or the CROT [Zaj18; Wat18a; Hua19; Pet20a; Noi22; Phi22] rely on the exchange interaction, which arises from the wave function overlap between two adjacent QDs. For electrons in Si, two-qubit gate fidelities have recently surpassed the fault-tolerance threshold of 99% [Noi22; Xue22; Mil22], but for holes in Si or FinFETs the demonstration of two-qubit logic is still missing due to the challenges in obtaining a controllable exchange interaction [Fan23]. Furthermore, exchange interaction in a system with strong SOI, such as holes in a one-dimensional confinement [KRL18; Bos21; BHL21; Fro21b; Wan22b; Cam22], is still largely unexplored.

Here, we make an important step towards a FinFET-based quantum processor by demonstrating a CROT for holes in a Si FinFET. The strong SOI in combination with a large and highly tunable exchange splitting enables the execution of a controlled spin-flip in just $\simeq 24\,\text{ns}$. While the exchange interaction is crucial for implementing high-fidelity two-qubit gates, it is, in particular for hole spins, still largely unexplored. We measure the dependence of the exchange splitting on the magnetic field direction and find large values in some directions, close-to-zero values in other directions. In addition, we develop a general theoretical framework, applicable to a wide range of devices, and identify the SOI as the main reason for the exchange anisotropy. From our measurements we can extract the full exchange matrix and hence accurately determine the Hamiltonian of the two coupled spins, allowing us to predict the optimum operating points for the gates. For holes unlike electrons, the strong exchange anisotropy facilitates CROTs with both high fidelity and high speed for an experimental setting that is robust against device variations.

6.1. TUNABLE EXCHANGE SPLITTING

Fig. 6.1a shows the device[1] cross-section along the triangular-shaped fin, revealing ultrashort lengths, highly uniform profiles and perfect alignment of the gate electrodes [Kuh18; Gey21]; Fig. 6.1b presents a 3D illustration of the device. The DQD hosting qubits Q1 and Q2 is formed beneath plunger gates P1 and P2, and the barrier gate B provides control over the inter-dot tunnel coupling t_c [Cam22]. The distance between the QDs was chosen to be similar to the spin-orbit length [Cam22; Gey21]. Taking advantage of the strong SOI, all-electrical spin control is implemented by EDSR [GBL06; Now07]. For this purpose, fast voltage pulses and MW bursts are applied to P1 and a spin-flip is detected in the form of an increased spin blockade leakage current. The device is tuned close to the (1,1)-(0,2) charge transition, where (n,m) denotes a state with n (m) excess holes on the left (right) QD. In Fig. 6.1c the eigenenergies of the two-spin states $(|\uparrow\uparrow\rangle, |\uparrow\downarrow\rangle, |\downarrow\uparrow\rangle, |\downarrow\downarrow\rangle)$ in the (1,1) and the singlet ground state S_{02} in the (0,2) charge region are plotted as a

---

[1] In this chapter we use device C (see Tab. A.1).

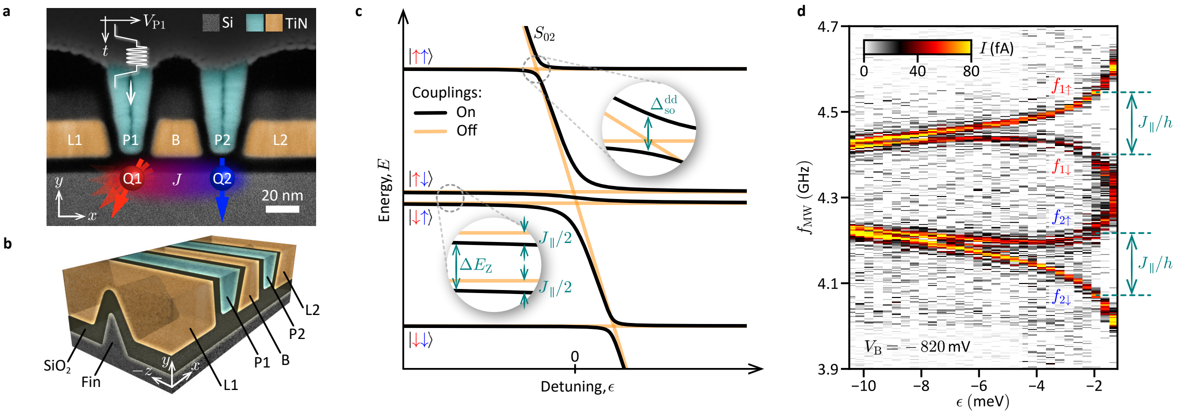

Fig. 6.1.: **Two-qubit system in a Si FinFET. a**, False-colour transmission electron microscope image of a co-fabricated device showing the cross-section along the fin. The qubits (Q1, Q2) are located underneath the plunger gates (P1, P2) and are manipulated by applying microwaves to the P1-gate. The barrier gate (B) controls the inter-dot tunnelling; the lead gates (L1, L2) accumulate the hole reservoirs. Measurements are performed on a device with $\simeq 20$ nm-wide B- and P-gates. **b**, A 3D render of the device illustrating the triangular-shaped fin covered by the wrap-around gates. **c**, Two-spin energy-level diagram close to the (1,1)-(0,2) charge transition with (black) and without (orange) interactions. The singlet state S_{02} hybridises with the antiparallel (parallel) two-spin states on account of spin-conserving tunnelling (SOI). A finite exchange splitting $J_\parallel$ lowers the energy of the antiparallel two-spin states with respect to the parallel ones. **d**, Exchange spin funnel measurements for both qubits, revealing an increase (decrease) in $f_{1\uparrow}$, $f_{2\uparrow}$ ($f_{1\downarrow}$, $f_{2\downarrow}$) at the upper (lower) branch. Data was taken at $V_{\mathrm{B}} = -820$ mV and $|\mathbf{B}| = 0.146$ T with orientation $\alpha = 30°$, $\beta = 0°$.

function of the detuning ϵ, which describes the energy difference between the (1,1) and (0,2) charge states. While spin-conserving tunnelling and a difference in g^*-factors causes an anticrossing between the S_{02} and the antiparallel two-spin states, spin-non-conserving tunnelling on account of the SOI results in an anticrossing between the S_{02} and the parallel two-spin states. As a consequence of the anticrossing with the singlet state, the energy of the antiparallel states decreases by $J_\parallel(\epsilon)/2$, where $J_\parallel(\epsilon)$ is the measured exchange splitting between the two spins (technical definition is provided in the appendix A.5.5). The energy level structure of the two-hole system can be probed by performing MW spectroscopy (Fig. 6.1d): at large negative ϵ, the resonance frequencies of both qubits differ due to the individual g-tensor g_i for each QD, and are independent of each other. At more positive detunings, closer to the (0,2) region, the exchange interaction splits both resonances by $J_\parallel/h$, resulting in four conditional transitions. The corresponding EDSR frequencies are denoted by $f_{i\sigma}$, where i is the index of the target qubit and σ the control qubit state $|{\uparrow}\rangle$ or $|{\downarrow}\rangle$.

We map out the ϵ-dependence of $J_\parallel$ that, as shown in Fig. 6.2a, is well described by

$$J_\parallel = J_0 \cos(2\tilde{\theta}) = \frac{2t_c^2}{U_0 - \epsilon} \cos(2\tilde{\theta}), \tag{6.1}$$

valid in the limit of $t_c \ll U_0 - \epsilon$ [Ste12; Rus18; Hen20a]. Here U_0 is an energy offset of

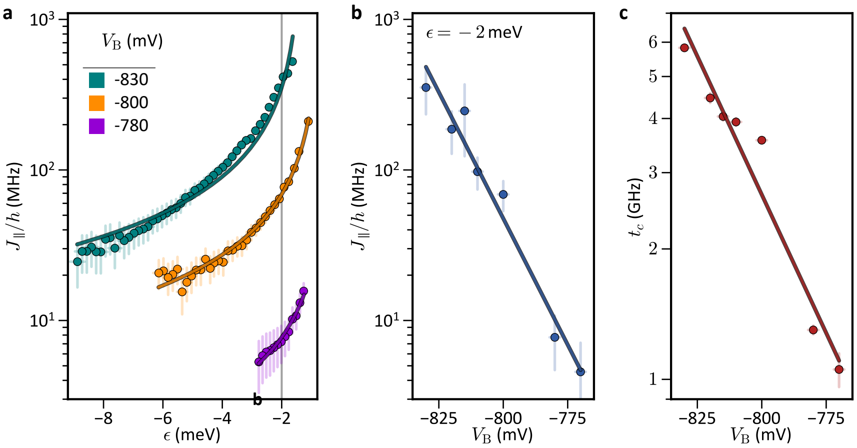

Fig. 6.2.: **Tunable exchange coupling.** **a**, Detuning dependence of the exchange frequency for $V_\mathrm{B} = -830$, -800 and -780 mV. The solid curves represent fits to Eq. (6.1) and errors the width of the EDSR resonance. **b**, $J_\parallel/h$ determined for $\epsilon = -2$ meV and **c** fitted tunnel coupling as a function of V_B. The solid lines show exponential function fits to the data. The error bars represent in **b** the estimated errors due to a detuning uncertainty, and in **c** the standard errors for the best-fit values.

the ϵ-axis, J_0 the bare exchange, and $\cos(2\tilde{\theta})$ a SOI-induced correction factor, which is independent of detuning and discussed later. The exchange splitting shows an exponential dependence on the barrier gate voltage V_B (Fig. 6.2b) and reaches values of up to $\simeq 525$ MHz. At the same time, exchange can be turned off within the resolution limit of our spectroscopy experiment that is given by the EDSR linewidth of $\simeq 2$ MHz [Hua19; Wat18a; Hen20a]. This means, using the two control knobs ϵ and V_B, we achieve excellent control over the exchange coupling. Since $t_c \propto J_\parallel^{1/2}$ the tunnel coupling is also exponentially dependent on V_B and tunable by almost one order of magnitude (Fig. 6.2c).

6.2. ANISOTROPIC EXCHANGE INTERACTION

In Figs. 6.3a-e the dependence of $J_\parallel$ on the magnetic field orientation is shown, revealing a striking anisotropy with vanishing splittings. The highly anisotropic exchange frequency is mainly due to the strong SOI and can be qualitatively understood from the gap size $\Delta_\mathrm{so}^\mathrm{dd}$ of the anticrossing between the S_{02} and the parallel two-spin states. $\Delta_\mathrm{so}^\mathrm{dd}$ is proportional to $|\boldsymbol{n}_\mathrm{so} \times \mathbf{B}|$, where $\boldsymbol{n}_\mathrm{so}$ is a unit vector pointing in the direction of the spin-orbit field and $\mathbf{B}$ the external magnetic field [Nad12]. Therefore, $\Delta_\mathrm{so}^\mathrm{dd}$ changes with magnetic field orientation and so do the two-hole energy levels (see Fig. 6.1c). However, we remark that from the dependence of $\Delta_\mathrm{so}^\mathrm{dd}$ on $\mathbf{B}/|\mathbf{B}|$ the exchange matrix $\mathcal{J}$ at the qubit manipulation point cannot be extracted.

We derive an equation for $\mathcal{J}$ starting from a Fermi-Hubbard model and including both the SOI as well as the anisotropic and differing hole g-factors (see appendix A.5.5). Tuned deep into the (1,1) charge regime where spin manipulation takes place, the system is

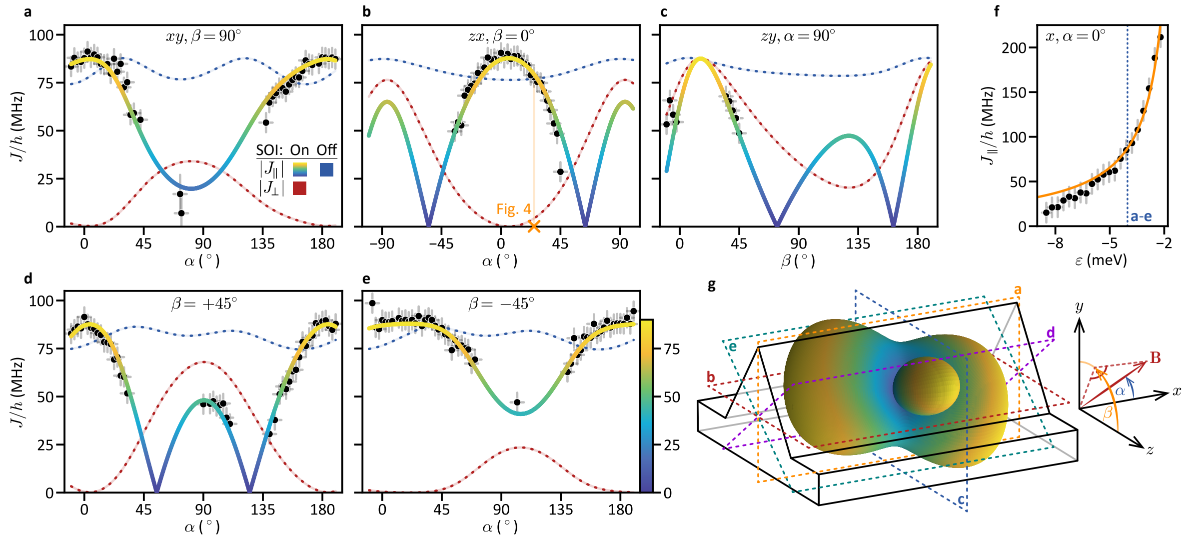

Fig. 6.3.: **Anisotropic exchange. a-e**, Exchange frequency as a function of magnetic field direction, which is expressed with the angles α and β (see coordinate system in **g**), for five different planes at $\epsilon = -4.03\,\text{meV}$. For certain **B**-orientations the qubits could not be read out via Pauli spin blockade and hence $J_\parallel/h$ (black points) could not be determined. **f,** Detuning dependence of $J_\parallel/h$ for **B** applied in x-direction. The multicoloured curves in **a-e** and the orange one in **f** represent a common fit of Eq. (6.3) to all the data presented in this figure. While the red dashed curves in **a-e** visualise $|J_\perp|/h$, the blue dashed ones illustrate the exchange modulation due to the different and anisotropic g-tensors in the absence of SOI. **g**, Schematic representation of the fin structure (black and grey lines) overlaid by a three-dimensional surface plot of $|J_\parallel|/h$. The coloured dashed rectangles indicate the planes of **a-e**. The data presented in this figure are taken at $V_\text{B} = -820\,\text{mV}$ and the error bars account for the EDSR linewidth and uncertainties in **B**-field due to magnetic flux trapping.

approximated by the Hamiltonian

$$H_{(1,1)} = \frac{1}{2}\mu_\text{B}\mathbf{B}\cdot g_1\boldsymbol{\sigma}_1 + \frac{1}{2}\mu_\text{B}\mathbf{B}\cdot g_2\boldsymbol{\sigma}_2 + \frac{1}{4}\boldsymbol{\sigma}_1\cdot\mathcal{J}\boldsymbol{\sigma}_2\,. \tag{6.2}$$

Here μ_B is Bohr's magneton and $\boldsymbol{\sigma}_i$ the vector of Pauli matrices for each QD. The exchange matrix is given by $\mathcal{J} = J_0 R_\text{so}(-2d/\lambda_\text{so})$, where $R_\text{so}(\varphi)$ is the counterclockwise rotation matrix around $\mathbf{n}_\text{so}$ by an angle φ, λ_so the spin-orbit length, and d the inter-dot distance. Here, we use the convention that displacing the spin by $\pi\lambda_\text{so}/2$ induces a spin rotation of π. The experimentally observed exchange splitting is given by (see appendix A.5.5)

$$J_\parallel = \mathbf{n}_1\cdot\mathcal{J}\mathbf{n}_2 = J_0\mathbf{n}_1\cdot R_\text{so}(-2d/\lambda_\text{so})\mathbf{n}_2\,, \tag{6.3}$$

where $\mathbf{n}_i = g_i\mathbf{B}/|g_i\mathbf{B}|$ denotes the Zeeman field direction. On comparing Eqs. (6.1) and (6.3) we find for the previously introduced correction term $\cos(2\tilde{\theta}) = \mathbf{n}_1\cdot R_\text{so}(-2d/\lambda_\text{so})\mathbf{n}_2$. Finally, by describing the magnetic field direction using the two angles α and β (Fig. 6.3), we obtain a fit equation $J_\parallel(\alpha,\beta)$ with five fitting parameters, namely t_c, U_0, $\mathbf{n}_\text{so}$ and λ_so.

Next, we apply this model to the data (black points) shown in Figs. 6.3a-f and perform a common fit to the full data set, consisting of measurements of $J_\parallel(\alpha,\beta)$ in five different planes (visualised in Fig. 6.3g) at constant detuning, and $J_{\parallel}(\epsilon)$ for $\mathbf{B}$ pointing in x-direction. There is excellent agreement between theory and experiment for the best-fit parameters: $\lambda_{\mathrm{so}} = 31\,\mathrm{nm}$, $\mathbf{n}_{\mathrm{so}} = (-0.06, 0.41, 0.91)$, $t_c = 5.61\,\mathrm{GHz}$ and $U_0 = 1.07\,\mathrm{meV}$. The spin-orbit length coincides with the values reported before [Gey21; Cam22], and corresponds to a spin rotation angle of $2\theta_{\mathrm{so}} = 2d/\lambda_{\mathrm{so}} \simeq 0.82\pi$ for a hole tunnelling from one QD to the other over $d \simeq 40\,\mathrm{nm}$. The direction of the spin-orbit field, represented by ($\alpha_{\mathrm{so}} = 93°$, $\beta_{\mathrm{so}} = 23°$), is as expected perpendicular to the long axis of the fin and thus orthogonal to the hole momentum [KRL18; BHL21]. The small out-of-the-substrate-plane tilt can arise on account of strain or electric fields not being perfectly aligned along the y-direction. Using the five best-fit parameter values we can, for the first time, reconstruct the full exchange matrix

$$\mathcal{J} = J_0 \begin{pmatrix} -0.87 & 0.41 & -0.28 \\ -0.49 & -0.60 & 0.64 \\ 0.10 & 0.69 & 0.72 \end{pmatrix}. \tag{6.4}$$

Because we also find the g-tensors when measuring $J_{\parallel}(\alpha, \beta)$ by means of MW spectroscopy, the two-spin Hamiltonian (6.2) is fully characterised, thus allowing us to optimise two-qubit gate operations as discussed later. Furthermore, we can analyse the different contributions to the exchange anisotropy with Eq. (6.3): by setting θ_{so} to zero, we are left with the effect of the anisotropic g-tensors. We find that the g-factor contribution to the $J_{\parallel}$-anisotropy was minor (dashed blue curves in Figs. 6.3a-e). Finally, we remark that the observed rotational exchange anisotropy relies on a strong SOI and the presence of an external magnetic field [Kav01; Kav04], as opposed to a weaker Ising-like anisotropy that can be found in inversion symmetric hole DQDs [HKL20] or at zero magnetic field [HBL22; Kat20].

6.3. TWO-QUBIT GATE FOR HOLES IN SILICON

We make use of the large exchange splitting to demonstrate a fast two-qubit gate for holes in Si, namely a controlled rotation [Wat18a; Hua19; Hen20a; Hen21; Noi22]. This gate operation is naturally implemented by driving just one of the four EDSR transitions (see Fig. 6.1d), resulting in a rotation of the target qubit conditional on the state of the control qubit. First, we initialise $|\mathrm{Q1}, \mathrm{Q2}\rangle$ in the $|{\downarrow\uparrow}\rangle$-state by pulsing from $\epsilon > 0$, where the spin-blockaded $|{\downarrow\downarrow}\rangle$-state is occupied, to $\epsilon = -2.9\,\mathrm{meV}$, where $J_{\parallel}/h \simeq 80\,\mathrm{MHz}$ and MW-induced state leakage is suppressed [Wat18a] (see appendix A.5.4). Subsequently, the state of the control qubit Q2 is prepared by a MW burst of length t_{b2} and frequency $f_{2\downarrow}$, and finally a controlled rotation of the target qubit Q1 is triggered by the following pulse with t_{b1} and $f_{1\uparrow}$ (Fig. 6.4a). The measurement outcome is presented in Fig. 6.4b, revealing the characteristic fading in and out of the target qubit's Rabi oscillations as a

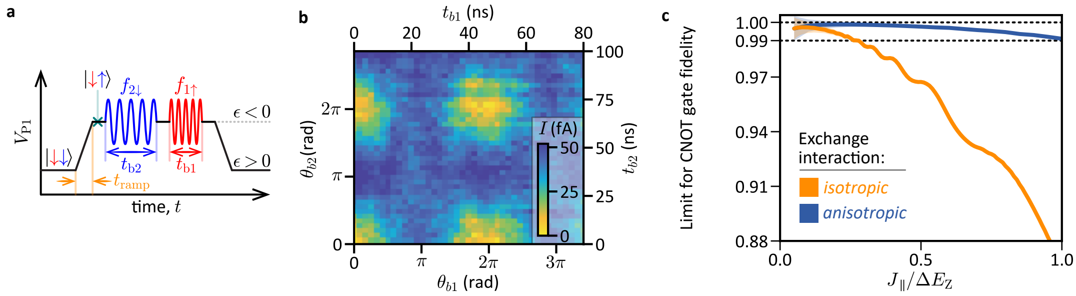

Fig. 6.4.: **Fast CROT with Si hole spin qubits.** **a**, Pulse sequence for the CROT gate operation. A trapezoidal waveform with a ramp time of 20 ns is used to initialise the spins in the $|\downarrow\uparrow\rangle$-state and to readout their state after applying two microwave bursts resonant with Q2 ($f_{2\downarrow}=4.25\,\text{GHz}$) and Q1 ($f_{1\uparrow}=4.66\,\text{GHz}$). **b**, Parity measurement of the qubits demonstrating a conditional rotation of Q1 controlled by the state of Q2. This data is taken at $J_{\|}/h\simeq 80\,\text{MHz}$, $V_{\rm B}=-810\,\text{mV}$, $|\mathbf{B}|=0.146\,\text{T}$, $\alpha=25°$, $\beta=0°$ and $\epsilon=-2.9\,\text{meV}$. **c**, Numerically calculated CNOT gate fidelity versus exchange splitting $J_{\|}$ (in units of $\Delta E_{\rm Z}$) for anisotropic (blue, with parameters of **b**) and isotropic (orange) exchange. The shaded regions indicate the precision of the numerics.

function of t_{b2}, that is, the spin state of the control qubit [Hen21; Hen20a]. A controlled spin flip for Q1 is executed in $\simeq 24\,\text{ns}$, which is short compared to other realisations with electrons in Si [Noi22] or holes in Ge [Hen20a; Hen21]. The missing single-shot readout or other means to get the spin-spin correlations prevent randomised benchmarking to determine a two-qubit gate fidelity[Kni08].

Two key requirements need to be fulfilled for high-fidelity CROT gates. First, in order to prevent a mixing of the antiparallel spin states ($|\uparrow\downarrow\rangle$, $|\downarrow\uparrow\rangle$), the Zeeman energy difference between the qubits $\Delta E_{\rm Z}$ must be much larger than the "perpendicular" exchange coupling $J_\perp$ (see appendix A.5.7). Second, either $J_{\|}\gg hf_{\rm Rabi}$ or $J_{\|}/\sqrt{15}=hf_{\rm Rabi}$ to avoid unwanted rotations of the off-resonant states [Rus18; Noi22]. Hence, for electrons with isotropic exchange ($J_{\|}=J_\perp=J$) the speed of high-fidelity CROT gates is bounded by $hf_{\rm Rabi}\ll J\ll\Delta E_{\rm Z}$ even in the absence of noise. However, for hole spins with highly anisotropic exchange interaction this fundamental theoretical limit can be overcome. In fact, $J_{\|}=J_0$ while $J_\perp=0$ is possible, for instance, if the g-tensors are isotropic, for $\theta_{\rm so}=\pi/2$ and $\mathbf{B}$ perpendicular to $\mathbf{n}_{\rm so}$; we remark that the latter condition also ensures fast single qubit rotations. Consequently, our theory predicts that for holes in comparison to electrons a controlled-NOT (CNOT) gate (differing from a CROT by a phase factor) with fidelity above the fault-tolerance threshold of 99% can be realised with much shorter gate times (see Fig. 6.4c and appendix A.5.7). For the CROT experiment presented in Fig. 6.4b the magnetic field orientation (marked by the vertical orange line in Fig. 6.3b) was chosen such that $|J_{\|}|=0.90\,J_0$ and $|J_\perp|=0.05\,J_0$. In Figs. 6.3a-e the red dashed curves show the dependence of $J_\perp$ on $\mathbf{B}/|\mathbf{B}|$, highlighting that the ideal configuration ($J_{\|}\simeq J_0$, $J_\perp\simeq 0$) is stretched over a wide range of directions. The CROT sweet spot is consequently robust against device variations, making it highly suitable for large qubit arrays (see appendix A.5.7).

6.4. Conclusion & outlook

In summary, we investigated the exchange coupling between two hole spins in a Si FinFET and found it to be both highly anisotropic and tunable, allowing for an interaction strength >0.5 GHz. We identify the strong SOI as the main microscopic origin of this anisotropy and propose a simple procedure for determining the exchange matrix. This measurement and analysis scheme applies to a wide variety of devices, for instance also to electron spin qubits with synthetic SOI in the presence of a magnetic field gradient (see appendix A.5.6) [Noi22; Wat18a; Phi22]. By fully characterising the Hamiltonian of the two coupled spins, the best possible configuration for implementing two-qubit gates can be identified. A strongly anisotropic exchange results in extended sweet spots in magnetic field orientation, where both fast and fault-tolerant CROTs can be performed. The robustness of these sweet spots against device variations makes CROT gate operations with anisotropic exchange highly attractive for large-scale qubit arrays. Finally, by choosing a close-to-ideal configuration we realise a CROT gate in just $\simeq 24$ ns. The advance reported here in combination with fast readout [Hua21] and high-fidelity single-qubit operations at temperatures above 1 K [Cam22] demonstrate that industrial FinFET technology has great potential for realising a universal quantum processor with all-around high-performance fidelities, integrated on the same chip with the classical control electronics.

7

PHASE DRIVE FOR HOLE SPIN QUBITS

Parts of this chapter have been published in:

Phase driving hole spin qubits
ArXiv (2023), doi:10.48550/arXiv.2303.03350
Stefano Bosco, Simon Geyer, Leon C. Camenzind, Rafael S. Eggli, Andreas Fuhrer, Richard J. Warburton, Dominik M. Zumbühl, J. Carlos Egues, Andreas V. Kuhlmann and Daniel Loss

In contrast to resonantly driven Rabi oscillations, this chapter explores an alternative driving mechanism of hole spin qubits, where a far-detuned oscillating field couples to the qubit phase. Phase driving at radio frequencies, orders of magnitude slower than the microwave qubit frequency, induces highly non-trivial spin dynamics. We demonstrate a controllable suppression of resonant Rabi oscillations and their revivals at tunable sidebands. Phase driving also decouples Rabi oscillations from noise, an effect due to a gapped Floquet spectrum.

(The theory presented in this chapter was developed by Stefano Bosco, Carlos Egues and Daniel Loss.)

Spin qubits in hole quantum dots are emerging as top candidates to build large-scale quantum processors [KL13; Sca20; Fan23; Hen21]. A key advantage of hole spins is their large and tunable SOI enabling ultrafast all-electrical qubit operations [Wan22b; Fro21b; Wat18b; Hen20b; Hen20a; Mau16; Cam22], on-demand coupling to microwave photons [Yu23; Bos22; Mic23], even without bulky micromagnets [Phi22; Mil22; Noi22]. The large SOI of holes leads to interesting physical phenomena, such as electrically tunable Zeeman [Fro21a; Fro21b; Lil21; Hud22; Ade22b; Bos21] and hyperfine interactions [BL21; Fis08; Pre16], or exchange anisotropies at finite [Gey22] and zero magnetic fields [Kat20; HBL22]. These effects can be leveraged for quantum information processing, e.g., to define operational sweet spots against noise [BHL21; BL22; Ade22a; Pio22; Wan21; Wan22a]; to date their potential remains largely unexplored.

Single qubit operations rely on flipping spin states on demand. A microwave pulse drives spin rotations, resulting in the well-known Rabi oscillations. For confined holes, these oscillations are fast and rely on either an electrically tunable and anisotropic g-tensor [Are13; Cri18; Ven18] or periodic spin motion in a SOI field [GBL06; Now07; KTL11; KRL18]. To date, however, these oscillations are qualitatively similar to competing qubit architectures [Bla21; Lei03; Gil23; Pla12; Kop06], and they occur at fixed microwave GHz frequencies determined by the qubit energy. Qubit responses to detuned frequencies are associated to non-linearities in the coupling to the driving field [Sca15; Stu06].

In this chapter, we investigate the dynamics of a hole spin qubit hosted in a Si FinFET under simultaneous application of longitudinal (phase) and transverse (Rabi) drives at radio frequency ω_z and microwave frequency ω_x, respectively, see Fig. 7.1(a). We demonstrate that the rich microscopic physics of hole nanostructures leads to a non-trivial response of the qubit state to these oscillating fields even at frequencies far detuned from the qubit energy. This anomalous response arises from a strong interplay between the phase and Rabi electrical drives in the *linear* regime. More specifically, we show that by driving the qubit phase at radio frequencies ω_z in the MHz range, i.e., three orders of magnitude lower than the microwave GHz-range Larmor frequency of the qubit ω_q, we can controllably (i) suppress the resonant Rabi oscillations at $\omega_x = \omega_q$ and (ii) revive them at sideband frequencies $\omega_x = \omega_q \pm m\omega_z$, with $m \in \mathbb{N}^+$. We observe this behaviour reproducibly on two different devices. The suppression of Rabi frequency can be exploited to detect longitudinal interactions between spins and microwave resonators [Bos22]. In future qubit processors using a global high-frequency driving field, sideband oscillations can provide ways to selectively address individual qubits by radio-frequency MHz signals, relieving demanding technological challenges for designing large-scale high-frequency circuits. We also predict that our two-tone drive protects Rabi oscillations from noise as the periodic phase driving gaps the Floquet spectrum of the system similar to the Bloch bands in periodic lattices. This noise suppression is a valuable tool for dressed spin qubit architectures [Lau16; See21;

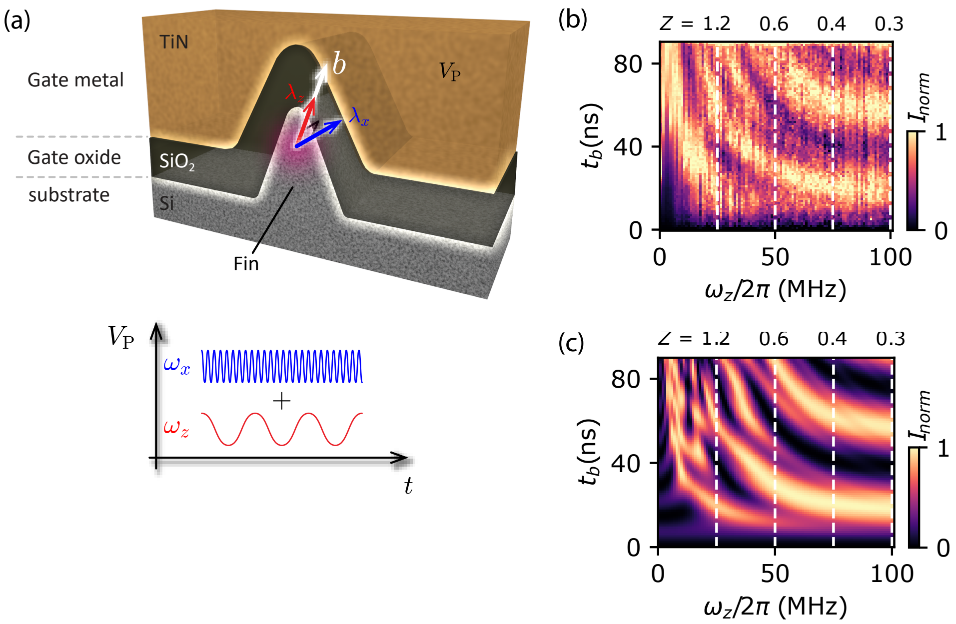

Fig. 7.1.: (a) Schematic of our phase driven qubit. A hole spin qubit in a Si FinFET with Zeeman field $\mathbf{b}$ is simultaneously driven by a microwave Rabi drive (blue) with amplitude λ_x and frequency $\omega_x \approx \omega_q = |\mathbf{b}|/\hbar$, and a radio-frequency phase drive (red) with amplitude λ_z and frequency $\omega_z \ll \omega_q$. (b)-(c) Phase-driving-induced slow down of Rabi oscillations in qubit 1 (Q1). The Rabi frequency is suppressed as $\omega_R = \lambda_x J_0(2Z)$, with $Z = \lambda_z/\omega_z$, and vanishes at $Z = 1.2$. This prediction is experimentally confirmed in (b) by sweeping ω_z and measuring the Pauli-spin-blockaded current I_{norm} normalised by the maximal current, proportional to the spin flip probability, for different burst times t_b. Regular oscillations are observed for $Z \lesssim 0.5$. For $Z \gtrsim 0.5$ phase driving causes non-trivial features that are captured by the simulation in (c) obtained from Eq. (7.1) with $\lambda_x/2\pi = 29$ MHz, $\lambda_z/2\pi = 30$ MHz and $\omega_q/2\pi = \omega_x/2\pi = 4.5$ GHz.

Han21; Han22] and for Floquet engineering high-fidelity quantum gates [Xue22; Boy19; Pet18; Yan19; Zen19; Rim22].

7.1. ELECTRICAL MANIPULATION OF HOLE SPINS

A hole spin qubit in an external magnetic field $\mathbf{B}$ is described by the Zeeman Hamiltonian $H_q = \mathbf{b}\cdot\boldsymbol{\sigma}/2$, where $\mathbf{b} = \mu_B \mathbf{B}\cdot\hat{g}$ is the Zeeman vector, $\hat{g}$ is the electrically-tunable g tensor of the system, and $\boldsymbol{\sigma}$ is the vector of Pauli matrices. Quite generally, an electrical pulse with frequency ω applied to the system gives rise to an oscillating vector field $\boldsymbol{\lambda}\cos(\omega t)$ that directly couples to the qubit via $H_d = \hbar\boldsymbol{\lambda}\cdot\boldsymbol{\sigma}\cos(\omega t)$ due to the SOI. The vector $\boldsymbol{\lambda}\cos(\omega t)$ models the drive as a time-dependent Zeeman field acting on the qubit. Its direction depends on the microscopic details of the nanostructure, and includes processes such as g tensor modulation and electric dipole spin resonance [GBL06; KTL11; KRL18], while its amplitude scales linearly with the applied microwave field. These processes enable electrical manipulation of qubits with multiple driving frequencies and amplitudes. Transitions between spin up and down states occur for $\boldsymbol{\lambda} \perp \mathbf{b}$ (Rabi driving), while only the phase of the qubit is addressed [Bos22; BTN15; RD16; RT21; RT19; Bøt22] for $\boldsymbol{\lambda} \parallel \mathbf{b}$

(phase driving). Interestingly, while phase driving alone cannot induce Rabi oscillations, a radio-frequency phase pulse can significantly alter the dynamics of the qubit when acting together with a Rabi driving field.

We stress that all of our findings lie within the scope of linear response in the driving field. Variations from this linear regime were detected at large driving powers [Yon17; Fro21b; Und22]. Non-linearities in the driving field $\propto \boldsymbol{\lambda}^2 \cos(\omega t)^2$ induced by excited states were also proposed as a source of higher-harmonic response in spin qubits [Sca15; Stu06].

7.2. PHASE DRIVEN QUBITS

We consider a spin qubit with GHz-range frequency $\omega_q = |\mathbf{b}|/\hbar$. A transverse Rabi drive $\lambda_x \cos(\omega_x t)$ with amplitude λ_x and frequency $\omega_x = \omega_q - \Delta$ induces Rabi oscillations when the MHz-range detuning Δ is small. This system exhibits Rabi oscillations with frequency $\omega_R = \sqrt{\Delta^2 + \lambda_x^2}$ and maximal spin-flip probability $P_R^{\max} = \lambda_x^2/(\Delta^2 + \lambda_x^2)$. We add an additional simultaneous longitudinal phase drive $\lambda_z \cos(\omega_z t)$, with amplitude λ_z and frequency $\omega_z \sim$ MHz, that is far detuned from ω_q. The two-tone Hamiltonian reads

$$H = \frac{\hbar\omega_q}{2}\sigma_z + \hbar\lambda_x\sigma_x \cos(\omega_x t) + \hbar\lambda_z\sigma_z \cos(\omega_z t) \ . \tag{7.1}$$

The direction $\hat{z}$ ($\hat{x}$) is parallel (perpendicular) to $\mathbf{b}$, Fig. 7.1(a).

By moving to the rotating frame defined by the transformation $U_r(t) = e^{-i\sigma_z[\omega_x t + 2Z\sin(\omega_z t)]/2}$ [Bos22], which exactly accounts for the phase driving, and neglecting terms rotating at frequencies $\sim 2\omega_x$, we obtain

$$\tilde{H} = \frac{\hbar\Delta}{2}\sigma_z + \frac{\hbar\lambda_x}{2}J_0(2Z)\sigma_x + \hbar\lambda_x \sum_{n=1}^{\infty}\Big(J_{2n}(2Z)\cos[2n\omega_z t]\sigma_x - J_{2n-1}(2Z)\sin[(2n-1)\omega_z t]\sigma_y\Big) \ , \tag{7.2}$$

with dimensionless parameter $Z = \lambda_z/\omega_z$ and Bessel functions J_n. Note that without phase drive, i.e., $\lambda_z = 0 \Rightarrow Z = 0$, and since $J_0(0) = 1$ and $J_{n\neq 0}(0) = 0$, Eq. (7.2) reduces to $\tilde{H} = \hbar(\Delta\sigma_z + \lambda_x\sigma_x)/2$, i.e., the rotating frame Hamiltonian for Rabi driven qubits in the rotating wave approximation (RWA).

Close to resonance $\Delta \lesssim \omega_z, \lambda_x$, we obtain $J_0(2Z) = 1 - Z^2 + \mathcal{O}(Z^4)$ and the first correction to the qubit dynamics caused by the phase driving is $\propto Z^2$. Consequently, at moderate values of λ_z and when $\omega_z \sim \omega_q$, then $Z \ll 1$, and the phase driving has no effect. Moreover, Rabi pulses with $\omega_x \ll \omega_q$ are off-resonant and do not affect the qubit. These considerations justify using the Hamiltonian H in Eq. (7.1) also in general cases where λ_x [λ_z] has an additional component parallel [perpendicular] to $\mathbf{b}$. Finally, a relative phase difference φ between the two driving signals is relevant at comparable values of ω_x and ω_z [Bos22], but can be neglected when $\omega_z \ll \omega_x$. Finite φ's become relevant in the presence of noise, as discussed later.

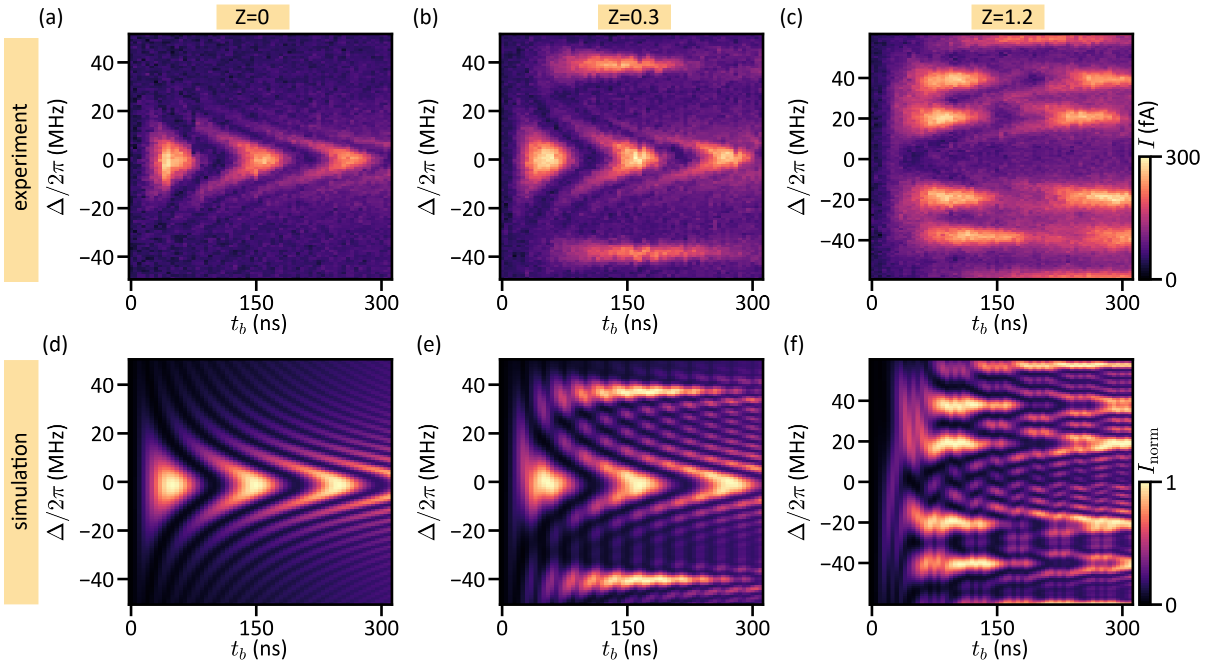

Fig. 7.2.: Sideband Rabi oscillations in qubit 2 (Q2). (a),(b),(c) Spin precession for simultaneous microwave Rabi driving and radio-frequency phase driving against burst time t_b and detuning Δ. We show results for $Z = 0$, $Z = 0.3$, and $Z = 1.2$. The typical chevron pattern centred at $\Delta = 0$ in (a) is modified in (b),(c) by additional sidebands at $\Delta/2\pi = \pm n \cdot \omega_z/2\pi = \pm n \cdot 40\,\text{MHz}$ and $\pm n \cdot 20\,\text{MHz}$, respectively. The $\Delta = 0$ oscillations are slower in (b) and completely vanish in (c). (d),(e),(f) Simulations of the time-evolution governed by Eq. (7.1), showing excellent agreement with experiments. We use $\omega_q/2\pi = 4.95\,\text{GHz}$, $\lambda_x/2\pi = 10\,\text{MHz}$ for the three Z values and $\lambda_z = 0$, $\lambda_z/2\pi = 0.3\omega_z/2\pi = 12\,\text{MHz}$, $\lambda_z/2\pi = 1.2\omega_z/2\pi = 24\,\text{MHz}$ for (d),(e),(f), respectively.

7.3. SIDEBAND RABI OSCILLATIONS

We study the influence of the phase drive on the oscillations for resonant ($\Delta = \omega_q - \omega_x = 0$) and non-resonant ($\Delta \neq 0$) Rabi drives. In the resonant case and when $\omega_z \gtrsim \lambda_x$, one can simplify $\tilde{H}$ in Eq. (7.2) by the RWA. The dominant contribution to $\tilde{H}$ is the static $n = 0$ component, yielding fully developed oscillations with frequency $\omega_R = \lambda_x J_0(2Z)$, Fig. 7.1(b), (c).

We verify this prediction experimentally in a hole spin qubit in two different Si FinFETs described in detail in Refs. [Cam22; Gey22; Gey21]. The first (second) qubit Q1 (Q2) is hosted in device C (D) (see Tab. A.1) and operated at $\omega_q/2\pi = 4.5\,\text{GHz}$ ($\omega_q/2\pi = 4.95\,\text{GHz}$) corresponding to a g factor $g = 2.14$ for $B = 0.15\,\text{T}$ ($g = 2.72$ for $B = 0.13$ T); g depends on the gate potential V with sensitivity $\partial g/\partial V \approx -0.05\,\text{V}^{-1}$ ($\partial g/\partial V \approx 0.41\,\text{V}^{-1}$). Our qubits are initialised and read out via Pauli spin blockade and direct current integration, see Refs. [Cam22; Gey22]. Our system enables high-bandwidth phase driving via the electrically tunable g tensor and Rabi driving via electric-dipole spin resonance. These contributions are generated by applying two oscillating electrical signals at different frequencies, Fig. 7.1(a). Generally these tones induce both Rabi and phase driving, however, as discussed before, we discard the negligible contributions of far-detuned Rabi driving and nearly-resonant phase driving.

For the measurements in Fig. 7.1(b), we apply simultaneously a resonant Rabi drive with $\omega_x = \omega_q$ and a phase drive with variable, far-detuned frequency ω_z to Q1. We measure the qubit state after the burst time t_b. The two pulses have comparable amplitudes, $\lambda_x/2\pi \approx \lambda_z/2\pi \approx 30\,\mathrm{MHz}$. Rabi oscillations can be observed along the vertical axis of the figure, and by sweeping ω_z, we map out the dependence of ω_R on $Z = \lambda_z/\omega_z$. We find good agreement between our measurement and the quantum dynamics simulated by using H in Eq. (7.1). For Q2 we observe a similar behaviour as shown in Fig. A.31, which especially emphasises the fact that the phase drive only affects the dynamics of the spin for small ω_z.

Remarkably, Rabi oscillations are suppressed at certain values of $Z = Z_j$, defined by the roots of the Bessel function $J_0(2Z_j) = 0$, where ω_R vanishes. The first root $Z_1 \approx 1.2$ corresponds to $\lambda_z \approx 1.2\omega_z$ and can be observed in our experiment. At $Z = 1.2$, the higher harmonic components in $\tilde{H}$ in Eq. (7.2) with $n \geq 1$ dominate the dynamics.

These higher harmonics are crucial to understand the Rabi sidebands appearing in the non-resonant case, comprising a finite detuning Δ, shown in Fig. 7.2(b),(c). At small values of $\Delta \ll \lambda_x$, the Rabi frequency increases as $\omega_R = \sqrt{\Delta^2 + \lambda_x^2 J_0(2Z)^2}$, resulting in the typical chevron pattern, and suppressing the oscillations at large Δ. However, when $\lambda_z \approx \omega_z$, oscillations are revived at finite values of Δ. In particular, at $\Delta = \pm m\omega_z$, the system is resonant with the m^{th}-harmonic in Eq. (7.2) ($m \in \mathbb{N}^+$), and sideband oscillations at frequencies $\omega_R^m = \lambda_x J_m(2Z)$ are restored.

In Fig. 7.2, we show measurements and simulations of Rabi oscillations against Δ at different values of Z for Q2. The Rabi chevron in (a) is modified by phase driving. In (b), we consider $Z = 0.3$, and we observe the appearance of sideband resonances at frequencies $\pm\omega_z/2\pi = \pm 40\,\mathrm{MHz}$. In (c), by reducing ω_z to $\omega_z/2\pi = 20\,\mathrm{MHz}$ and increasing λ_z, we reach $Z = 1.2$, where the resonant oscillations at $\Delta = 0$ vanish and only sideband oscillations remain. As shown in (d)-(f), these sidebands are well explained by our model, which is linear in the driving field amplitudes. We emphasise that in contrast to non-linear driving, where the $\Delta = 0$ resonance does not disappear and sidebands oscillations appear at fixed frequencies $\omega_x = \omega_q/m$ with $m \in \mathbb{N}^+$, by operating our qubit at $Z = 1.2$ we completely remove the $\Delta = 0$ oscillations and still fully control the sideband frequencies $\Delta = \pm m\omega_z = m\lambda_z/1.2$ by varying the amplitude λ_z of the radio-frequency pulse.

Our driving scheme opens the possibility of dynamically shifting the qubit frequency to higher harmonics, thus reducing frequency-crowding issues in dense large-scale quantum processors and enabling individual qubit addressability in global microwave fields by technologically inexpensive MHz circuits.

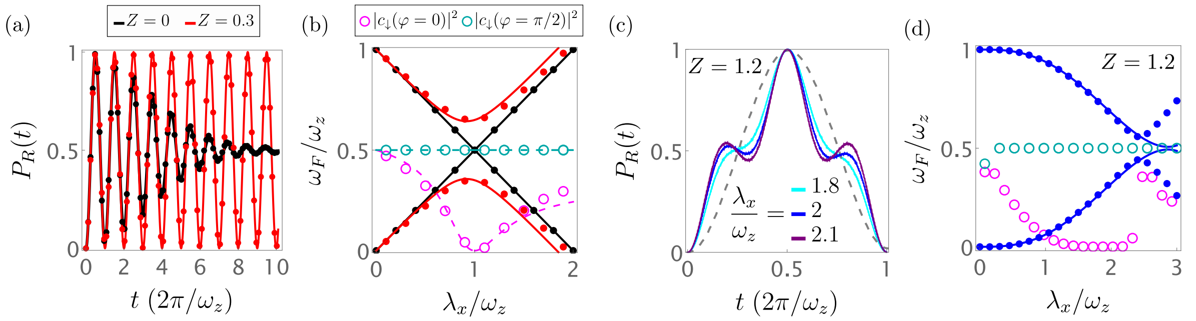

Fig. 7.3.: (a) Simulated phase-driving-induced undamped Rabi oscillations at $\omega_z = \lambda_x$. Black (red) dots denote Rabi probability averaged over $N = 10^3$ realisations of the noise Hamiltonian H_N for $\lambda_z = 0$ ($\lambda_z = 0.3\omega_z$) picked from a Gaussian distribution with zero mean and standard deviation $\bar{\sigma} = 0.1\omega_z$. The results match Eq. (7.3) with $T_2^R = 2\sqrt{2}\hbar/\bar{\sigma}$ ($T_2^R \to \infty$). (c) Noisy Rabi oscillation at $Z = 1.2$ and various λ_x/ω_z ratios. The grey dashed line corresponds to the red line in (a). (b),(d) Floquet spectra against λ_x/ω_z. (b) Solid black (red) dots show numerically computed Floquet energies ω_F at $\lambda_z = 0$ ($\lambda_z = 0.3\omega_z$); the lines denote the approximation in Eq. (7.4). Magenta (cyan) circles exhibit the probability $|c_\downarrow|^2 = |\langle\downarrow|0_F\rangle|^2$ for a two-tone relative phase $\varphi = 0$ ($\varphi = \pi/2$). Dashed lines show Eq. (7.5). (d) Blue dots show the Floquet spectrum at $Z = 1.2$, while the lines display the fitting formula $\omega_F^{0,1} = \pm\omega_z[0.084(\lambda_x/\omega_z)^3 - 0.022(\lambda_x/\omega_z)^4] \bmod(\omega_z)$. We use $\omega_q = 10^3\omega_z$.

7.4. PROTECTION OF RABI OSCILLATIONS FROM NOISE

The coupling to the environment causes decoherence and damps the Rabi oscillations in a time T_2^R, see Fig. 7.3(a), black curve. The Rabi decay time T_2^R is dominated by noise at frequencies close to the driving frequency ω_x. We model this phenomenologically by the noise Hamiltonian $H_N = \cos(\omega_x t)\mathbf{h}\cdot\boldsymbol{\sigma}/2$, describing the spin coupling to a stochastic Gaussian distributed vector $\mathbf{h}$, with zero mean and diagonal covariance matrix $\Sigma_{ij} = \delta_{ij}\bar{\sigma}^2$. This model accurately describes high-frequency noise form different sources [Yan19; BL21; CYL16; Wan21].

After ensemble averaging and focusing on the resonant case $\Delta = 0$, we find that for conventional Rabi driving, H_N suppresses the Rabi oscillations as

$$P_R(t) = \frac{1}{2}\left[1 - e^{-(t/T_2^R)^2}\cos(\omega_R t)\right], \tag{7.3}$$

with $T_2^R = 2\sqrt{2}\hbar/\bar{\sigma}$. The decay time T_2^R is larger than the dephasing time T_2^* and determines the lifetime of dressed spin qubits [Lau16; See21; Han21; Han22], utilising nearly-resonant always-on global microwave fields. However, when the SOI is large, T_2^R is significantly shortened, and becomes comparable to T_2^* [Wan22b; Fro21b], thus limiting the advantages of these architectures.

We simulate the effect of an additional phase pulse with $\lambda_z \ll \lambda_x$ at frequency $\omega_z \approx \lambda_x$. As shown in Fig. 7.3(a), even a small phase driving (red curve) decouples Rabi oscillations from noise and enhances T_2^R by orders of magnitude. We also verified that these decay-free oscillations are robust against noise at different frequencies.

The origin of persistent oscillations can be understood in terms of the Floquet modes $|0_F\rangle, |1_F\rangle$ [BDP15; RL20]. These are eigenstates of the Floquet operator $U(T) = U_r(T)\mathcal{T}e\left[-i\int_0^T \tilde{H}(\tau)d\tau/\hbar\right]$ with eigenvalues $e^{-i\omega_F^0 T}, e^{-i\omega_F^1 T}$, respectively. Here, $\mathcal{T}e$ is the time-ordered exponential, the period $T = 2\pi/\omega_z$, and U_r transforms the system back to the lab frame [1].

The eigenvalues and eigenvectors of $U(T)$ are shown in Fig. 7.3(b). First, in contrast to the usual Rabi driving, when a phase driving pulse is applied at frequencies comparable to λ_x and is in-phase with the Rabi drive, the spin states in the lab frame coincide with the Floquet modes, i.e. $|\uparrow\rangle = |0_F\rangle$, $|\downarrow\rangle = |1_F\rangle$ (magenta line). Second, phase driving opens a gap of size $\omega_F^1 - \omega_F^0 \approx \lambda_z$ in the Floquet spectrum (black and red lines), that protects the system from moderate noise sources with $\bar{\sigma} \lesssim \lambda_z$. For $\lambda_z \ll \lambda_x \sim \omega_z$, the Floquet eigenenergies are

$$\omega_F^{0,1} = \pm\frac{1}{2}\left[\omega_z + \sqrt{(\lambda_x - \omega_z)^2 + \frac{\lambda_x^2}{\omega_z^2}\lambda_z^2}\right] \mathrm{mod}(\omega_z) \ . \tag{7.4}$$

In analogy to disorder potentials in Bloch bands, when the system is initialised in an eigenstate, transitions to other eigenstates are suppressed as long as the standard deviation of the disorder is smaller than the energy gap. This comparison allows us to identify the decay-free oscillations shown in red in Fig. 7.3(a) as the temporal evolution of an individual Floquet mode.

The decay-free Rabi oscillations depend on the gapped Floquet spectrum and the possibility of preparing a Floquet eigenmode. In Fig. 7.3(b), we show that a relative, experimentally-tunable phase φ between the Rabi and phase tones can be used to select arbitrary superpositions of Floquet states (magenta and cyan curves). The amplitudes $c_s = \langle s|0_F\rangle$ between the spin state $|s = \uparrow\downarrow\rangle$ and the Floquet state $|0_F\rangle$ are

$$c_{\uparrow\downarrow}(\varphi) \approx \frac{\cos(\theta) \pm \sin(\theta)e^{i\varphi}}{\sqrt{2}} \ , \ \tan(2\theta) = \frac{\lambda_x\lambda_z}{\omega_z|\lambda_x - \omega_z|} \ . \tag{7.5}$$

For strong phase drivings, where $\lambda_z \sim \lambda_x$, Eqs. (7.4) and (7.5) are inaccurate, but simulations still predict decay-free oscillations and gapped Floquet spectrum. For example, in Fig. 7.3(c),(d) we examine the oscillations and the Floquet spectrum at $Z = 1.2$. The Floquet bands touch at $\lambda_x = 0 \ \mathrm{mod}(\omega_z)$; at $\lambda_x \gtrsim \omega_z$, the gap becomes significant and decay-free oscillations persist for a wide range of parameters. Because of the strong phase driving the oscillations are not sinusoidal. Their peculiar shape probes the temporal structure of the Floquet mode and is shown in Fig. 7.3(d) for different values of λ_x.

We note that relaxation between Floquet modes is suppressed, as reflected in persistent

---

[1] To use Floquet theory, we assume that $\omega_x = \omega_q$ is commensurate with ω_z. However our results are valid generally when $\omega_x \gg \omega_z, \lambda_x, \lambda_z$, ω_x and fast oscillating corrections $\propto 1/\omega_x$ are negligible.

oscillations, but superpositions of Floquet modes are still subjected to dephasing with characteristic time T_2^R. We envision that the possibility to stabilise Floquet modes by phase driving opens a wide range of exciting opportunities to optimise dressed qubits, and to prepare exotic states in future Floquet metamaterials.

7.5. CONCLUSION & OUTLOOK

We demonstrated that radio-frequency phase driving of hole spin qubits induces collapse and revival of Rabi oscillations, resulting in oscillations at sidebands of the qubit frequency. These sidebands do not require non-linear coupling of the spin to the driving field. We show theoretically that phase driving also leads to decay-free Rabi oscillations in noisy qubits. Our two-tone driving scheme provides an alternative way of implementing individual addressability in global microwave fields in future large-scale qubit architectures, and Floquet engineering high-fidelity qubit gates.

8

Conclusions and outlook

In summary, we have investigated the physics of hole spins in FinFETs and established the bulk-Si FinFET hole spin qubit as a platform for quantum computing. First, we presented a fabrication process flow for FinFET QD devices with a self-aligned second gate layer. Next, a hole DQD in a FinFET was used to investigate PSB, SOI and characteristic QD metrics. The DQD was then turned into a qubit by combining the spin readout mechanism of PSB with electrical spin manipulation via EDSR. We demonstrated the operation of the first hole spin qubit at elevated temperatures above 4 K and achieved fast spin manipulation >100 MHz and long coherence $T_2^* > 400\,\mathrm{ns}$. We use randomised benchmarking to determine a single-qubit gate fidelity of $\sim 99\%$ and analysed the noise spectrum for temperatures ranging from 1.5 K to 4.2 K, observing a whitening of noise for higher temperature. Furthermore, the anisotropy of hole spins was investigated by recording and modelling the dependence of various qubit properties on the magnetic field orientation, revealing qubit sweet spots that combine fast driving and long coherence. After turning on the exchange interaction, we were able to demonstrate the first two-qubit gate for hole spins in Si by performing a fast CROT gate in just 24 ns. Furthermore, a SOI-based model allowed us to extract the full exchange matrix, characterising the anisotropic nature of the exchange interaction and allowing us to predict sweet spots for fast and high-fidelity two-qubit gates. Finally, we investigated a new driving mechanism, the phase drive, and its coupling to a traditional Rabi drive. The additional RF phase drive heavily modified or completely suppressed resonant Rabi oscillations, which reappeared at tunalbe sidebands. This driving scheme might be useful for noise mitigation or individual qubit addressability.

The FinFET qubit devices investigated in this thesis still leave room for improvement. For example, our measurements have shown that the device-to-device variability of QD and qubit metrics is still significant. This can have different origins, such as variations in device dimensions, strain, impurities, doping, work functions, interface quality or electronic configuration in the qubit operation regime. To select a hero device with ideal properties for qubit experiments, a large number of devices had to be fabricated and individually tested. We conclude that, even though the device yield in terms of gate leakage is good, we need to optimise the fabrication process to improve the qubit yield, which is essential when increasing the device complexity and the number of qubits per device. Here, we propose to characterise the fabrication process not by measuring single devices but by using automated high-throughput measurements [Kru23] for a statistical analysis of characteristic qubit parameters. While variations between different devices should be reduced, also the uniformity within a single device is important. Our measurements indicate different properties for QDs at different locations along the channel, a non-uniformity which should also be addressed by the proposed statistical analysis on a large number of devices.

The charge stability diagrams of many devices show artefacts that can be attributed to charge states of impurities, charge traps or unwanted additional dots, which couple to the DQD under investigation. As their locations are largely unknown, it is hard to identify their origins and mitigate their formation. While some charge traps in the oxide layer could be eliminated by improving the oxide quality or reduce the effect of oxygen scavenging [Cam21; Fil19], it is harder to identify the formation mechanism of additional dots. Dots outside of the Si fin could form due to strain, an effect that was not investigated so far in bulk-Si FinFET devices. We propose to either mitigate strain by introducing poly-silicon as a material for the gate stack, which has similar thermal expansion properties as the silicon substrate and could therefore reduce strain [Cam21], or by numerically simulating the strain environment and accounting for it in the device design. Another possibility for the formation of additional dots are the nano-gates, which extend to the area next to the fin and can electrically accumulate additional dots next to the fin when applying high electric potentials. Their formation could be suppressed by the introduction of screening gates or thicker oxides next to the fin [Zwe22]. These measures would screen respectively reduce the accumulating electric field next to the fin, such that a larger gate voltage parameter space is accessible without accumulation of unwanted dots. Furthermore, defects in the silicon crystal, which can potentially create spurious dots, could be introduced by the high-energy radiation during fabrication, e.g. during EBL or dry-etching. Here, a fabrication relying on all-optical lithography and chemical-mechanical polishing [Zwe22] could mitigate the creation of some of these defects, albeit at the cost of fabrication turnaround and innovation speed [Li20]. Mitigating the interference of the DQD with unwanted charge states is important when moving away from a transport-based readout scheme towards other readout schemes, which usually require a more stable charge environment for high-fidelity qubit readout.

Many of the measurements presented in this work were limited in one way or another by our d.c. parity readout scheme. Our method comes with some disadvantages: the lack of single-shot readout, limited manipulation time and parity readout. Therefore, we propose to implement a fast, single-shot spin readout. This can be done e.g. by using gate-based sensing [Col13; Wes19; Egg23] which is compatible with the current device design in parity readout mode. If we accept an enlarged device footprint, alternatively a RF [Sch98; Noi20] charge sensor could be added to the device. Here, we envision a second parallel fin hosting a sensing dot, that is capacitively coupled to the fin that hosts the qubits [Zwe22]. Alternatively, a square cross-section of the fin could be used to accumulate two rows of dots in their corners, allowing us to use one side of the fin for qubit formation while the other side serves as sensing dots [Cha20]. These methods can be complemented with the introduction of additional ancilla QDs that can be used to overcome the limitation of parity readout and realise true single spin readout [Phi22]. Using such an improved readout scheme would help to improve the measurements in various ways: first, longer manipulation time would enable the execution of more complex quantum algorithms, such as CPMG sequences with increased number of decoupling gates or interleaved randomised benchmarking. Second, single-shot spin readout would allow us to perform gate set tomography to better analyse qubit gate infidelites [Nie21]. Finally, single-spin readout would enable full readout of two-qubit processes and two-qubit algorithms. One of the key features of the FinFET qubits is their temperature resilience, which is useful for large-scale integration. Hence, when improving the qubit readout, the temperature resilience should be preserved. This could be realised by decoupling the qubits and the relevant parts of the readout mechanism from temperature-broadened reservoirs [Hua21]. Single-shot spin readout at elevated temperatures is an important ingredient for a high-temperature spin qubit processor [Pet20a; Pet20b; Yan20].

Comparing the FinFET hole spin qubits to other qubit platforms, we can identify some ways in which certain qubit characteristics can be improved. We have demonstrated that the coherence of the qubits might already be limited by the hyperfine interaction of the hole spins with the nuclei of the host material. Replacing natural silicon with isotopically purified silicon could therefore lead to increased qubit coherence due to the absence of hyperfine noise [Yon17]. Furthermore, qubit speed could be enhanced by optimising the device geometry and crystal orientations to engineer an ultra-strong and electrically switchable SOI [KRL18; Fro21b; BHL21]. Together, these improvements increase the qubit quality factor, which would allow longer quantum algorithms to be performed. Another way of improving the qubits is to further investigate sweet spots [Pio22; Lil21]. If simultaneous control over sweet spots for long coherence, fast manipulation and high-fidelity two-qubit gates can be achieved by means of local electric tuning, a qubit's properties can be significantly improved. However, further theoretical and experimental investigation of the various anisotropic properties discussed throughout this thesis are needed to fully understand the involved physics and to achieve the necessary level of electrical control over the respective properties. Furthermore, to increase the fidelity of single- and two-qubit gates, the currently used square envelope functions for microwave pulses could be replaced by optimised gate pulses [Yan19]. Additionally, automatic re-calibration routines could enable high-fidelity operation of the qubit processor over an extended period of time without manual tuning [Phi22].

Large-scale quantum computing still lies in the distant future. The currently available leading quantum processors using superconducting circuits or trapped ions are pushing slowly into the NISQ regime [IBMa; Aru19; Rig; Ion; Pin21], but they mostly rely on brute-force methods of scaling up: increasing the number of channels of the control electronics at room temperature, the number of connections to low temperature and the size of the refrigerator [IBMb]. Quantum processors based on semiconductor spin qubits, especially in Si, promise to scale up their potential in a smarter fashion. First, operation at elevated temperatures would allow us to integrate control electronics and qubits in the same package, circumventing the wiring bottleneck. Recent examples of cryogenic control electronics [Xue22; Pra22] operate within the same temperature range as was demonstrated for the FinFET hole spin qubit presented in this work. Second, dense integration in combination with the small footprint of spin qubits promises large numbers of qubits on a single chip.

To scale up the basics FinFET device to a larger quantum processor, a fin (which can naturally be extended into a long one-dimensional array) has to be connected coherently to other fins via T-junctions, floating gates [SKL17] or superconducting resonators [Har22]. In this way, a sparsely interconnected two-dimensional qubit array can be formed, which leaves spaces in-between the qubits for on-chip control electronics [Bot19; Bot22]. Other qubit architectures, which propose separate blocks of classical control electronics and qubits [Van17], might also be compatible with FinFETs. To achieve this level of scaling and build a large-scale quantum processor based on FinFETs, many challenges that are already present in our small-scale devices have to be overcome, such as hole spin qubit uniformity, cross-talk and initialisation, gate and readout-infidelities. Furthermore, our visions for large-scale quantum processors leaves many points unspecified, such as the unit cell dimensions, type of qubit readout, implementation of reservoirs, wiring and routing, distribution of control electronics, individual qubit addressability and driving schemes or density and connectivity of qubits. Here, a series of extensive studies and experimental prototyping is required to find the optimal design for a quantum processor. Similar challenges, however, also apply for competing semiconductor spin qubit platforms and other platforms. It remains an open question which platform will win the race for large-scale quantum computing, but hole spin qubits in FinFETs are certainly a strong candidate.

ACKNOWLEDGEMENTS

This thesis, like many things, would not have been possible without the help and inputs from all the people around me, whose unwavering support and invaluable contributions have been instrumental in shaping this work.

First and foremost, I am deeply grateful to my supervisor Richard Warburton. He gave me the opportunity to join his exceptional research group and work on this remarkable research project. Richard's insightful guidance and encouragement have been of great value. Engaging in discussions on the fundamental principles of physics with him has been a truly enriching experience.

I extend my sincere thanks to Andreas Kuhlmann, whose mentorship over the past five years has been transformative. Andreas introduced me to almost all aspects of experimental physics, from tedious cleanroom work to exciting experiments. He was never tired of answering my numerous questions or providing feedback to my work and has been helping me with useful tips and tricks whenever problems emerged.

I would like to express my gratitude to my co-supervisor Dominik Zumbühl for providing the necessary lab infrastructure to conduct my experiments and for his close involvement in the project. I especially appreciate Dominik's willingness to share his insights and expertise of experimental physics, which have been instrumental in advancing the experiments.

Special thanks go to Leon Camenzind, whose countless hours spent with me in the lab to set up and conduct experiments have been truly remarkable. Leon, the Igor-wizard and qubit expert, was an exceptional mentor and found new aspects of the lab to teach to me every day.

I would like to express my sincere appreciation to the rest of the FinFET-team: Rafael Eggli, Mathieu de Kruijf, Toni Berger and Carlos Dos Santos. Their helping hands and unwavering willingness to engage in critical discussions have been invaluable.

I would like to thank Arne Laucht for accepting the role of the external expert on the Doctoral Committee and taking the time to read my dissertation.

Also, I am very grateful to the Nanophotonics research group, whose members never got tired of lecturing me on the advantages of light-based experiments until they had to re-align their mirrors. My heartfelt appreciation goes to Lukas Sponfeldner, Clemens Spinnler, Nadia Antoniadis, Nam Nguyen, Viktoria Yurgens, Sigurd Flågan, Yannik Fontana, Mark Hogg, Malwina Marczak, Marcel Erbe, Andrea Corazza, Alisa Javadi, Tomek Jakubczyk, Liang Zhai, Daniel Najer and Rahel Kaiser. Thanks for the incredible time we shared

together. I would like to give a special shout-out to the "usual suspects" for the numerous activities we enjoyed together, including hiking, skiing, Rhein-swimming or brewing beer!

Additionally, I express my gratitude to the Quantum Coherence Lab and its members: Christian Scheller, Taras Patlatiuk, Miguel Carballido, Henok Weldeyesus, Omid Sharifi, Simon Svab, Pierre Chevalier Kwon, Kris Cerveny, Aldo Tarascio, Artemii Efimov, Moe Samani and Tim Camenzind. Their invaluable help in the lab was always appreciated and I fondly recall countless interesting discussions we had on qubits, lobsters and the dark arts of Igor coding.

I extend my thanks to Bence Hetényi, Stefano Bosco, Peter Stano and Carlos Egues for sharing their invaluable theoretical expertise with me. Despite the occasional language barriers between experimental and theoretical physics, our discussions have been enlightening and transmuting. Their input was key in unravelling many mysteries of my experiments. Moreover, I acknowledge the theoretical support from Daniel Loss.

I would like to thank the members of the electical and mechanical workshop for their impressive work. Michael Steinacher, Sascha Martin, Patrick Stöcklin and Dominik Sifrig showed dedication and expertise by helping to solve every challenge in the lab with practical and ingenious solutions.

Furthermore, I would like to acknowledge all the collaborators from outside of the University of Basel who contributed to the success of this project. The team at IBM Research in Zurich has played a key role in this project. Our collaboration in device fabrication and our regular meetings to discuss latest advances in measurements has been invaluable. I express my sincere appreciation to Andreas Fuhrer, Gian Salis, Patrick Harvey-Collard, Matthias Mergenthaler, Felix Schupp, Eoin Kelly, Michele Aldeghi, Kostas Tsoukalas, Lisa Sommer, Jessica Richter, Nico Hendrickx and the entire BRNC cleanroom team, especially Ute Drechsler, Diana Davila Pineda and Antonis Olziersky.

I am wholeheartedly grateful for our collaboration with Natalia Ares and her exceptional team, including Dominic Lennon, Jonas Schuff, Brandon Severin, Seb Orbell, Joe Hickie and David Craig. They introduced me to the intricacies of machine learning and applied it to the FinFET experiments. Their skills and expertise have been invaluable in broadening the horizons of this research.

Finally, I would like to acknowledge the immense support from individuals outside the realm of physics. I am deeply grateful for the untiring support from my parents, who have been with me every step of the way offering their continuous encouragement. My heartfelt thanks also go to my sister Kathrin and my grandparents for their love and support. I extend my thanks to my dear friends Malte Eckert, Chrisitan Eisele, Sven Klassa, Marcel Neidinger, Michael Plagge, Nikola Racic and Bernhard Roth for their continuous support throughout this journey. Their presence has been a source of strength, and I am grateful for their steady reassurance and belief in my success. I would also like to express my gratitude to all the individuals who have lent a helping hand, shared laughter and cheered for my accomplishments.

BIBLIOGRAPHY

[Ade22a] C. Adelsberger, M. Benito, S. Bosco, J. Klinovaja, and D. Loss. “Hole-spin qubits in Ge nanowire quantum dots: Interplay of orbital magnetic field, strain, and growth direction”. *Physical Review B* **105** (2022), p. 075308. DOI: `10.1103/physrevb.105.075308`.

[Ade22b] C. Adelsberger, S. Bosco, J. Klinovaja, and D. Loss. “Enhanced orbital magnetic field effects in Ge hole nanowires”. *Physical Review B* **106** (2022), p. 235408. DOI: `10.1103/physrevb.106.235408`.

[Ang07] S. J. Angus, A. J. Ferguson, A. S. Dzurak, and R. G. Clark. “Gate-Defined Quantum Dots in Intrinsic Silicon”. *Nano Letters* **7** (2007), pp. 2051–2055. DOI: `10.1021/nl070949k`.

[Ans23] F. Ansaloni, H. Bohuslavskyi, F. Fedele, T. Rasmussen, B. Brovang, F. Berritta, A. Heskes, J. Li, L. Hutin, B. Venitucci, B. Bertrand, M. Vinet, Y.-M. Niquet, A. Chatterjee, and F. Kuemmeth. “Gate reflectometry in dense quantum dot arrays”. *New Journal of Physics* **25** (2023), p. 033023. DOI: `10.1088/1367-2630/acc126`.

[Are13] N. Ares, G. Katsaros, V. N. Golovach, J. J. Zhang, A. Prager, L. I. Glazman, O. G. Schmidt, and S. D. Franceschi. “SiGe quantum dots for fast hole spin Rabi oscillations”. *Applied Physics Letters* **103** (2013), p. 263113. DOI: `10.1063/1.4858959`.

[Aru19] F. Arute, K. Arya, R. Babbush, D. Bacon, J. C. Bardin, R. Barends, R. Biswas, S. Boixo, F. G. S. L. Brandao, D. A. Buell, B. Burkett, Y. Chen, Z. Chen, B. Chiaro, R. Collins, W. Courtney, A. Dunsworth, E. Farhi, B. Foxen, A. Fowler, C. Gidney, M. Giustina, R. Graff, K. Guerin, S. Habegger, M. P. Harrigan, M. J. Hartmann, A. Ho, M. Hoffmann, T. Huang, T. S. Humble, S. V. Isakov, E. Jeffrey, Z. Jiang, D. Kafri, K. Kechedzhi, J. Kelly, P. V. Klimov, S. Knysh, A. Korotkov, F. Kostritsa, D. Landhuis, M. Lindmark, E. Lucero, D. Lyakh, S. Mandrà, J. R. McClean, M. McEwen, A. Megrant, X. Mi, K. Michielsen, M. Mohseni, J. Mutus, O. Naaman, M. Neeley, C. Neill, M. Y. Niu, E. Ostby, A. Petukhov, J. C. Platt, C. Quintana, E. G. Rieffel, P. Roushan, N. C. Rubin, D. Sank, K. J. Satzinger, V. Smelyanskiy, K. J. Sung, M. D. Trevithick, A. Vainsencher, B. Villalonga, T. White, Z. J. Yao,

P. Yeh, A. Zalcman, H. Neven, and J. M. Martinis. “Quantum supremacy using a programmable superconducting processor”. *Nature* **574** (2019), pp. 505–510. DOI: 10.1038/s41586-019-1666-5.

[Ass11] L. V. C. Assali, H. M. Petrilli, R. B. Capaz, B. Koiller, X. Hu, and S. D. Sarma. “Hyperfine interactions in silicon quantum dots”. *Physical Review B* **83** (2011), p. 165301. DOI: 10.1103/physrevb.83.165301.

[Ass22] S. Assali, A. Attiaoui, P. D. Vecchio, S. Mukherjee, J. Nicolas, and O. Moutanabbir. “A Light-Hole Germanium Quantum Well on Silicon”. *Advanced Materials* **34** (2022), p. 2201192. DOI: 10.1002/adma.202201192.

[Aut12] C. Auth, C. Allen, A. Blattner, D. Bergstrom, M. Brazier, M. Bost, M. Buehler, V. Chikarmane, T. Ghani, T. Glassman, R. Grover, W. Han, D. Hanken, M. Hattendorf, P. Hentges, R. Heussner, J. Hicks, D. Ingerly, P. Jain, S. Jaloviar, R. James, D. Jones, J. Jopling, S. Joshi, C. Kenyon, H. Liu, R. McFadden, B. McIntyre, J. Neirynck, C. Parker, L. Pipes, I. Post, S. Pradhan, M. Prince, S. Ramey, T. Reynolds, J. Roesler, J. Sandford, J. Seiple, P. Smith, C. Thomas, D. Towner, T. Troeger, C. Weber, P. Yashar, K. Zawadzki, and K. Mistry. “A 22nm high performance and low-power CMOS technology featuring fully-depleted tri-gate transistors, self-aligned contacts and high density MIM capacitors”. *2012 Symposium on VLSI Technology (VLSIT)*. IEEE, 2012. DOI: 10.1109/vlsit.2012.6242496.

[Aut17] C. Auth, A. Aliyarukunju, M. Asoro, D. Bergstrom, V. Bhagwat, J. Birdsall, N. Bisnik, M. Buehler, V. Chikarmane, G. Ding, Q. Fu, H. Gomez, W. Han, D. Hanken, M. Haran, M. Hattendorf, R. Heussner, H. Hiramatsu, B. Ho, S. Jaloviar, I. Jin, S. Joshi, S. Kirby, S. Kosaraju, H. Kothari, G. Leatherman, K. Lee, J. Leib, A. Madhavan, K. Marla, H. Meyer, T. Mule, C. Parker, S. Parthasarathy, C. Pelto, L. Pipes, I. Post, M. Prince, A. Rahman, S. Rajamani, A. Saha, J. D. Santos, M. Sharma, V. Sharma, J. Shin, P. Sinha, P. Smith, M. Sprinkle, A. S. Amour, C. Staus, R. Suri, D. Towner, A. Tripathi, A. Tura, C. Ward, and A. Yeoh. “A 10nm high performance and low-power CMOS technology featuring 3rd generation FinFET transistors, Self-Aligned Quad Patterning, contact over active gate and cobalt local interconnects”. *2017 IEEE International Electron Devices Meeting (IEDM)*. IEEE, 2017. DOI: 10.1109/iedm.2017.8268472.

[Bal16] C. Ballance, T. Harty, N. Linke, M. Sepiol, and D. Lucas. “High-Fidelity Quantum Logic Gates Using Trapped-Ion Hyperfine Qubits”. *Physical Review Letters* **117** (2016), p. 060504. DOI: 10.1103/physrevlett.117.060504.

[BDP15] M. Bukov, L. D'Alessio, and A. Polkovnikov. "Universal high-frequency behavior of periodically driven systems: from dynamical stabilization to Floquet engineering". *Advances in Physics* **64** (2015), pp. 139–226. DOI: `10.1080/00018732.2015.1055918`.

[Bee91] C. W. J. Beenakker. "Theory of Coulomb-blockade oscillations in the conductance of a quantum dot". *Physical Review B* **44** (1991), pp. 1646–1656. DOI: `10.1103/physrevb.44.1646`.

[BHL21] S. Bosco, B. Hetényi, and D. Loss. "Hole Spin Qubits in Si FinFETs With Fully Tunable Spin-Orbit Coupling and Sweet Spots for Charge Noise". *PRX Quantum* **2** (2021), p. 010348. DOI: `10.1103/prxquantum.2.010348`.

[Bie15] D. Biesinger, C. Scheller, B. Braunecker, J. Zimmerman, A. Gossard, and D. Zumbühl. "Intrinsic Metastabilities in the Charge Configuration of a Double Quantum Dot". *Physical Review Letters* **115** (2015), p. 106804. DOI: `10.1103/physrevlett.115.106804`.

[BL05] D. V. Bulaev and D. Loss. "Spin Relaxation and Decoherence of Holes in Quantum Dots". *Physical Review Letters* **95** (2005), p. 076805. DOI: `10.1103/physrevlett.95.076805`.

[BL07] D. V. Bulaev and D. Loss. "Electric Dipole Spin Resonance for Heavy Holes in Quantum Dots". *Physical Review Letters* **98** (2007), p. 097202. DOI: `10.1103/physrevlett.98.097202`.

[BL21] S. Bosco and D. Loss. "Fully Tunable Hyperfine Interactions of Hole Spin Qubits in Si and Ge Quantum Dots". *Physical Review Letters* **127** (2021), p. 190501. DOI: `10.1103/physrevlett.127.190501`.

[BL22] S. Bosco and D. Loss. "Hole Spin Qubits in Thin Curved Quantum Wells". *Physical Review Applied* **18** (2022), p. 044038. DOI: `10.1103/physrevapplied.18.044038`.

[Bla21] A. Blais, A. L. Grimsmo, S. Girvin, and A. Wallraff. "Circuit quantum electrodynamics". *Reviews of Modern Physics* **93** (2021), p. 025005. DOI: `10.1103/revmodphys.93.025005`.

[Bor19] F. Borjans, X. G. Croot, X. Mi, M. J. Gullans, and J. R. Petta. "Resonant microwave-mediated interactions between distant electron spins". *Nature* **577** (2019), pp. 195–198. DOI: `10.1038/s41586-019-1867-y`.

[Bos21] S. Bosco, M. Benito, C. Adelsberger, and D. Loss. "Squeezed hole spin qubits in Ge quantum dots with ultrafast gates at low power". *Physical Review B* **104** (2021), p. 115425. DOI: `10.1103/physrevb.104.115425`.

[Bos22] S. Bosco, P. Scarlino, J. Klinovaja, and D. Loss. "Fully Tunable Longitudinal Spin-Photon Interactions in Si and Ge Quantum Dots". *Physical Review Letters* **129** (2022), p. 066801. DOI: 10.1103/physrevlett.129.066801.

[Bot19] J. M. Boter, J. P. Dehollain, J. P. G. van Dijk, T. Hensgens, R. Versluis, J. S. Clarke, M. Veldhorst, F. Sebastiano, and L. M. K. Vandersypen. "A sparse spin qubit array with integrated control electronics". *2019 IEEE International Electron Devices Meeting (IEDM)*. IEEE, 2019. DOI: 10.1109/iedm19573.2019.8993570.

[Bot22] J. M. Boter, J. P. Dehollain, J. P. van Dijk, Y. Xu, T. Hensgens, R. Versluis, H. W. Naus, J. S. Clarke, M. Veldhorst, F. Sebastiano, and L. M. Vandersypen. "Spiderweb Array: A Sparse Spin-Qubit Array". *Physical Review Applied* **18** (2022), p. 024053. DOI: 10.1103/physrevapplied.18.024053.

[Bøt22] C. G. L. Bøttcher, S. P. Harvey, S. Fallahi, G. C. Gardner, M. J. Manfra, U. Vool, S. D. Bartlett, and A. Yacoby. "Parametric longitudinal coupling between a high-impedance superconducting resonator and a semiconductor quantum dot singlet-triplet spin qubit". *Nature Communications* **13** (2022). DOI: 10.1038/s41467-022-32236-w.

[Bow68] R. W. Bower, H. G. Dill, K. G. Aubuchon, and S. A. Thompson. "MOS field effect transistors formed by gate masked ion implantation". *IEEE Transactions on Electron Devices* **15** (1968), pp. 757–761.

[Boy19] E. Boyers, M. Pandey, D. K. Campbell, A. Polkovnikov, D. Sels, and A. O. Sushkov. "Floquet-engineered quantum state manipulation in a noisy qubit". *Physical Review A* **100** (2019), p. 012341. DOI: 10.1103/physreva.100.012341.

[Bra19] C. Bradley, J. Randall, M. Abobeih, R. Berrevoets, M. Degen, M. Bakker, M. Markham, D. Twitchen, and T. Taminiau. "A Ten-Qubit Solid-State Spin Register with Quantum Memory up to One Minute". *Physical Review X* **9** (2019), p. 031045. DOI: 10.1103/physrevx.9.031045.

[BTN15] P.-M. Billangeon, J. S. Tsai, and Y. Nakamura. "Circuit-QED-based scalable architectures for quantum information processing with superconducting qubits". *Physical Review B* **91** (2015), p. 094517. DOI: 10.1103/physrevb.91.094517.

[Bur21] G. Burkard, T. D. Ladd, J. M. Nichol, A. Pan, and J. R. Petta. *Semiconductor Spin Qubits*. 2021. DOI: 10.48550/ARXIV.2112.08863.

[Byl11] J. Bylander, S. Gustavsson, F. Yan, F. Yoshihara, K. Harrabi, G. Fitch, D. G. Cory, Y. Nakamura, J.-S. Tsai, and W. D. Oliver. "Noise spectroscopy through dynamical decoupling with a superconducting flux qubit". *Nature Physics* **7** (2011), pp. 565–570. DOI: `10.1038/nphys1994`.

[Cai21] W. Cai, Y. Ma, W. Wang, C.-L. Zou, and L. Sun. "Bosonic quantum error correction codes in superconducting quantum circuits". *Fundamental Research* **1** (2021), pp. 50–67. DOI: `10.1016/j.fmre.2020.12.006`.

[Cam12] L. C. Camenzind. "Master Thesis: Quantum transport signatures of electric dipole spin resonance near the persistent spin helix in GaAs quantum wells" (2012).

[Cam19] L. C. Camenzind. "PhD Thesis: Spins and Orbitsin Semiconductor Quantum Dots" (2019).

[Cam21] T. N. Camenzind, A. Elsayed, F. A. Mohiyaddin, R. Li, S. Kubicek, J. Jussot, P. Van Dorpe, B. Govoreanu, I. Radu, and D. M. Zumbühl. *High mobility SiMOSFETs fabricated in a full 300mm CMOS process*. 2021. DOI: `10.48550/ARXIV.2106.05254`.

[Cam22] L. C. Camenzind, S. Geyer, A. Fuhrer, R. J. Warburton, D. M. Zumbühl, and A. V. Kuhlmann. "A hole spin qubit in a fin field-effect transistor above 4 kelvin". *Nature Electronics* **5** (2022), pp. 178–183. DOI: `10.1038/s41928-022-00722-0`.

[Cha20] E. Chanrion, D. J. Niegemann, B. Bertrand, C. Spence, B. Jadot, J. Li, P.-A. Mortemousque, L. Hutin, R. Maurand, X. Jehl, M. Sanquer, S. D. Franceschi, C. Bäuerle, F. Balestro, Y.-M. Niquet, M. Vinet, T. Meunier, and M. Urdampilleta. "Charge Detection in an Array of CMOS Quantum Dots". *Physical Review Applied* **14** (2020), p. 024066. DOI: `10.1103/physrevapplied.14.024066`.

[Chr20] J. E. Christensen, D. Hucul, W. C. Campbell, and E. R. Hudson. "High-fidelity manipulation of a qubit enabled by a manufactured nucleus". *npj Quantum Information* **6** (2020). DOI: `10.1038/s41534-020-0265-5`.

[Chu09] H. O. H. Churchill, A. J. Bestwick, J. W. Harlow, F. Kuemmeth, D. Marcos, C. H. Stwertka, S. K. Watson, and C. M. Marcus. "Electron–nuclear interaction in ^{13}C nanotube double quantum dots". *Nature Physics* **5** (2009), pp. 321–326. DOI: `10.1038/nphys1247`.

[Col13] J. I. Colless, A. C. Mahoney, J. M. Hornibrook, A. C. Doherty, H. Lu, A. C. Gossard, and D. J. Reilly. "Dispersive Readout of a Few-Electron Double Quantum Dot with Fast rf Gate Sensors". *Physical Review Letters* **110** (2013), p. 046805. DOI: `10.1103/physrevlett.110.046805`.

[CP66] M. Cardona and F. H. Pollak. “Energy-Band Structure of Germanium and Silicon: The k·p Method”. *Physical Review* **142** (1966), pp. 530–543. DOI: `10.1103/physrev.142.530`.

[Cri18] A. Crippa, R. Maurand, L. Bourdet, D. Kotekar-Patil, A. Amisse, X. Jehl, M. Sanquer, R. Laviéville, H. Bohuslavskyi, L. Hutin, S. Barraud, M. Vinet, Y.-M. Niquet, and S. D. Franceschi. “Electrical Spin Driving by g -Matrix Modulation in Spin-Orbit Qubits”. *Physical Review Letters* **120** (2018), p. 137702. DOI: `10.1103/physrevlett.120.137702`.

[Cri19] A. Crippa, R. Ezzouch, A. Aprá, A. Amisse, R. Laviéville, L. Hutin, B. Bertrand, M. Vinet, M. Urdampilleta, T. Meunier, M. Sanquer, X. Jehl, R. Maurand, and S. D. Franceschi. “Gate-reflectometry dispersive readout and coherent control of a spin qubit in silicon”. *Nature Communications* **10** (2019). DOI: `10.1038/s41467-019-10848-z`.

[CYL16] S. Chesi, L.-P. Yang, and D. Loss. “Dephasing due to Nuclear Spins in Large-Amplitude Electric Dipole Spin Resonance”. *Physical Review Letters* **116** (2016), p. 066806. DOI: `10.1103/physrevlett.116.066806`.

[Din23] Q. Ding, A. V. Kuhlmann, A. Fuhrer, and A. Schenk. “A generalizable TCAD framework for silicon FinFET spin qubit devices with electrical control”. *Solid-State Electronics* **200** (2023), p. 108550. DOI: `10.1016/j.sse.2022.108550`.

[DN09] J. Danon and Y. V. Nazarov. “Pauli spin blockade in the presence of strong spin-orbit coupling”. *Physical Review B* **80** (2009), p. 041301. DOI: `10.1103/physrevb.80.041301`.

[Dua21] J. Duan, J. S. Lehtinen, M. A. Fogarty, S. Schaal, M. M. L. Lam, A. Ronzani, A. Shchepetov, P. Koppinen, M. Prunnila, F. Gonzalez-Zalba, and J. J. L. Morton. “Dispersive readout of reconfigurable ambipolar quantum dots in a silicon-on-insulator nanowire”. *Applied Physics Letters* **118** (2021), p. 164002. DOI: `10.1063/5.0040259`.

[Een19] H. G. J. Eenink, L. Petit, W. I. L. Lawrie, J. S. Clarke, L. M. K. Vandersypen, and M. Veldhorst. “Tunable Coupling and Isolation of Single Electrons in Silicon Metal-Oxide-Semiconductor Quantum Dots”. *Nano Letters* **19** (2019), pp. 8653–8657. DOI: `10.1021/acs.nanolett.9b03254`.

[Egg23] R. S. Eggli, S. Svab, T. Patlatiuk, D. Trüssel, M. J. Carballido, P. C. Kwon, S. Geyer, A. Li, E. P. A. M. Bakkers, A. V. Kuhlmann, and D. M. Zumbühl. *Cryogenic hyperabrupt strontium titanate varactors for sensitive reflectometry of quantum dots*. 2023. DOI: `10.48550/ARXIV.2303.02933`.

[Elz04] J. M. Elzerman, R. Hanson, L. H. W. van Beveren, B. Witkamp, L. M. K. Vandersypen, and L. P. Kouwenhoven. “Single-shot read-out of an individual electron spin in a quantum dot”. *Nature* **430** (2004), pp. 431–435. DOI: `10.1038/nature02693`.

[Esr16] M. Esro, O. Kolosov, P. J. Jones, W. I. Milne, and G. Adamopoulos. “Structural and Electrical Characterization of SiO_2 Gate Dielectrics Deposited from Solutions at Moderate Temperatures in Air”. *ACS Applied Materials & Interfaces* **9** (2016), pp. 529–536. DOI: `10.1021/acsami.6b11214`.

[Fan23] Y. Fang, P. Philippopoulos, D. Culcer, W. A. Coish, and S. Chesi. “Recent advances in hole-spin qubits”. *Materials for Quantum Technology* **3** (2023), p. 012003. DOI: `10.1088/2633-4356/acb87e`.

[Fas07] C. Fasth, A. Fuhrer, L. Samuelson, V. N. Golovach, and D. Loss. “Direct Measurement of the Spin-Orbit Interaction in a Two-Electron InAs Nanowire Quantum Dot”. *Physical Review Letters* **98** (2007), p. 266801. DOI: `10.1103/physrevlett.98.266801`.

[Fie93] M. Field, C. G. Smith, M. Pepper, D. A. Ritchie, J. E. F. Frost, G. A. C. Jones, and D. G. Hasko. “Measurements of Coulomb blockade with a noninvasive voltage probe”. *Physical Review Letters* **70** (1993), pp. 1311–1314. DOI: `10.1103/physrevlett.70.1311`.

[Fil19] E. O. Filatova, S. S. Sakhonenkov, A. S. Konashuk, S. A. Kasatikov, and V. V. Afanas’ev. “Inhibition of Oxygen Scavenging by TiN at the TiN/SiO_2 Interface by Atomic-Layer-Deposited Al_2O_3 Protective Interlayer”. *The Journal of Physical Chemistry C* **123** (2019), pp. 22335–22344. DOI: `10.1021/acs.jpcc.9b05800`.

[Fis08] J. Fischer, W. A. Coish, D. V. Bulaev, and D. Loss. “Spin decoherence of a heavy hole coupled to nuclear spins in a quantum dot”. *Physical Review B* **78** (2008). DOI: `10.1103/physrevb.78.155329`.

[Fog18] M. A. Fogarty, K. W. Chan, B. Hensen, W. Huang, T. Tanttu, C. H. Yang, A. Laucht, M. Veldhorst, F. E. Hudson, K. M. Itoh, D. Culcer, T. D. Ladd, A. Morello, and A. S. Dzurak. “Integrated silicon qubit platform with single-spin addressability, exchange control and single-shot singlet-triplet readout”. *Nature Communications* **9** (2018). DOI: `10.1038/s41467-018-06039-x`.

[Fow12] A. G. Fowler, M. Mariantoni, J. M. Martinis, and A. N. Cleland. “Surface codes: Towards practical large-scale quantum computation”. *Phys. Rev. A* **86** (3 2012), p. 032324. DOI: `10.1103/PhysRevA.86.032324`. URL: `https://link.aps.org/doi/10.1103/PhysRevA.86.032324`.

[Fra01] S. D. Franceschi, S. Sasaki, J. M. Elzerman, W. G. van der Wiel, S. Tarucha, and L. P. Kouwenhoven. “Electron Cotunneling in a Semiconductor Quantum Dot”. *Physical Review Letters* **86** (2001), pp. 878–881. DOI: `10.1103/physrevlett.86.878`.

[Fra19] D. Franke, J. Clarke, L. Vandersypen, and M. Veldhorst. “Rent’s rule and extensibility in quantum computing”. *Microprocessors and Microsystems* **67** (2019), pp. 1–7. DOI: `10.1016/j.micpro.2019.02.006`.

[Fro21a] F. N. M. Froning, M. J. Rančić, B. Hetényi, S. Bosco, M. K. Rehmann, A. Li, E. P. A. M. Bakkers, F. A. Zwanenburg, D. Loss, D. M. Zumbühl, and F. R. Braakman. “Strong spin-orbit interaction and g-factor renormalization of hole spins in Ge/Si nanowire quantum dots”. *Physical Review Research* **3** (2021), p. 013081. DOI: `10.1103/physrevresearch.3.013081`.

[Fro21b] F. N. M. Froning, L. C. Camenzind, O. A. H. van der Molen, A. Li, E. P. A. M. Bakkers, D. M. Zumbühl, and F. R. Braakman. “Ultrafast hole spin qubit with gate-tunable spin–orbit switch functionality”. *Nature Nanotechnology* (2021). DOI: `10.1038/s41565-020-00828-6`.

[FYI10] P. Fallahi, S. T. Yılmaz, and A. Imamoğlu. “Measurement of a Heavy-Hole Hyperfine Interaction in InGaAs Quantum Dots Using Resonance Fluorescence”. *Physical Review Letters* **105** (2010), p. 257402. DOI: `10.1103/physrevlett.105.257402`.

[Gao20] F. Gao, J.-H. Wang, H. Watzinger, H. Hu, M. J. Rančić, J.-Y. Zhang, T. Wang, Y. Yao, G.-L. Wang, J. Kukučka, L. Vukušić, C. Kloeffel, D. Loss, F. Liu, G. Katsaros, and J.-J. Zhang. “Site-Controlled Uniform Ge/Si Hut Wires with Electrically Tunable Spin–Orbit Coupling”. *Advanced Materials* **32** (2020), p. 1906523. DOI: `10.1002/adma.201906523`.

[GBL06] V. N. Golovach, M. Borhani, and D. Loss. “Electric-dipole-induced spin resonance in quantum dots”. *Physical Review B* **74** (2006), p. 165319. DOI: `10.1103/physrevb.74.165319`.

[Gey19a] S. Geyer. “Master Thesis: Quantum Dots in Silicon CMOS Fin Field-Effect Transistors” (2019).

[Gey19b] S. Geyer. “Project Thesis: Experiments and Simulations on Ambipolar Quantum Dots in Silicon Fin Field-Effect Transistors” (2019).

[Gey21] S. Geyer, L. C. Camenzind, L. Czornomaz, V. Deshpande, A. Fuhrer, R. J. Warburton, D. M. Zumbühl, and A. V. Kuhlmann. “Self-aligned gates for scalable silicon quantum computing”. *Applied Physics Letters* **118** (2021), p. 104004. DOI: `10.1063/5.0036520`.

[Gey22] S. Geyer, B. Hetényi, S. Bosco, L. C. Camenzind, R. S. Eggli, A. Fuhrer, D. Loss, R. J. Warburton, D. M. Zumbühl, and A. V. Kuhlmann. *Two-qubit logic with anisotropic exchange in a fin field-effect transistor*. 2022. DOI: 10.48550/ARXIV.2212.02308.

[Gil23] W. Gilbert, T. Tanttu, W. H. Lim, M. Feng, J. Y. Huang, J. D. Cifuentes, S. Serrano, P. Y. Mai, R. C. C. Leon, C. C. Escott, K. M. Itoh, N. V. Abrosimov, H.-J. Pohl, M. L. W. Thewalt, F. E. Hudson, A. Morello, A. Laucht, C. H. Yang, A. Saraiva, and A. S. Dzurak. "On-demand electrical control of spin qubits". *Nature Nanotechnology* **18** (2023), pp. 131–136. DOI: 10.1038/s41565-022-01280-4.

[Gon21] M. F. Gonzalez-Zalba, S. de Franceschi, E. Charbon, T. Meunier, M. Vinet, and A. S. Dzurak. "Scaling silicon-based quantum computing using CMOS technology". *Nature Electronics* **4** (2021), pp. 872–884. DOI: 10.1038/s41928-021-00681-y.

[Han07] R. Hanson, L. P. Kouwenhoven, J. R. Petta, S. Tarucha, and L. M. K. Vandersypen. "Spins in few-electron quantum dots". *Reviews of Modern Physics* **79** (2007), pp. 1217–1265. DOI: 10.1103/revmodphys.79.1217.

[Han21] I. Hansen, A. E. Seedhouse, A. Saraiva, A. Laucht, A. S. Dzurak, and C. H. Yang. "Pulse engineering of a global field for robust and universal quantum computation". *Physical Review A* **104** (2021), p. 062415. DOI: 10.1103/physreva.104.062415.

[Han22] I. Hansen, A. E. Seedhouse, K. W. Chan, F. E. Hudson, K. M. Itoh, A. Laucht, A. Saraiva, C. H. Yang, and A. S. Dzurak. "Implementation of an advanced dressing protocol for global qubit control in silicon". *Applied Physics Reviews* **9** (2022), p. 031409. DOI: 10.1063/5.0096467.

[Har22] P. Harvey-Collard, J. Dijkema, G. Zheng, A. Sammak, G. Scappucci, and L. M. Vandersypen. "Coherent Spin-Spin Coupling Mediated by Virtual Microwave Photons". *Physical Review X* **12** (2022), p. 021026. DOI: 10.1103/physrevx.12.021026.

[HBL22] B. Hetényi, S. Bosco, and D. Loss. "Anomalous Zero-Field Splitting for Hole Spin Qubits in Si and Ge Quantum Dots". *Physical Review Letters* **129** (2022), p. 116805. DOI: 10.1103/physrevlett.129.116805.

[Hen20a] N. W. Hendrickx, D. P. Franke, A. Sammak, G. Scappucci, and M. Veldhorst. "Fast two-qubit logic with holes in germanium". *Nature* **577** (2020), pp. 487–491. DOI: 10.1038/s41586-019-1919-3.

[Hen20b] N. W. Hendrickx, W. I. L. Lawrie, L. Petit, A. Sammak, G. Scappucci, and M. Veldhorst. “A single-hole spin qubit”. *Nature Communications* **11** (2020), p. 3478. doi: `10.1038/s41467-020-17211-7`.

[Hen21] N. W. Hendrickx, W. I. L. Lawrie, M. Russ, F. van Riggelen, S. L. de Snoo, R. N. Schouten, A. Sammak, G. Scappucci, and M. Veldhorst. “A four-qubit germanium quantum processor”. *Nature* **591** (2021), pp. 580–585. doi: `10.1038/s41586-021-03332-6`.

[HKL20] B. Hetényi, C. Kloeffel, and D. Loss. “Exchange interaction of hole-spin qubits in double quantum dots in highly anisotropic semiconductors”. *Physical Review Research* **2** (2020), p. 033036. doi: `10.1103/physrevresearch.2.033036`.

[HL21] W. Hu and F. Li. “Scaling Beyond 7nm Node: An Overview of Gate-All-Around FETs”. *2021 9th International Symposium on Next Generation Electronics (ISNE)*. IEEE, 2021. doi: `10.1109/isne48910.2021.9493305`.

[Hon20] S. S. Hong, A. T. Papageorge, P. Sivarajah, G. Crossman, N. Didier, A. M. Polloreno, E. A. Sete, S. W. Turkowski, M. P. da Silva, and B. R. Johnson. “Demonstration of a parametrically activated entangling gate protected from flux noise”. *Physical Review A* **101** (2020), p. 012302. doi: `10.1103/physreva.101.012302`.

[Hua19] W. Huang, C. H. Yang, K. W. Chan, T. Tanttu, B. Hensen, R. C. C. Leon, M. A. Fogarty, J. C. C. Hwang, F. E. Hudson, K. M. Itoh, A. Morello, A. Laucht, and A. S. Dzurak. “Fidelity benchmarks for two-qubit gates in silicon”. *Nature* **569** (2019), pp. 532–536. doi: `10.1038/s41586-019-1197-0`.

[Hua21] J. Y. Huang, W. H. Lim, R. C. C. Leon, C. H. Yang, F. E. Hudson, C. C. Escott, A. Saraiva, A. S. Dzurak, and A. Laucht. “A High-Sensitivity Charge Sensor for Silicon Qubits above 1 K”. *Nano Letters* **21** (2021), pp. 6328–6335. doi: `10.1021/acs.nanolett.1c01003`.

[Hud22] K. Hudson, A. Srinivasan, D. Miserev, Q. Wang, O. Klochan, O. Sushkov, I. Farrer, D. Ritchie, and A. Hamilton. *Observation of oscillating g-factor anisotropy arising from strong crystal lattice anisotropy in GaAs spin-3/2 hole quantum point contacts*. 2022. doi: `10.48550/ARXIV.2211.00253`.

[Hut16] L. Hutin, R. Maurand, D. Kotekar-Patil, A. Corna, H. Bohuslavskyi, X. Jehl, S. Barraud, S. D. Franceschi, M. Sanquer, and M. Vinet. “Si CMOS platform for quantum information processing”. *2016 IEEE Symposium on VLSI Technology*. IEEE, 2016. doi: `10.1109/vlsit.2016.7573380`.

[Hut18] L. Hutin, B. Bertrand, R. Maurand, A. Crippa, M. Urdampilleta, Y. Kim, A. Amisse, H. Bohuslavskyi, L. Bourdet, S. Barraud, X. Jeh, Y.-M. Niquet, M. Sanquer, C. Bauerle, T. Meunier, S. D. Franceschi, and M. Vinet. "Si MOS technology for spin-based quantum computing". *2018 48th European Solid-State Device Research Conference (ESSDERC)*. IEEE, 2018. DOI: `10.1109/essderc.2018.8486863`.

[Hut19] L. Hutin, T. Lundberg, A. Chatterjee, A. Crippa, J. Li, R. Maurand, X. Jehl, M. Sanquer, M. F. Gonzalez-Zalba, F. Kuemmeth, Y.-M. Niquet, B. Bertrand, S. D. Franceschi, M. Urdampilleta, T. Meunier, M. Vinet, E. Chanrion, H. Bohuslavskyi, F. Ansaloni, T.-Y. Yang, J. Michniewicz, D. J. Niegemann, and C. Spence. "Gate reflectometry for probing charge and spin states in linear Si MOS split-gate arrays". *2019 IEEE International Electron Devices Meeting (IEDM)*. IEEE, 2019. DOI: `10.1109/iedm19573.2019.8993580`.

[IBMa] IBM. URL: `https://newsroom.ibm.com/2022-11-09-IBM-Unveils-400-Qubit-Plus-Quantum-Processor-and-Next-Generation-IBM-Quantum-System-Two`.

[IBMb] IBM. URL: `https://research.ibm.com/blog/goldeneye-cryogenic-concept-system`.

[Ion] IonQ. URL: `https://ionq.com/quantum-systems/forte`.

[Joc18] R. M. Jock, N. T. Jacobson, P. Harvey-Collard, A. M. Mounce, V. Srinivasa, D. R. Ward, J. Anderson, R. Manginell, J. R. Wendt, M. Rudolph, T. Pluym, J. K. Gamble, A. D. Baczewski, W. M. Witzel, and M. S. Carroll. "A silicon metal-oxide-semiconductor electron spin-orbit qubit". *Nature Communications* **9** (2018). DOI: `10.1038/s41467-018-04200-0`.

[Joh05] A. C. Johnson, J. R. Petta, C. M. Marcus, M. P. Hanson, and A. C. Gossard. "Singlet-triplet spin blockade and charge sensing in a few-electron double quantum dot". *Physical Review B* **72** (2005), p. 165308. DOI: `10.1103/physrevb.72.165308`.

[Kat03] Y. Kato. "Gigahertz Electron Spin Manipulation Using Voltage-Controlled g-Tensor Modulation". *Science* **299** (2003), pp. 1201–1204. DOI: `10.1126/science.1080880`.

[Kat20] G. Katsaros, J. Kukučka, L. Vukušić, H. Watzinger, F. Gao, T. Wang, J.-J. Zhang, and K. Held. "Zero Field Splitting of Heavy-Hole States in Quantum Dots". *Nano Letters* **20** (2020), pp. 5201–5206. DOI: `10.1021/acs.nanolett.0c01466`.

[Kav01] K. V. Kavokin. “Anisotropic exchange interaction of localized conduction-band electrons in semiconductors”. *Physical Review B* **64** (2001), p. 075305. DOI: `10.1103/physrevb.64.075305`.

[Kav04] K. V. Kavokin. “Symmetry of anisotropic exchange interactions in semiconductor nanostructures”. *Physical Review B* **69** (2004), p. 075302. DOI: `10.1103/physrevb.69.075302`.

[Kaw14] E. Kawakami, P. Scarlino, D. R. Ward, F. R. Braakman, D. E. Savage, M. G. Lagally, M. Friesen, S. N. Coppersmith, M. A. Eriksson, and L. M. K. Vandersypen. “Electrical control of a long-lived spin qubit in a Si/SiGe quantum dot”. *Nature Nanotechnology* **9** (2014), pp. 666–670. DOI: `10.1038/nnano.2014.153`.

[Kel14] J. Kelly, R. Barends, B. Campbell, Y. Chen, Z. Chen, B. Chiaro, A. Dunsworth, A. Fowler, I.-C. Hoi, E. Jeffrey, A. Megrant, J. Mutus, C. Neill, P. O’Malley, C. Quintana, P. Roushan, D. Sank, A. Vainsencher, J. Wenner, T. White, A. Cleland, and J. M. Martinis. “Optimal Quantum Control Using Randomized Benchmarking”. *Physical Review Letters* **112** (2014), p. 240504. DOI: `10.1103/physrevlett.112.240504`.

[Kit03] A. Kitaev. “Fault-tolerant quantum computation by anyons”. *Annals of Physics* **303** (2003), pp. 2–30. DOI: `10.1016/s0003-4916(02)00018-0`.

[KL13] C. Kloeffel and D. Loss. “Prospects for Spin-Based Quantum Computing in Quantum Dots”. *Annual Review of Condensed Matter Physics* **4** (2013), pp. 51–81. DOI: `10.1146/annurev-conmatphys-030212-184248`.

[KLG02] A. V. Khaetskii, D. Loss, and L. Glazman. “Electron Spin Decoherence in Quantum Dots due to Interaction with Nuclei”. *Physical Review Letters* **88** (2002), p. 186802. DOI: `10.1103/physrevlett.88.186802`.

[Kni08] E. Knill, D. Leibfried, R. Reichle, J. Britton, R. B. Blakestad, J. D. Jost, C. Langer, R. Ozeri, S. Seidelin, and D. J. Wineland. “Randomized benchmarking of quantum gates”. *Physical Review A* **77** (2008), p. 012307. DOI: `10.1103/physreva.77.012307`.

[KNV08] F. H. L. Koppens, K. C. Nowack, and L. M. K. Vandersypen. “Spin Echo of a Single Electron Spin in a Quantum Dot”. *Physical Review Letters* **100** (2008), p. 236802. DOI: `10.1103/physrevlett.100.236802`.

[Kog04] A. Kogan, S. Amasha, D. Goldhaber-Gordon, G. Granger, M. A. Kastner, and H. Shtrikman. “Measurements of Kondo and Spin Splitting in Single-Electron Transistors”. *Physical Review Letters* **93** (2004), p. 166602. DOI: `10.1103/physrevlett.93.166602`.

[Kop06] F. H. L. Koppens, C. Buizert, K. J. Tielrooij, I. T. Vink, K. C. Nowack, T. Meunier, L. P. Kouwenhoven, and L. M. K. Vandersypen. “Driven coherent oscillations of a single electron spin in a quantum dot”. *Nature* **442** (2006), pp. 766–771. DOI: `10.1038/nature05065`.

[KRL18] C. Kloeffel, M. J. Rančić, and D. Loss. “Direct Rashba spin-orbit interaction in Si and Ge nanowires with different growth directions”. *Physical Review B* **97** (2018), p. 235422. DOI: `10.1103/physrevb.97.235422`.

[Kru23] M. de Kruijf, S. Geyer, T. Berger, M. Mergenthaler, F. Braakman, R. J. Warburton, and A. V. Kuhlmann. “A compact and versatile cryogenic probe station for quantum device testing”. *Review of Scientific Instruments* **94** (2023). DOI: `10.1063/5.0139825`.

[KTL11] C. Kloeffel, M. Trif, and D. Loss. “Strong spin-orbit interaction and helical hole states in Ge/Si nanowires”. *Physical Review B* **84** (2011), p. 195314. DOI: `10.1103/physrevb.84.195314`.

[Kuh13] A. V. Kuhlmann, J. Houel, A. Ludwig, L. Greuter, D. Reuter, A. D. Wieck, M. Poggio, and R. J. Warburton. “Charge noise and spin noise in a semiconductor quantum device”. *Nature Physics* **9** (2013), pp. 570–575. DOI: `10.1038/nphys2688`.

[Kuh18] A. V. Kuhlmann, V. Deshpande, L. C. Camenzind, D. M. Zumbühl, and A. Fuhrer. “Ambipolar quantum dots in undoped silicon fin field-effect transistors”. *Applied Physics Letters* **113** (2018), p. 122107. DOI: `10.1063/1.5048097`.

[Lai11] N. S. Lai, W. H. Lim, C. H. Yang, F. A. Zwanenburg, W. A. Coish, F. Qassemi, A. Morello, and A. S. Dzurak. “Pauli Spin Blockade in a Highly Tunable Silicon Double Quantum Dot”. *Scientific Reports* **1** (2011), p. 110. DOI: `10.1038/srep00110`.

[Lau16] A. Laucht, R. Kalra, S. Simmons, J. P. Dehollain, J. T. Muhonen, F. A. Mohiyaddin, S. Freer, F. E. Hudson, K. M. Itoh, D. N. Jamieson, J. C. McCallum, A. S. Dzurak, and A. Morello. “A dressed spin qubit in silicon”. *Nature Nanotechnology* **12** (2016), pp. 61–66. DOI: `10.1038/nnano.2016.178`.

[Law20] W. I. L. Lawrie, H. G. J. Eenink, N. W. Hendrickx, J. M. Boter, L. Petit, S. V. Amitonov, M. Lodari, B. P. Wuetz, C. Volk, S. G. J. Philips, G. Droulers, N. Kalhor, F. van Riggelen, D. Brousse, A. Sammak, L. M. K. Vandersypen, G. Scappucci, and M. Veldhorst. “Quantum dot arrays in silicon and germanium”. *Applied Physics Letters* **116** (2020), p. 080501. DOI: `10.1063/5.0002013`.

[Law21] W. I. L. Lawrie, M. Russ, F. van Riggelen, N. W. Hendrickx, S. L. de Snoo, A. Sammak, G. Scappucci, and M. Veldhorst. *Simultaneous driving of semiconductor spin qubits at the fault-tolerant threshold*. 2021. DOI: `10.48550/ARXIV.2109.07837`.

[LD98] D. Loss and D. P. DiVincenzo. "Quantum computation with quantum dots". *Physical Review A* **57** (1998), pp. 120–126. DOI: `10.1103/PhysRevA.57.120`. URL: `https://link.aps.org/doi/10.1103/PhysRevA.57.120`.

[Lei03] D. Leibfried, R. Blatt, C. Monroe, and D. Wineland. "Quantum dynamics of single trapped ions". *Reviews of Modern Physics* **75** (2003), pp. 281–324. DOI: `10.1103/revmodphys.75.281`.

[Li15] R. Li, F. E. Hudson, A. S. Dzurak, and A. R. Hamilton. "Pauli Spin Blockade of Heavy Holes in a Silicon Double Quantum Dot". *Nano Lett.* **15** (2015), pp. 7314–7318. DOI: `10.1021/acs.nanolett.5b02561`.

[Li20] R. Li, N. I. D. Stuyck, S. Kubicek, J. Jussot, B. T. Chan, F. A. Mohiyaddin, A. Elsayed, M. Shehata, G. Simion, C. Godfrin, Y. Canvel, T. Ivanov, L. Goux, B. Govoreanu, and I. P. Radu. "A flexible 300 mm integrated Si MOS platform for electron- and hole-spin qubits exploration". *2020 IEEE International Electron Devices Meeting (IEDM)*. IEEE, 2020. DOI: `10.1109/iedm13553.2020.9371956`.

[Lil21] S. D. Liles, F. Martins, D. S. Miserev, A. A. Kiselev, I. D. Thorvaldson, M. J. Rendell, I. K. Jin, F. E. Hudson, M. Veldhorst, K. M. Itoh, O. P. Sushkov, T. D. Ladd, A. S. Dzurak, and A. R. Hamilton. "Electrical control of the g tensor of the first hole in a silicon MOS quantum dot". *Physical Review B* **104** (2021), p. 235303. DOI: `10.1103/physrevb.104.235303`.

[Lim09] W. H. Lim, F. A. Zwanenburg, H. Huebl, M. Möttönen, K. W. Chan, A. Morello, and A. S. Dzurak. "Observation of the single-electron regime in a highly tunable silicon quantum dot". *Applied Physics Letters* **95** (2009), p. 242102. DOI: `10.1063/1.3272858`.

[Mad22] M. T. Madzik, S. Asaad, A. Youssry, B. Joecker, K. M. Rudinger, E. Nielsen, K. C. Young, T. J. Proctor, A. D. Baczewski, A. Laucht, V. Schmitt, F. E. Hudson, K. M. Itoh, A. M. Jakob, B. C. Johnson, D. N. Jamieson, A. S. Dzurak, C. Ferrie, R. Blume-Kohout, and A. Morello. "Precision tomography of a three-qubit donor quantum processor in silicon". *Nature* **601** (2022), pp. 348–353. DOI: `10.1038/s41586-021-04292-7`.

[Mal16] F. K. Malinowski, F. Martins, P. D. Nissen, E. Barnes, Ł. Cywiński, M. S. Rudner, S. Fallahi, G. C. Gardner, M. J. Manfra, C. M. Marcus, and F. Kuemmeth. “Notch filtering the nuclear environment of a spin qubit”. *Nature Nanotechnology* **12** (2016), pp. 16–20. DOI: `10.1038/nnano.2016.170`.

[Mau16] R. Maurand, X. Jehl, D. Kotekar-Patil, A. Corna, H. Bohuslavskyi, R. Laviéville, L. Hutin, S. Barraud, M. Vinet, M. Sanquer, and S. D. Franceschi. “A CMOS silicon spin qubit”. *Nature Communications* **7** (2016), p. 13575. DOI: `10.1038/ncomms13575`.

[Med12] J. Medford, Ł. Cywiński, C. Barthel, C. M. Marcus, M. P. Hanson, and A. C. Gossard. “Scaling of Dynamical Decoupling for Spin Qubits”. *Physical Review Letters* **108** (2012), p. 086802. DOI: `10.1103/physrevlett.108.086802`.

[MG58] S. Meiboom and D. Gill. “Modified Spin-Echo Method for Measuring Nuclear Relaxation Times”. *Review of Scientific Instruments* **29** (1958), pp. 688–691. DOI: `10.1063/1.1716296`.

[Mic23] V. P. Michal, J. C. Abadillo-Uriel, S. Zihlmann, R. Maurand, Y.-M. Niquet, and M. Filippone. “Tunable hole spin-photon interaction based on g-matrix modulation”. *Physical Review B* **107** (2023), p. l041303. DOI: `10.1103/physrevb.107.l041303`.

[Mil22] A. R. Mills, C. R. Guinn, M. J. Gullans, A. J. Sigillito, M. M. Feldman, E. Nielsen, and J. R. Petta. “Two-qubit silicon quantum processor with operation fidelity exceeding 99%”. *Science Advances* **8** (2022), p. 14. DOI: `10.1126/sciadv.abn5130`.

[Mue15] F. Mueller, G. Konstantaras, P. C. Spruijtenburg, W. G. van der Wiel, and F. A. Zwanenburg. “Electron–Hole Confinement Symmetry in Silicon Quantum Dots”. *Nano Letters* **15** (2015), pp. 5336–5341. DOI: `10.1021/acs.nanolett.5b01706`.

[Muh15] J. T. Muhonen, A. Laucht, S. Simmons, J. P. Dehollain, R. Kalra, F. E. Hudson, S. Freer, K. M. Itoh, D. N. Jamieson, J. C. McCallum, A. S. Dzurak, and A. Morello. “Quantifying the quantum gate fidelity of single-atom spin qubits in silicon by randomized benchmarking”. *Journal of Physics: Condensed Matter* **27** (2015), p. 154205. DOI: `10.1088/0953-8984/27/15/154205`.

[Nad10a] S. Nadj-Perge, S. M. Frolov, E. P. A. M. Bakkers, and L. P. Kouwenhoven. “Spin–orbit qubit in a semiconductor nanowire”. *Nature* **468** (2010), pp. 1084–1087. DOI: `10.1038/nature09682`.

[Nad10b] S. Nadj-Perge, S. M. Frolov, J. W. W. van Tilburg, J. Danon, Y. V. Nazarov, R. Algra, E. P. A. M. Bakkers, and L. P. Kouwenhoven. "Disentangling the effects of spin-orbit and hyperfine interactions on spin blockade". *Physical Review B* **81** (2010), p. 201305. DOI: 10.1103/physrevb.81.201305.

[Nad12] S. Nadj-Perge, V. S. Pribiag, J. W. G. van den Berg, K. Zuo, S. R. Plissard, E. P. A. M. Bakkers, S. M. Frolov, and L. P. Kouwenhoven. "Spectroscopy of Spin-Orbit Quantum Bits in Indium Antimonide Nanowires". *Physical Review Letters* **108** (2012), p. 166801. DOI: 10.1103/physrevlett.108.166801.

[NC10] M. A. Nielsen and I. L. Chuang. *Quantum Computation and Quantum Information*. Cambridge University Pr., 2010. URL: https://www.ebook.de/de/product/13055864/michael_a_nielsen_isaac_l_chuang_quantum_computation_and_quantum_information.html.

[NCC] NCCRSPIN. URL: www.nccr-spin.ch.

[Nie21] E. Nielsen, J. K. Gamble, K. Rudinger, T. Scholten, K. Young, and R. Blume-Kohout. "Gate Set Tomography". *Quantum* **5** (2021), p. 557. DOI: 10.22331/q-2021-10-05-557.

[Noi20] A. Noiri, K. Takeda, J. Yoneda, T. Nakajima, T. Kodera, and S. Tarucha. "Radio-Frequency-Detected Fast Charge Sensing in Undoped Silicon Quantum Dots". *Nano Letters* **20** (2020), pp. 947–952. DOI: 10.1021/acs.nanolett.9b03847.

[Noi22] A. Noiri, K. Takeda, T. Nakajima, T. Kobayashi, A. Sammak, G. Scappucci, and S. Tarucha. "Fast universal quantum gate above the fault-tolerance threshold in silicon". *Nature* **601** (2022), pp. 338–342. DOI: 10.1038/s41586-021-04182-y.

[Now07] K. C. Nowack, F. H. L. Koppens, Y. V. Nazarov, and L. M. K. Vandersypen. "Coherent Control of a Single Electron Spin with Electric Fields". *Science* **318** (2007), pp. 1430–1433. DOI: 10.1126/science.1148092.

[Nur22] M. Nurizzo, B. Jadot, P.-A. Mortemousque, V. Thiney, E. Chanrion, D. Niegemann, M. Dartiailh, A. Ludwig, A. D. Wieck, C. Bäuerle, M. Urdampilleta, and T. Meunier. *Complete readout of two-electron spin states in a double quantum dot*. 2022. DOI: 10.48550/ARXIV.2209.00535.

[Ono02] K. Ono, D. Austing, Y. Tokura, and S. Tarucha. "Current Rectification by Pauli Exclusion in a Weakly Coupled Double Quantum Dot System". *Science* **297** (2002), pp. 1313–1317. DOI: 10.1126/science.1070958.

[Pal14] E. Paladino, Y. Galperin, G. Falci, and B. Altshuler. "$1/f$ noise: Implications for solid-state quantum information". *Reviews of Modern Physics* **86** (2014), pp. 361–418. DOI: 10.1103/revmodphys.86.361.

[Pet05] J. R. Petta, A. C. Johnson, J. M. Taylor, E. A. Laird, A. Yacoby, M. D. Lukin, C. M. Marcus, M. P. Hanson, and A. C. Gossard. “Coherent Manipulation of Coupled Electron Spins in Semiconductor Quantum Dots”. *Science* **309** (2005), pp. 2180–2184. DOI: 10.1126/science.1116955.

[Pet18] F. Petiziol, B. Dive, F. Mintert, and S. Wimberger. “Fast adiabatic evolution by oscillating initial Hamiltonians”. *Physical Review A* **98** (2018), p. 043436. DOI: 10.1103/physreva.98.043436.

[Pet20a] L. Petit, H. G. J. Eenink, M. Russ, W. I. L. Lawrie, N. W. Hendrickx, S. G. J. Philips, J. S. Clarke, L. M. K. Vandersypen, and M. Veldhorst. “Universal quantum logic in hot silicon qubits”. *Nature* **580** (2020), pp. 355–359. DOI: 10.1038/s41586-020-2170-7.

[Pet20b] L. Petit, M. Russ, H. G. J. Eenink, W. I. L. Lawrie, J. S. Clarke, L. M. K. Vandersypen, and M. Veldhorst. *High-fidelity two-qubit gates in silicon above one Kelvin*. 2020. DOI: 10.48550/ARXIV.2007.09034.

[Pfu07] A. Pfund, I. Shorubalko, K. Ensslin, and R. Leturcq. “Spin-state mixing in InAs double quantum dots”. *Physical Review B* **76** (2007), p. 161308. DOI: 10.1103/physrevb.76.161308.

[Phi22] S. G. J. Philips, M. T. Mądzik, S. V. Amitonov, S. L. de Snoo, M. Russ, N. Kalhor, C. Volk, W. I. L. Lawrie, D. Brousse, L. Tryputen, B. P. Wuetz, A. Sammak, M. Veldhorst, G. Scappucci, and L. M. K. Vandersypen. “Universal control of a six-qubit quantum processor in silicon”. *Nature* **609** (2022), pp. 919–924. DOI: 10.1038/s41586-022-05117-x.

[Pie23] O. Pietx-Casas, E. Raymenants, B. Undseth, L. Vandersypen, G. Scappucci, M. Madzik, S. Philips, S. Amitonov, and A. Sammak. *Temperature scaling of spin qubit performance in Si/SiGe quantum dots*. Bulletin of the American Physical Society. 2023.

[Pin21] J. M. Pino, J. M. Dreiling, C. Figgatt, J. P. Gaebler, S. A. Moses, M. S. Allman, C. H. Baldwin, M. Foss-Feig, D. Hayes, K. Mayer, C. Ryan-Anderson, and B. Neyenhuis. “Demonstration of the trapped-ion quantum CCD computer architecture”. *Nature* **592** (2021), pp. 209–213. DOI: 10.1038/s41586-021-03318-4.

[Pio08] M. Pioro-Ladrière, T. Obata, Y. Tokura, Y.-S. Shin, T. Kubo, K. Yoshida, T. Taniyama, and S. Tarucha. “Electrically driven single-electron spin resonance in a slanting Zeeman field”. *Nature Physics* **4** (2008), pp. 776–779. DOI: 10.1038/nphys1053.

[Pio22] N. Piot, B. Brun, V. Schmitt, S. Zihlmann, V. P. Michal, A. Apra, J. C. Abadillo-Uriel, X. Jehl, B. Bertrand, H. Niebojewski, L. Hutin, M. Vinet, M. Urdampilleta, T. Meunier, Y.-M. Niquet, R. Maurand, and S. D. Franceschi. “A single hole spin with enhanced coherence in natural silicon”. *Nature Nanotechnology* **17** (2022), pp. 1072–1077. DOI: 10.1038/s41565-022-01196-z.

[Pla12] J. J. Pla, K. Y. Tan, J. P. Dehollain, W. H. Lim, J. J. L. Morton, D. N. Jamieson, A. S. Dzurak, and A. Morello. “A single-atom electron spin qubit in silicon”. *Nature* **489** (2012), pp. 541–545. DOI: 10.1038/nature11449.

[Pra22] M. Prathapan, P. Mueller, C. Menolfi, M. Brandli, M. Kossel, P. A. Francese, D. Heim, M. V. Oropallo, A. Ruffino, C. Zota, and T. Morf. “A cryogenic SRAM based arbitrary waveform generator in 14 nm for spin qubit control”. *ESSCIRC 2022- IEEE 48th European Solid State Circuits Conference (ESSCIRC)*. IEEE, 2022. DOI: 10.1109/esscirc55480.2022.9911459.

[Pre16] J. H. Prechtel, A. V. Kuhlmann, J. Houel, A. Ludwig, S. R. Valentin, A. D. Wieck, and R. J. Warburton. “Decoupling a hole spin qubit from the nuclear spins”. *Nature Materials* **15** (2016), pp. 981–986. DOI: 10.1038/nmat4704.

[Pre18] J. Preskill. “Quantum Computing in the NISQ era and beyond”. *Quantum* **2** (2018), p. 79. DOI: 10.22331/q-2018-08-06-79.

[Pri13] V. S. Pribiag, S. Nadj-Perge, S. M. Frolov, J. W. G. van den Berg, I. van Weperen, S. R. Plissard, E. P. A. M. Bakkers, and L. P. Kouwenhoven. “Electrical control of single hole spins in nanowire quantum dots”. *Nature Nanotechnology* **8** (2013), pp. 170–174. DOI: 10.1038/nnano.2013.5.

[QCW09] F. Qassemi, W. A. Coish, and F. K. Wilhelm. “Stationary and Transient Leakage Current in the Pauli Spin Blockade”. *Physical Review Letters* **102** (2009), p. 176806. DOI: 10.1103/physrevlett.102.176806.

[QD22] J. H. Qvist and J. Danon. *Probing details of spin–orbit coupling through Pauli spin blockade*. 2022. DOI: 10.48550/ARXIV.2204.12546.

[RD16] S. Richer and D. DiVincenzo. “Circuit design implementing longitudinal coupling: A scalable scheme for superconducting qubits”. *Physical Review B* **93** (2016), p. 134501. DOI: 10.1103/physrevb.93.134501.

[Rei17] M. Reiher, N. Wiebe, K. M. Svore, D. Wecker, and M. Troyer. “Elucidating reaction mechanisms on quantum computers”. *Proceedings of the National Academy of Sciences* **114** (2017), pp. 7555–7560. DOI: 10.1073/pnas.1619152114.

[Rig] Rigetti. URL: https://qcs.rigetti.com/qpus.

[Rim22] M. Rimbach-Russ, S. G. J. Philips, X. Xue, and L. M. K. Vandersypen. *Simple framework for systematic high-fidelity gate operations*. 2022. DOI: 10.48550/ARXIV.2211.16241.

[RL20] M. S. Rudner and N. H. Lindner. "Band structure engineering and non-equilibrium dynamics in Floquet topological insulators". *Nature Reviews Physics* **2** (2020), pp. 229–244. DOI: 10.1038/s42254-020-0170-z.

[Rol19] M. Rol, F. Battistel, F. Malinowski, C. Bultink, B. Tarasinski, R. Vollmer, N. Haider, N. Muthusubramanian, A. Bruno, B. Terhal, and L. DiCarlo. "Fast, High-Fidelity Conditional-Phase Gate Exploiting Leakage Interference in Weakly Anharmonic Superconducting Qubits". *Physical Review Letters* **123** (2019), p. 120502. DOI: 10.1103/physrevlett.123.120502.

[RT19] R. Ruskov and C. Tahan. "Quantum-limited measurement of spin qubits via curvature couplings to a cavity". *Physical Review B* **99** (2019), p. 245306. DOI: 10.1103/physrevb.99.245306.

[RT21] R. Ruskov and C. Tahan. "Modulated longitudinal gates on encoded spin qubits via curvature couplings to a superconducting cavity". *Physical Review B* **103** (2021), p. 035301. DOI: 10.1103/physrevb.103.035301.

[Rus18] M. Russ, D. M. Zajac, A. J. Sigillito, F. Borjans, J. M. Taylor, J. R. Petta, and G. Burkard. "High-fidelity quantum gates in Si/SiGe double quantum dots". *Physical Review B* **97** (2018), p. 085421. DOI: 10.1103/physrevb.97.085421.

[SAN10] S. Shevchenko, S. Ashhab, and F. Nori. "Landau–Zener–Stückelberg interferometry". *Physics Reports* **492** (2010), pp. 1–30. DOI: 10.1016/j.physrep.2010.03.002.

[Sca15] P. Scarlino, E. Kawakami, D. Ward, D. Savage, M. Lagally, M. Friesen, S. Coppersmith, M. Eriksson, and L. Vandersypen. "Second-Harmonic Coherent Driving of a Spin Qubit in a Si/SiGe Quantum Dot". *Physical Review Letters* **115** (2015), p. 106802. DOI: 10.1103/physrevlett.115.106802.

[Sca20] G. Scappucci, C. Kloeffel, F. A. Zwanenburg, D. Loss, M. Myronov, J.-J. Zhang, S. D. Franceschi, G. Katsaros, and M. Veldhorst. "The germanium quantum information route". *Nature Reviews Materials* **6** (2020), pp. 926–943. DOI: 10.1038/s41578-020-00262-z.

[Sch98] R. J. Schoelkopf, P. Wahlgren, A. A. Kozhevnikov, P. Delsing, and D. E. Prober. "The Radio-Frequency Single-Electron Transistor (RF-SET): A Fast and Ultrasensitive Electrometer". *Science* **280** (1998), pp. 1238–1242. DOI: 10.1126/science.280.5367.1238.

[See21] A. E. Seedhouse, T. Tanttu, R. C. Leon, R. Zhao, K. Y. Tan, B. Hensen, F. E. Hudson, K. M. Itoh, J. Yoneda, C. H. Yang, A. Morello, A. Laucht, S. N. Coppersmith, A. Saraiva, and A. S. Dzurak. “Pauli Blockade in Silicon Quantum Dots with Spin-Orbit Control”. *PRX Quantum* **2** (2021), p. 010303. DOI: 10.1103/prxquantum.2.010303.

[Shi22] S. Shi, B. Xu, K. Zhang, G.-S. Ye, D.-S. Xiang, Y. Liu, J. Wang, D. Su, and L. Li. “High-fidelity photonic quantum logic gate based on near-optimal Rydberg single-photon source”. *Nature Communications* **13** (2022). DOI: 10.1038/s41467-022-32083-9.

[Sho94] P. Shor. “Algorithms for quantum computation: discrete logarithms and factoring”. *Proceedings 35th Annual Symposium on Foundations of Computer Science*. IEEE Comput. Soc. Press, 1994. DOI: 10.1109/sfcs.1994.365700.

[Sho95] P. W. Shor. “Scheme for reducing decoherence in quantum computer memory”. *Physical Review A* **52** (1995), R2493–R2496. DOI: 10.1103/physreva.52.r2493.

[SKL17] M. Serina, C. Kloeffel, and D. Loss. “Long-range interaction between charge and spin qubits in quantum dots”. *Physical Review B* **95** (2017), p. 245422. DOI: 10.1103/physrevb.95.245422.

[SL22] P. Stano and D. Loss. “Review of performance metrics of spin qubits in gated semiconducting nanostructures”. *Nature Reviews Physics* **4** (2022), pp. 672–688. DOI: 10.1038/s42254-022-00484-w.

[Sta21] P. Stano. *Fitting g-factor data measured for a FinFET Si hole*. manuscript in preparation. 2021.

[Ste12] D. Stepanenko, M. Rudner, B. I. Halperin, and D. Loss. “Singlet-triplet splitting in double quantum dots due to spin-orbit and hyperfine interactions”. *Physical Review B* **85** (2012), p. 075416. DOI: 10.1103/physrevb.85.075416.

[Stu06] S. Stufler, P. Machnikowski, P. Ester, M. Bichler, V. M. Axt, T. Kuhn, and A. Zrenner. “Two-photon Rabi oscillations in a single $\mathrm{In}_x\ \mathrm{Ga}_{1-x}\mathrm{As}/\mathrm{GaAs}$ quantum dot”. *Physical Review B* **73** (2006), p. 125304. DOI: 10.1103/physrevb.73.125304.

[Tak16] K. Takeda, J. Kamioka, T. Otsuka, J. Yoneda, T. Nakajima, M. R. Delbecq, S. Amaha, G. Allison, T. Kodera, S. Oda, and S. Tarucha. “A fault-tolerant addressable spin qubit in a natural silicon quantum dot”. *Science Advances* **2** (2016), e1600694. DOI: 10.1126/sciadv.1600694.

[Tan19] T. Tanttu, B. Hensen, K. W. Chan, C. H. Yang, W. W. Huang, M. Fogarty, F. Hudson, K. Itoh, D. Culcer, A. Laucht, A. Morello, and A. Dzurak. "Controlling Spin-Orbit Interactions in Silicon Quantum Dots Using Magnetic Field Direction". *Physical Review X* **9** (2019), p. 021028. DOI: `10.1103/physrevx.9.021028`.

[Und22] B. Undseth, X. Xue, M. Mehmandoost, M. Russ, P. T. Eendebak, N. Samkharadze, A. Sammak, V. V. Dobrovitski, G. Scappucci, and L. M. K. Vandersypen. *Nonlinear response and crosstalk of electrically driven silicon spin qubits*. 2022. DOI: `10.48550/ARXIV.2205.04905`.

[Vad69] L. L. Vadasz, A. S. Grove, T. A. Rowe, and G. E. Moore. "Silicon-gate technology". *IEEE Spectrum* **6** (1969), pp. 28–35.

[Van17] L. M. K. Vandersypen, H. Bluhm, J. S. Clarke, A. S. Dzurak, R. Ishihara, A. Morello, D. J. Reilly, L. R. Schreiber, and M. Veldhorst. "Interfacing spin qubits in quantum dots and donors-hot, dense, and coherent". *npj Quantum Information* **3** (2017), p. 34. DOI: `10.1038/s41534-017-0038-y`.

[VE19] L. M. K. Vandersypen and M. A. Eriksson. "Quantum computing with semiconductor spins". *Physics Today* **72** (2019), pp. 38–45. DOI: `10.1063/pt.3.4270`.

[Vel14] M. Veldhorst, J. C. C. Hwang, C. H. Yang, A. W. Leenstra, B. de Ronde, J. P. Dehollain, J. T. Muhonen, F. E. Hudson, K. M. Itoh, A. Morello, and A. S. Dzurak. "An addressable quantum dot qubit with fault-tolerant control-fidelity". *Nature Nanotechnology* **9** (2014), pp. 981–985. DOI: `10.1038/nnano.2014.216`.

[Vel15] M. Veldhorst, C. H. Yang, J. C. C. Hwang, W. Huang, J. P. Dehollain, J. T. Muhonen, S. Simmons, A. Laucht, F. E. Hudson, K. M. Itoh, A. Morello, and A. S. Dzurak. "A two-qubit logic gate in silicon". *Nature* **526** (2015), pp. 410–414. DOI: `10.1038/nature15263`.

[Vel17] M. Veldhorst, H. G. J. Eenink, C. H. Yang, and A. S. Dzurak. "Silicon CMOS architecture for a spin-based quantum computer". *Nature Communications* **8** (2017), p. 1766. DOI: `10.1038/s41467-017-01905-6`.

[Ven18] B. Venitucci, L. Bourdet, D. Pouzada, and Y.-M. Niquet. "Electrical manipulation of semiconductor spin qubits within the g-matrix formalism". *Physical Review B* **98** (2018), p. 155319. DOI: `10.1103/physrevb.98.155319`.

[Vig23] F. Vigneau, F. Fedele, A. Chatterjee, D. Reilly, F. Kuemmeth, M. F. Gonzalez-Zalba, E. Laird, and N. Ares. "Probing quantum devices with radio-frequency reflectometry". *Applied Physics Reviews* **10** (2023). DOI: `10.1063/5.0088229`.

[Voi15] B. Voisin, R. Maurand, S. Barraud, M. Vinet, X. Jehl, M. Sanquer, J. Renard, and S. D. Franceschi. “Electrical Control of g-Factor in a Few-Hole Silicon Nanowire MOSFET”. *Nano Letters* **16** (2015), pp. 88–92. DOI: `10.1021/acs.nanolett.5b02920`.

[Wan21] Z. Wang, E. Marcellina, A. R. Hamilton, J. H. Cullen, S. Rogge, J. Salfi, and D. Culcer. “Optimal operation points for ultrafast, highly coherent Ge hole spin-orbit qubits”. *npj Quantum Information* **7** (2021). DOI: `10.1038/s41534-021-00386-2`.

[Wan22a] C.-A. Wang, G. Scappucci, M. Veldhorst, and M. Russ. *Modelling of planar germanium hole qubits in electric and magnetic fields*. 2022. DOI: `10.48550/ARXIV.2208.04795`.

[Wan22b] K. Wang, G. Xu, F. Gao, H. Liu, R.-L. Ma, X. Zhang, Z. Wang, G. Cao, T. Wang, J.-J. Zhang, D. Culcer, X. Hu, H.-W. Jiang, H.-O. Li, G.-C. Guo, and G.-P. Guo. “Ultrafast coherent control of a hole spin qubit in a germanium quantum dot”. *Nature Communications* **13** (2022), p. 206. DOI: `10.1038/s41467-021-27880-7`.

[Wat16] H. Watzinger, C. Kloeffel, L. Vukušić, M. D. Rossell, V. Sessi, J. Kukučka, R. Kirchschlager, E. Lausecker, A. Truhlar, M. Glaser, A. Rastelli, A. Fuhrer, D. Loss, and G. Katsaros. “Heavy-Hole States in Germanium Hut Wires”. *Nano Letters* **16** (2016), pp. 6879–6885. DOI: `10.1021/acs.nanolett.6b02715`.

[Wat18a] T. F. Watson, S. G. J. Philips, E. Kawakami, D. R. Ward, P. Scarlino, M. Veldhorst, D. E. Savage, M. G. Lagally, M. Friesen, S. N. Coppersmith, M. A. Eriksson, and L. M. K. Vandersypen. “A programmable two-qubit quantum processor in silicon”. *Nature* **555** (2018), pp. 633–637. DOI: `10.1038/nature25766`.

[Wat18b] H. Watzinger, J. Kukučka, L. Vukušić, F. Gao, T. Wang, F. Schäffler, J.-J. Zhang, and G. Katsaros. “A germanium hole spin qubit”. *Nature Communications* **9** (2018). DOI: `10.1038/s41467-018-06418-4`.

[Wes19] A. West, B. Hensen, A. Jouan, T. Tanttu, C.-H. Yang, A. Rossi, M. F. Gonzalez-Zalba, F. Hudson, A. Morello, D. J. Reilly, and A. S. Dzurak. “Gate-based single-shot readout of spins in silicon”. *Nature Nanotechnology* **14** (2019), pp. 437–441. DOI: `10.1038/s41565-019-0400-7`.

[Wie02] W. G. van der Wiel, S. D. Franceschi, J. M. Elzerman, T. Fujisawa, S. Tarucha, and L. P. Kouwenhoven. “Electron transport through double quantum dots”. *Reviews of Modern Physics* **75** (2002), pp. 1–22. DOI: `10.1103/revmodphys.75.1`.

[Win03] R. Winkler. *Spin—Orbit Coupling Effects in Two-Dimensional Electron and Hole Systems*. Springer Berlin Heidelberg, 2003. doi: 10.1007/b13586.

[Wu21] Y. Wu, W.-S. Bao, S. Cao, F. Chen, M.-C. Chen, X. Chen, T.-H. Chung, H. Deng, Y. Du, D. Fan, M. Gong, C. Guo, C. Guo, S. Guo, L. Han, L. Hong, H.-L. Huang, Y.-H. Huo, L. Li, N. Li, S. Li, Y. Li, F. Liang, C. Lin, J. Lin, H. Qian, D. Qiao, H. Rong, H. Su, L. Sun, L. Wang, S. Wang, D. Wu, Y. Xu, K. Yan, W. Yang, Y. Yang, Y. Ye, J. Yin, C. Ying, J. Yu, C. Zha, C. Zhang, H. Zhang, K. Zhang, Y. Zhang, H. Zhao, Y. Zhao, L. Zhou, Q. Zhu, C.-Y. Lu, C.-Z. Peng, X. Zhu, and J.-W. Pan. "Strong Quantum Computational Advantage Using a Superconducting Quantum Processor". *Physical Review Letters* **127** (2021), p. 180501. doi: 10.1103/physrevlett.127.180501.

[Xue21] X. Xue, B. Patra, J. P. G. van Dijk, N. Samkharadze, S. Subramanian, A. Corna, B. P. Wuetz, C. Jeon, F. Sheikh, E. Juarez-Hernandez, B. P. Esparza, H. Rampurawala, B. Carlton, S. Ravikumar, C. Nieva, S. Kim, H.-J. Lee, A. Sammak, G. Scappucci, M. Veldhorst, F. Sebastiano, M. Babaie, S. Pellerano, E. Charbon, and L. M. K. Vandersypen. "CMOS-based cryogenic control of silicon quantum circuits". *Nature* **593** (2021), pp. 205–210. doi: 10.1038/s41586-021-03469-4.

[Xue22] X. Xue, M. Russ, N. Samkharadze, B. Undseth, A. Sammak, G. Scappucci, and L. M. K. Vandersypen. "Quantum logic with spin qubits crossing the surface code threshold". *Nature* **601** (2022), pp. 343–347. doi: 10.1038/s41586-021-04273-w.

[Yan19] C. H. Yang, K. W. Chan, R. Harper, W. Huang, T. Evans, J. C. C. Hwang, B. Hensen, A. Laucht, T. Tanttu, F. E. Hudson, S. T. Flammia, K. M. Itoh, A. Morello, S. D. Bartlett, and A. S. Dzurak. "Silicon qubit fidelities approaching incoherent noise limits via pulse engineering". *Nature Electronics* **2** (2019), pp. 151–158. doi: 10.1038/s41928-019-0234-1.

[Yan20] C. H. Yang, R. C. C. Leon, J. C. C. Hwang, A. Saraiva, T. Tanttu, W. Huang, J. C. Lemyre, K. W. Chan, K. Y. Tan, F. E. Hudson, K. M. Itoh, A. Morello, M. Pioro-Ladrière, A. Laucht, and A. S. Dzurak. "Operation of a silicon quantum processor unit cell above one kelvin". *Nature* **580** (2020), pp. 350–354. doi: 10.1038/s41586-020-2171-6.

[Yon14] J. Yoneda, T. Otsuka, T. Nakajima, T. Takakura, T. Obata, M. Pioro-Ladrière, H. Lu, C. Palmstrøm, A. Gossard, and S. Tarucha. "Fast Electrical Control of Single Electron Spins in Quantum Dots with Vanishing Influence from Nuclear Spins". *Physical Review Letters* **113** (2014), p. 267601. doi: 10.1103/physrevlett.113.267601.

[Yon17] J. Yoneda, K. Takeda, T. Otsuka, T. Nakajima, M. R. Delbecq, G. Allison, T. Honda, T. Kodera, S. Oda, Y. Hoshi, N. Usami, K. M. Itoh, and S. Tarucha. "A quantum-dot spin qubit with coherence limited by charge noise and fidelity higher than 99.9%". *Nature Nanotechnology* **13** (2017), pp. 102–106. DOI: `10.1038/s41565-017-0014-x`.

[Yon21] J. Yoneda, W. Huang, M. Feng, C. H. Yang, K. W. Chan, T. Tanttu, W. Gilbert, R. C. C. Leon, F. E. Hudson, K. M. Itoh, A. Morello, S. D. Bartlett, A. Laucht, A. Saraiva, and A. S. Dzurak. "Coherent spin qubit transport in silicon". *Nature Communications* **12** (2021). DOI: `10.1038/s41467-021-24371-7`.

[Yu23] C. X. Yu, S. Zihlmann, J. C. Abadillo-Uriel, V. P. Michal, N. Rambal, H. Niebojewski, T. Bedecarrats, M. Vinet, É. Dumur, M. Filippone, B. Bertrand, S. D. Franceschi, Y.-M. Niquet, and R. Maurand. "Strong coupling between a photon and a hole spin in silicon". *Nature Nanotechnology* (2023). DOI: `10.1038/s41565-023-01332-3`.

[Zaj18] D. M. Zajac, A. J. Sigillito, M. Russ, F. Borjans, J. M. Taylor, G. Burkard, and J. R. Petta. "Resonantly driven CNOT gate for electron spins". *Science* **359** (2018), pp. 439–442. DOI: `10.1126/science.aao5965`.

[Zar17] A. Zarassi, Z. Su, J. Danon, J. Schwenderling, M. Hocevar, B. M. Nguyen, J. Yoo, S. A. Dayeh, and S. M. Frolov. "Magnetic field evolution of spin blockade in Ge/Si nanowire double quantum dots". *Physical Review B* **95** (2017), p. 155416. DOI: `10.1103/physrevb.95.155416`.

[Zen19] J. Zeng, C. H. Yang, A. S. Dzurak, and E. Barnes. "Geometric formalism for constructing arbitrary single-qubit dynamically corrected gates". *Physical Review A* **99** (2019), p. 052321. DOI: `10.1103/physreva.99.052321`.

[Zha19] R. Zhao, T. Tanttu, K. Y. Tan, B. Hensen, K. W. Chan, J. C. C. Hwang, R. C. C. Leon, C. H. Yang, W. Gilbert, F. E. Hudson, K. M. Itoh, A. A. Kiselev, T. D. Ladd, A. Morello, A. Laucht, and A. S. Dzurak. "Single-spin qubits in isotopically enriched silicon at low magnetic field". *Nature Communications* **10** (2019). DOI: `10.1038/s41467-019-13416-7`.

[Zha21] T. Zhang, H. Liu, F. Gao, G. Xu, K. Wang, X. Zhang, G. Cao, T. Wang, J. Zhang, X. Hu, H.-O. Li, and G.-P. Guo. "Anisotropic g-Factor and Spin–Orbit Field in a Germanium Hut Wire Double Quantum Dot". *Nano Letters* **21** (2021), pp. 3835–3842. DOI: `10.1021/acs.nanolett.1c00263`.

[ZhI] ZhInst. *MFLI User Manual.* URL: `https://docs.zhinst.com/pdf/ziMFLI_UserManual.pdf`.

[Zum04] D. M. Zumbühl, C. M. Marcus, M. P. Hanson, and A. C. Gossard. "Cotunneling Spectroscopy in Few-Electron Quantum Dots". *Physical Review Letters* **93** (2004), p. 256801. DOI: 10.1103/physrevlett.93.256801.

[Zwa13] F. A. Zwanenburg, A. S. Dzurak, A. Morello, M. Y. Simmons, L. C. L. Hollenberg, G. Klimeck, S. Rogge, S. N. Coppersmith, and M. A. Eriksson. "Silicon quantum electronics". *Reviews of Modern Physics* **85** (2013), pp. 961–1019. DOI: 10.1103/revmodphys.85.961.

[Zwe21] A. M. J. Zwerver, T. Krähenmann, T. F. Watson, L. Lampert, H. C. George, R. Pillarisetty, S. A. Bojarski, P. Amin, S. V. Amitonov, J. M. Boter, R. Caudillo, D. Corras-Serrano, J. P. Dehollain, G. Droulers, E. M. Henry, R. Kotlyar, M. Lodari, F. Luthi, D. J. Michalak, B. K. Mueller, S. Neyens, J. Roberts, N. Samkharadze, G. Zheng, O. K. Zietz, G. Scappucci, M. Veldhorst, L. M. K. Vandersypen, and J. S. Clarke. "Qubits made by advanced semiconductor manufacturing" (2021). DOI: 10.48550/ARXIV.2101.12650.

[Zwe22] A. M. J. Zwerver, T. Krähenmann, T. F. Watson, L. Lampert, H. C. George, R. Pillarisetty, S. A. Bojarski, P. Amin, S. V. Amitonov, J. M. Boter, R. Caudillo, D. Correas-Serrano, J. P. Dehollain, G. Droulers, E. M. Henry, R. Kotlyar, M. Lodari, F. Lüthi, D. J. Michalak, B. K. Mueller, S. Neyens, J. Roberts, N. Samkharadze, G. Zheng, O. K. Zietz, G. Scappucci, M. Veldhorst, L. M. K. Vandersypen, and J. S. Clarke. "Qubits made by advanced semiconductor manufacturing". *Nature Electronics* **5** (2022), pp. 184–190. DOI: 10.1038/s41928-022-00727-9.

A

APPENDIX

A.1. FABRICATION

Parts of this appendix section have been published in the supplementary material of S. Geyer *et al.*, Self-aligned gates for scalable silicon quantum computing, Applied Physics Letters **118**, 104004 (2021), doi:10.1063/5.0036520

A.1.1. ELECTRICAL ISOLATION OF THE TWO GATE LAYERS

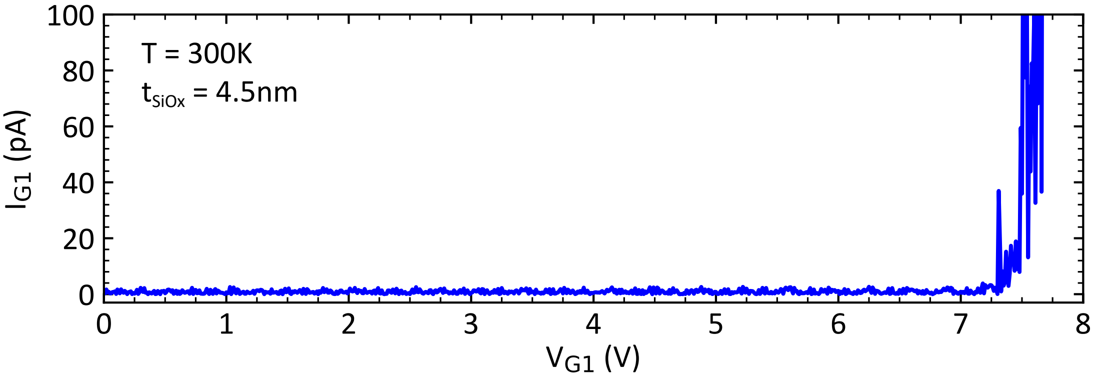

Fig. A.1.: The two gate layers are electrically isolated by a thin SiO_x layer of $t_{SiOx} \simeq 4.5$ nm thickness, measured by ellipsometry. The oxide is deposited by means of atomic layer deposition, allowing for a monolayer control of t_{SiOx}. A typical oxide breakdown curve is presented in the above figure, where the current flowing between the two gate layers is plotted while sweeping the voltage difference between them. Here, oxide breakdown occurs for a voltage difference >7 V, corresponding to a breakdown field strength of 16 MV/cm. While the measurement is performed at room temperature, impurity freeze-out at cryogenic temperatures will shift the breakdown point to higher voltages.

A.1.2. DEVICE CHARACTERISATION MEASUREMENT

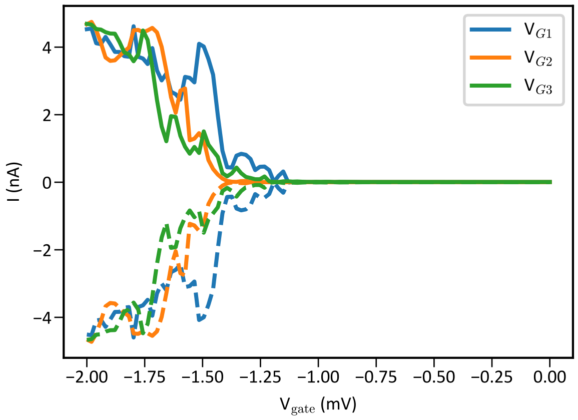

Fig. A.2.: Nano gate pinch-off test. For this test all nano gate voltages are chosen such that the current through the channel is saturated, typically $V \sim 2$ V. Then the gates are individually ramped down and the current at source (solid curve) and drain (dashed line) are measured to observe pinching of the channel. In the displayed measurement all nano gates show similar pinch-off voltages at ~ 20 mK, indicating a good device.

A.1.3. Device overview

Tab. A.1.: Device parameters for all devices used throughout this thesis using the gate nomenclature for DQD accumulation. The dimensions (dim.) of the devices are characterised by the barrier gate length l_B, plunger gate length l_P and fin width w. They are estimated from the lithography dimensions l, dx and w, the thickness of the gate oxide of the second gate layer and SEM/TEM analysis of co-fabricated devices.

device	estimated dim. (nm)			device ID	lithography dim. (nm)		
	l_B	l_P	w		l	dx	w
A	25	15	20	T6A_c5C	20	30	20
B	35	15	25	T6A_c6E	30	30	25
C	20	20	10	T6A_c7A	15	35	10
D	25	15	25	T7D_c5H	20	30	25
N	different gate layout			T3B_c1B	10	25	10

A.2. Quantum dot characterisation

Parts of this appendix section have been published in the supplementary material of S. Geyer *et al.*, Self-aligned gates for scalable silicon quantum computing, Applied Physics Letters **118**, 104004 (2021), doi:10.1063/5.0036520

A.2.1. Single- and double dot operation regimes

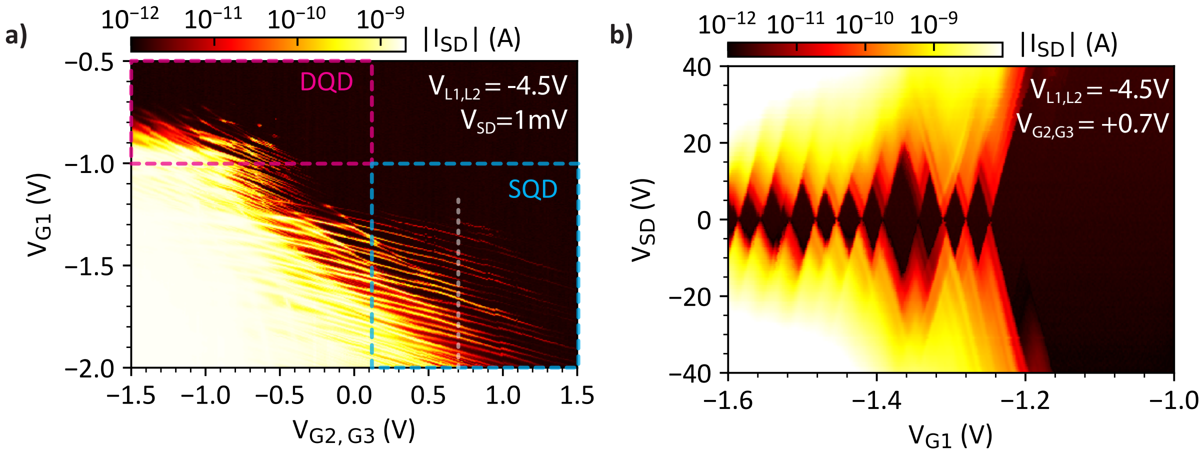

Fig. A.3.: The device gate layout allows for a dual-mode operation as single QD (SQD) or DQD. In (a) we present a map of source-drain current I_{SD} as a function of $V_{G2,G3}$ (same voltage applied to both gates) and V_{G1} (we use the generic nomenclature G1-G3 for the nano gates in SQD operation mode) for device A. The SQD regime is located in the bottom right corner of this map: a positive voltage applied to gates G2 & G3 induces tunnel barriers to source and drain reservoirs, and the voltage applied to gate G1 forms the dot and controls its occupancy. In this regime Coulomb oscillations are observed along the V_{G1} axis. A single dot charge stability diagram for $V_{G2,G3} = +0.7\,V$, marked by the white dashed line in (a), is shown in (b). Clear Coulomb diamonds are observed and the their closing at zero bias suggests the formation of a SQD. The less positive $V_{G2,G3}$ the more transparent the barriers to source and drain become. In the top left corner of (a) the device is operated as a DQD. Gates G2 & G3 are at negative voltages and accumulate holes, while gate G1 is at more positive voltages and creates the inter-dot tunnel barrier.

A.2.2. Tuning of the inter-dot tunnel coupling with gate B

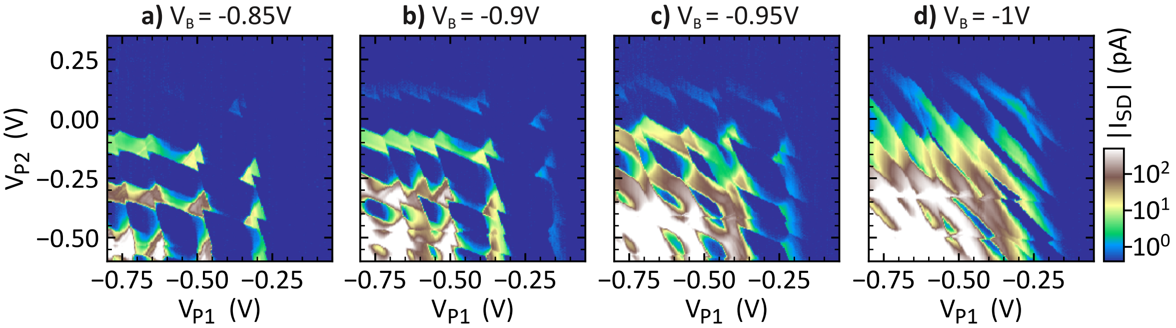

Fig. A.4.: Charge stability diagrams of device A for different values of voltage applied to the central nano gate B. By decreasing V_B the inter-dot tunnel coupling is increased, as evident from the transition from a double quantum dot (a) to a more single-dot-like configuration (d). Data were taken at $V_{SD} = -5\,\text{mV}$ and $V_{L1,L2} = -4.5\,\text{V}$.

A.2.3. Charge stability diagram of a similar device

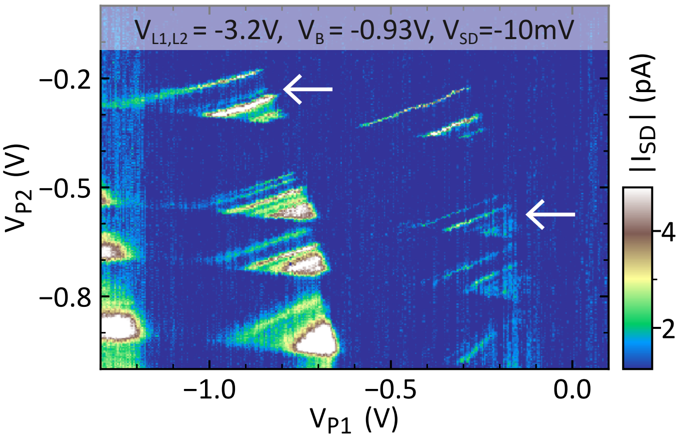

Fig. A.5.: Double dot charge stability diagram of device B, which is similar to the one discussed for device A in chapter 3. While the devices share a common plunger gate length of ≃ 15 nm, they differ in the inter-dot barrier length: here ≃ 35 nm instead of ≃ 25 nm. The wider barrier leads to a current reduction. The pairs of bias triangles are arranged in a very similar way to Fig. 3.1 (a) of the main text. Again, signatures of Pauli spin blockade are observed for the bias triangles indicated by the white arrows. The high degree of similarities between the data presented in here and the main article demonstrates that reproducible double dot formation is achieved.

A.2.4. SPIN BLOCKADE FOR $(1,1) \leftrightarrow (2,0)$ CHARGE TRANSITION

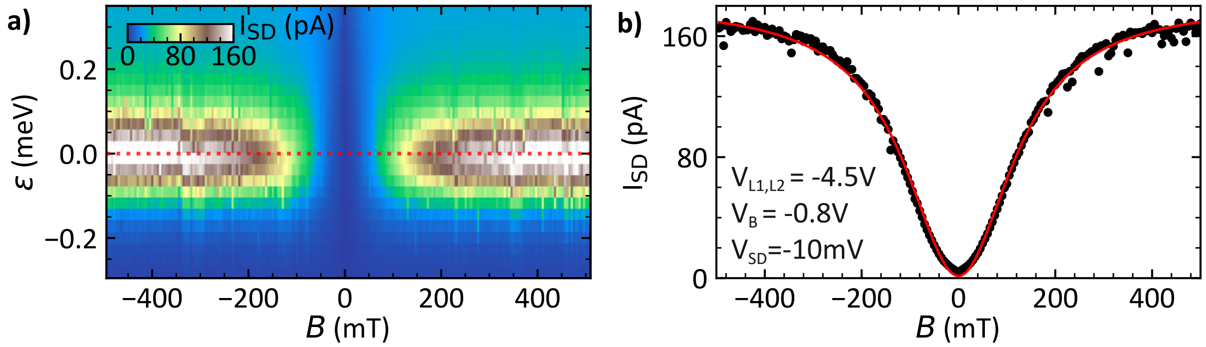

Fig. A.6.: Analogue to Fig. 3.2 of the main text for the pair of bias triangles highlighted by a solid magenta circle in Fig. 3.1 (a) of the main article, corresponding to $(1,1) \leftrightarrow (2,0)$ charge transitions. As expected current suppression due to spin-conserved tunnelling is now observed for negative V_{SD}, i.e. the opposite bias direction compared to the data presented in the main article. A cut along B at zero detuning reveals again a dip in the leakage current, indicating that spin blockade lifting is dominated by SOI. This dip has a Lorentzian lineshape with FWHM = 270 mT.

A.2.5. PSB LEAKAGE CURRENT LINESHAPES DEVIATING FROM LORENTZIAN

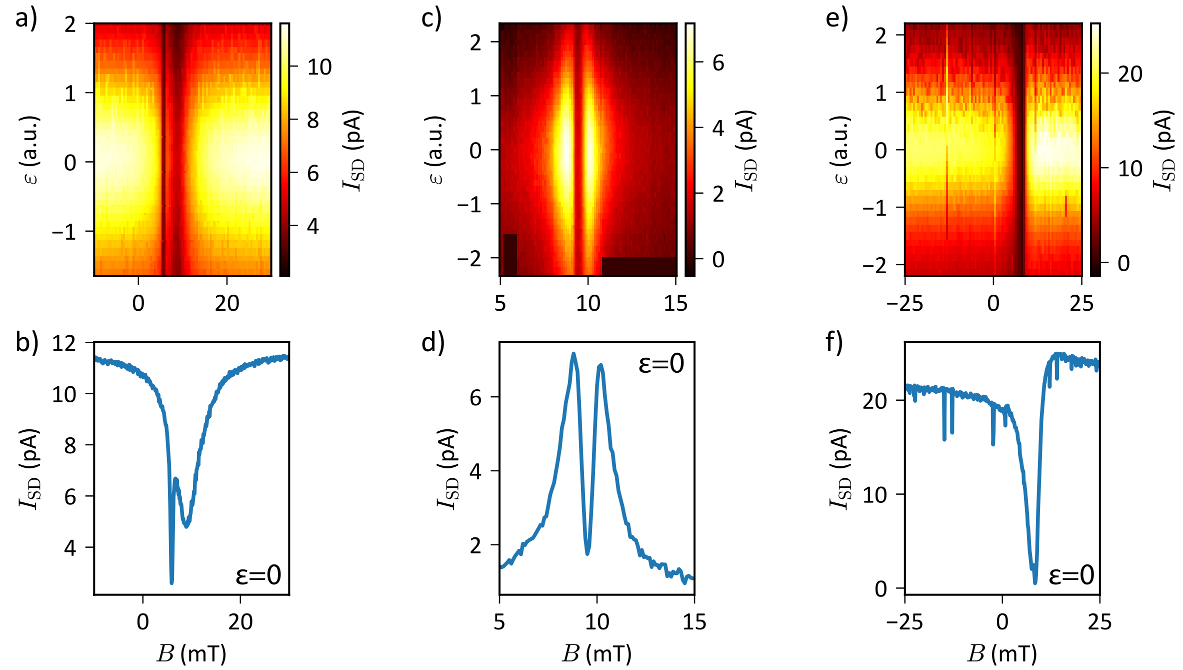

Fig. A.7.: **PSB leakage current.** Various combinations of magnetic field orientation and $-730 \leq V_B \leq -710$ mV lead to PSB current suppression in device A with lineshapes different from the Lorentzians observed in the main text: a),b) two Lorentzian dips at centred at different fields and with different amplitude and FWHM; c),d) a double peak; e),f) a asymmetric single dip. These features might originate from hyperfine interaction or spin-flip co-tunnelling processes [DN09] and require further investigation and modelling. Note that the offset in magnetic field (approximately 10 mT) probably originates from trapped flux in the magnet and might not be a real feature of the device.

A.3. Hot hole spin qubits

Parts of this appendix section have been published in the supplementary material of L. C. Camenzind, S. Geyer *et al.*, A hole spin qubit in a fin field-effect transistor above 4 kelvin, Nature Electronics **5**, 178-183 (2022), doi:10.1038/s41928-022-00722-0

A.3.1. Experimental setup

In this section, differences of the measurement setup in chapter 4 as compared to the improved setup presented in section 4.1 are explained. A schematic of the circuitry to operate and measure the qubits is shown in Fig. A.8.

We used a square-wave signal instead of a trapezoid pulse to drive the system from Pauli spin blockade into Coulomb blockade (see Fig. 4.2 d). Further, the MW signal was generated with a Keysight E8267D vector signal generator, which had a smaller IQ input bandwidth compared to the SGS100A and caused ringing of the MW burst. The square-wave and MW signals were combined with a Mini-Circuits ZC2PD-5R264-S+ signal combiner, introducing an additional attenuation of 3db. The output of a Signal Recovery 7265 lock-in amplifier was connected to the pulse modulation (PM) input of the VSG to chop the MW signal at a frequency of 89.17 Hz. The transport signal from the sample was demodulated with the lock-in amplifier.

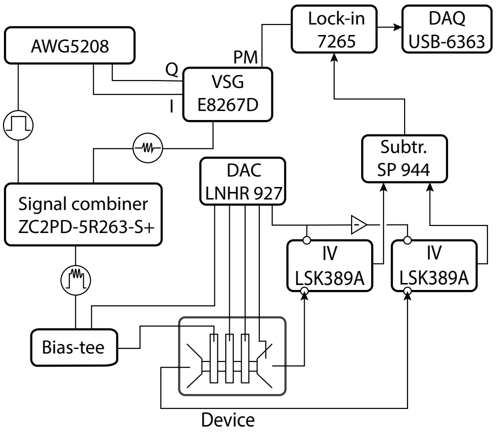

Fig. A.8.: **Experimental setup.** Schematic circuit of the measurement and control electronics.

In this setup the maximum current expected upon completely lifting PSB by applying a π-rotation pulse to either of the spins is $I_{max} = e\Gamma$ where Γ is the repetition rate of the pulse cycle and e the elementary charge. In the example shown in Fig. 4.2h, $I_{max} \sim 200\,\mathrm{fA}$ was found. This agrees very well with the expectation for a total pulse cycle of $\sim 800\,\mathrm{ns}$ ($\Gamma = 1.25\,\mathrm{MHz}$) used for this measurement. Our method of readout only allows us to determine the statistical average of events and does not allow for single-shot readout.

This transport-based readout requires a high repetition rate (∼1 MHz), such that our signal can be distinguished from the noise. Therefore the duration of the manipulation stage is limited and hence the number of gate operations in a randomised benchmarking experiment (see Fig. 4.4) or decoupling pulses in a CPMG experiment (see Fig. 4.5) is limited. This limitation becomes more severe as temperature increases, since the readout contrast degrades (see appendix A.3.8) and noise increases.

A.3.2. QUANTUM DOT OCCUPANCIES

Our transport-based measurement scheme does not allow us to determine the exact hole occupation number. In Fig. A.9 a the first observable pairs of bias triangles are shown. Even at a high source-drain voltage of $V_{\mathrm{SD}} = 100\,\mathrm{mV}$ no additional bias triangles appear (see Fig. A.9 c). PSB is observed for the two pairs of bias triangles indicated by the blue and green dot for opposite bias direction. We assign these triangles to (1,1) - (0,2)/(2,0) charge transitions. Here, (m, n) denotes the effective number of holes in the DQD, while the absolute number of holes in the DQD is $(m + m_0, n + n_0)$.

We were able to form and operate qubits at both transitions and found similar operation speeds as well as coherence times. In this work, we only discuss the qubits energised and measured at the green transition.

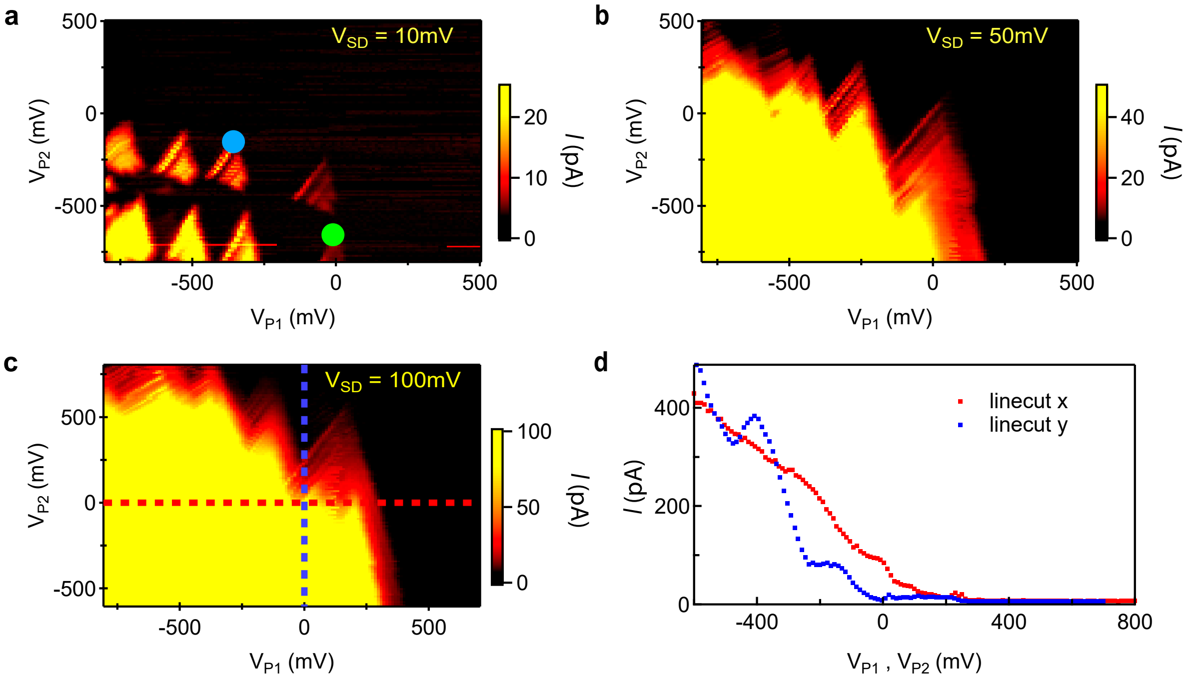

Fig. A.9.: **Double dot charge occupation.** Charge stability diagrams of device B for $V_{\mathrm{SD}} = 10\,\mathrm{mV}$ **a**, $V_{\mathrm{SD}} = 50\,\mathrm{mV}$ **b** and $V_{\mathrm{SD}} = 100\,\mathrm{mV}$ **c**. No additional bias triangles become visible when increasing V_{SD} from 10 mV to 100 mV. The line-cuts in **d** are taken along the indicated lines in **c**. The blue and green dot in **a** indicate the transition showing spin blockade for opposite bias direction. The qubits discussed in the main text were energised at the green transition.

A.3.3. Microwave power calibration

The attenuation of the MW signal from the MW signal generator to the qubit is a function of frequency, caused by e.g. impedance mismatches and resonances due to the PCB or bonding wires. Therefore, the MW power that arrives at the qubit has to be calibrated. Because the Rabi frequency f_{Rabi} depends on the MW power (see Fig. 4.2 i), this calibration is necessary to compare the Rabi frequency at different Larmor frequencies.

To calibrate the MW power, the qubit's response to a continuous wave excitation is measured. In the limit of a large dot-reservoir tunnel coupling in comparison to the MW signal frequency [Now07; Fro21b], the $(1,1)-(0,2)$ charge transition at the baseline of the bias-triangle (see inset of Fig. A.10, Fig. A.14 a and Fig. 4.2 c) is broadened by the MW power due to photon-assisted tunnelling (PAT). The broadening $\Delta\varepsilon$ is measured along the detuning axis and then converted into a voltage $eA_{\mathrm{MW}} = \Delta\varepsilon$ which drops over the inter-dot tunnel barrier [Nad10a] (see Fig. A.10). This broadening of the transition depends on the MW signal that effectively arrives at the qubit. Therefore, the measured MW amplitude A_{MW} permits a calibration and thus a comparison of the Rabi frequency at different Larmor frequencies for the same driving strength A_{MW} (see Fig. 4.2 i).

The calibrated voltage amplitude A_{MW} allows us to estimate the electric field $|E_{\mathrm{MW}}|$ at the QDs, necessary in order to estimate the spin-orbit length l_{SO} (see appendix A.3.7).

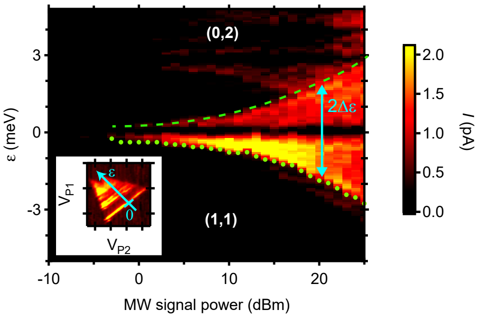

Fig. A.10.: **Example of calibrating A_{MW}.** Due to a capacitive coupling to the QD, the zero-detuning line is broadened upon applying a MW signal on the left plunger gate P1. This broadening $2\Delta\varepsilon$ (blue) allows A_{MW} to be calculated. A_{MW} is the MW-induced voltage drop over the inter-dot tunnel barrier as $eA_{\mathrm{MW}} = \Delta\varepsilon$. A larger amplitude, here given as the power of the MW signal at the signal generator output, results in an increase of the transition broadening $\Delta\varepsilon$. The green data points are values of $\Delta\varepsilon$ extracted using a signal threshold algorithm. The inset shows the bias triangle and the axis used to define the detuning ε (blue axis).

A.3.4. RABI AND RAMSEY EXPERIMENTS AT DIFFERENT TEMPERATURES

In Fig. A.11 we show Rabi and Ramsey measurements at T = 1.5, 3 and 4.2 K.

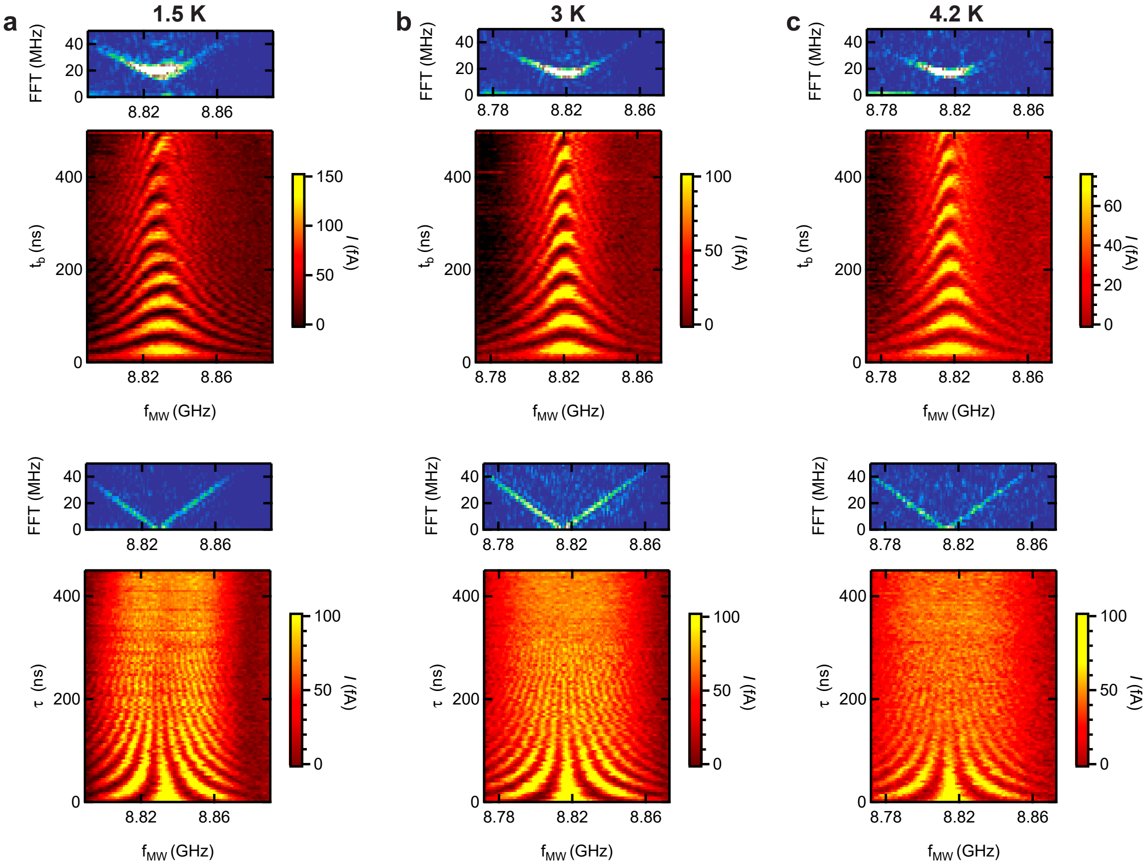

Fig. A.11.: **Coherent qubit control at different temperatures.** Comparison of Rabi chevron patterns and Ramsey fringes at **a** 1.5, **b** 3 and **c** 4.2 K for Q2. The FFTs show the quadratic dependence of f_{Rabi} on the frequency detuning in the Rabi measurements and a linear dependence on the frequency detuning in the Ramsey experiments.

A.3.5. FAST RABI OSCILLATIONS

Hole spin qubits allow for fast all-electrical spin rotations. In our experiments, we observed Rabi frequencies as high as $f_{\mathrm{Rabi}} = 147\,\mathrm{MHz}$ for Q1.

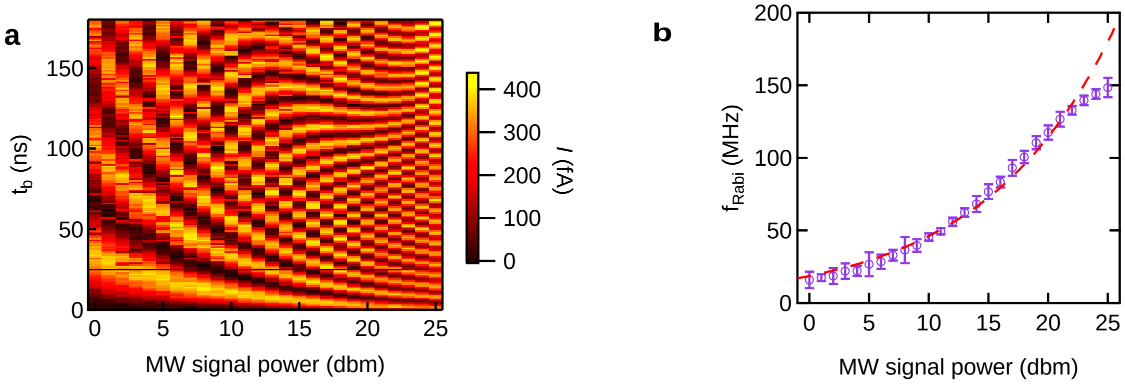

Fig. A.12.: **Fast Rabi oscillations a** Rabi oscillations at $T = 1.5\,\mathrm{K}$ and $f_{\mathrm{L}} \sim 8\,\mathrm{GHz}$ as a function of MW signal power. **b** The Rabi frequency extracted by a FFT-analysis of the data in **a** shows the maximum $f_{\mathrm{Rabi}} = 147\,\mathrm{MHz}$ at 25 dbm. f_{Rabi} follows a square-root dependence on the the MW signal power at the VS output (red dashed line). The MW signal power is quadratically related to the calibrated MW voltage A_{MW}. Therefore, this dependence agrees very well with the linear dependence of f_{Rabi} on A_{MW} in Fig. 4.2 i. The observed saturation at higher power could be an indication of an anharmonic confinement potential [Fro21b; Yon14; Tak16].

A.3.6. ESTIMATE OF EFFECTIVE DOT SIZES

In this section we estimate the effective dot size. We assign Q1/Q2 to the left/right QD, i.e. Q1 is closer to the MW drive applied to the left plunger gate P1. This assignment is based on the fact that Q1 has the higher Rabi frequency f_{Rabi} and larger g-factor tunability with the square pulse amplitude A_{p} (see Fig. 4.2 g).

The effective dot size can be estimated by $l_{\mathrm{dot}} = \hbar/\sqrt{(m^*\Delta)}$, where m^* denotes the effective mass and Δ the orbital energy. Assuming a weak exchange interaction, Δ is given by the single-dot singlet-triplet splitting Δ_{ST}, such that $\Delta_{\mathrm{Q1}} = 5.3\,\mathrm{meV}$ and $\Delta_{\mathrm{Q2}} = 3.3\,\mathrm{meV}$. Ref. [KRL18] states values for the effective mass for holes in silicon nanowires ranging from $0.184\,m_0$ to $0.794\,m_0$, depending on the nanowire orientation. Since the exact shape and orientation of our hole wave function is unknown, and also strain is neglected in Ref. [KRL18], we assume an average effective mass of $m^* = 0.45\,m_0$ to extract $l_{\mathrm{dot}}^{\mathrm{Q1}} \approx 6\,\mathrm{nm}$ and $l_{\mathrm{dot}}^{\mathrm{Q2}} \approx 7\,\mathrm{nm}$. The estimated size of the QDs compare well with the plunger gate length of $\sim 15\,\mathrm{nm}$.

A.3.7. ESTIMATE OF SPIN-ORBIT LENGTH

The strength of the spin-orbit interaction can be characterised by the spin-orbit length l_{SO}, where $\pi l_{\mathrm{SO}}/2$ describes the distance a hole has to be displaced to induce a spin-orbit mediated spin flip. We estimate l_{SO} using the following equation for spin-orbit mediated

EDSR [GBL06; Now07]:

$$l_{\mathrm{SO}} = \frac{g\mu_B}{2hf_{\mathrm{Rabi}}}\left(2|B_{\mathrm{ext}}|\frac{\hbar^2}{\Delta^2 m^*}e|E_{\mathrm{MW}}|\right), \tag{A.1}$$

where B_{ext} denotes the external magnetic field, Δ the orbital energy of the QD hosting the qubit, $|E_{\mathrm{MW}}|$ the electric field strength of the MW driving field, m^* the effective mass of the charge carrier and g is the Landé g-factor in the direction of B_{ext}. Here, we assume that EDSR is driven by a periodic displacement of the wave function as a whole without modulating the spin splitting (sometimes referred to as iso-Zeeman EDSR [Cri18]). We use an effective mass $m^* = 0.45m_0$ (see appendix A.3.6).

To estimate the electric field strength $|E_{\mathrm{MW}}|$ at the location of the qubits, the MW amplitude A_{MW} extracted from PAT measurements is used (see appendix A.3.3). A_{MW} drops across the inter-dot tunnel barrier, which we estimate by the distance between the two QDs $d_{\mathrm{dd}} \sim 45 - 60\,\mathrm{nm}$ (see Fig. 4.2 b) [Nad10a]. Consequently, $|E^{\mathrm{Q1}}_{\mathrm{MW}}| = A_{\mathrm{MW}}/d_{dd}$ is the electric field in Q1, the qubit below gate P1. We assume that $|E^{\mathrm{Q2}}_{\mathrm{MW}}|$ is smaller than $|E^{\mathrm{Q1}}_{\mathrm{MW}}|$ by a factor of 4 (for $d_{\mathrm{dd}} = 45\,\mathrm{nm}$) to 6 (for $d_{\mathrm{dd}} = 60\,\mathrm{nm}$) due to its larger distance to P1 ($\sim 45 - 60\,\mathrm{nm}$ for Q2 in comparison to $\sim 10\,\mathrm{nm}$ for Q1).

In Fig. A.13 a, b we show l_{SO} extracted for different MW signal amplitudes A_{MW} for Q1 (red) and Q2 (blue) using the data from Fig. 4.2 i. From this data we estimate an average $l_{\mathrm{SO}} \sim 20 - 60\,\mathrm{nm}$. Using $E_{SO} = \hbar^2/(2m^* l^2_{\mathrm{SO}})$, l_{SO} can be converted into a spin-orbit energy $E_{\mathrm{SO}} \sim 30 - 150\,\mu\mathrm{eV}$ (see Fig. A.13 c, d) which is in good agreement with theoretical predictions for a Si nanowire with rectangular cross section of diameter $4 - 10\,\mathrm{nm}$ (green box) [KRL18].

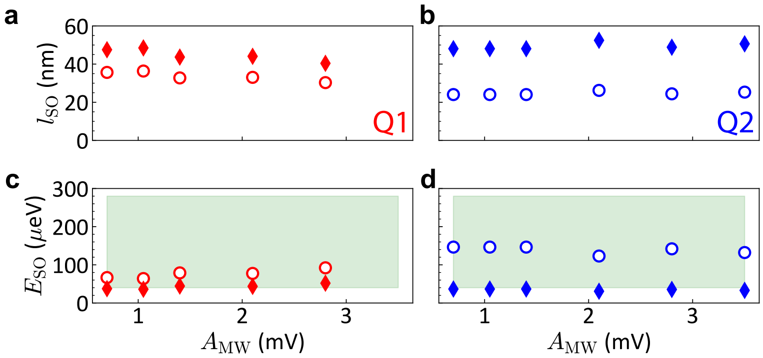

Fig. A.13.: **Spin-orbit length.** Estimated spin-orbit length l_{SO} using the data from Fig. 4.2 i for **a** Q1 (red) and **b** Q2 (blue). A distance $d_{dd} = 45\,\mathrm{nm}$ ($60\,\mathrm{nm}$) and a ratio of $E^{\mathrm{Q1}}_{\mathrm{MW}}/E^{\mathrm{Q2}}_{\mathrm{MW}} = 4$ (6) was used for the data depicted as diamonds (circles). **c**,**d** Spin-orbit energy E_{SO} corresponding to l_{SO} from **a** and **b**. The data is in good agreement with the theoretical prediction (green box) [KRL18].

A.3.8. Temperature dependence of Pauli spin blockade

In this section we discuss the temperature dependence of the Pauli spin blockade, which is closely linked to the temperature dependence of our qubit readout. Spin blockade is revealed by a suppression of current flow through the base of the bias triangles at $B_{\mathrm{ext}} = 0\,\mathrm{T}$, as shown in Fig. A.14 a. A finite magnetic field B_{ext} lifts PSB and a leakage current is observed (see Fig. A.14 b). The presence of a zero-field dip is an indication that lifting of PSB is dominated by spin-orbit interaction [DN09]. Note that the dip is offset from $B_{\mathrm{ext}} = 0\,\mathrm{T}$ due to trapped flux in the magnet.

Fig. A.14 c shows line-cuts of the leakage current along B_{ext} at $\varepsilon = 0$ for temperatures in the range of 1.5 to 14 K. The dips, that can be observed up to $\sim 12\,\mathrm{K}$, are well fitted by a Lorentzian function [DN09]. To characterise the efficiency of PSB we plot the dip amplitude A_{PSB} as a function of temperature T in Fig. A.14 d (left axis, purple data). We find that A_{PSB} shows a Gaussian decay with T.

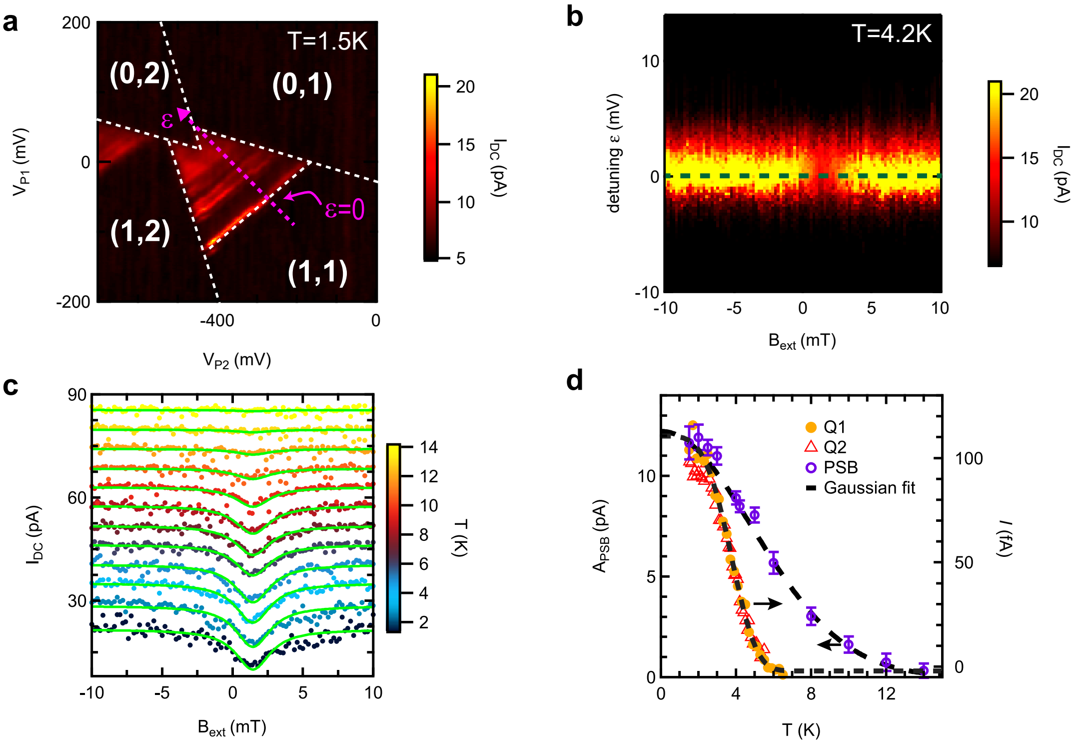

Fig. A.14.: **Spin blockade temperature dependence.** **a** Pair of bias triangles with detuning axis (pink arrow) at $V_{\mathrm{SD}} = 12\,\mathrm{mV}$. **b** Spin blockade leakage current as a function of magnetic field and detuning. Close to zero magnetic field the current is strongly suppressed, indicating Pauli spin blockade. In presence of spin-orbit interaction, spin blockade is lifted by applying a finite magnetic field. The dip offset from $B_{\mathrm{ext}} = 0\,\mathrm{T}$ is due to trapped flux in our magnet. **c** Line cuts along B_{ext} at $\varepsilon = 0$ at T = 1.5 to 14 K. The spin blockade efficiency decreases with increasing temperature, which is seen from the decay of the dip amplitude. **d** T-dependence of PSB efficiency A_{PSB} extracted from Lorentzian fits from the cuts in **c** (left axis, purple points). The data fit well to a Gaussian function $A_{\mathrm{PSB}} \propto \exp\left(-(T/T_A)^2\right)$ with width $T_A \approx 6.9 \pm 0.2\,\mathrm{K}$. The decay of the Rabi signals in both qubits (yellow/red symbols), on the other hand, shows a stronger temperature dependence and fits well to $I \propto \exp\left(-(T/T_I)^{\gamma}\right)$ with $\gamma \approx 4 \pm 0.2$ and $T_I \approx 4.1 \pm 0.1$.

Since our qubit readout scheme relies on PSB, we compare the PSB efficiency with our temperature-dependent qubit readout signal. In Fig. A.14 d the qubit readout current $I(t_b = t_\pi)$ after applying a π-pulse is shown for temperatures from 1.5 to 6.5 K (right axis, yellow and red data). I shows a stronger exponential decay with temperature than the Gaussian decay observed for A_{PSB}, such that the qubit readout only works up to $\sim$6 K. When comparing the decay of A_{PSB} and I, one has to take into account that EDSR experiments were performed at $B_{\mathrm{ext}} > 50\,\mathrm{mT}$. Therefore, A_{PSB} and I might have a different sensitivity to T.

PSB is protected against temperature by the single dot singlet-triplet splitting $\Delta_{\mathrm{Q1}} = 5.3\,\mathrm{meV}$ and $\Delta_{\mathrm{Q2}} = 3.3\,\mathrm{meV}$. Spin-flip co-tunnelling experiences a strong thermal smearing of $5.4\,k_B T$ [Kog04], such that the extracted orbital energies correspond to temperatures of 11 K and 7 K. This analysis suggests that the suppression of PSB with increasing temperature is in good agreement with spin-flip co-tunnelling.

A.3.9. EDSR SPECTRAL LINEWIDTH

We confirm the T_2^* temperature dependence presented in Fig. 4.3 d by measuring the EDSR linewidth in a continuous-wave experiment using low MW power to avoid power-broadening. A set of data for Q2 at $f_L \sim 8.8\,\mathrm{GHz}$ is shown Fig. A.15 for temperatures up to 6 K. A Gaussian function is fitted to the resonance to determine the full width at half maximum Δf_{FWHM}. The coherence time T_2^* is related to Δf_{FWHM} by [Han07; Kaw14]

$$T_2^* = \frac{2\sqrt{\ln 2}}{\pi \cdot \Delta f_{\mathrm{FWHM}}}. \tag{A.2}$$

In Fig. A.15 b the extracted temperature dependence of T_2^* is presented. The results from this continuous-wave experiment are in agreement with the pulsed experiments shown in Fig. 4.3 b-d.

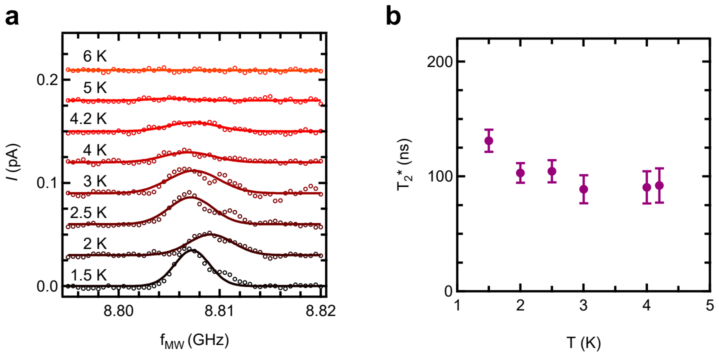

Fig. A.15.: T_2^* **temperature dependence extracted from EDSR linewidth measurements. a** Response of Q2 to a continuous-wave excitation at $f_L \sim 8.8\,\mathrm{GHz}$ for different temperatures. Close to the spin resonance condition, spin blockade is lifted and a current is detected. The width of the peak is related to the coherence time T_2^* by Eq. A.2. **b** Extracted T_2^* from the data shown in **a**.

A.3.10. LONGEST DEPHASING TIME T_2^*

In Fig. A.16 we show Ramsey fringes of Q2 with a decay time of $T_2^* = 441 \pm 34\,\mathrm{ns}$.

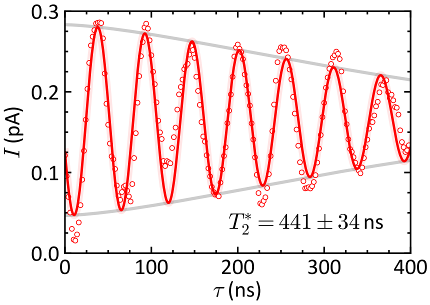

Fig. A.16.: **Ramsey experiment demonstrating a long coherence time.** A $T_2^* = 441 \pm 34\,\mathrm{ns}$ was obtained at $f_L = 5.85\,\mathrm{GHz}$ and T = 1.5 K for Q2. The data were taken on resonance with a τ-dependent phase $\phi(\tau)$, which adds an artificial oscillation [Wat18a]. The solid curve shows a fit to $A + B\sin(\omega\tau + \theta)\exp[-(\tau/T_2^*)^{\beta+1}]$ using $\beta = 0.88$ from Fig. 4.5 c.

A.3.11. HYPERFINE LIMIT OF T_2^*

In natural silicon there are 4.7% ^{29}Si spin-carrying isotopes present which will lead to dephasing of the qubit. In this section, we give an estimation of the dephasing time T_2^* limited by the finite hyperfine interaction due to the presence of these nuclear spins in the Si host material.

The maximum Overhauser field A experienced by an electron (e) in natural silicon is $A_e = 1.85\,\mathrm{mT}$ [Ass11]. Here, A corresponds to the field if all nuclear spins are polarised. For holes, the hyperfine interaction has been found to be about an order of magnitude weaker [Pri13; Pre16; FYI10; Voi15]. Thus, we assume $A_h \sim 0.185\,\mathrm{mT}$. The random Overhauser field fluctuations δA_h are given by

$$\delta A_h = A_h/\sqrt{N_S}, \tag{A.3}$$

where N_S is the number of non-zero nuclear spins inside the wave function of the QD [KLG02]. The spin coherence time is then

$$T_2^* = \frac{\hbar\sqrt{N_S}}{g\mu_B A_h}. \tag{A.4}$$

where g is the hole spin g-factor, μ_B is the Bohr magneton and $\hbar$ is the reduced Planck constant.

In order to estimate N_S, we need to calculate the volume of the QD. We assume a cylindrical hole wave function, elongated along the fin and with a diameter of $d \sim 5\,\mathrm{nm}$. For the dimension along the fin, we use the dimensions extracted from the singlet-triplet splitting: $l_{\mathrm{Q1}} = 5.7\,\mathrm{nm}$ and $l_{\mathrm{Q2}} = 7.1\,\mathrm{nm}$ (see also appendix A.3.7). For the density of silicon $\sim 50\,\text{atoms/nm}^3$ and 4.7% spin carrying ^{29}Si atoms, we find $N_S \sim 280$ ($N_S \sim 350$) in the left (right) QD.

Using the g-factors extracted from EDSR measurements (see Fig. 4.2 f), we find $T_2^* \sim 520\,\text{ns}$ for Q1 and $T_2^* \sim 490\,\text{ns}$ for Q2. The expected increase in coherence for holes in comparison to electron spin qubits [Kaw14] due to a smaller A_h is counteracted by our much smaller silicon hole spin qubits and thus a lower N_S. However, while for electrons in Si the hyperfine interaction is isotropic, it is anisotropic for holes. Therefore, we note that the estimated limit for T_2^* corresponds to the worst case scenario in terms of magnetic field orientation [Pre16].

Strikingly, these estimates match rather well with the longest T_2^* found in our experiments, see appendix A.3.10. This indicates that the residual nuclear spins of the host material may play an important role in limiting the coherence also for hole spin qubits. Furthermore, we estimate an increase to $T_2^* \sim 11\,\mu s$ ($\sim 4\,\mu s$) when the qubit is hosted in an isotopically purified ^{28}Si layer with 100 ppm (800 ppm) residual nuclear spins. These coherence times are comparable to the coherence of state-of-the-art electron spin qubits in isotopically enriched Si using micromagnets [Yon17], but the electron spin qubits still lack behind in operation speed in comparison to their hole counterparts.

A.3.12. SPIN RELAXATION TIME T_1

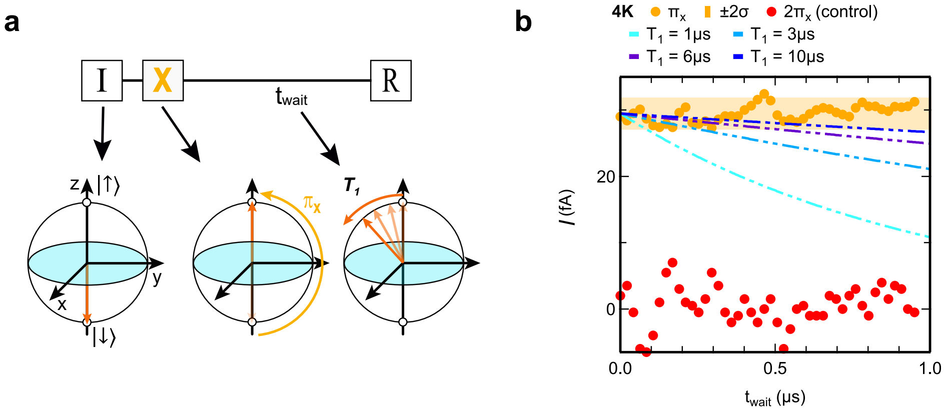

Fig. A.17.: **Spin relaxation. a** Qubit manipulation scheme to measure spin relaxation: after initialisation in the spin ground state $|{\downarrow}\rangle$, a π_x pulse brings the qubit into the spin excited state $|{\uparrow}\rangle$. On a timescale given by the spin relaxation time T_1, the spin polarisation decays from $|{\uparrow}\rangle$ to $|{\downarrow}\rangle$. After a waiting time t_wait, the residual polarisation $P_{|\uparrow\rangle}$ is measured. This polarisation is expected to show an exponential decay according to $P_{|\uparrow\rangle} \propto e^{-t_\text{wait}/T_1}$. **b** Orange data points shows the measurement results for Q2 at $\text{T} = 4\,\text{K}$ and $f_L = 7.7\,\text{GHz}$. No T_1-decay is observed for the maximum waiting time of $t_\text{wait} = 1\,\mu s$. Guides to the eye, showing the decay curves for $T_1 = 1, 3, 6$ and $10\,\mu s$, indicate $T_1 > 10\,\mu s$. The yellow shaded region shows the two-sigma uncertainty of the measured data. A control measurement with a $2\pi_x$ pulse (red data) instead of the π_x-gate shows that the current after a full 2π spin rotation becomes minimal as expected. The larger noise on the red data is due to a shorter integration time.

In Fig. A.17 we present an attempt to measure T_1 for Q2 at T = 4 K and $f_L = 7.7\,\text{GHz}$. The longest waiting time that could be applied was 1 μs. Guides to the eye show the expected decay curves for $T_1 = 1$, 3, 6 and 10 μs. The data suggest a spin relaxation time T_1 longer than 10 μs. Since T_1 is much longer than our measurement cycles, spin relaxation has no influence on our results. The observed relaxation rate is in good agreement with other experiments and theory [Cri19; Li20].

A.3.13. QUBIT QUALITY FACTOR

We show the dependence of the qubit quality on the MW signal power at 1.5 and 4.2 K. Because of limits on the maximal pulsing time impose by our read-out method, we could not observe T_2^{Rabi} in this experiment. Instead of the gate quality factor $Q = T_2^{\text{Rabi}} \cdot 2f_{\text{Rabi}}$, we therefore investigate a coherence-limited quality factor or qubit quality factor Q^* which we define as

$$Q^* = T_2^* \cdot 2f_{\text{Rabi}} = T_2^*/t_\pi \tag{A.5}$$

where t_π is the spin-flip time.

The data in Fig. A.18 were taken for Q2 at $f_L = 8.8\,\text{GHz}$, the same configuration as discussed in Fig. 4.3. As expected for a power-independent T_2^*, Q^* shows a roughly linear dependence on A_{MW} (see appendix A.3.3) due to a linear increase of f_{Rabi} on A_{MW} (see Fig. 4.2 i).

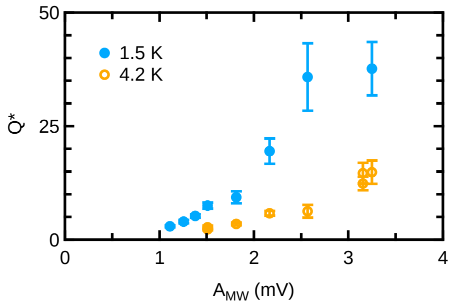

Fig. A.18.: **Qubit quality factor** $Q^* = T_2^* \cdot 2f_{\text{Rabi}}$ as a function of power at 1.5 and 4.2 K. These data were recorded on Q2 at $f_L = 8.8\,\text{GHz}$. The increase of Q^* with driving amplitude A_{MW} is due to faster Rabi oscillations and thus a shorter spin-flip time t_π.

A.3.14. DYNAMICAL DECOUPLING

In this section, we compare the extended coherence time from dynamical decoupling of Q2 for different numbers of decoupling pulses and temperatures. The measurements presented in Fig. A.19 show the normalised difference ΔI of the readout current measured after a projection of the qubit into $|\uparrow\rangle$ and $|\downarrow\rangle$. Ideally, if there is no free evolution of the qubit ($\tau = 0$), $\Delta I(\text{normalised}) = 1$ because the normalised current after projecting into $|\downarrow\rangle = 0$ and $|\uparrow\rangle = 1$. Due to decoherence, the signal decays with increasing τ on a time scale given by the coherence time T_2^* (Ramsey), T_2^{Hahn} (Hahn-echo), or T_2^{CPMG} (CPMG), depending on the pulsing scheme applied. We investigate the free induction decay (Ramsey), one decoupling pulse $n = 1$ (Hahn-echo) and $n = 2, 4, 8, 16$ and 32 decoupling pulses (CPMG-n). Schematics of the pulse sequences are shown at the top of Fig. A.19. Note that τ is defined as the free evolution time and thus equals the total time no gate is applied to the qubit. The generally observed decrease of the readout signal with higher temperatures (see Fig. A.14) was partially compensated by using shorter pulse cycles (and thus shorter maximal τ). As a consequence, the maximal τ differs for the different traces. In particular for the 4.2 K data, the signal was only measurable for a comparably short maximal $\tau \sim 1\,\mu s$.

For the Ramsey and Hahn-echo experiment, the signal of the full rotation of the second $\pi_\phi/2$ pulse was measured (from $\phi = 0$ to 2π) [Mau16]. The CPMG signal amplitude ΔI was obtained by measuring the difference in current between $\phi = 0$ and $\phi = \pi$, which corresponds to projection onto $|\uparrow\rangle$ and $|\downarrow\rangle$, respectively. These data are used to extract CPMG-n coherence times in Fig. 4.5 a and β in Fig. 4.5 c for 1.5 and 3 K.

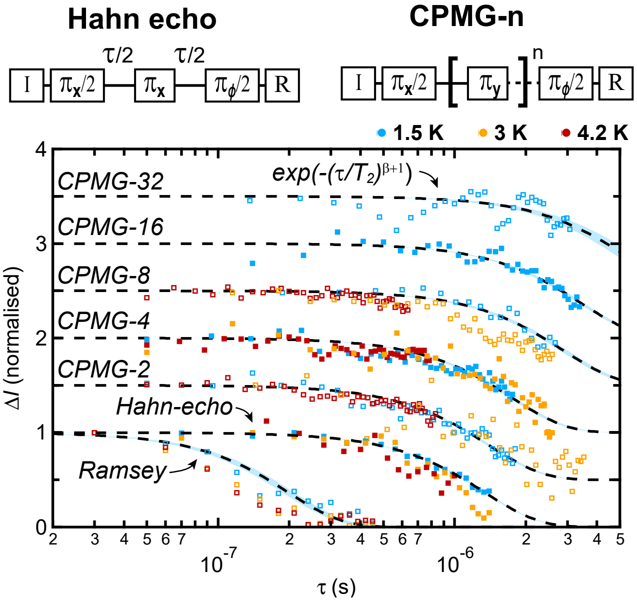

Fig. A.19.: **Active noise decoupling**. Decoupling of Q2 at $f_L = 8.8\,\mathrm{GHz}$ from low-frequency noise using Hahn-echo and CPMG-n decoupling schemes for 1.5 K (blue), 3 K (orange) and 4.2 K (red). This data was fitted to $\propto \exp\left(-\left(\tau/T_2\right)^{\beta+1}\right)$ (dashed curves) as discussed in the main text. β was obtained by iteratively fitting the decays to extract $T_2^{\mathrm{CPMG\text{-}n}}$ and fitting a power-law to the $T_2^{\mathrm{CPMG\text{-}n}}$ to extract β [Med12], as described in Fig. 4.5 a. The obtained CPMG coherence times are summarised in Fig. 4.5 a and the extracted β in Fig. 4.5 c for 1.5 and 3 K. Due to low signal-to-noise which only allowed for a short $\tau \sim 1\mu s$, it was not possible to reliably extract β from the data set at T = 4.2 K.

A.3.15. CLIFFORD BENCHMARKING PROTOCOL.

Randomised benchmarking is performed by applying a randomised sequence of a varying number of Clifford gates m before the spin state is rotated such that the final state ideally becomes either the $|\uparrow\rangle$ or $|\downarrow\rangle$ state. Each of the 24 gates in the Clifford group is constructed from the set $\{\mathrm{I}, \pm\mathrm{X}, \pm\mathrm{Y}, \pm\mathrm{X}/2, \pm\mathrm{Y}/2\}$ [Muh15]. The gate I is implemented as idle time for the duration of an X gate, which can limit the fidelity due to a finite T_2^*. Assuming that the qubit initial state is $|\downarrow\rangle$, a current flow is only observed when spin blockade is lifted for a final $|\uparrow\rangle$ state. Thus, the difference in current between sequences designed to output either a $|\uparrow\rangle$ or $|\downarrow\rangle$ state, $\Delta\mathrm{I} = \mathrm{I}^{|\uparrow\rangle} - \mathrm{I}^{|\downarrow\rangle}$, is proportional to $p_{\uparrow}^{|\uparrow\rangle} - p_{\uparrow}^{|\downarrow\rangle}$. For each m we average over 10 randomised sequences and the average Clifford-gate fidelity F_{c} is obtained from fitting the normalised current difference to $(2F_{\mathrm{c}} - 1)^m$. Since a Clifford gate consists of on average 1.875 gates, the average single-qubit gate fidelity F_{s} is derived by $F_{\mathrm{s}} = 1-(1-F_{\mathrm{c}})/1.875$.

A.4. HOLES SPIN QUBIT ANISOTROPY

A.4.1. QUBIT CHARACTERISTICS OF Q1/Q2 IN DEVICE C

Fig. A.20 shows characteristic measurements of the DQD as well as Q1/Q2 in Device C. The measurements in b-f are performed in the same way as described in chapter 4. A different method was used to extract qubit coherence [Mau16]: The Ramsey experiment is performed on resonance with the qubit frequency while we vary the waiting time τ_{Ramsey} of the Ramsey sequence and the phase ϕ_{Ramsey} of the second Ramsey pulse independently. The resulting data in Fig. A.20 g shows a signal that decays along the time axis and is sinusoidally modulated along the phase axis. Next, line cuts along ϕ_{Ramsey} for each τ_{Ramsey} are fitted by a cosine function (see inset of Fig. A.20 h) to extract the amplitude A. The decay of A as a function of τ_{Ramsey} is then fitted by $A(\tau) = A_0 \exp\left(-(\tau/T_2^*)^{1.6}\right)$ to extract the qubit coherence time T_2^*. We choose a decay exponent of 1.6, corresponding to a noise power spectral density scaling with $f^{-0.6}$, which is consistent with previous measurements (see chapter 4). The method is found particularly robust against small detunings or drifts of f_L compared to the Rabi frequency, since the additional rotation around the z-axis of the Bloch sphere adds to the phase ϕ_{Ramsey}, which is irrelevant for the extraction of A.[1]

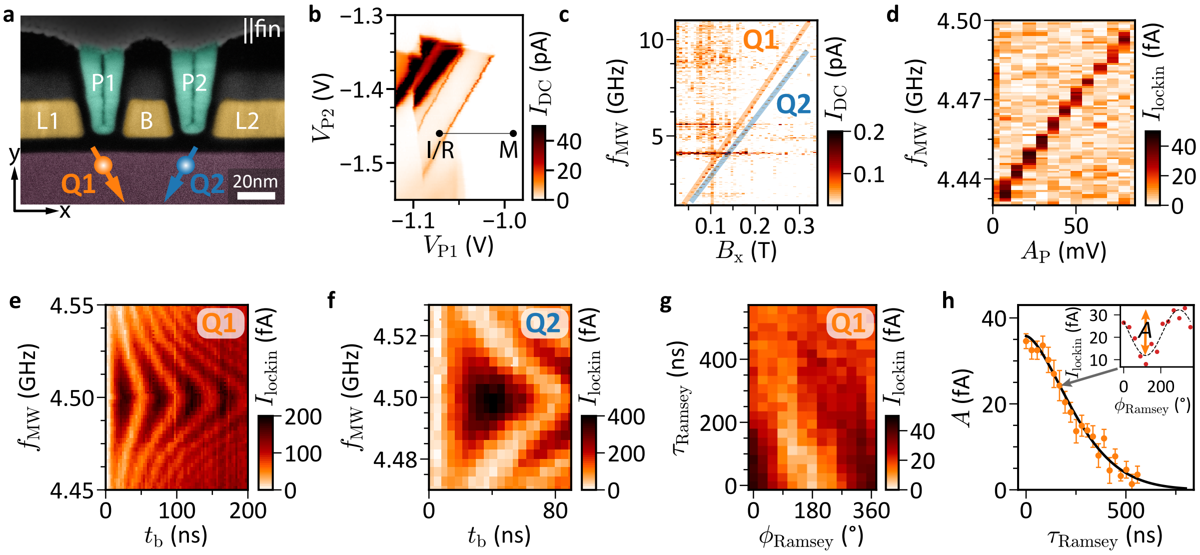

Fig. A.20.: **Device and qubit characteristics. a**, Device schematic indicating the expected location of Q1 and Q2. **b**, Charge stability map in the qubit operation regime for $V_{\mathrm{B}} = -0.75\,\mathrm{V}$ and $V_{\mathrm{SD}} = 10\,\mathrm{mV}$ indicating configurations for qubit initialisation/readout (I/R) and manipulation (M) point. **c**, EDSR resonance of Q1 and Q2 as function of magnetic field B_x orientated along x-axis when applying a MW burst to gate P1. **d**, Shift of qubit Larmor frequency when Coulomb pulse amplitude A_{P} is varied, i.e. the qubit manipulation point M is moved to I/R for $A_{\mathrm{P}} \to 0$. **e,f**, Rabi chevron measurement for Q1 and Q2 respectively. **g**, Ramsey experiment using the method of Ref. [Mau16] described in the text. **h**, Fitting of the Ramsey measurement data from **g** using $A(\tau) = A_0 \exp\left(-(\tau/T_2^*)^{1.6}\right)$, which yields $T_2^* = 305 \pm 11\,\mathrm{ns}$.

---

[1] We highly recommend this method over other methods to extract T_2^*. The downside is the amount of wave forms that have to be stored on the AWG, which can be tricky when using a Tektronix AWG5208. If memory is a limiting factor, the next best method was found to be an on-resonance 1D Ramsey measurement using an artificial oscillation. See chapter 4 for more details.

A.4.2. FITTING PROCEDURE FOR g-TENSORS

We follow the fitting procedure described by Ref. [Cri18]. We define the effective g-tensor $\hat{\mathbf{g}}$ via the Zeeman splitting $E_Z = \mu_B|\hat{\mathbf{g}}\mathbf{B}|$, where μ_B is Bohr's magneton and $\mathbf{B}$ is the magnetic field. We define the unit vector $\mathbf{b} = (\cos\varphi\sin\theta, \sin\varphi\sin\theta, \cos\theta)$ in direction of $\mathbf{B}$. From measurements we determine the absolute value of the magnetic field $B_{\text{abs}} = |\mathbf{B}|$ for each orientation (φ, θ) of the magnetic field, at which the qubit Larmor frequency $f_L = 4.5\,\text{GHz}$. Then, we fit the symmetric Zeeman tensor $\hat{\mathbf{G}}$ using the relation

$$^{t}\mathbf{b}\hat{\mathbf{G}}\mathbf{b} = {}^{t}\mathbf{b}({}^{t}\hat{\mathbf{g}} \cdot \hat{\mathbf{g}})\mathbf{b} = \frac{E_Z^2}{\mu_B^2 B_{\text{abs}}^2} = \frac{h^2 f_L^2}{\mu_B^2 B_{\text{abs}}^2}, \tag{A.6}$$

where h is Planck's constant. Since the tensor $\hat{\mathbf{G}}$ has to be symmetric, we have 6 degrees of freedom in this fit. This procedure is very stable and converges always to the same minimum. As a starting parameter we use the identity matrix.

Next, we exploit the fact that the principal axes of $\hat{\mathbf{G}}$ and $\hat{\mathbf{g}}$ are the same. We extract the eigenvalues e_i and eigenvectors $\mathbf{v}_i$ of $\hat{\mathbf{G}}$. The entries on the main diagonal of the g-tensor in its eigenbasis $\hat{\mathbf{g}}_e$ are now given by $g_{e,i} = \sqrt{e_i}$. We obtain for Q1/Q2:

$$\hat{\mathbf{g}}_e^{\text{Q1}} = \text{diag}\,(2.68, 1.68, 1.46)\,, \qquad \hat{\mathbf{g}}_e^{\text{Q2}} = \text{diag}\,(3.04, 1.62, 1.42)\,. \tag{A.7}$$

The g-tensor in the standard basis is obtained by the coordinate transformation up to a unitary transformation

$$\hat{\mathbf{g}} = \hat{\mathbf{S}}\hat{\mathbf{g}}_e\hat{\mathbf{S}}^{-1}, \tag{A.8}$$

where $\hat{\mathbf{S}} = (\mathbf{v_1}, \mathbf{v_2}, \mathbf{v_3})$. By following this procedure individually for both qubits we obtain the g-tensors reported in the main text.

A.4.3. MICROSCOPIC MODEL FOR g-TENSOR ANISOTROPY BASED ON STRAIN

This model is based on the microscopic models for g-tensor anisotropy described in the main text in section 5.1 and was also developed by the authors of Ref. [Sta21]. Here, the confinement orientation is constrained to the device geometry, but we add a strain term to the Hamiltonian $\mathcal{H}_{\text{LK}}$:

$$H_S = \frac{2}{3}\left[D_u\epsilon_{xx}J_x^2 + D'_u\epsilon_{xy}\frac{J_xJ_y + J_yJ_x}{2} + \text{c.p.}\right]. \tag{A.9}$$

Here, ϵ_{ij} are the elements of the symmetric 3x3 strain tensor and D_u and D'_u are material constants from Ref. [Win03]. For easier handling of the strain tensor, we parameterise it as

$\boldsymbol{\epsilon} = \mathrm{E}_{\alpha,\beta,\gamma} \cdot \boldsymbol{\epsilon}_0 \cdot \mathrm{E}_{\alpha,\beta,\gamma}$, where $\mathrm{E}_{\alpha,\beta,\gamma}$ is the Euler matrix parameterised by three angles and

$$\boldsymbol{\epsilon}_0 = \epsilon 10^{-|\epsilon|} \begin{pmatrix} 1+\sinh(\delta/2) & 0 & 0 \\ 0 & 1+\sinh(\delta/2) & 0 \\ 0 & 0 & -2 \end{pmatrix}. \tag{A.10}$$

The scalar parameters ϵ determines the strength of strain and is typically on the order of 4, whereas δ induces the asymmetry between the x and y axis in the eigenbasis of the strain tensor. Again, we parameterise the confinement by introducing r_{in} and r_{xy} analogue to the main text.

In Fig. A.21 we present the resulting fit of this model with 7 independent fitting parameters. We find three different local minima with different sets of starting parameters, which can be roughly described as a spherical dot (Fig. A.21 a, d and Tab. A.2), an elongated dot (Fig. A.21 b, e and Tab. A.3) and a disc-like dot (Fig. A.21 c, f and Tab. A.4). All three scenarios result ins similar residuals and seem to reproduce the data equally well. At the same time, some parameters reported in Tabs. A.2- A.4 show huge error bars. Therefore, we conclude that the fits of this model are not reliable, but a strain tensor can in principle reproduce the tilted g-tensor that is observed in the experiment.

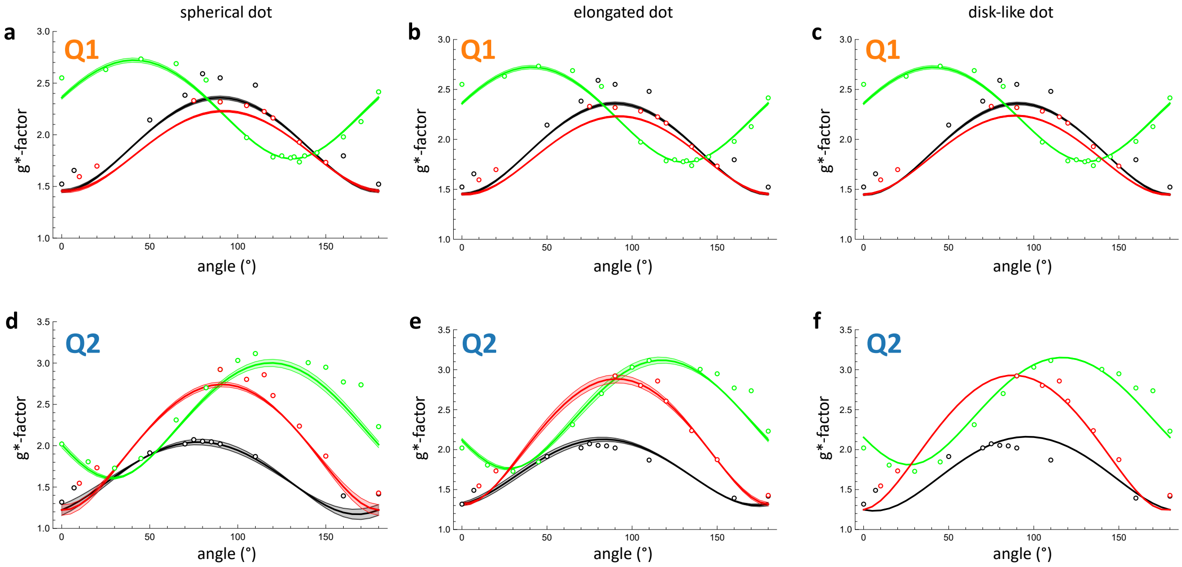

Fig. A.21.: **Fitting results of the strain model for different starting conditions.** Fit (lines) of measured g^*-factors (points) of Q1. Green, black and red correspond to the sweeps of ϕ at $\theta = 90°$, θ at $\phi = 0°$ and θ for $\phi = 90°$ respectively. **a**, Fit for Q1 with initial parameters of a spherical dot. **b**, Fit for Q1 with initial parameters of an elongated, cigar-like dot. **c**, Fit for Q1 with initial parameters of a disk-like dot. **d,e,f**, same analysis for Q2. The figure is adapted from Ref. [Sta21].

Tab. A.2.: Fitting parameters corresponding to the fits shown in Fig. A.21 a,d with a spherical dot as initial parameters.

parameter	fit value	error
ϵ	5.3	±4.4
δ	−27	±unknown
α	12°	±189°
β	102°	±60°
γ	−33°	±564°
r_{in}	1.08	±63%
r_{xy}	1.07	±101%
$l_x : l_y : l_z$	2.73 : 2.56 : 2.85	

parameter	fit value	error
ϵ	5.8	±24
δ	−8.8	±512
α	−76°	±44°
β	86°	±10°
γ	72°	±81°
r_{in}	1.005	±15%
r_{xy}	1	±10%
$l_x : l_y : l_z$	2.71 : 2.71 : 2.72	

Tab. A.3.: Fitting parameters corresponding to the fits shown in Fig. A.21 b,e with an elongated dot as initial parameters.

parameter	fit value	error
ϵ	5.3	±3.9
δ	−34	±unknown
α	12.5°	±202
β	102°	±67°
γ	−33°	±600°
r_{in}	1.09	±63%
r_{xy}	1.08	±101%
$l_x : l_y : l_z$	2.73 : 2.53 : 2.88	

parameter	fit value	error
ϵ	4.4	±0.9
δ	−8.4	±124
α	19°	±8°
β	1°	±12°
γ	−20°	±7°
r_{in}	2.4	±148%
r_{xy}	1.3	±21%
$l_x : l_y : l_z$	2.3 : 1.7 : 4.9	

Tab. A.4.: Fitting parameters corresponding to the fits shown in Fig. A.21 c,f with a disk-like dot as initial parameters.

parameter	fit value	error
ϵ	5.2	±3.6
δ	40	±unknown
α	12.4°	±207
β	79°	±70°
γ	−57°	±626°
r_{in}	1.1	±60%
r_{xy}	1.09	±113%
$l_x : l_y : l_z$	2.74 : 2.52 : 2.90	

parameter	fit value	error
ϵ	3.5	±6.5
δ	23	±unknown
α	−79°	±15°
β	86°	±2°
γ	−59°	±42°
r_{in}	25	±1900%
r_{xy}	0.93	±40%
$l_x : l_y : l_z$	0.88 : 0.96 : 24	

A.4.4. QUBIT DEPENDENCE ON FIELD AMPLITUDE

In Fig. A.22 we present measurements of the linear dependence of Rabi frequency f_{Rabi} on field amplitudes. Further, we observe and anti-proportional relation between the coherence time T_2^* and magnetic field amplitude.

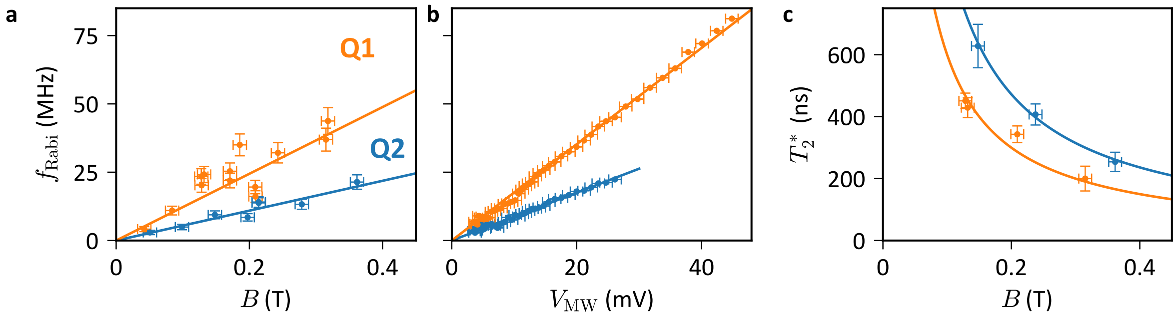

Fig. A.22.: **Qubit drive and coherence dependence on field amplitudes.** For both Q1 (orange) and Q2 (blue) we find a linear dependence of the Rabi frequency f_{R} on **a** the magnetic field amplitude B and **b** the electric driving field amplitude $V_{\mathrm{MW,P1}}$ as indicated by linear fits. **c**, We measure the qubit coherence time T_2^* for different magnetic field amplitudes B, which is fitted well by $T_2^* \propto 1/B$.

A.4.5. FITTING PROCEDURE FOR g-TENSOR DERIVATIVE

In this section we will describe the details of the fitting procedure to extract the full $\hat{\mathbf{g}}'$, following the recipe of Ref. [Cri18]. This elaborate fitting procedure is necessary since we cannot determine $\hat{\mathbf{g}}$ and $\hat{\mathbf{g}}'$ directly in the same Kramer's basis, as explained in the chapter 5. For this analysis to work we have to measure g^*, $\partial g^*/\partial V$ and f_{Rabi} for a few magnetic field orientations. The measurement data of $g^* = g^*(V_0)$, taken at a specific gate voltage V_0, is used to fit $\hat{\mathbf{g}}$ at V_0 with 6 independent fitting parameters according to appendix A.4.2 and is determined up to a unitary transformation (choice of spin basis). In this process, we also determined the symmetric Zeeman tensor $\hat{\mathbf{G}} = \hat{\mathbf{G}}(V_0)$ at V_0. Next, we use the measured $\partial g^*/\partial V$ and calculate $g^*(V_1) = g^*(V_0) + \delta V \partial g^*/\partial V$ for a small voltage difference $\delta V = V_1 - V_0$. Then, again following the method in appendix A.4.2, we extract $\hat{\mathbf{G}}(V_1)$ using 6 independent fitting parameters. We determine $\hat{\mathbf{G}}'(V_0) \approx [\hat{\mathbf{G}}(V_1) - \hat{\mathbf{G}}(V_0)]/\delta V$ valid for small δV. The contribution to $\hat{\mathbf{g}}'$ due to gTMR is now given by $\hat{\mathbf{g}}'_{\mathrm{TMR}} = {}^t\hat{\mathbf{g}}^{-1}\hat{\mathbf{G}}'/2$.

To determine the contribution to $\hat{\mathbf{g}}'$ that is responsible for IZR we write $\hat{\mathbf{g}}'_{\mathrm{IZR}} = {}^t\hat{\mathbf{g}}^{-1}\hat{\mathbf{A}}$ with antisymmetric matrix $\hat{\mathbf{A}} = [[0, a_1, a_2], [-a_1, 0, a_3], [-a_2, -a_3, 0]]$. Then, we use the measured data of f_{Rabi} to fit the four independent parameters a_1, a_2, a_3 and the correction factor β using the formula

$$f_{\mathrm{Rabi}} = |\mathbf{f}_{\mathrm{Rabi}}| = \frac{\mu_{\mathrm{B}} V_{\mathrm{MW}} \beta B}{2hg^*} \left|(\hat{\mathbf{g}}\mathbf{b}) \times ([\hat{\mathbf{g}}'_{\mathrm{IZR}} + \hat{\mathbf{g}}'_{\mathrm{TMR}}]\mathbf{b})\right|. \tag{A.11}$$

We introduce β to account for miss-calibrations of V_{MW} or a frequency dependence of the lever arm between the high-frequency calibration of V_{MW} and the low-frequency measurements of $g^{*\prime}$, which could be due to a frequency-dependent dielectric constant in the gate stack [Esr16] resulting in a frequency-dependence of the lever arm. Finally, we have determined $\hat{\mathbf{g}}' = \hat{\mathbf{g}}'_{\mathrm{IZR}} + \hat{\mathbf{g}}'_{\mathrm{TMR}}$ in the same basis as $\hat{\mathbf{g}}$.

The resulting $\hat{\mathbf{g}}'$ for both qubits and both driving gates are

$$\hat{\mathbf{g}}'^{\mathrm{Q1}}_{\mathrm{P1}} = \begin{pmatrix} -0.36 & 1.51 & 0.25 \\ 1.56 & -0.70 & -0.18 \\ 0.40 & -0.59 & -0.87 \end{pmatrix} \mathrm{V}^{-1}, \tag{A.12}$$

$$\hat{\mathbf{g}}'^{\mathrm{Q2}}_{\mathrm{P1}} = \begin{pmatrix} 0.17 & 0.30 & 0.19 \\ 0.22 & 0.54 & 0.12 \\ -0.20 & -0.15 & 0.12 \end{pmatrix} \mathrm{V}^{-1}, \tag{A.13}$$

$$\hat{\mathbf{g}}'^{\mathrm{Q1}}_{\mathrm{B}} = \begin{pmatrix} 0.61 & -0.89 & 0.32 \\ -1.10 & 0.67 & -0.41 \\ -1.30 & 0.88 & 0.25 \end{pmatrix} \mathrm{V}^{-1} \quad \text{and} \tag{A.14}$$

$$\hat{\mathbf{g}}'^{\mathrm{Q2}}_{\mathrm{B}} = \begin{pmatrix} 0.63 & -0.47 & 1.02 \\ -0.48 & -1.40 & 0.24 \\ -1.55 & 1.54 & -0.48 \end{pmatrix} \mathrm{V}^{-1}. \tag{A.15}$$

A.4.6. RABI FREQUENCY MODEL SEPARATED INTO IZR AND g-TMR CONTRIBUTIONS

We present the Rabi frequency obtained from only IZR or only g-TMR drive, disentangled as explained in the main text. Even though theoretical work is needed to connect the formalism of Ref. [GBL06] and Ref. [Cri18] in the case of an anisotropic g^*, we attempt to extract a rough estimate of the orientation of the spin-orbit orientation $\mathbf{n}_{\mathrm{so}}$. In our approximation we assume $\mathbf{b} \parallel \hat{\mathbf{g}}\mathbf{b}$, which is considerably violated since the orientation of the two vectors can disagree up to $\sim 23°$ (determined by numerically sampling the orientation of $\hat{\mathbf{g}}\mathbf{b}$). The model according to Ref. [Cri18] allows us to plot only the IZR contribution. To find $\mathbf{n}_{\mathrm{so}}$ in the formalism of Ref. [GBL06], we realise that $f_{\mathrm{R}} \propto |\mathbf{b} \times \mathbf{n}_{\mathrm{so}}| = 0$ when $\mathbf{b} \parallel \mathbf{n}_{\mathrm{so}}$. Thus, the orientation of minimum Rabi frequency is extracted for the IZR drive model for both qubits and both driving mechanisms and marked by a red circle in Figs. A.23 and A.24. The extracted orientations of $\mathbf{n}_{\mathrm{so}}$ are displayed in Tab. A.5. We observe a large spread of these values for different driving scenarios, but the y-axis (out-of-plane direction) given by $\theta = 90°, \phi = 90°$ can be roughly identified as centre with deviations of up to ∼ 40°. This is consistent with Rashba SOI which is perpendicular to the momentum vector, which we assume is along x. However, eq.(1.1) would indicate that the electric field in the device has to be along z, which is the in-plane orientation, to have $\mathbf{n}_{\mathrm{so}}$ along y. This is not expected, since the device exhibits a mirror symmetry along the z axis and the electric field is usually assumed to be within the xy plane. The differences between $\mathbf{n}_{\mathrm{so}}$ for Q1 and Q2 could be due to probing the SOI at different locations in the device, but the differences between the plunger drive and barrier drive case are likely due to the approximative character of this method.

The extracted orientation of the SOI vector disagrees with both the orientation obtained from the Pauli spin blockade leakage current measurement in chapter 3 and with the orientation obtained by mapping out exchange splitting in chapter 6. Due to the previously state concerns about the rough approximations made in this estimation, we conclude that this method might not be suitable in our device which exhibits a strong anisotropy in the g-tensor and the results might not be reliable.

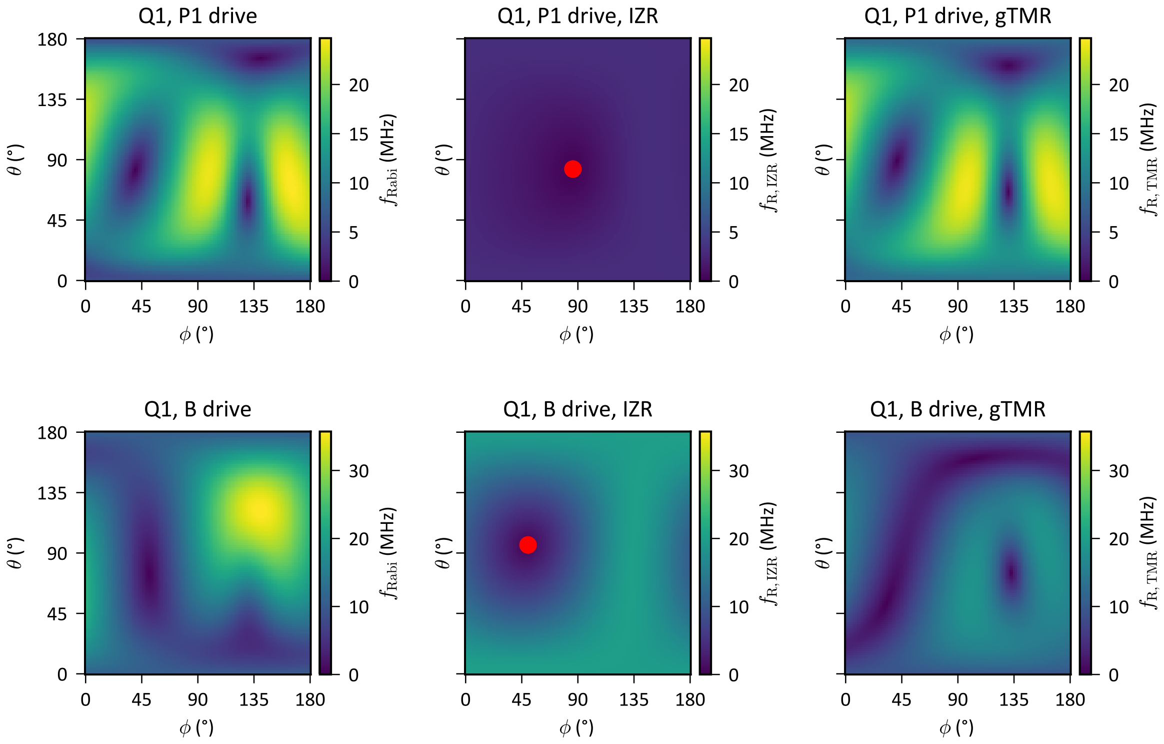

Fig. A.23.: **Q1 drive separated into IZR and g-TMR contributions.** We show the model prediction for $|\mathbf{f}_{\mathrm{Rabi}}|$, $|\mathbf{f}_{\mathrm{R,IZR}}|$ and $|\mathbf{f}_{\mathrm{R,TMR}}|$ for both driving gates P1 and B. The red dots mark the extracted orientations of $\mathbf{n}_{\mathrm{so}}$.

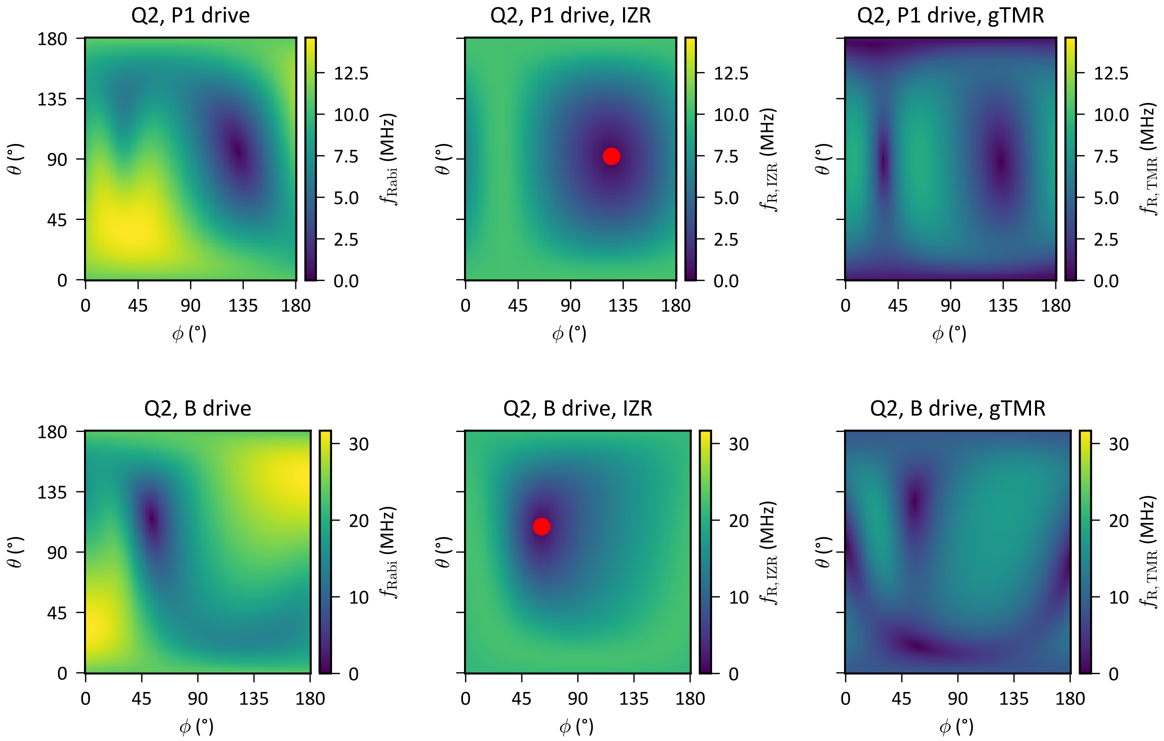

Fig. A.24.: **Q2 drive separated into IZR and g-TMR contributions.** We show the model prediction for $|\mathbf{f}_{\text{Rabi}}|$, $|\mathbf{f}_{\text{R,IZR}}|$ and $|\mathbf{f}_{\text{R,TMR}}|$ for both driving gates P1 and B. The red dots mark the extracted orientations of $\mathbf{n}_{\text{so}}$.

Tab. A.5.: Extracted orientations of n_{so} from IZR component of the Rabi drive. Note that this is only a rough approximation since the model does not account for an anisotropic g^*.

	n_{so} P1 drive		n_{so} B drive	
	θ_{so}	ϕ_{so}	θ_{so}	ϕ_{so}
Q1	83	86	96	50
Q2	92	125	109	61

A.4.7. Alternative fit for Q2

In this section we want to present an alternative fit for the plunger P1-driven Q2 Rabi frequency data. In contrast to the best fit in the main thesis, here we want to limit the parameter β, which is a correction factor for a frequency-dependence of the lever arm. In formula (A.11) we multiply V_{MW} and $\hat{\mathbf{g}}'$, which ideally cancels out the lever arm between the gate P1 and Q2, as both quantities are measured in terms of the gate voltage. However, these two quantities are recorded at different frequencies, such that a frequency-dependence of the lever arm has to be accounted for. When fitting this quantity we obtain a correction on the order of a few % for all configurations, except for $\beta = 2.5$ for P1-driven qubit Q2. Here we want to present a fit of $\hat{\mathbf{g}}'$ while assuming $\beta = 1$ similar to the three other scenarios (analogue to in appendix section A.4.5). We obtain

$$\hat{\mathbf{g}}'^{\mathrm{Q2}}_{\mathrm{P1}} = \begin{pmatrix} -1.29 & 10.05 & 9.75 \\ -6.28 & 2.17 & 5.37 \\ -11.33 & -7.19 & -0.54 \end{pmatrix} \mathrm{V}^{-1} \tag{A.16}$$

and see that the model also agrees quite well with the data (see Fig. A.25). Note that the matrix entries are now larger, as β is "absorbed" into the $\hat{\mathbf{g}}'$ matrix. Furthermore, we can again separate $\hat{\mathbf{g}}'$ into the driving contributions from IZR and g-TMR (see Fig. A.25) and extract the ratio of IZR and g-TMR (see Tab. A.6). From this analysis we can conclude that we are in the regime of predominant IZR driving, which we assume to be the case for strong electric fields along the fin, the weakest dimension of confinement. This might be the case, as P1 is far away from Q2 and is also discussed in Ref. [Din23]. The corresponding fit presented in the main text, where also β was fitted, showed an overall smaller residue, but involved one more fitting parameter. Our current data set, which only involves measurements of f_{Rabi} along three specific axes, might not be enough to precisely distinguish these two interpretations. Even though the fits both roughly fit within the three planes presented here, we note that visually their difference is larger in the plots where f_{Rabi} was predicted for the full surface of the sphere. Hence, we suggest that further measurements scanning the whole sphere could help to distinguish whether the model with fitted β or the model with $\beta = 1$ describe the setup more precisely. Furthermore, an analysis of the MW amplitude calibration uncertainty and an experimental investigation of the frequency dependence of lever arms could help to set boundaries for the fit of β.

Tab. A.6.: Extracted values of r, a and m for Q2 in the alternative fit using $\beta = 1$.

	plunger P1 drive		
	r_{P1}	a_{P1}	m_{P1}
Q2	0.740	0.809	0.788

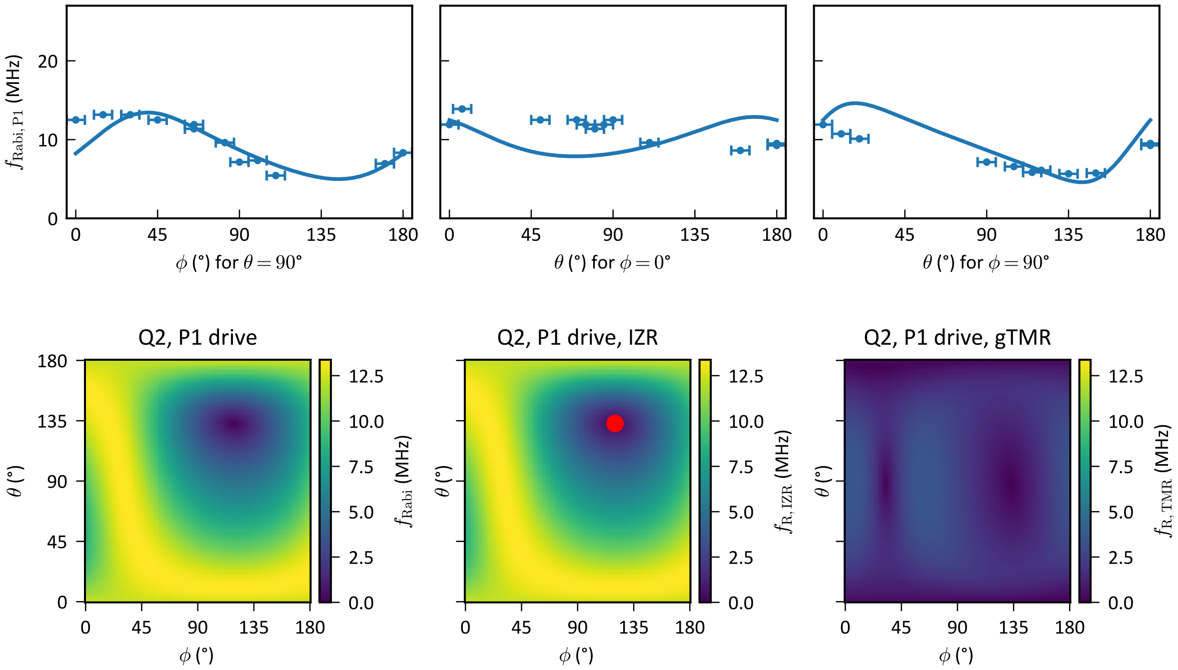

Fig. A.25.: **Alternative fit of Q2 using** $\beta = 1$ resulting in a spin-orbit orientation $\theta_{\mathrm{so}} = 133°$, $\phi_{\mathrm{so}} = 120°$ and ratios of IZR and g-TMR presented in Tab. A.6.

A.4.8. LEVER ARMS OF DEVICE C

In Tab. A.7 we report the lever arms of device C extracted following the method provided in Ref. [Wie02].

Tab. A.7.: Lever arms α of device C for different gates acting on Q1/Q2.

	α_{P1}	α_{B}	α_{P2}
Q1	0.125 ± 0.002	0.208 ± 0.005	0.007 ± 0.002
Q2	0.006 ± 0.002	0.214 ± 0.005	0.062 ± 0.002

A.5. Two-qubit gates with anisotropic exchange

Parts of this appendix section have been published in the supplementary material of S. Geyer *et al.*, Two-qubit logic with anisotropic exchange in a fin field-effect transistor, arXiv (2022), doi:10.48550/arXiv.2212.02308

A.5.1. Setup

This section describes the difference between the setup for the experiments in chapter 6 from the setup presented in section 4.1: a Signal Recovery 7265 lock-in amplifier was used to chop the MW signal of the VS via pulse modulation (PM) to create a reference cycle for the measurement (see Fig. A.26 a). A typical Rabi chevron is shown in Fig. A.26 c, where an increase in background current is observed. The origin of this effect is not yet fully understood, but might be due to photon-assisted PSB leakage current.

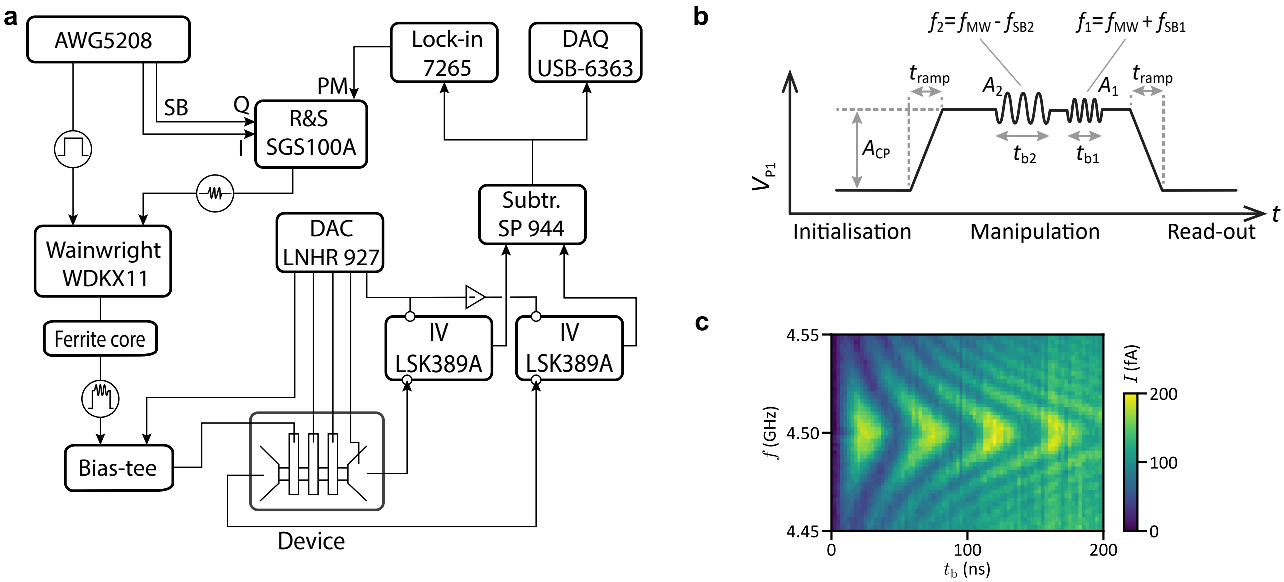

Fig. A.26.: **a**, Schematic of the setup of chapter 6. **b**, Typical pulse scheme to drive multiple qubits at different frequencies. **c**, Typical Rabi chevron measurement recorded around $f_L = 4.5\,\text{GHz}$ of Q1 showing Rabi oscillations of $f_{\text{Rabi}} \sim 20\,\text{MHz}$.

A.5.2. Spectroscopy data for qubit anisotropy characterisation

In Fig. A.27, we present the raw data of the qubit spectroscopy experiments that were used to extract the g-tensors of Q1 and Q2 and the exchange matrix $\mathcal{J}$. Furthermore, we observe correlations between the qubit readout signal in the lock-in current and the DC current measured at the base line of the bias triangle. Further investigation is required to fully understand this correlation.

Moreover, we observe an apparently frequency-independent increase of current whenever the two qubit frequency are close to degeneracy, as e.g. for $(\alpha, \beta) \approx (70°, 90°)$ or $(90°, 170°)$. This is yet another interesting feature of this data set, that is not yet fully understood and calls for further research.

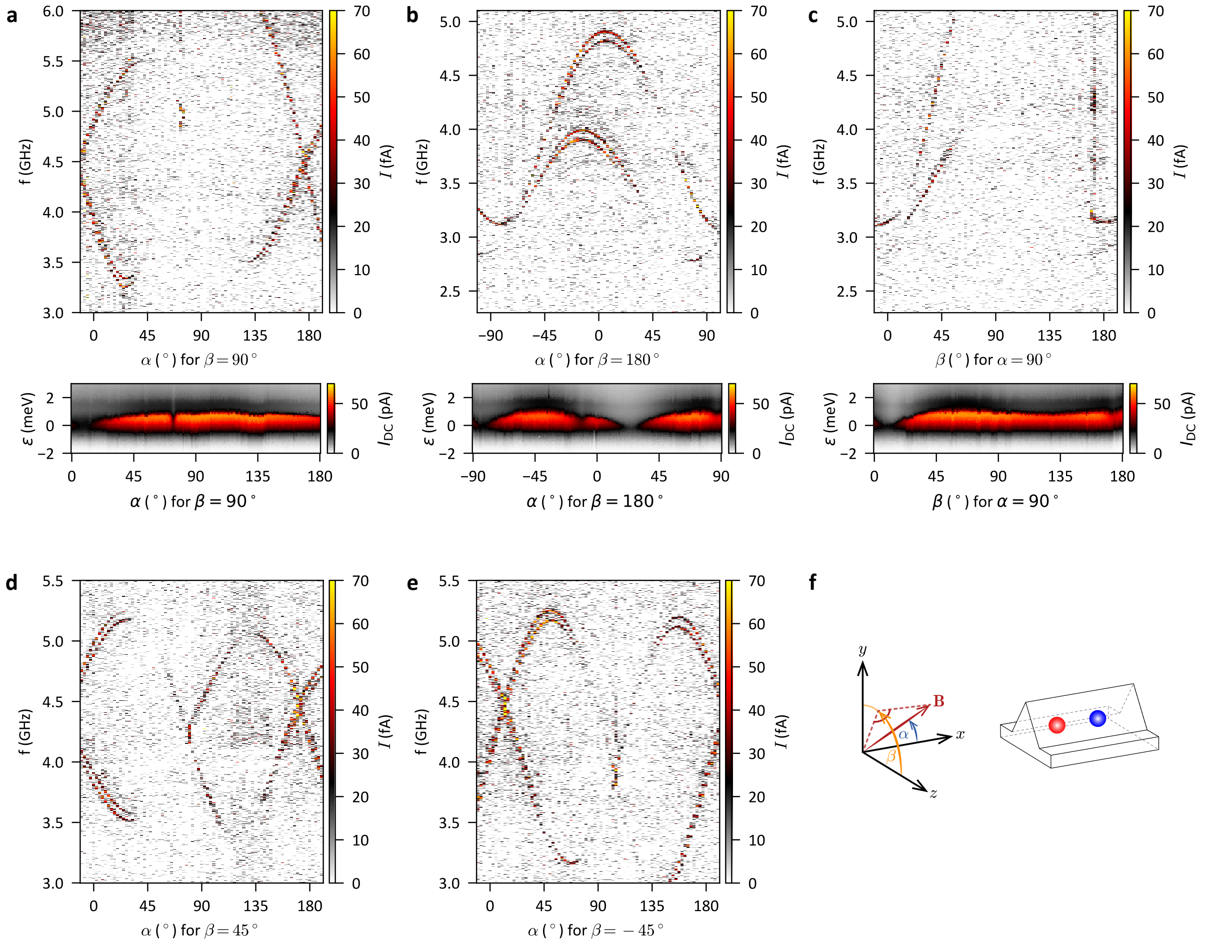

Fig. A.27.: **Qubit spectroscopy data. a-e**, Spectroscopy measurement as a function of magnetic field orientation (α, β) for sweeping $\mathbf{B}$ along 5 different planes with $V_B = -820\,\text{mV}$ and $\epsilon = -4.025\,\text{meV}$. For a fixed magnetic field orientation 4 transitions can be identified as described in Fig. 1, which allows to extract $E_{Z,i}$ and $J_{\parallel}$ for each configuration. The gaps in the data come from a vanishing qubit readout signal for certain magnetic field orientations. Note that for some orientations only 1-3 transitions are vanishing. For **a-c** we additionally show the direct current I_{DC} of the zero detuning transition of the DQD as a function of magnetic field orientation at $|\mathbf{B}| = 0.1\,\text{T}$. A correlation between a large current and a vanishing qubit visibility is observed. **f** Coordinate system and definition of the sweep parameters α and β.

A.5.3. *g*-TENSORS FOR Q1 AND Q2

The g-tensors were extracted according to A.4.2 and Ref. [Cri18] by measuring $E_{Z,i}$ by MW spectroscopy in at least 6 different orientations. The extraction was performed on the data presented in Fig. A.27.

$$g_1 = \begin{pmatrix} 2.31 & 0.50 & -0.06 \\ 0.50 & 2.00 & 0.06 \\ -0.06 & 0.06 & 1.50 \end{pmatrix}, \qquad g_2 = \begin{pmatrix} 1.86 & -0.57 & 0.09 \\ -0.57 & 2.76 & -0.01 \\ 0.09 & -0.01 & 1.46 \end{pmatrix} \tag{A.17}$$

The g-tensors can be diagonalised, such that the effective g-factors along the principal axes can be easily read off:

$$g_1^{\mathrm{diag}} = \mathrm{diag}\,(2.68, 1.68, 1.46)\,, \qquad g_2^{\mathrm{diag}} = \mathrm{diag}\,(3.04, 1.62, 1.42)\,. \tag{A.18}$$

A.5.4. 2-QUBIT INITIALISATION

The qubits are initialised by pulsing from the spin-blocked region to the (1,1) manipulation point with a linear ramp within the time t_{ramp}. By varying t_{ramp} and observing the allowed qubit transitions in a spectroscopy experiment (see Fig. A.28), we identify the necessary ramp time of $\sim 20\,\mathrm{ns}$ to initialise into the $|{\downarrow\uparrow}\rangle$ state. The background of the measurement shows an interference pattern. This could be explained by Landau-Zener-Stückelberg interference due to repeatedly pulsing the system across an anticrossing [SAN10].

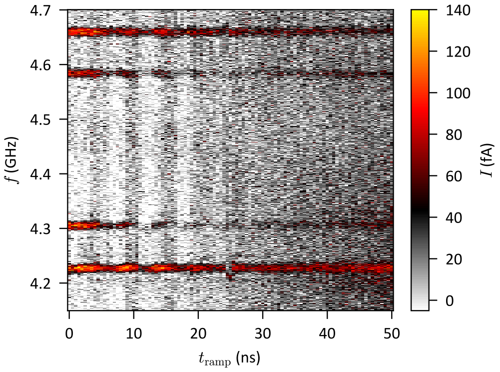

Fig. A.28.: **Qubit initialisation.** MW spectroscopy measurement as a function of ramp time t_{ramp} for a trapezoid initialisation and readout pulse (see section A.5.1). The vanishing contrast of the inner two transitions indicates an initialisation into the $|{\downarrow\uparrow}\rangle$ state, which only allows transitions with the highest and lowest frequency. This experiment was used to calibrate $t_{\mathrm{ramp}} \sim 20\,\mathrm{ns}$ for the CROT experiment in the main paper (see Fig. 6.4).

A.5.5. DERIVATION OF THE FIT FUNCTION FOR THE EXCHANGE MATRIX.

Using a Fermi-Hubbard model with a single orbital state $|i\rangle$ per site $i = \{1,2\}$, our DQD system is described by the Hamiltonian

$$H_{\mathrm{FH}} = \sum_{i,j\in\{1,2\}} \sum_{ss'\in\{\uparrow,\downarrow\}} \tilde{H}_{ij}^{ss'} a_{is}^{\dagger} a_{js'} + U \sum_{i\in\{1,2\}} n_{i\uparrow} n_{i\downarrow}\,. \tag{A.19}$$

Here $a^\dagger_{is}$ (a_{is}) creates (removes) a hole on site i and spin $s = \{|\uparrow\rangle, |\downarrow\rangle\}$, $n_{is} = a^\dagger_{is}a_{is}$ is the occupation number operator, and U is the charging energy. The single-particle Hamiltonian $\tilde{H}$ is given by

$$\tilde{H} = \frac{\tilde{\epsilon}}{2}\tau_z + t_c\cos(\theta_{\mathrm{so}})\tau_x + t_c\sin(\theta_{\mathrm{so}})\tau_y\mathbf{n}_{\mathrm{so}}\cdot\boldsymbol{\sigma} + \frac{1}{2}\mu_B\mathbf{B}\cdot\left[\frac{1+\tau_z}{2}g_1\boldsymbol{\sigma} + \frac{1-\tau_z}{2}g_2\boldsymbol{\sigma}\right], \tag{A.20}$$

and contains spin-conserving inter-dot tunnelling $t_c\cos(\theta_{\mathrm{so}})\tau_x$ and a SOI-induced spin-flip hopping term $t_c\sin(\theta_{\mathrm{so}})\tau_y\mathbf{n}_{\mathrm{so}}\cdot\boldsymbol{\sigma}$. Here (τ_x, τ_y, τ_z) are the Pauli matrices for the orbital degree of freedom, e.g. $\tau_z = |1\rangle\langle 1| - |2\rangle\langle 2|$ and $\boldsymbol{\sigma}$ is the vector of Pauli matrices acting on the spin degree of freedom. In the lab frame, as defined in Fig. 6.1, the g-tensors g_1 and g_2 are symmetric (see appendix A.5.3). Finally, $\tilde{\epsilon}$ is the energy difference for a hole occupying the left or the right QD, and is expressed in terms of the detuning energy ϵ between the (1,1) and (0,2) charge states by $\tilde{\epsilon} = \epsilon + U - U_0$.

We perform a transformation from the lab frame to the so-called "spin-orbit frame" and find

$$\tilde{H}^{\mathrm{so}} = U^\dagger_{\mathrm{so}}\tilde{H}U_{\mathrm{so}} = \frac{\tilde{\epsilon}}{2}\tau_z + t_c\tau_x + \frac{1}{2}\mu_B\mathbf{B}\cdot\left[\frac{1+\tau_z}{2}g_1^{\mathrm{so}}\boldsymbol{\sigma} + \frac{1-\tau_z}{2}g_2^{\mathrm{so}}\boldsymbol{\sigma}\right]. \tag{A.21}$$

In the spin-orbit frame non-spin-conserving tunnelling is gauged away by the unitary transformation $U_{\mathrm{so}} = \exp(-i\theta_{\mathrm{so}}\tau_z\mathbf{n}_{\mathrm{so}}\cdot\boldsymbol{\sigma}/2)$, and the g-tensors are given by $g_1^{\mathrm{so}} = g_1R_{\mathrm{so}}(\theta_{\mathrm{so}})$ and $g_2^{\mathrm{so}} = g_2R_{\mathrm{so}}(-\theta_{\mathrm{so}})$. Here $R_{\mathrm{so}}(\varphi)$ denotes a counterclockwise rotation around $\mathbf{n}_{\mathrm{so}}$ by an angle φ. Since our DQD system is operated close to the $|S_{02}\rangle$-$|S\rangle$ anticrossing, the Hamiltonian H_{FH} can be represented in the basis $\{|S_{02}\rangle, |S\rangle, |T_-\rangle, |T_+\rangle, |T_0\rangle\}$

$$H_{5\times5} = \begin{pmatrix} U_0-\epsilon & \sqrt{2}t_c & 0 & 0 & 0 \\ \sqrt{2}t_c & 0 & -\frac{\delta\mathrm{b}_x+i\delta\mathrm{b}_y}{\sqrt{2}} & \frac{\delta\mathrm{b}_x-i\delta\mathrm{b}_y}{\sqrt{2}} & \delta\mathrm{b}_z \\ 0 & -\frac{\delta\mathrm{b}_x-i\delta\mathrm{b}_y}{\sqrt{2}} & \bar{b}_z & 0 & \frac{\bar{b}_x-i\bar{b}_y}{\sqrt{2}} \\ 0 & \frac{\delta\mathrm{b}_x+i\delta\mathrm{b}_y}{\sqrt{2}} & 0 & -\bar{b}_z & \frac{\bar{b}_x+i\bar{b}_y}{\sqrt{2}} \\ 0 & \delta\mathrm{b}_z & \frac{\bar{b}_x+i\bar{b}_y}{\sqrt{2}} & \frac{\bar{b}_x-i\bar{b}_y}{\sqrt{2}} & 0 \end{pmatrix}, \tag{A.22}$$

where the average and gradient Zeeman fields $\bar{\mathbf{b}} = \mu_B\mathbf{B}(g_1^{\mathrm{so}} + g_2^{\mathrm{so}})/2$ and $\delta\mathbf{b} = \mu_B\mathbf{B}(g_1^{\mathrm{so}} - g_2^{\mathrm{so}})/2$ were introduced. In the spin-orbit frame, the singlet subspace $\{|S_{02}\rangle, |S\rangle\}$ is coupled by the total tunnel coupling t_c and the hybridised singlets $S_\pm$ have energies $E_{S_+} = U_0-\epsilon+J_0$ and $E_{S_-} = -J_0$ with $J_0 = \sqrt{2}\tan(\gamma/2) = -(U_0-\epsilon)[1-\sqrt{1+8t_c^2/(U_0-\epsilon)^2}]/2$ and mixing angle $\gamma = \arctan[\sqrt{8}t_c/(U_0-\epsilon)]$. Furthermore, we remark that $J_0 \simeq 2t_c^2/(U_0-\epsilon)$ in the limit of $t_c/(U_0-\epsilon) \ll 1$. Because S_+ couples only weakly to the triplet states, our Hilbert space can be restricted to the four levels $\{|S_-\rangle, |T_-\rangle, |T_+\rangle, |T_0\rangle\}$ and we obtain

$$H_{4\times4} = \begin{pmatrix} -J_0 & -\frac{\delta \mathrm{b}_x + i\delta \mathrm{b}_y}{\sqrt{2}}\cos(\frac{\gamma}{2}) & \frac{\delta \mathrm{b}_x - i\delta \mathrm{b}_y}{\sqrt{2}}\cos(\frac{\gamma}{2}) & \delta \mathrm{b}_z\cos(\frac{\gamma}{2}) \\ -\frac{\delta \mathrm{b}_x - i\delta \mathrm{b}_y}{\sqrt{2}}\cos(\frac{\gamma}{2}) & \bar{b}_z & 0 & \frac{\bar{b}_x - i\bar{b}_y}{\sqrt{2}} \\ \frac{\delta \mathrm{b}_x + i\delta \mathrm{b}_y}{\sqrt{2}}\cos(\frac{\gamma}{2}) & 0 & -\bar{b}_z & \frac{\bar{b}_x + i\bar{b}_y}{\sqrt{2}} \\ \delta \mathrm{b}_z\cos(\frac{\gamma}{2}) & \frac{\bar{b}_x + i\bar{b}_y}{\sqrt{2}} & \frac{\bar{b}_x - i\bar{b}_y}{\sqrt{2}} & 0 \end{pmatrix}. \tag{A.23}$$

Hole spin manipulation is performed deep in the (1,1) charge stability region, allowing us to introduce the localised spin operators $\boldsymbol{\sigma}_1^{\mathrm{so}}$ and $\boldsymbol{\sigma}_2^{\mathrm{so}}$. The Hamiltonian (A.23) can then be written as

$$H_{(1,1)}^{\mathrm{so}} = \frac{1}{2}\mu_B \mathbf{B}\cdot g_1^{\mathrm{so}}\boldsymbol{\sigma}_1^{\mathrm{so}} + \frac{1}{2}\mu_B \mathbf{B}\cdot g_2^{\mathrm{so}}\boldsymbol{\sigma}_2^{\mathrm{so}} + \frac{1}{4}J_0\boldsymbol{\sigma}_1^{\mathrm{so}}\cdot\boldsymbol{\sigma}_2^{\mathrm{so}}\,, \tag{A.24}$$

revealing that the exchange interaction is isotropic in the spin-orbit frame. To find an expression for the experimentally measured values, we first rewrite Eq. (A.24) in the lab frame

$$H_{(1,1)}^{\mathrm{lab}} = \frac{1}{2}\mu_B \mathbf{B}\cdot g_1\boldsymbol{\sigma}_1 + \frac{1}{2}\mu_B \mathbf{B}\cdot g_2\boldsymbol{\sigma}_2 + \frac{1}{4}\boldsymbol{\sigma}_1\cdot\mathcal{J}\boldsymbol{\sigma}_2\,. \tag{A.25}$$

Here $\mathcal{J} = J_0 R_{\mathrm{so}}(-2\theta_{\mathrm{so}})$ represents the exchange matrix in the lab frame, $\boldsymbol{\sigma}_1 = R^{\mathrm{so}}(-\theta_{\mathrm{so}})\boldsymbol{\sigma}_1^{\mathrm{so}}$ and $\boldsymbol{\sigma}_2 = R^{\mathrm{so}}(\theta_{\mathrm{so}})\boldsymbol{\sigma}_2^{\mathrm{so}}$. In addition, independent rotations R_1 and R_2 are applied to Q1 and Q2, such that the single particle terms of the Hamiltonian (A.25) become diagonal:

$$H_{(1,1)}^{\mathrm{Q}} = \frac{1}{2}E_{Z,1}\sigma_{z,1}^{\mathrm{Q}} + \frac{1}{2}E_{Z,2}\sigma_{z,2}^{\mathrm{Q}} + \frac{1}{4}\boldsymbol{\sigma}_1^{\mathrm{Q}}\cdot\mathcal{J}^{\mathrm{Q}}\boldsymbol{\sigma}_2^{\mathrm{Q}}\,, \tag{A.26}$$

where $E_{Z,i}\mathbf{e}_z^{\mathrm{Q}} = \mu_B R_i g_i \mathbf{B}$ is the i-th site's Zeeman splitting, $\mathbf{e}_z^{\mathrm{Q}}$ the spin quantisation axis and $\mathcal{J}^{\mathrm{Q}} = J_0 R_1 R_{\mathrm{so}}(-2\theta_{\mathrm{so}})R_2^T$ the exchange matrix in the so-called "qubit frame", wherein the exchange splitting $J_{\parallel}$ is experimentally observed. To obtain an expression for $J_{\parallel}$ we rewrite the Hamiltonian of Eq. (A.26) in matrix form using the two-qubit basis $\{|\uparrow\uparrow\rangle, |\uparrow\downarrow\rangle, |\downarrow\uparrow\rangle, |\downarrow\downarrow\rangle\}$

$$H_{(1,1)}^{\mathrm{Q}} = \begin{pmatrix} E_Z + \frac{1}{4}J_{zz}^{\mathrm{Q}} & 0 & 0 & 0 \\ 0 & \frac{1}{2}\Delta E_Z - \frac{1}{4}J_{zz}^{\mathrm{Q}} & \frac{1}{2}J_{\perp} & 0 \\ 0 & \frac{1}{2}(J_{\perp})^* & -\frac{1}{2}\Delta E_Z - \frac{1}{4}J_{zz}^{\mathrm{Q}} & 0 \\ 0 & 0 & 0 & -E_Z + \frac{1}{4}J_{zz}^{\mathrm{Q}} \end{pmatrix}. \tag{A.27}$$

Here we neglect every coupling that would contribute to the eigenvalues in $\mathcal{O}(J_0^2/E_Z)$ and introduce $J_{\perp} = [J_{xx}^{\mathrm{Q}} + J_{yy}^{\mathrm{Q}} + i(J_{xy}^{\mathrm{Q}} - J_{yx}^{\mathrm{Q}})]/2$, $E_Z = (E_{Z,1} + E_{Z,2})/2$ and $\Delta E_Z = E_{Z,1} - E_{Z,2}$. The eigenenergies of Eq. (A.27) are

$$E_{\uparrow\uparrow} = E_Z + \frac{1}{4}J_{zz}^{\mathrm{Q}}\,, \qquad E_{\downarrow\downarrow} = -E_Z + \frac{1}{4}J_{zz}^{\mathrm{Q}}\,, \tag{A.28a}$$

$$E_{\widetilde{\uparrow\downarrow}} = \frac{1}{2}\Delta\tilde{E}_Z - \frac{1}{4}J^{\mathrm{Q}}_{zz}\,, \qquad E_{\widetilde{\downarrow\uparrow}} = -\frac{1}{2}\Delta\tilde{E}_Z - \frac{1}{4}J^{\mathrm{Q}}_{zz}\,, \tag{A.28b}$$

with $\Delta\tilde{E}_Z = \sqrt{\Delta E_Z^2 + |J_\perp|^2}$. We thus find for the exchange splitting, which is defined as the energy difference between the two transitions flipping the same spin, $J_\parallel = E_{\uparrow\uparrow} - E_{\widetilde{\uparrow\downarrow}} - (E_{\widetilde{\downarrow\uparrow}} - E_{\downarrow\downarrow}) = J^{\mathrm{Q}}_{zz}$. The matrix element J^{Q}_{zz} in turn is given by

$$J^{\mathrm{Q}}_{zz} = J_\parallel = \mathbf{e}^{\mathrm{Q}}_z \cdot \mathcal{J}^{\mathrm{Q}}\mathbf{e}^{\mathrm{Q}}_z = \mathbf{n}_1 \cdot \mathcal{J}\mathbf{n}_2 = J_0\,\mathbf{n}_1 \cdot R_{\mathrm{so}}(-2\theta_{\mathrm{so}})\mathbf{n}_2\,. \tag{A.29}$$

Eq. (A.29) is the fit function employed to describe the observed exchange anisotropy, where the effect of both spin-orbit interaction and the anisotropy of the g-tensors is accounted for. We note that an explicit dependence on the magnetic field direction arises from $\mathbf{n}_i = g_i\mathbf{B}/|g_i\mathbf{B}|$. Further details of the derivation are found in Ref. [Gey22].

A.5.6. EXCHANGE MATRIX FOR ELECTRON QDS IN SILICON

Our analysis can be straightforwardly extended to the case of electron QDs in silicon where the SOI is induced by the gradient field of a micromagnet [Pio08; Noi22; Xue22]. The inhomogeneous magnetic field induced by the magnet is fixed in the lab frame as opposed to the external magnetic field, the direction of which needs to be changed in order to map out the g-tensors and the exchange matrix. The low-energy Hamiltonian of such a double QD system with two-electron occupation in the $(1,1)$ charge configuration is similar to Eq. (A.25) but needs to be extended by the magnetic field of the micromagnets as

$$H_{(1,1)} = \frac{1}{2}\mu_B(\mathbf{B}+\mathbf{M}_1)\cdot g_1\boldsymbol{\sigma}_1 + \frac{1}{2}\mu_B(\mathbf{B}+\mathbf{M}_2)\cdot g_2\boldsymbol{\sigma}_2 + \frac{1}{4}\boldsymbol{\sigma}_1\cdot\mathcal{J}\boldsymbol{\sigma}_2\,, \tag{A.30}$$

where $\mathbf{M}_i$ is the magnetic field induced by the micromagnet on site i, and the exchange matrix is still anisotropic due to the spin-flip tunnelling process induced by the spatially inhomogeneous magnetic field between the two QDs. In analogy with the case of SOI, the spin rotation angle can be estimated as $\tan(\theta_{\mathrm{so}}) \sim \mu_B|\mathbf{M}_1 - \mathbf{M}_2|/\hbar\omega_0$, where $\hbar\omega_0$ is the orbital splitting of the QD. Because this angle is typically small, the exchange interaction is roughly isotropic, in agreement with the fact that no exchange anisotropy was reported in recent works with micromagnets [Noi22; Xue22]. The strong exchange anisotropy to date is unique to hole systems with strong SOI. As it will be presented in the next section, this anisotropy can be the key to achieve fast and high-fidelity two-qubit gates for holes that keep up with the exceptionally fast single-qubit gates in these systems.

In the case of electrons, fitting the parameters of the model in Eq. (A.30) involves an additional step due to the field of the micromagnet. This field can be mapped out component by component, by changing the strength of the magnetic field along a given direction and determining the offset of the minimum of the Zeeman splitting with respect to $\mathbf{B} = 0$. Accounting for this fixed magnetic field on each QD, one could proceed to fit the g tensors and the exchange matrix as presented in appendix A.5.5 using $\mathbf{n}_j = g_j(\mathbf{B} + \mathbf{M}_j)/|g_j(\mathbf{B} + \mathbf{M}_j)|$.

A.5.7. THEORETICAL LIMIT OF THE CNOT GATE FIDELITY

In this section we calculate numerically the fidelity of a CNOT gate, implemented via a CROT and additional correction gates. For this purpose, we extend the qubit Hamiltonian including anisotropic exchange with a driving term. Using the rotating wave approximation (RWA), we show that Rabi oscillations for Q1 can be controlled by the state of Q2. We find sequences of single- and two-qubit gates to transform a CROT into a CNOT and simulate CNOT fidelities for anisotropic and isotropic exchange interaction. We show that for anisotropic exchange and certain magnetic field orientations, the CNOT gate errors are strongly reduced in comparison to isotropic exchange and faster gate speeds are possible. Further, we show that the CNOT gate fidelity for isotropic exchange is strongly limited by $J_\perp$.

Starting from Eq. (A.27) we add the drive $H_{\mathrm{MW}} = \nu_R \sin(\omega_{\mathrm{MW}} t)\sigma_{x,1}$ to Q1, where $\nu_R = hf_R$ is the strength of the drive for zero frequency detuning and ω_{MW} is the frequency of the drive, and obtain

$$H^Q_{(1,1)}(t) = \begin{pmatrix} E_Z + \frac{1}{4}J_\parallel & 0 & \nu_R \sin(\omega_{\mathrm{MW}} t) & 0 \\ 0 & \frac{1}{2}\Delta E_Z - \frac{1}{4}J_\parallel & \frac{1}{2}J_\perp & \nu_R \sin(\omega_{\mathrm{MW}} t) \\ \nu_R \sin(\omega_{\mathrm{MW}} t) & \frac{1}{2}(J_\perp)^* & -\frac{1}{2}\Delta E_Z - \frac{1}{4}J_\parallel & 0 \\ 0 & \nu_R \sin(\omega_{\mathrm{MW}} t) & 0 & -E_Z + \frac{1}{4}J_\parallel \end{pmatrix}. \tag{A.31}$$

The gate operation that is applied to the qubits in the experiment is found by numerically calculating the time evolution of the Hamiltonian in Eq. (A.31)

$$\mathrm{CROT}_{\mathrm{num}} = \mathcal{T} \exp\left[-\frac{i}{\hbar} \int_0^{t_\pi} dt H^Q_{(1,1)}(t) \right], \tag{A.32}$$

where t_π is the time needed to perform a spin-flip on the target qubit and $\mathcal{T}$ indicates the time-ordered exponential. Next, we want to compare the numerically computed CROT gate operation to a perfect CNOT gate. For this purpose, we need to apply a sequence of correction gates that turn a CROT into a CNOT, which can be identified by analysing the Hamiltonian (A.31) analytically.

First, we move to a rotating frame to eliminate the time-dependence in $H^Q_{(1,1)}(t)$, in which the Hamiltonian is given by

$$H_{\mathrm{rot}} = -i\hbar U^\dagger_{\mathrm{rot}} \dot{U}_{\mathrm{rot}} + U^\dagger_{\mathrm{rot}} H^Q_{(1,1)}(t)\, U_{\mathrm{rot}}\,, \tag{A.33}$$

where $U_{\mathrm{rot}}(t) = \mathrm{diag}[\exp(-i\omega_{\mathrm{MW}}t),\, 1,\, 1,\, \exp(i\omega_{\mathrm{MW}}t)]$ is the transformation between the rotating frame and the qubit frame. Using the RWA we drop the rapidly oscillating terms, e.g., $\propto \exp(-i2\omega_{\mathrm{MW}}t)$, and find

$$H_{\mathrm{RWA}} = \begin{pmatrix} E_Z + \frac{1}{4}J_\parallel - \hbar\omega_{\mathrm{MW}} & 0 & \frac{i}{2}\nu_R & 0 \\ 0 & \frac{1}{2}\Delta E_Z - \frac{1}{4}J_\parallel & \frac{1}{2}J_\perp & \frac{i}{2}\nu_R \\ -\frac{i}{2}\nu_R & \frac{1}{2}(J_\perp)^* & -\frac{1}{2}\Delta E_Z - \frac{1}{4}J_\parallel & 0 \\ 0 & -\frac{i}{2}\nu_R & 0 & -E_Z + \frac{1}{4}J_\parallel + \hbar\omega_{\mathrm{MW}} \end{pmatrix}. \tag{A.34}$$

Then, we transform to the eigenbasis of the Hamiltonian (A.27). This transformation accounts for the mixing of $|{\uparrow\downarrow}\rangle$ and $|{\downarrow\uparrow}\rangle$ basis states by $J_\perp$ and is defined as $\tilde{H}_{\mathrm{RWA}} = U^\dagger_{\phi,\xi} H_{\mathrm{RWA}} U_{\phi,\xi}$, where the transformation matrix is given by

$$U_{\phi,\xi} = \begin{pmatrix} 1 & 0 & 0 & 0 \\ 0 & \cos\frac{\phi}{2} & -e^{-i\xi}\sin\frac{\phi}{2} & 0 \\ 0 & e^{i\xi}\sin\frac{\phi}{2} & \cos\frac{\phi}{2} & 0 \\ 0 & 0 & 0 & 1 \end{pmatrix}, \tag{A.35}$$

with $\exp(i\xi) = J_\perp/|J_\perp|$ and the mixing angle $\phi = \arctan(|J_\perp|/\Delta E_Z)$. Note that this transformation commutes with $U_{\mathrm{rot}}(t)$. We obtain

$$\tilde{H}_{\mathrm{RWA}} = \begin{pmatrix} -\frac{1}{2}\Delta\tilde{E}_Z - \frac{1}{4}J_\parallel & \frac{i}{2}e^{i\xi}\nu_R\sin\frac{\phi}{2} & \frac{i}{2}\nu_R\cos\frac{\phi}{2} & 0 \\ -\frac{i}{2}e^{i\xi}\nu_R\sin\frac{\phi}{2} & \frac{1}{2}\Delta\tilde{E}_Z - \frac{1}{4}J_\parallel & 0 & \frac{i}{2}\nu_R\cos\frac{\phi}{2} \\ -\frac{i}{2}\nu_R\cos\frac{\phi}{2} & 0 & -\frac{1}{2}\Delta\tilde{E}_Z - \frac{1}{4}J_\parallel & -\frac{i}{2}e^{-i\xi}\nu_R\sin\frac{\phi}{2} \\ 0 & -\frac{i}{2}\nu_R\cos\frac{\phi}{2} & \frac{i}{2}e^{-i\xi}\nu_R\sin\frac{\phi}{2} & \frac{1}{2}\Delta\tilde{E}_Z + \frac{3}{4}J_\parallel \end{pmatrix}, \tag{A.36}$$

where we substituted the resonance condition for the transition that we want to drive, i.e. $|{\downarrow\uparrow}\rangle \to |{\uparrow\uparrow}\rangle$, as $\hbar\omega_{\mathrm{MW}} = E_Z + \frac{1}{2}\Delta\tilde{E}_Z + \frac{1}{2}J_\parallel$. We note that, depending on the sign of $J_\parallel$, we obtain a CROT or a not-controlled rotation (NCROT). In the RWA Hamiltonian we call the off-diagonal terms that connect degenerate states *resonant* transitions, i.e. $|{\downarrow\uparrow}\rangle \to |{\uparrow\uparrow}\rangle$, whereas terms connecting two states that are not degenerate are the *off-resonant* transitions. Off-resonant transitions are highly suppressed by the energy mismatch, hence we neglect all off-resonant terms. Note that off-resonant terms that include $\sin(\phi/2)$ vanish completely for $\phi = 0$, i.e. $J_\perp = 0$, reducing the error introduced by the approximation for this specific case.

Next, we calculate the complete time evolution of the qubit states. Within the rotating frame and the RWA, the time evolution of a state in the qubit frame is given by $|\psi(t)\rangle = U_{\mathrm{rot}}(t)U_{\mathrm{RWA}}(t)\,|\psi(0)\rangle$, where $U_{\mathrm{RWA}}(t)$ is the free time evolution according to the RWA Hamiltonian (A.34). Because $U_{\phi,\xi}$ commutes with the rotating frame transformation U_{rot}, one may write $U_{\mathrm{rot}}(t)U_{\mathrm{RWA}}(t) = U_{\phi,\xi}U_{\mathrm{rot}}(t)\exp(-i/\hbar\tilde{H}_{\mathrm{RWA}}t)U^{\dagger}_{\phi,\xi} = U_{\phi,\xi}U_{\mathrm{rot}}(t)\tilde{U}_{\mathrm{RWA}}(t)U^{\dagger}_{\phi,\xi}$. The full time evolution under the Hamiltonian in the mixed basis is then

$$\begin{aligned}\widetilde{\mathrm{CROT}} =& U_{\mathrm{rot}}(t_\pi)\tilde{U}_{\mathrm{RWA}}(t_\pi) = \\ & \begin{pmatrix} 0 & 0 & e^{i\pi\kappa\left(-\frac{E_Z}{J_\parallel}-\frac{1}{4}\right)} & 0 \\ 0 & e^{i\pi\kappa\left(-\frac{\Delta\tilde{E}_Z}{2J_\parallel}+\frac{1}{4}\right)} & 0 & 0 \\ -e^{i\pi\kappa\left(\frac{\Delta\tilde{E}_Z}{2J_\parallel}+\frac{1}{4}\right)} & 0 & 0 & 0 \\ 0 & 0 & 0 & e^{i\pi\kappa\left(\frac{E_Z}{J_\parallel}-\frac{1}{4}\right)} \end{pmatrix},\end{aligned} \tag{A.37}$$

where the operation time for a π-rotation is $t_\pi = h/(2\nu_R\cos(\phi/2))$ and we imposed $\nu_R\cos(\phi/2) = J_\parallel/\kappa$ with $\kappa = \sqrt{16k^2-1}$ and k is an integer as in Ref. [Rus18]. These conditions restrict the maximal driving strength to $\nu_R = J_\parallel/\sqrt{15}$, but ensure that no net spin rotation of Q1 occurs for the $|{\downarrow}\rangle$-state of the control qubit Q2. This is standard practise to reduce fidelity loss due to off-resonant driving effects [Noi22].

The controlled rotation in the mixed basis in Eq. (A.37) is now compared to an ideal CNOT, which is controlled by Q2 and targeted on Q1, in the basis $\{\uparrow\uparrow,\uparrow\downarrow,\downarrow\uparrow,\downarrow\downarrow\}$

$$\mathrm{CNOT} = \begin{pmatrix} 1 & 0 & 0 & 0 \\ 0 & 0 & 0 & 1 \\ 0 & 0 & 1 & 0 \\ 0 & 1 & 0 & 0 \end{pmatrix}. \tag{A.38}$$

This allows us to find a sequence of elementary single-qubit gates such that

$$\widetilde{\mathrm{CROT}} = e^{i\pi(\Delta E_Z/2\nu_R + J_\parallel/4\nu_R + 1)}\, X_1\, Z_2^{E_{Z,2}/\nu_R+1/2}\, Z_1^{-E_{Z,1}/\nu_R+1/2}\, \mathrm{CNOT}\, Z_1^{-J_\parallel/2\nu_R+1/2}. \tag{A.39}$$

Here, Z_i is the Z-gate with the convention $(-1)^a = e^{i\pi a}$ and X_i is the X-gate acting on the ith qubit. We consider the gate $Z_i^a = (Z_i)^a$ as directly accessible for spin qubits, since arbitrary Z-rotations can be implemented e.g. by an arbitrary detuning pulse [Cam22; Yon17] or by virtual phase gates [Noi22]. Note that the decomposition into correction gates is not unique.

If $U_{\phi,\xi} = 1$ at $\phi = 0$, hence the mixed basis is equal to the qubit basis, the CNOT gate can be constructed from the CROT gate using Eq. (A.39). However, having a finite mixing angle ϕ, i.e. $J_\perp \neq 0$, we also have to account for the additional transformation $\mathrm{CROT} = U_{\phi,\xi}\,\widetilde{\mathrm{CROT}}\,U^{\dagger}_{\phi,\xi}$. Hence, we have to decompose $U_{\phi,\xi}$ into elementary gates

$$U_{\phi,\xi} = Z_1^{-\xi/\pi-1/2}\, X_1\, (\mathrm{CZ})^{\phi/2\pi}\, X_1\, X_2\, (\mathrm{CZ})^{\phi/2\pi}\, X_2\, (\mathrm{SWAP})^{-\phi/\pi}\, Z_1^{\xi/\pi+1/2}, \tag{A.40}$$

where the controlled-Z gate (CZ) is controlled by Q1 and targeted on Q2. Note that this decomposition contains in addition to elementary single-qubit gates also multiple two-qubit gates. Introducing additional two-qubit gates creates new sources for errors, that can lower the overall-fidelity of the CNOT gate. Additionally, this creates a large overhead of correction gates, making it desirable to work in the regime of $\Delta E_Z \gg J_\perp$, where $U_{\phi,\xi} \approx 1$. Further, since SWAP and CZ gates typically require opposite regimes of $\Delta E \ll J_\parallel$ and $\Delta E \gg J_\parallel$, these correction gates are not practical in any experimental realisation and will only be considered here to investigate the sources of errors.

Finally, we define $\mathrm{CNOT}_{\mathrm{num}}$ as the numerically simulated CROT gate from Eq. (A.32) after applying single-qubit correction gates as described in Eq. (A.39). The fidelity of this two-qubit gate is then calculated by comparing it to the ideal CNOT gate:

$$\mathcal{F} = \frac{1}{4}\mathrm{Tr}\left[\mathrm{CNOT}_{\mathrm{num}}\mathrm{CNOT}^\dagger\right] , \tag{A.41}$$

Analogously, we define $\mathrm{CNOT}^{\phi,\xi}_{\mathrm{num}}$ as the numerically simulated CROT gate from Eq. (A.32) after applying both the single-qubit correction gates from Eq. (A.39) as well as the single- and two-qubit correction gates from eq. (A.40) and calculate the fidelity analogously.

We present the numerical simulations of the fidelity (see Fig. A.29) for four different cases, which differ by the exchange interaction (isotropic vs anisotropic exchange) and the correction gates that are applied (only single-qubit corrections or both correction sequences). The simulation is performed by calculating the time evolution operator U with the full time-dependence of Eq. (A.32). Due to discretisation of time, a small numerical error caused by the numerical precision is added in every time step. This contribution is not unitary and leads to $|\mathrm{Tr}[U^\dagger U]/4| \lesssim 1$. Therefore, we associate $1 - |\mathrm{Tr}[U^\dagger U]/4|$ with the precision of our calculations and plot it as error bar in Fig. A.29. We present the CNOT fidelity as a function of $J_\parallel/\Delta E_Z$. Since $J_\parallel = \sqrt{15}\nu_R$ was fixed for maximal driving strength without inducing unwanted off-resonant driving, this can be seen as evaluating the fidelity as a function of gate speed. We note that for a small gate speed, requiring more time steps, the error bars are increased. Overall, we see a drop of fidelity with gate speed, which is much more pronounced for isotropic than anisotropic exchange. For the case of isotropic exchange, the fidelity drops rapidly for large $J_\parallel/\Delta E_Z$, even when applying all correction gates ($\mathrm{CNOT}^{\phi,\xi}_{\mathrm{num}}$). This loss of fidelity can be understood as the effect of the off-resonant terms that were neglected in eq. (A.36), which become relevant at large driving strength. When looking at isotropic exchange and only single-qubit correction gates ($\mathrm{CNOT}_{\mathrm{num}}$), we see a further reduction of fidelity, which originates from the strong mixing of qubit basis states due to large $J_\perp = J_\parallel$. This is the dominant effect for the loss of fidelity of the CNOT gate at small driving speeds $J_\parallel/\Delta E_Z < 0.5$. Note that the wiggle features in the fidelity probably originate from an interplay of the single-qubit correction gates and the unwanted effects of $U_{\phi,\xi}$ that are not corrected here. Comparing

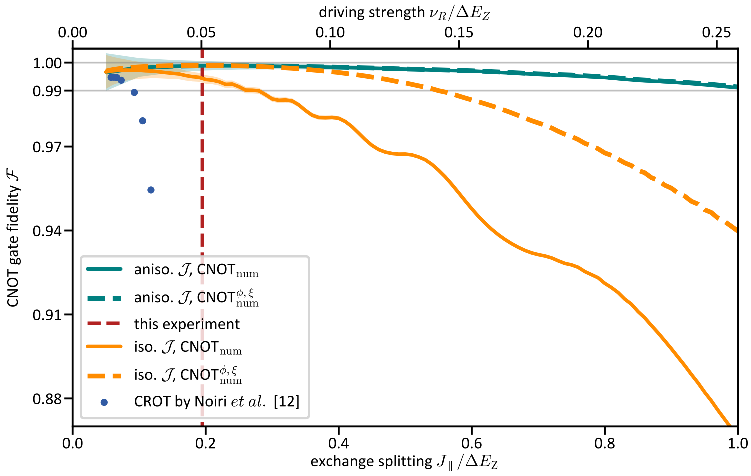

Fig. A.29.: CNOT gate fidelities as a function of $J_{\parallel}$ and driving strength ($\nu_R = J_{\parallel}/\sqrt{15}$) using (i) anisotropic exchange interaction (green) for the configuration used in Fig. 6.4; (ii) and isotropic exchange interaction (orange) e.g. for electrons in silicon. CNOT gates obtained using single-qubit correction gates only ($\mathrm{CNOT}_{\mathrm{num}}$) are shown as solid lines, while CNOT gates also corrected for basis mixing errors ($\mathrm{CNOT}^{\phi,\xi}_{\mathrm{num}}$) are shown as dashed lines. Red line and blue points indicate the working point of the present experiment and fidelities measured in Ref. [Noi22], respectively. The horizontal grey line marks the fault tolerance threshold ($\mathcal{F} = 99\%$). The shaded regions indicate the precision of the numerics.

the theoretical fidelity to current experimental realisations of CROT gates with isotropic exchange, e.g. Noiri *et al.* [Noi22], we find that the fidelity seem to be limited mainly by the experimental implementation. Further, these experiments are performed at very small driving strength, where the maximum theoretical CNOT fidelity is not significantly limiting the fidelity of the implemented gate.

In the anisotropic case, the fidelity depends on the magnetic field orientation, since it determines $J_{\perp}$. Here, we look at the case of the magnetic field orientation and $\mathcal{J}$ of the CROT experiment in Fig. 6.4 of the main text. In Fig. A.30 we show $J_{\parallel}$ and $J_{\perp}$ as a function of magnetic field orientation and indicate the orientation that was used with a red star, showing a large $|J_{\parallel}| = 0.902 J_0$ and small $|J_{\perp}| = 0.049 J_0$. We note that there is a large range of orientations, where such a combination of $|J_{\parallel}|/|J_{\perp}| \gg 1$ can be found. In this case, the fidelity stays above the threshold for error correction of 99% up to strong driving of $J_{\parallel}/\Delta E_Z \sim 1$. There is almost no difference between $\mathrm{CNOT}_{\mathrm{num}}$ and $\mathrm{CNOT}^{\phi,\xi}_{\mathrm{num}}$, indicating that the basis mixing by $U_{\phi,\xi}$ is not limiting the fidelity. This is expected, since for the chosen magnetic field orientation $|J_{\perp}| \ll \Delta E_Z$ and thus $U^{\phi,\xi} \sim 1$. The main reduction in fidelity originates from neglecting the off-resonant terms and the rapidly oscillating terms in the RWA. Hence, two-qubit correction gates, which are relevant in the isotropic case already at small driving strength, are not needed here. For much stronger driving $J_{\parallel}/\Delta E_Z \gtrsim 0.5$ the benefits for fidelity of anisotropic exchange become even stronger: In this regime, even when using the impractical two-qubit correction gates, the fidelity for isotropic exchange is limited to much smaller values than for anisotropic

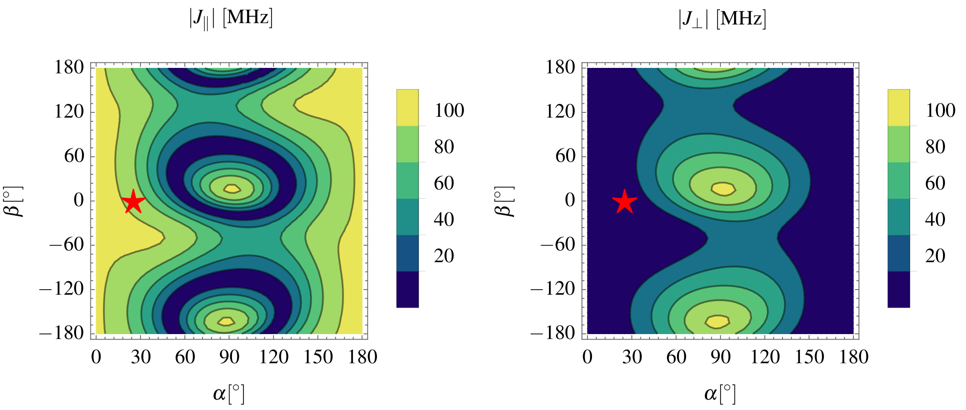

Fig. A.30.: Exchange interaction $|J_\parallel|$ and $|J_\perp|$ as a function of magnetic field orientation (α, β), using the experimental g-tensors, spin rotation angle θ_{so} and SOI orientation $\mathbf{n}_{\mathrm{so}}$. Red stars denote the magnetic field direction used for the implementation of the CROT gate in the main paper and for calculating the gate fidelity in Fig. A.29.

exchange.

The red dashed line in Fig. A.29 indicates the value of $J_\parallel/\Delta E_Z \sim 0.2$ that was used in this experiment, showing that the fidelity of our CROT implementation is not significantly limited by the maximum theoretical fidelity. However, for isotropic exchange this diving strength would already induce a significant reduction of fidelity, unless the very hard to realise and computationally demanding two-qubit correction gates are implemented. Hence, this experiment already benefits from the anisotropic exchange interaction.

A.6. Phase drive for hole spin qubits

Parts of this appendix section have been published in the supplementary material of S. Bosco *et al.*, Phase driving hole spin qubits, arXiv (2023), doi:10.48550/arXiv.2303.03350

A.6.1. Additional measurements of our first and second device

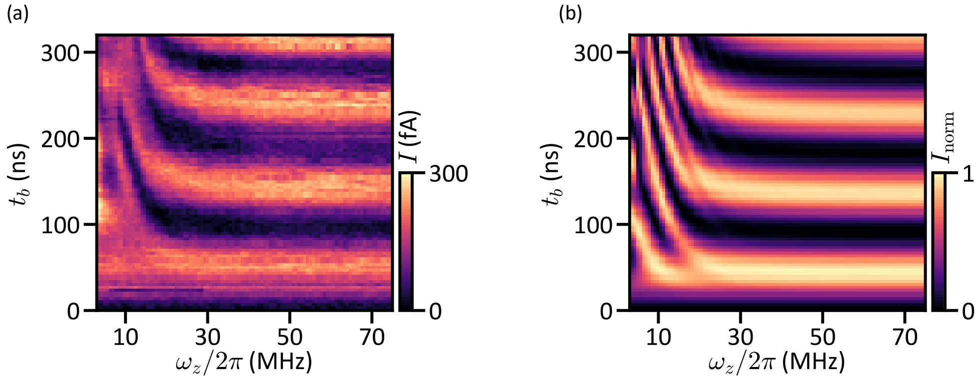

Fig. A.31.: Phase-driving-induced slowing down of Rabi oscillations in qubit 2 (Q2). Measurements (a) and simulations (b) match well, and this trend is analogous to the one reported in chapter 7 for Q1, see Fig. 7.1(b),(c). Here, we used $\omega_x/2\pi = \omega_q/2\pi = 3.115\,\mathrm{GHz}$, $\lambda_x/2\pi = 11$ MHz, and $\lambda_z/2\pi = 6.1$ MHz.

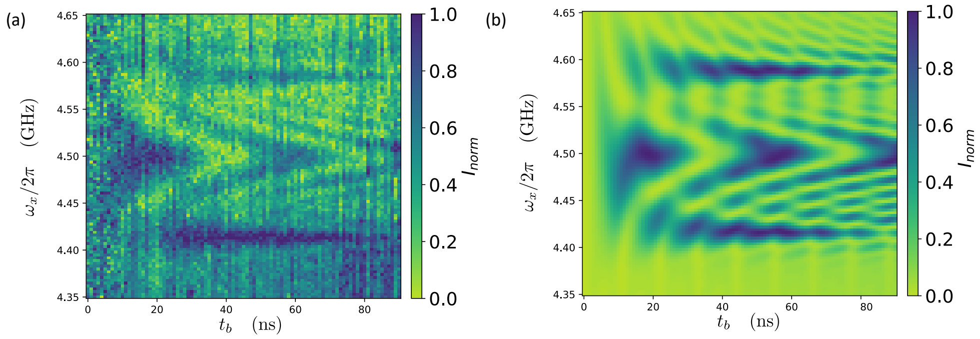

Fig. A.32.: Phase-driving-induced sideband Rabi oscillations in qubit 1 (Q1). Measurements (a) and simulations (b) are in good agreement, and these sidebands are analogous to the ones reported in the main text for Q2, see Fig. 2(b),(e). Here, we used $\omega_q/2\pi = 4.5\,\mathrm{GHz}$, $\lambda_x/2\pi = \lambda_z/2\pi = 30$ MHz, and $\omega_z/2\pi = 90.5$ MHz, corresponding to $Z = 0.33$.

We present here additional data from our two qubits, Q1 and Q2, encoded in two different devices. In Fig. 7.1, we show the slowing down of Rabi oscillations by phase driving Q2. Compared to Figs. 1(b),(c) in the main text, we observe a similar trend, with a lower Rabi and phase driving amplitudes. The measurement in Fig. 7.1(a) matches well the numerical simulation in Fig. 7.1(b). In Fig. A.32, we show phase-driving-induced sideband oscillations appearing at finite detuning in Q1. These results are comparable to the ones obtained for Q2 and shown in Figs. 7.2(b),(e). Also in this case, we observe a good agreement between measurements (a) and simulations (b).

CV

Simon Geyer

Birth	15th February 1996, Lörrach, Germany
Citizenship	German

Education

2019–2023	PhD in Physics at University of Basel, Switzerland on “Spin Qubits in Silicon Fin Field-Effect Transistors”
2017–2019	MSc in Physics at University of Basel, Switzerland Thesis: “Quantum Dots in Silicon CMOS FinFETs”
2017	Semester abroad at University of Lund, Sweden
2014–2017	BSc in Physics at University of Basel, Switzerland
2006–2014	Abitur at Hans-Thoma-Gymnasium Lörrach, Germany

Honours and awards

2023	American Physical Society Distinguished Students Award 2023 in Las Vegas, USA
2022	Swiss Nanotechnology PhD Prize 2022 from Swiss MNT in Fribourg, Switzerland
2022	Excellent Paper Award from NCCR SPIN for L.C. Camenzind, S. Geyer *et al.*, Nat Electron **5**, 178-183 in Pontresina, Switzerland

LIST OF PUBLICATIONS

1. Self-aligned gates for scalable silicon quantum computing
   Simon Geyer, Leon C. Camenzind, Lukas Czornomaz, Veeresh Deshpande, Andreas Fuhrer, Richard J. Warburton, Dominik M. Zumbühl and Andreas V. Kuhlmann
   Appl. Phys. Lett. **118**, 104004 (2021), doi:10.1063/5.0036520

2. Cross-architecture Tuning of Silicon and SiGe-based Quantum Devices Using Machine Learning
   Brandon Severin, Dominic T. Lennon, Leon C. Camenzind, Florian Vigneau, Federico Fedele, Daniel Jirovec, Andrea Ballabio, Daniel Chrastina, Giovanni Isella, Mathieu de Kruijf, Miguel J. Carballido, Simon Svab, Andreas V. Kuhlmann, Floris R. Braakman, Simon Geyer, Florian N. M. Froning, Hyungil Moon, Michael A. Osborne, Dino Sejdinovic, Georgios Katsaros, Dominik M. Zumbühl, Andrew D. Briggs and Natalia Ares
   arXiv:2107.12975 (2021)

3. Identifying Pauli spin blockade using deep learning
   Jonas Schuff, Dominic T. Lennon, Simon Geyer, David L. Craig, Federico Fedele, Florian Vigneau, Leon C. Camenzind, Andreas V. Kuhlmann, G. Andrew D. Briggs, Dominik M. Zumbühl, Dino Sejdinovic and Natalia Ares
   arXiv:2202.00574 (2022)

4. A hole spin qubit in a fin field-effect transistor above 4 kelvin
   Leon C. Camenzind*, Simon Geyer*, Andreas Fuhrer, Richard J. Warburton, Dominik M. Zumbühl and Andreas V. Kuhlmann
   Nature Electronics **5**, 178-183 (2022), doi:10.1038/s41928-022-00722-0

5. Two-qubit logic with anisotropic exchange in a fin field-effect transistor
   Simon Geyer, Bence Hetényi, Stefano Bosco, Leon C. Camenzind, Rafael S. Eggli, Andreas Fuhrer, Daniel Loss, Richard J. Warburton, Dominik M. Zumbühl and Andreas V. Kuhlmann
   arXiv:2212.02308 (2022)

---

* these authors contributed equally

6. Spin Qubits in Silicon FinFET Devices
Andreas Fuhrer, Michele Aldeghi, Toni Berger, Leon C. Camenzind, Rafael S. Eggli, Simon Geyer, Patrick Harvey-Collard, Nico W. Hendrickx, Eoin G. Kelly, Leonardo Massai, Matthias Mergenthaler, Peter Müller, Andreas V. Kuhlmann, Taras Patlatiuk, Stephan Paredes, Felix J. Schupp, Gian Salis, Lisa Sommer, Konstantinos Tsoukalas, Noelia Vico Trivino, Richard J. Warburton, Dominik M. Zumbühl
2022 IEDM, San Francisco, USA, doi: 10.1109/IEDM45625.2022.10019477 (2022)

7. Cryogenic hyperabrupt strontium titanate varactors for sensitive reflectometry of quantum dots
Rafael S. Eggli, Simon Svab, Taras Patlatiuk, Dominique Trüssel, Miguel J. Carballido, Pierre Chevalier Kwon, Simon Geyer, Ang Li, Erik P. A. M. Bakkers, Andreas V. Kuhlmann, Dominik M. Zumbühl
arXiv:2303.02933 (2023)

8. Phase driving hole spin qubits
Stefano Bosco, Simon Geyer, Leon C. Camenzind, Rafael S. Eggli, Andreas Fuhrer, Richard J. Warburton, Dominik M. Zumbühl, J. Carlos Egues, Andreas V. Kuhlmann and Daniel Loss
arXiv:2303.03350 (2023)

9. A compact and versatile cryogenic probe station for quantum device testing
Mathieu de Kruijf, Simon Geyer, Toni Berger, Matthias Mergenthaler, Floris Braakman, Richard J. Warburton and Andreas V. Kuhlmann
Rev. Sci. Instrum. **94**, 054707 (2023), doi: 10.1063/5.0139825 (2023)